

Admittance and noise detection in mesoscopic systems via GHz impedance matching

Inauguraldissertation

zur
Erlangung der Würde eines Doktors der Philosophie
vorgelegt der
Philosophisch-Naturwissenschaftlichen Fakultät
der Universität Basel

VON

**Vishal Ranjan
aus Indien**

Basel, 2017

Genehmigt von der Philosophisch-Naturwissenschaftlichen Fakultät
auf Antrag von

Prof. Dr. Christian Schönenberger

Prof. Dr. Hugues Pothier

Dr. Mark Buitelaar

Basel, 21.02.2017

Prof. Dr. Martin Spiess
Dekan

Contents

1. Introduction	1
1.1. Mesoscopic transport	1
1.2. Signal and noise	2
1.3. Thesis outline	3
2. Theoretical background	5
2.1. Graphene	5
2.2. From graphene to carbon nanotubes	7
2.3. InAs nanowires	8
2.4. Different transport regimes	9
2.5. Quantum dots	10
2.5.1. Single quantum dots	10
2.5.2. Double quantum dots	14
2.6. Quantum dots coupled to superconductors	15
2.6.1. Andreev transport	16
2.6.2. Josephson effect	18
2.6.3. Competing Kondo effect	19
2.7. Noise characterisation	20
2.7.1. Thermal noise	22
2.7.2. Shot noise	22
2.7.3. Flicker noise	24
3. Impedance Matching	25
3.1. Transmission line theory	26
3.1.1. Terminated transmission lines	27
3.2. Coplanar transmission lines	28
3.2.1. Kinetic inductance	29
3.2.2. Superconducting resonators	30
3.2.3. Microwave losses in superconducting resonators	32
3.3. Stub tuner	33
3.3.1. Impedance matching for lossless case	34
3.3.2. Reflectance response	36
3.3.3. Effect of losses	38
3.3.4. Measurement bandwidth	38
3.3.5. Output impedance	39
3.3.6. Transmission function	40
3.3.7. Figure of merit	42
3.3.8. Open stub tuner measurements	43
3.3.9. Why 50 Ω ?	44

4. Device fabrication, measurement and characterization techniques	45
4.1. Nb stub tuner	45
4.2. CNT devices	46
4.2.1. Deterministic CNT device	46
4.2.2. Probabilistic CNT device	49
4.2.3. Superconducting contacts	51
4.3. InAs-Al nanowire devices	53
4.3.1. Nanowire deposition and localization	53
4.3.2. NW etching and metallization	54
4.4. Graphene devices	55
4.5. Measurement setup	56
4.5.1. Dilution refrigerator	56
4.5.2. Fridge wiring	57
4.5.3. RF dipstick	59
5. Reflectometry of CNT Quantum Dots using GHz matching circuits	61
5.1. Matching at high impedance	62
5.2. Single quantum dot regime	63
5.2.1. High frequency conductance	64
5.3. Double quantum dot regime	66
5.3.1. Inter-dot coupling	68
5.3.2. Dipole coupling of hybridized double dots to a resonator	69
5.3.3. Dephasing of hybridized double dots	71
5.4. Triple quantum dot regime	72
5.5. Summary and discussion	73
6. Quantum Capacitance and Dissipation in Graphene p-n junctions	75
6.1. Device layout	75
6.1.1. Measurement principle	76
6.2. Reflectance results	78
6.2.1. Quantum capacitance	79
6.2.2. Renormalization of Fermi velocity	80
6.2.3. Charge relaxation resistance	80
6.3. Summary and discussions	81
7. Quantum dot spectroscopy through shot noise	83
7.1. Noise detection scheme	83
7.1.1. Gain extraction	85
7.2. Shot noise in single quantum dot regime	87
7.2.1. Sample layout	87
7.2.2. Stub transmission function	88
7.2.3. Shot noise results	90
7.2.4. Noise suppression in single channel regime	91
7.2.5. Inelastic cotunnelling assisted sequential tunnelling	91
7.2.6. Excited blocking states	92
7.3. Theoretical Model	93

7.4. Summary and discussion	96
8. Shot noise of quantum dots coupled to superconducting leads	97
8.1. Andreev transport in few transport channels	97
8.1.1. Shot noise results	99
8.1.2. Supercurrent: noisy or silent?	100
8.1.3. Quasiparticle relaxation	102
8.2. Kondo effect in QD with superconducting leads	103
8.2.1. Shot noise results	104
8.3. Summary and discussions	107
9. Summary and outlook	109
9.1. Future directions	110
9.1.1. Admittance measurements	110
9.1.2. Noise measurements	111
Bibliography	122
A. Fabrication Recipes	123
B. List of Setup Components	127
Curriculum Vitae	129
Publications	131
Acknowledgments	133

1 Introduction

The ability to observe is one of the most impressive attributes of a human brain. To this end, we are gifted with senses to comprehend objects, distance, color and sound. But human senses are prone to errors in perception rendering observations subjective and qualitative. Consequently, a unanimous verdict over mechanisms of a physical phenomenon is difficult to establish. Moreover, human senses are limited in magnitude of detection. These are the reasons why scientific tools or detectors have been developed to standardize measurements.

In the past decades, sophisticated detectors for heat, sound, charge, light have surfaced. Each better than their predecessors, these have gained in both speed and resolution. It is safe to say that the ever decreasing size, fabrication cost and increasing performance is the main catalyst behind the surge of cameras, sensors and computers. It has further enabled the discoveries of myriad of physical phenomena which were previously inaccessible due to the lack of technology to observe them. Needless to mention, the next generation of detectors will continue to investigate next magnitudes of a physical quantity. Of course, the justification for observing new phenomena is on the basis of scientific interest, the debate over “is all of that useful?” is expected to linger. In this spirit of pure scientific interest, this thesis attempts to develop an efficient probe for physical phenomena that yield very small electrical signals and their fluctuations: for example, in nanostructures.

1.1. Mesoscopic transport

Amid rapid miniaturization of electrical devices, microchips are no longer state of the art and an enormous progress has been made in fabricating, controlling and understanding nanostructures. Studies of nanostructures benefit from the fact that in many scenarios control over the size and shape becomes equivalent to controlling chemical and physical properties. These properties, however, drastically differ from those of the 3D bulk and can even become independent of the material composition [1]. The description of charge transport thus lies somewhere in between the macroscopic and microscopic models and is referred to as *mesoscopic transport*.

In a nutshell, mesoscopic phenomena capture the behaviour of electrons when only a few of them are available for transport. Of particular importance is the size of the material system, as the scale over wave nature of electrons dictated by quantum mechanics and even the granularity of charges become apparent. As early as the 1980s, signatures of quantum interference such as weak localization [2], Aharonov-Bohm oscillations [3] and universal conductance fluctuations [4] were observed in disordered metallic systems. Very soon, the observation of conductance steps [5] constituted a remarkable proof of

quantum confinement and low dimensionality in mesoscopic systems.

Quantum dots (QDs), nanostructures confined in all three directions, serve as an exceptional playground for designing quantum interactions on a chip. They are sometimes referred to as artificial atoms [6] due to discrete energy levels that result from Coulomb repulsion and quantum confinement. Many attributes of QDs such as the number of charges on a dot or its coupling to another dot can be controlled via local gate voltages. Moreover, these can be easily tunnel coupled to source/ drain leads allowing studies of few electron systems in a field effect transistor (FET) geometry. Aside from detecting charge currents in FET, energy spectroscopy can also reveal spin-spin interactions such as exchange coupling [7], singlet-triplet transitions [8], Pauli blockade [9], Kondo effect [10], and valley blockade effects [11, 12]. Moreover, by coupling the dots to superconducting leads Andreev bound states [13], Cooper pair splitting [14, 15] and Majorana bound states [16, 17] have been observed. The possibilities to access such effects have stimulated a new era of solid state quantum computing, whose speed-up and scaling transcends those of its classical counterpart [18].

1.2. Signal and noise

The conventional way to characterize charge transport is by measuring current or conductance. Just like any other signal, these are subject to random fluctuations or noise, obscuring the information contained within. Naturally, one would average the signal as much as possible to reduce the noise. Especially for nano-structures, currents can be tiny and thus a fast detector at our disposal can be quite handy. But every effect, however unpleasant it may seem, has a cause. Unwanted sources of the noise are the fluctuating environment and unstable instruments. On the other hand, fluctuations also arise from scattering of charge carriers in the devices. Though random in time, these are caused by a well defined probability distribution arising for example from thermal motion or discrete nature of charges [19]. The aforementioned types of noise are referred to as thermal and shot noise, respectively.

Already in 1928, equilibrium thermal agitation studied by Johnson [20] and Nyquist [21] was shown to scale linearly with temperature. As a consequence, an alternative determination of the absolute zero of temperature and value of the Boltzmann constant became possible. Thermal noise serves as a good calibration check for experiments now. The shot noise was even proposed earlier, by Schottky in 1918, in connection with vacuum tubes [22]. Its scaling with the unit of charge provided a good diagnostic on the doubled charge of Cooper pairs [23] and fractional charges of Laughlin quasiparticles in context of fractional quantum Hall effect [24, 25]. Studies of the current fluctuations have thus become routine in understanding the mechanisms responsible for electrical transport that are generally not provided by averaged signals [26].

A fast measurement of small currents and even smaller fluctuations in devices with impedances of 100 k Ω is not trivial. Standard low frequency lock-in measurements suffer from stray capacitance of the order of nF reducing the bandwidth to merely kHz and a time resolution of ms. One approach of increasing the bandwidth is to connect the high-impedance device next to a low input impedance amplifier [27, 28]. The signal is however decreased by the ratio of the impedances of the device and the amplifier (50 Ω),

easily a factor of a thousand. Therefore, long averaging times are required to detect the small signal. Moreover, $1/f$ noise still affects the measurements. The issues of small bandwidth, impedance mismatch and $1/f$ noise can be simultaneously addressed using resonant LC circuits. Originally developed for metallic single electron transistors [29], they have been already applied to other systems such as quantum point contacts [30–32], quantum dots [33] and atomic point contacts [34]. The success of these impedance transformers lies in replacing the slow operation of applying voltages and measuring currents by applying fast radio frequency signals and measuring the reflectance. LC circuits remain appealing because of a rather simple assembly. Nonetheless, the challenge to reproducibly achieve the resonance frequencies in gigahertz (GHz) range while matching to high impedance still remains due to the large parallel stray capacitance of the measurement setup.

1.3. Thesis outline

It is the goal of this thesis to develop GHz impedance matching circuits as a probe of quantum transport in high impedance devices. Resonance frequency in GHz range is desirable for two reasons. Firstly, measurements are faster and $1/f$ noise smaller. Yet more importantly, one can profit from the wide range of measurement techniques developed in the context of circuit quantum electrodynamics, such as FPGA based hardware [35] and quantum limited Josephson parametric amplifiers [36]. The thesis is structured as follows.

We start in **Chapter 2** with a theoretical background of the material systems (such as carbon nanotubes and semiconducting nanowires) on which quantum dots are formed. This is followed by their electronic transport properties with ground and excited states transitions. We also discuss the situations in which the Coulomb repulsive energy of quantum dots competes with the attractive macroscopic correlations of the Kondo effect and superconductivity. The chapter ends with a discussion on noise characterizations arising from the statistical fluctuations of current in our devices.

Chapter 3 is dedicated to stub tuners - our approach to impedance matching. Using numerical calculations, we show that from a design of a pair of shunted transmission lines typical device impedance of $\sim 100\text{ k}\Omega$ can be transformed to the characteristic value of $50\ \Omega$, maximizing the power transfer into and out of the device. We discuss their response to complex device admittance and circuit losses and provide useful theoretical figures of merit in terms of measurement bandwidth and signal-to-noise ratios. **Chapter 4** deals with device fabrication and measurement techniques. In particular, we discuss the adaptations needed for optimal performance of the circuit and the device when integrated simultaneously on a chip.

In **Chapter 5** we present reflectance results of locally tunable quantum dots coupled to stub tuner circuits. We demonstrate matching at impedances higher than $150\text{ k}\Omega$ and circuit bandwidths in the MHz range. The complex reflectance response can be measured with a large sensitivity even at very low powers, enabling non-invasive mea-

measurements of device properties. In particular, we study dephasing of charge qubits formed in double quantum dots. **Chapter 6** extends the measurement principle to graphene devices where we show extraction of equilibrium density of states and associated dissipation, without needing any conventional contact electrodes.

Finally, we show the real strength of the stub tuner circuits in measuring the emissions emanating from the quantum devices. **Chapter 7** investigates shot noise measurements of a single quantum dot with an average impedance larger than $150\text{ k}\Omega$. Large collection efficiency allows us to address the differences in the transition rates from leads to the resonant dot states, both inside and outside the Coulomb diamonds. The latter is also compared with a theoretical model based on full counting statistics. The devices in the final **Chapter 8** incorporates an additional complication as compared to the ones from chapters 5 and 7. The normal contact leads are replaced by superconductors creating a competition between single charging effects of quantum dots and the macroscopic condensate of Cooper pairs. New insights into quasiparticle coherence of Andreev processes are provided. We also discuss the competition in the Kondo effect.

2 Theoretical background

In this introductory chapter, we provide a brief theoretical background of the experimental results presented later. Firstly, the material systems are introduced and their band structure explained with focus on spatial confinements. We then discuss the electronic transport properties, mainly in quantum dots, for two cases: the contact leads are fermionic like in normal metals or bosonic as in superconductors. These properties are explained in terms of averaged measurable quantities such as current or conductance. Finally, noise characteristics due to the random fluctuations of the electronic signals are elucidated. The explanations below are condensed and a comprehensive literature can be found in the references provided in each section.

The material systems studied in this thesis are graphene, carbon nanotubes and InAs nanowires. Each system provides an excellent platform for charge transport with large electron mobility. The latter has especially attracted a great deal of attention for fabricating new generation of field effect transistors. However for scientific interest, the main advantages of such low-dimensional systems are their easy fabrication and great control of energy scales using local electrical fields. These advantages allow us to design, control and study quantum interactions on a chip.

2.1. Graphene

Graphene has a two dimensional hexagonal lattice as shown in Fig 2.1(a) with a lattice constant $a = 1.4 \text{ \AA}$. It is not a Bravais lattice but can be considered a triangular lattice with 2-atom basis. The two carbon atoms A and B are chemically equivalent, all sp^2 bonded, however different on symmetry. One can conventionally define the unit cell vectors as follows

$$\vec{a}_1 = \frac{a}{2}(3, \sqrt{3}), \quad \vec{a}_2 = \frac{a}{2}(3, -\sqrt{3}). \quad (2.1)$$

Using the periodic boundary conditions, Bloch states can be characterized by the momentum vectors of the form $\vec{q} = (m_1/N_1)\vec{b}_1 + (m_2/N_2)\vec{b}_2$, where m_i are integers from 0 to $N_i - 1$ and N_i is the number of unit cells. The reciprocal lattice also has a hexagonal symmetry which is rotated by 90 degrees with respect to the direct lattice. Its vectors \vec{b}_i shown in Fig. 2.1(b) are given by

$$\vec{b}_1 = \frac{2\pi}{3a}(1, \sqrt{3}), \quad \vec{b}_2 = \frac{2\pi}{3a}(1, -\sqrt{3}). \quad (2.2)$$

The Hamiltonian of graphene, under the tight binding model considering only the nearest neighbours, can then be written in the momentum space as follows [37]

$$H = -t \sum_{\vec{q}} \left[\xi_{\vec{q}} a_{\vec{q}}^{\dagger} b_{\vec{q}} + \xi_{\vec{q}}^* a_{\vec{q}} b_{\vec{q}}^{\dagger} \right] \quad (2.3)$$

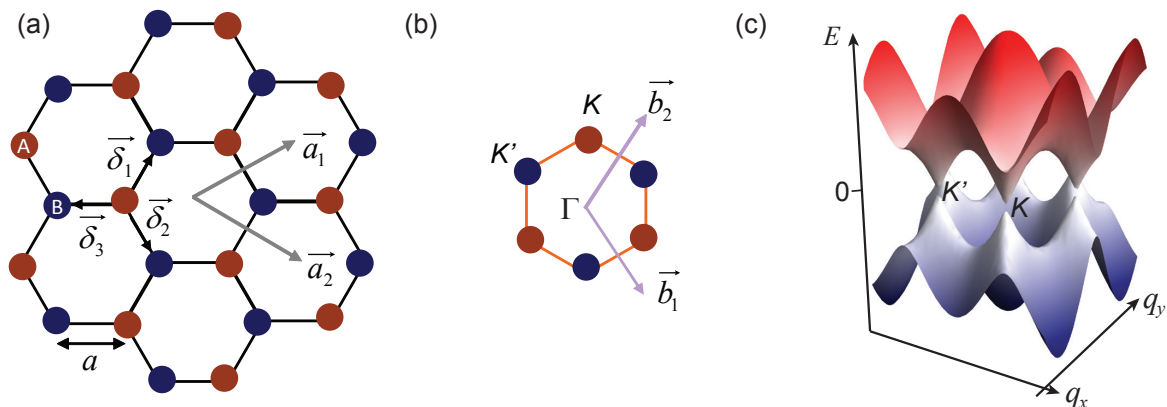


Figure 2.1. Graphene band structure (a) The unit cell vectors \vec{a}_i of a hexagonal graphene lattice. A and B denote two inequivalent atomic sites. The nearest neighbours $\vec{\delta}_i$ for site A. (b) Reciprocal lattice vectors \vec{b}_i with high symmetry points K and K' at the corners of its Brillouin zone. (c) Energy dispersion calculated from tight binding model. Conduction band and valence band meet each other at K and K' corners. Around zero energy, the dispersion is linear. Image adapted from [37].

where $a_{\vec{q}}$ and $a_{\vec{q}}^{\dagger}$ ($b_{\vec{q}}$ and $b_{\vec{q}}^{\dagger}$) are the annihilation and creation operators for the A(B) sites, $\xi_{\vec{q}} = \sum_1^3 e^{j\vec{q}\cdot\vec{\delta}_i}$ and t the hopping (transfer) integral. Spin states here have been omitted for simplicity. $\vec{\delta}_i$ are vectors corresponding to three nearest neighbours shown in the Fig. 2.1(a) which can be written as follows

$$\vec{\delta}_1 = \frac{a}{2}(1, \sqrt{3}), \quad \vec{\delta}_2 = \frac{a}{2}(1, -\sqrt{3}), \quad \vec{\delta}_3 = a(-1, 0). \quad (2.4)$$

As seen in Eq. 2.3, under a transformation $a_{\vec{q}} \rightarrow a_{\vec{q}}^{\dagger}$ and $b_{\vec{q}} \rightarrow -b_{\vec{q}}^{\dagger}$, the Hamiltonian remains invariant. This means that for every electron state with energy ϵ , there is a hole state with energy $-\epsilon$. Solving the Hamiltonian considering 3 nearest neighbors describes the dispersion relation given in Eq. 2.5 [37] and is shown in Fig. 2.1(c). The conduction band and valence band here meet at high symmetry K and K' points, also called charge neutrality points, where charge density vanishes. Hence for pristine graphene at zero temperature, the Fermi energy will exactly pass through these points. Moreover, because of above properties, the system can be considered as a semi-metal or a zero-bandgap semiconductor. Note that zero band gap is a consequence of symmetry (A and B are equivalent) and not because of the 3 nearest neighbour approximation.

$$E(q_x, q_y) = \pm t \left[3 + 4 \cos\left(\frac{\sqrt{3}q_y a}{2}\right) \cos\left(\frac{3q_x a}{2}\right) + 2 \cos(\sqrt{3}q_y a) \right]^{1/2} \quad (2.5)$$

At low energies ($\epsilon < 1$ eV) near K points, this dispersion relation can be expanded as $\vec{q} = \vec{K} + \vec{k}$, with $|\vec{k}| \ll |\vec{K}|$, where \vec{K} is the vector from Γ point to K point, to yield

$$E = \pm \hbar |\vec{k}| v_F + \mathcal{O}(k^2/K^2), \quad (2.6)$$

with $\hbar v_F = 3at/2$, \hbar the reduced Planck constant and $v_F \sim 10^6$ m/s the Fermi velocity [37]. Such linear dispersion can be seen in the cones near K and K' points in

Fig. 2.1(c). Due to the similarity with massless photons in the Dirac equation, the charge neutrality points are known as the Dirac points. Taking into account the spin, valley and angular degeneracy, the density of states per unit area $g_{2D}(\epsilon)$ can be calculated as follows

$$g_{2D}(E)dE = 4 \frac{2\pi k}{(2\pi)^2} dk = \frac{2E}{\pi(\hbar v_F)^2} dE. \quad (2.7)$$

Additionally the carrier density n_e for a degenerate system, $\mu \gg k_B T$, where μ is the electrochemical potential and k_B the Boltzmann constant, can be given by

$$n_e = \int_0^\mu g_{2D} dE = \frac{\mu^2}{\pi(\hbar v_F)^2}. \quad (2.8)$$

2.2. From graphene to carbon nanotubes

The graphene sheet can be simply rolled into a seamless cylinder to form carbon nanotubes (CNT). The manner of rolling is described by a chiral vector constructed with real space vectors as $\vec{c} = v\vec{a}_1 + w\vec{a}_2$ and shown in Fig. 2.2(a). The vectors \vec{a}_i are defined in Eq. 2.1 and the v, w are integers, such that $v \leq w$. The indices uniquely determine the structure of the CNTs. For example, if $v = 0$ or $w = 0$, the chiral vector is parallel to the A-B bonds and CNTs are called armchair. Those with $v = w$, the A-B bonds remain perpendicular to the chiral vector and CNTs are called Zigzag. All other cases are referred to as chiral CNTs.

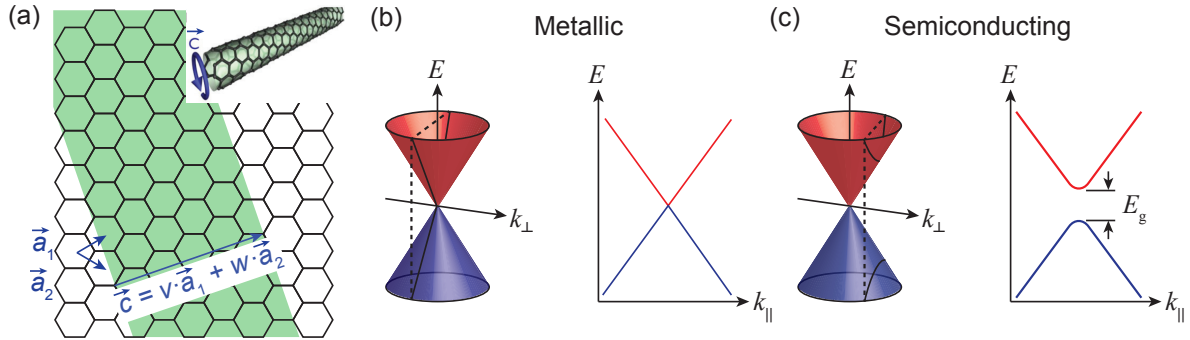


Figure 2.2. CNT band structure (a) Hexagonal lattice of graphene rolled into a CNT around a chiral vector \vec{c} . Adapted from [38]. Periodic boundary condition around the diameter of the CNT imposes quantization of k_{\perp} . A vertical slice of the graphene cone at a fixed k_{\perp} results in the one-dimensional band structure of the CNT, which could be (b) metallic if $k_{\perp} = 0$ or (c) semiconducting if $k_{\perp} \neq 0$.

The zone folding approximation introduces an additional boundary condition on the electronic wave function of graphene. While the parallel component of momentum k_{\parallel} along the length of CNT is not affected, the component in the circumferential direction k_{\perp} becomes quantized and can only change in steps $\Delta k_{\perp} = 2\pi/\pi d$, where d is the CNT diameter. The periodicity of k_{\perp} results in many one dimensional sub-bands from the Dirac cone whose energy can now be given as

$$E^n(k_{\parallel}) = \pm \hbar v_F \sqrt{(k_{\parallel})^2 + (k_{\perp}^n)^2}, \quad (2.9)$$

where index n denotes the sub-band number and $k_{\perp}^n = k_{\perp}^0 + n\Delta k_{\perp}$. Because of the small diameters $\sim 1 - 5$ nm, the excitation energy of CNTs lies in the eV range and only the lowest subband is occupied even at room temperature. Single wall CNTs are hence truly a one-dimensional system.

Depending on the magnitude of k_{\perp}^0 , two kinds of CNTs occur. The band structure realizations can be easily visualized by the vertical slices of the Dirac cones. As shown in Fig. 2.2(b), if the slice crosses the Dirac point i.e. $k_{\perp}^0 = 0$, CNTs maintain the linear dispersion of graphene and the semi-metallic nature. In contrast, CNTs are semiconducting when a slice for finite $k_{\perp} \neq 0$ misses the Dirac point with an energy bandgap of $E_g = 2v_F k_{\perp}^0$. Interestingly, it has been shown that even nominally metallic tubes can have small bandgaps due to strain, curvature, or electron-electron interactions [39, 40].

2.3. InAs nanowires

InAs is a semiconductor with a direct bandgap energy of 0.4 eV. The nanowires are simply a 1D realization of the material which can be grown bottom-up by the vapor-liquid-solid [41] method. These have gained much attention due to large electron mobilities [42] owing to a small effective mass, $m^* = 0.02m_e$. The crystal structure of InAs shown in Fig. 2.3(a) can adopt two configurations, Zincblende (ZB) or Wurtzite (WZ), with slightly different bandgaps. The close packing follows a ABCABC... sequence for ZB while it is ABAB... for Wurtzite. Due to similarity in the structure, the formation energy of the two phases are very similar and sudden changes in the lattice, called stacking faults, can occur during the growth. These can lead to unwanted potential barriers and modify the transport properties.

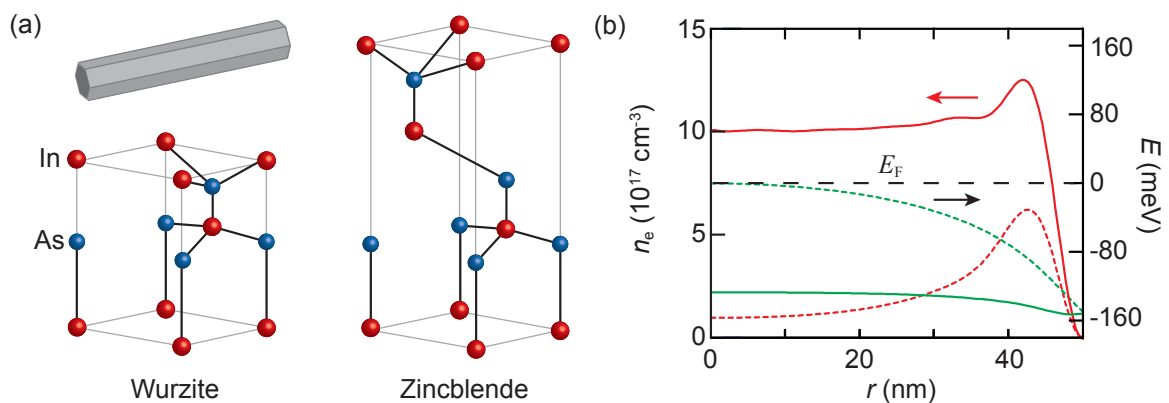


Figure 2.3. InAs nanowires (a) Two configurations of the crystal structure of hexagonal InAs nanowire. (b) Calculated electron density and conduction band energy for electron doped case with a density of 10^{18} cm^{-3} (solid) and the undoped case (dashed) as a function of radial distance (r). Adapted from ref [43].

Due to large bulk bandgap, the nanowires are generally doped with carriers to have finite carrier density near the Fermi level. A calculated conduction band energies E and carrier densities n_e for cases of doping and no doping [43] are presented in Fig. 2.3(b). The quantities show non-uniform dependence against the radial distance r with screen-

ing lengths ~ 10 nm. Moreover, large doping shifts the Fermi level deep into the conduction band and hence transport through only electrons can be expected.

The band structure of a bulk semiconductor can be calculated by considering solutions of the 3D Schrödinger equation for a confining potential $U \sim 0$, whose solutions are

$$E = E_C + \frac{\hbar^2(k_x^2 + k_y^2 + k_z^2)}{2m^*}. \quad (2.10)$$

The quasi-cylindrical symmetry and small diameters of the nanowires allow us to impose radial confinement and expand the electronic wave function as

$$\psi = \exp(jk_z z) \exp(jl\varphi) \chi_{n,l}(r), \quad (2.11)$$

where, z is the axial coordinate, φ the azimuthal angle. The first part of the wave function is the plane wave description of free motion along z direction. The second part describes angular dependence with quantum numbers $l = 0, \pm 1, \pm 2, \dots$ describing the number of nodes that the wave function makes in the circumferential direction. The last part $\chi_{n,l}(r)$ is the radial wave function with subband number $n = 1, 2, 3, \dots$ which depends on l too. Due to strong spatial dependence of wave function and relative large diameters $\sim 50 - 100$ nm in the nanowires, more than one subband can be occupied even at zero energy. These are hence called quasi-1D systems.

2.4. Different transport regimes

While the magnitude of the Fermi wavelength λ_F relative to the device dimension determines the dimensionality of the system, the carrier transport is governed by the scattering lengths. To this end, a mean free path l_m can be defined as the average distance travelled by a charge carrier between scattering events. If the system length $L \gg l_m$, the scattering happens several times along the device and the transport is called diffusive. The scattering can happen at stationary crystal dislocations and impurities. These kind generally conserve the energy of carriers and are called elastic scattering. More importantly, inelastic scattering can happen due to phonons and other surrounding carriers. The interaction of carriers with environment is parameterized by a diffusion constant \mathcal{D} which can be related to the Fermi velocity as

$$\mathcal{D} = v_F l_m / d, \quad (2.12)$$

where d is the dimensionality of the transport. Additionally, the momentum scattering time can be related as $l_m = v_F \tau_m$. When the temperature of the system is lowered to sub mK, the scattering from phonons can be drastically suppressed, and the l_m is limited by the electronic interactions, crystal imperfections and impurity sites. Especially, for small device dimensions with defect-free crystals, a ballistic regime can be reached, $L \leq l_m$, where carriers can move without scattering. Furthermore, when carriers preserve their phase during the time of flight across the device dimension, phase coherent transport occurs. This leads to interference effects such as weak localization [2], Aharonov-Bohm oscillations [3] and universal conductance fluctuations [4]. Observation of these effects in electronic systems is a stepping stone in the establishment of quantum mechanics within which particles can be described by waves with complex probability amplitudes ψ .

2.5. Quantum dots

Quantum dots (QD) are quasi-zero-dimensional islands. These are subject to the condition that the λ_F is longer than all three physical dimensions. As a consequence, the wave function is confined in all directions giving rise to discrete energy spectra. QDs are therefore called *artificial atoms* [6]. Unlike natural atoms, QDs can be easily tunnel coupled to source, drain leads and capacitively coupled to gate electrodes to change the dot potential allowing studies of charge transport in a field effect transistor (FET) geometry. The manifestation of quantization however demands low temperatures ~ 10 mK to 10 K due the bigger size compared to natural atoms. Moreover, the tunnelling resistances must be larger than h/e^2 to obey the Heisenberg energy uncertainty.

Quantum dots have been realized in several materials. Notable systems are two dimensional electron gases in semiconductor heterostructures, semiconducting nanowires, graphene and CNTs. Because of the small device size, self capacitance of the island becomes small and the resulting large charging energy provides strong Coulomb repulsion for the added electrons. The resulting *Coulomb blockade* of electronic transport is a universal property of quantum dots. In contrast, shell filling and spin orbit coupling is dependent on the physics of the host material. In this thesis, CNTs and semiconducting nanowires constitute the platform to create QDs.

2.5.1. Single quantum dots

To obtain the full energy spectrum of a QD, we need to consider the Coulomb interaction as well as the quantum confinement. The latter imposes a spacing between the energy levels δE similar to a quantum mechanical particle in a box situation. For a metallic CNT, which has a linear dispersion, $\delta E = \hbar v_F/2L$. The shell filling of each level is further governed by the spin degeneracy and the Pauli principle, similar to an atom. For CNT, valley degeneracy introduces another factor of two.

Effects of Coulomb repulsion can be described within the *constant interaction model* framework [6]. This leads to two simplifications. Firstly, the quantum dot can be assigned a constant self capacitance. Secondly, quantum mechanical excitation energies E_n are assumed to be unaffected by the electron-electron interaction.

Coulomb blockade

The FET schematic of the quantum dot with gate voltage V_G and bias voltage V_{SD} is shown in Fig. 2.5(a). In this model [44], the capacitive coupling of the dot to source, drain and gate electrodes leads to a total capacitance $C = C_G + C_S + C_D$. Total energy of the dot with N electrons is therefore

$$E_{\text{tot}}(N) = \frac{1}{2C} \left[-|e|(N - N_0) + \sum_i C_i V_i \right]^2 + \sum_{n=1}^N E_n, \quad (2.13)$$

with $i = G, S, D$ and $N = N_0$ when all voltages are zero. The first term is the sum of all electrostatic energies where N changes in discrete fashion and the voltage induced charge $C_i V_i$ varies continuously. The last term is the sum over occupied quantized energy levels. For zero-bias transport properties ($V_{SD} = 0$), only ground state transitions need

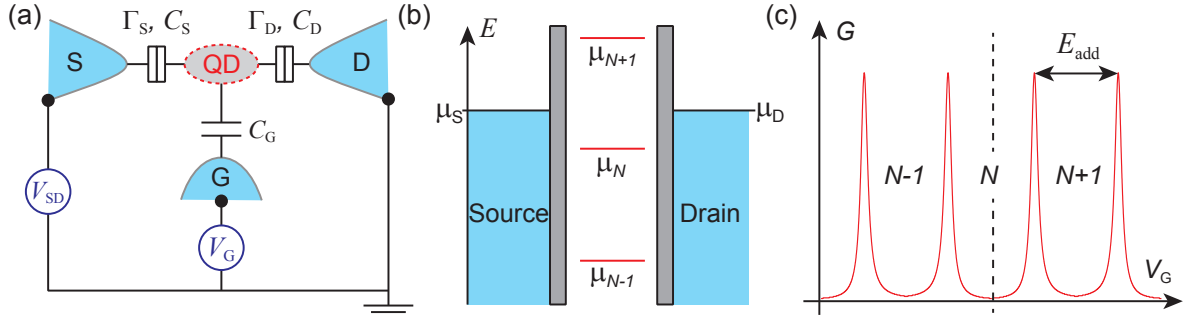


Figure 2.4. Coulomb blockade (a) A schematic of the quantum dot tunnel coupled to source (S), drain (D) leads and capacitively coupled to gate (G) electrode. (b) A ladder of electrochemical potential energies at zero bias and the dot containing N electrons. (c) Conductance peaks due to resonant tunnelling at zero bias. The dashed line represents the Coulomb blockade shown in the panel (b).

to be considered. The electrochemical potential energy of the dot with N electrons can be defined as $\mu_N = E_{\text{tot}}(N) - E_{\text{tot}}(N - 1)$ which is simply the energy needed to add the N^{th} electron to the dot and reads as

$$\mu_N = E_N + \frac{e^2}{C} \left[N - N_0 - \frac{1}{2} \right] - \frac{|e|}{C} C_G V_G. \quad (2.14)$$

It is apparent the the gate electrode not only tunes the electrostatic potential of the dot but also the electrochemical potential. The changes in V_G consequently can modify the ground state of the system by adding or removing electrons from the dot. The Eq. 2.14 describes a ladder of electrochemical potentials shown in Fig. 2.4(b) which can be pushed up or down linearly with V_G . This motivates us to define a gate *lever-arm* given by $\alpha_G = \Delta\mu/|e|\Delta V_G = C_G/C$. Furthermore, the electronic transport can only happen when the electrochemical potentials of the dot are aligned with those of the source, μ_S , and drain, μ_D , contacts. This situation of resonant tunnelling is referred to as Coulomb resonances shown as conductance peaks in Fig. 2.4(c). In other cases, the system remains in the Coulomb blockade. The spacing between two Coulomb peaks is given by the addition energy

$$E_{\text{add}} = \mu_{N+1} - \mu_N = \frac{e^2}{C} + \delta E, \quad (2.15)$$

where the first term is the charging energy E_C and the second term the quantum mechanical level spacing between two energy levels. This means that for a level degeneracy g_n , addition of first electron to an orbital shell requires both E_C and δE while the next $g_n - 1$ electrons require only the charging energy.

The linewidth of the Coulomb peaks arises from two main contributions. The first one is the thermal broadening of the fermionic leads which can be suppressed at low temperatures. The second contribution is an intrinsic broadening due to the Heisenberg uncertainty lifetime of the tunnel coupling energies of the source (Γ_S) and drain (Γ_D) leads. In the limit $\Gamma_S + \Gamma_D \gg k_B T$, the conductance peaks take a Lorentzian lineshape [45]

$$G = g_n \frac{e^2}{h} \frac{\Gamma_S \Gamma_D}{(\Delta\epsilon)^2 + (\Gamma_S + \Gamma_D)^2/4}, \quad (2.16)$$

where $\Delta\epsilon = |e|\alpha_G\Delta V_G$ is the detuning from the position of the Coulomb resonance. Within this framework, the height of the Coulomb peaks also provides a direct evidence of the asymmetry between Γ_S and drain Γ_D .

Coulomb diamonds

Coulomb blockade is additionally lifted when applied V_{SD} is enough to contain one or more QD levels within the bias window. Some of these situations are schematically shown in Fig. 2.5(a-c) for a fixed positive V_{SD} or negative $\mu_S - \mu_D$. Charges can then hop from one of the leads into the QD level and exit into the second lead. Electronic transport in such finite bias regimes is therefore referred to as sequential tunnelling where QD population fluctuates between N and $N + 1$. Moreover, if the bias is larger than the additional energy, more than one channel can be available in the bias window and a parallel transport can happen.

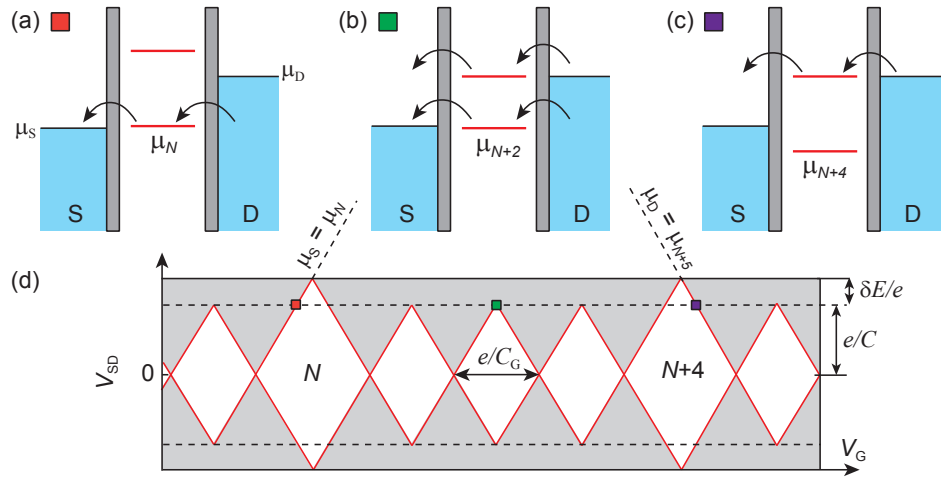


Figure 2.5. Coulomb diamonds (a-c) Energy diagrams of a QD in CNT at finite and fixed bias voltage. Arrows indicate the electronic transport. (d) Charge stability diagram as a function of bias and gate voltages showing four-fold degeneracy. Shaded areas represent the areas where Coulomb blockade is lifted. Red contours map the points where either μ_S or μ_D is aligned with the dot electrochemical potential. Symbols are explained in the text.

The interplay of bias and gate voltages is manifested by the Coulomb diamonds, shown in Fig. 2.5(d) for a quantum dot in CNT. The four-fold shell filling is shown by a big diamond followed by three small ones. This behaviour is also a direct evidence for the simultaneous measurement of charging energy and quantum mechanical level spacing. Furthermore, the horizontal size of the diamond can be used to calculate the gate lever arm α_G . Inside the diamonds, charge number is fixed and the system stays in Coulomb blockade. Outside the diamonds, at least one of the dot levels lies in the bias window allowing charge transport.

Along the diamond contours, either μ_S (positive slope) or μ_D (negative slope) is aligned with the electrochemical potential of the quantum dot, as shown by red solid lines in Fig. 2.5(d). The slopes of these lines can be calculated by considering linear change of

QD levels from the applied voltages. The drain voltage can be conveniently kept at zero. This leads for the negative slope a relation $0 = \frac{C_G}{C} \Delta V_G + \frac{C_S}{C} \Delta V_{SD}$ which yields $s^- = -\frac{C_G}{C_S}$. For the positive slope, QD level follows μ_S resulting in $\Delta V_{SD} = \frac{C_G}{C} \Delta V_G + \frac{C_S}{C} \Delta V_{SD}$ and yields $s^+ = \frac{C_G}{C-C_S}$. The slopes together with the lever arm are sufficient to calculate individual capacitances.

Excited states and cotunnelling

So far the discussion was limited to ground state transitions. When a large bias is applied, the transitions can occur between the ground states and the excited states. To this end, we draw the energy diagram of the QD with the *first excited state* as dashed lines in Fig. 2.6(a). The energy needed to add N^{th} electron can now be described as

$$\mu_N^{i,j} = E_{\text{tot}}^j(N) - E_{\text{tot}}^i(N-1) \quad (2.17)$$

where indices denote the ground states when $[i, j] = 0$ and the excited states when $[i, j] = 1$. The excited states introduce extra conduction channels in the bias window and may lead to enhanced current. The onset of this process can be seen as the dashed lines in Fig. 2.6(b) that run parallel to the diamond edges, however stop when bias drops below $|eV_{SD}| < |\delta E|$. The transport process is schematically shown in Fig. 2.6(c) where μ_D is aligned with $\mu_N^{1,0}$. We note that in this case only one channel at a time can contribute to the transport, because the charging energy is still bigger than the bias. In particular, the transition $\mu_{N+1}^{0,1}$, which takes the dot from an excited state (N) to a ground state ($N+1$), is also possible. But the transition gets blocked as soon as the dot relaxes to the ground state.

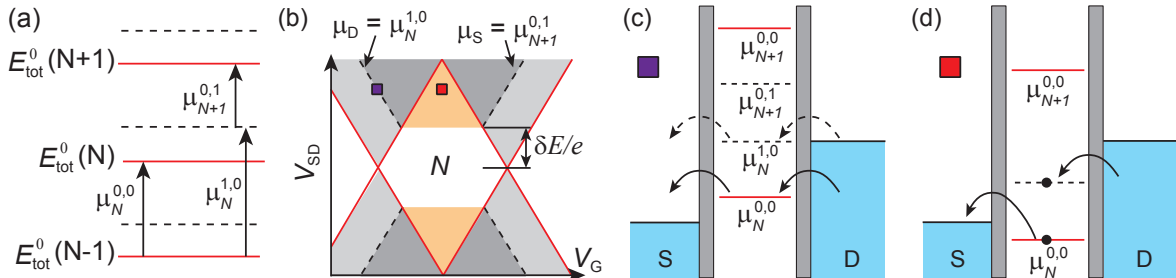


Figure 2.6. Excited states (a) Transitions between the ground state and excited states of the QD for a fixed bias and gate voltages. (b) Charge stability diagram with first excited state of the QD denoted by dashed lines. Darker gray areas represent higher current. Orange areas denote the inelastic-cotunnelling. (c) Sequential tunnelling via an excited state denoted by dashed line. (d) An inelastic cotunnelling event. Symbols are explained in the text.

The preceding discussion described the first order process of the conductance in the quantum dot. Irrespective of bias conditions, the Heisenberg uncertainty principle however permits so-called cotunnelling where an electron can leave from the dot to the drain lead and get repopulated from the source lead within a time $\approx \hbar/E_C$. This results in a small current even inside the Coulomb diamonds. If the state of the dot does not change during the event, the cotunnelling is elastic. In this case the differential

conductance turns out to be constant and scales as $G \propto \Gamma_S \Gamma_D / E_C^2$ [46]. In particular, when the bias is larger than δE , inelastic cotunnelling events start to occur. As shown in Fig. 2.6(d), the QD can switch from the ground to the excited state during the cotunnelling event. If the excited state is long lived, it can support sequential tunnelling till it is blocked again from a relaxation event, yielding a bunched charge transport. The resulting conductance step can be seen at the border between white and orange areas in Fig. 2.6(b).

2.5.2. Double quantum dots

If single dots resemble atoms, double quantum dots can be used to create artificial molecules. Similar to the previous section, we model two charge islands with tunnel and capacitive couplings to respective electrodes as shown in Fig. 2.7(a). The QD levels can be tuned with their respective gates, V_{LG} or V_{RG} , bringing them in resonance with electrochemical potential of the adjacent leads. For simplicity, we discuss only ground state transitions at zero bias case and highlight the differences from those in the single dot framework explained in the previous section.

The finite cross capacitances C_3 , C_4 from the gate electrodes tilt the otherwise horizontal and vertical charging diagram of a double dot. More importantly, owing to the interdot capacitance, the electrochemical potential of the left dot is affected by the occupation of the right dot and vice versa. Therefore adding an electron to each QD, even when two dot levels are brought in resonance, cannot happen at fixed gate voltages. These interactions result in a honeycomb pattern of the charge stability diagram as shown by gray lines in Fig. 2.7(b). The charges on the dots are fixed inside the hexagons. The crossings of charge configurations (n, m) , $(n, m + 1)$ and $(n + 1, m)$ are referred to as triple points.

In this non-interacting limit of the charge stability diagram shown in Fig. 2.7(c), the strength of capacitive couplings can be calculated by the distance between the edges of the hexagonal [47]. It is apparent that in the limit of C_3 or C_4 approaching zero, the long edges of the hexagons become horizontal and vertical respectively. Moreover, the separation between the triple points is determined by the C_t . The horizontal and vertical separations are also shown in Fig. 2.7(c) where $C_{L(R)}$ is the sum of all capacitances attached to the left (right) dot i.e. $C_{L(R)} = C_{S(D)} + C_{1(2)} + C_t + C_{4(3)}$.

In addition to the interdot capacitance, a finite tunnel coupling t_C can exist between the dots. This allows de-localization of charges from one QD to another. The effect becomes stronger especially if the resonant level of one dot is in close proximity to the other, for example near the triple points. The non-interacting eigenstates ϕ_L and ϕ_R thus hybridize to create bonding and anti-bonding molecular orbitals

$$\psi_{\pm} = a\phi_L \pm b\phi_R, \quad (2.18)$$

where a and b are the respective weights of the superposition. This results in the smoothing of the triple points as shown by black solid lines in Fig. 2.7(d). The strength of the avoided crossing t_C can be furthermore seen as the separation of the smooth triple point from the non-interacting case. In case of very strong t_C , the charges are completely delocalized over two dots and honeycomb pattern evolves into set of parallel lines corresponding to a large QD tuned by two gates.

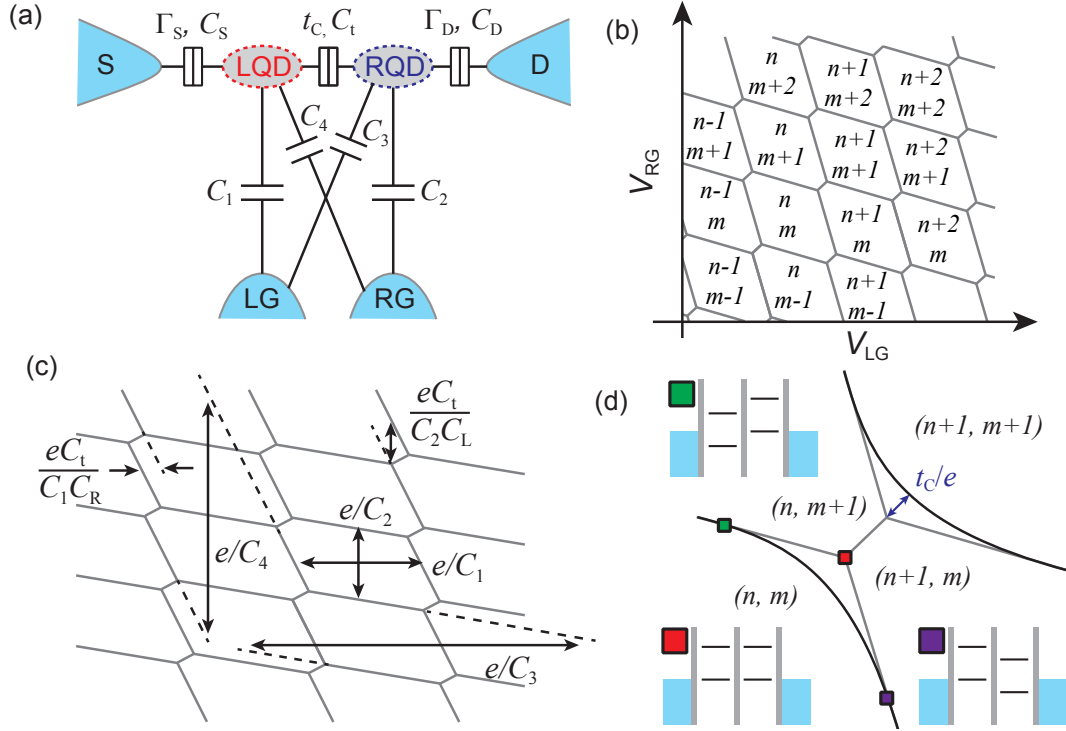


Figure 2.7. Double quantum dots (a) Capacitive model of two tunnel coupled QDs in series. (b) Honeycomb charge stability diagram in a weak coupling limit as a function of left and right gate voltages. The numbers (n, m) denote the electronic occupation of left and right QD. (c) Strength of capacitive couplings estimated from the distance between the edges of the hexagon. (d) Close-up of one of the honeycomb short edge for large (black) and small coupling (gray) strengths. Insets show energy diagrams at various points of the honeycomb.

The first order transport can happen only near the triple points, where the electrochemical potentials of the dots and the leads are aligned, see the inset of Fig. 2.7(d). In all other cases, the system remains in Coulomb blockade. However, similar to a single dot system, cotunnelling processes can contribute to the conductance. These show up as long edges of the honeycomb, where one of the dot levels is aligned with the adjacent lead potential. The situation is quite different for measurements of QDs with microwave resonator where interdot and dot-lead transitions of charges lead can be detected through capacitance changes ([48], [49], chapter 5).

2.6. Quantum dots coupled to superconductors

Coupling quantum dots to a superconducting reservoir creates a direct conflict between two very distinct phenomena. Quantum dots as discussed in the previous section, because of the large charging energy, allow electrons to pass one by one. In contrast, superconductivity arises from a macroscopic condensation of electrons bound as Cooper pairs. The difficult marriage of attractive and repulsive interactions have nonetheless enabled interesting studies of Josephson effect [50], Andreev bound states [13] in the

previous decade and recently Cooper pair splitting [14] and Majorana bound states [16]. The interplay can be further complicated with Kondo correlations or spin-orbit coupling. In this section, we review basic properties of S-QD-S systems within a framework of quantum transport of Cooper pairs under applied bias voltage.

The microscopic model of superconductivity is well understood by the Bardeen, Cooper, and Schrieffer (BCS) theory. Within this model, the electrons owing to indirect attractive electron-lattice interactions overcome the Coulomb repulsion and form Cooper pairs of opposite spins. At sufficiently low temperatures, the pairs have a high degree of wave function overlap producing a collective Bose-Einstein condensate at the Fermi level. In this condensed state, Cooper pairs defy perturbations that are smaller than the pairing energy. The latter is the energy needed to break a Cooper pair, which is twice the superconducting gap 2Δ . The gap further ensures a high cost of momentum scattering and consequently facilitates a dissipation-free flow of current through the superconductor, also called supercurrent.

At finite temperature or large bias, excitations can be created in the superconductors. It turns out that the nature of the excitations in the superconductor is the same as the one in normal metals [51]. Accordingly one has for the density of states $g_S(E)dE = g_N(\chi)d\chi$. The only difference is in their energies which are modified to $E = \chi^2 + \Delta^2$ because of the pairing gap. Moreover, every unpaired electron in the superconductor is equivalent to a missing electron from a Cooper pair. The quasiparticles are hence described as a superposition of an electron and a hole. Using the two identities described above, we get

$$g_S(E)dE = \begin{cases} g_N(0) \frac{|E|}{\sqrt{E^2 - \Delta^2}} dE, & |E| \geq \Delta \\ 0, & |E| < \Delta \end{cases} \quad (2.19)$$

where we approximate the normal metal density of states $g_N(\chi) \approx g_N(0)$ to be a constant within few meV around the Fermi energy. In this formulation the excitations below the gap are simply pushed to the gap edge conserving the total number of states. Additionally, the gap of the superconductor scales with the temperature T as $\Delta(T) = \Delta(0)\sqrt{1 - T/T_C}$. This expression is valid only near T_C , the critical temperature of the superconductor at which it turns into the normal state.

2.6.1. Andreev transport

We consider a S-QD-S system and focus on the off-resonant levels of a QD through which finite-bias tunnelling of quasiparticles is mediated via the Γ broadened tails. The difference of transport from a normal metal case is imposed by the gapped density of states in the superconductor. The first order transport processes happen only if the bias $|V_{SD}| > 2\Delta/e$, which aligns the filled quasiparticle band of source with the empty one of the drain lead as shown in Fig. 2.8(a). Such transport leads to conductance peaks at $V_{SD} = \pm 2\Delta/e$. This behaviour including the ones at lower bias, discussed below, is independent of gate voltage in the regime away from the QD resonance.

At a bias voltage smaller than the pairing energy, higher order processes can contribute to the *subgap* conductance. So-called Andreev reflection is shown in Fig. 2.8(b) where an electron like quasiparticle emerging from source is reflected as a hole-like quasiparticle with negative energy at the drain lead. Consequently, a Cooper pair is

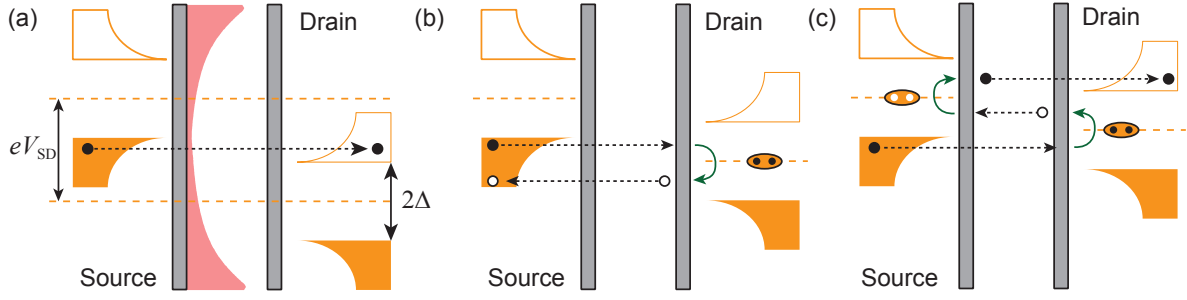


Figure 2.8. Quasiparticle transport in S-QD-S system Source and drain leads with BCS density of states are coupled to a quantum dot in off-resonant but large lead coupling limit to allow transport from the Γ broadened tails, shown by the red area. Lowest order tunnelling processes for (a) bias voltage $|eV_{SD}| > 2\Delta$, (b) $2\Delta > |eV_{SD}| > \Delta$ and (c) $\Delta > |eV_{SD}| > 2\Delta/3$. Subgap tunnelling is facilitated by Andreev reflection wherein an electron or a hole impinging on the superconducting lead is reflected as a hole or an electron with relative negative or positive energy respectively. These are shown by green arrows in panel (b) and (c).

transferred to the drain lead at the Fermi level and the reflected hole is relaxed in the quasiparticle band of the source. In the collective process, charge and energy are conserved. If the eV_{SD} is smaller than Δ , the second-order process described earlier cannot happen anymore. The quasiparticles now need to reflect at least twice to reach the quasiparticle band. This is shown in Fig. 2.8(c) with the first Andreev reflection creating a Cooper pair and the second reflection removing a Cooper pair. On decreasing V_{SD} even further, fourth, fifth etc. become the lowest order tunnelling process. In general, the lowest order n of *multiple Andreev reflections* (MAR) occurs at a bias of $V_{SD} = 2\Delta/ne$, n is an integer. The probability for experimental observation of higher order MAR is however reduced due to the increasing number of tunnelling events needed. Moreover, the conductance becomes increasingly smaller at larger n owing to a decreasing effective transmission $T_{\text{eff}} = T^n$, where T is the single channel transmission in the normal state of the leads.

Near the QD resonance, behavior of the MAR peaks becomes rather complex [52, 53]. We consider two scenarios. The first regime corresponds to charging energy $E_C \gg \Delta \gg \Gamma$ where MAR processes are strongly suppressed[54]. In the second regime $E_C \sim \Delta \sim \Gamma$, Coulomb effects can be neglected and the system behaves as if the BCS spectral density of the leads is coupled to a spin-degenerate resonance [52, 55]. In this formalism, MAR trajectories which connect the resonant dot-level to the superconducting quasiparticle states can tremendously enhance specific MAR process [53]. To cite an example, if the resonance level sits precisely in the middle of the chemical potential of the leads, odd MAR processes, for example the one shown in Fig 2.8(c), benefit from the large transmission of the central passage. The even processes are not affected and happen in the same way as for the off-resonance case. Since the dot level is generally gate-tunable, additional conductance peaks arise near the QD resonance when either the dot level stays aligned with the Fermi level of the leads or follows the BCS gap edge as an initial or final state of the Andreev reflection process [53, 55].

2.6.2. Josephson effect

At zero bias, the Fermi level of two superconducting leads is aligned and transport via Cooper pairs can happen. So-called supercurrent was first predicted by Josephson and can be derived from the boundary conditions of the macroscopic Ginzburg-Landau theory [51]. In contrast to a bulk description of BCS theory, the latter employs spatial variation of a complex order parameter $\psi(r) = |\psi(r)|e^{j\phi(r)}$. In this formalism, $|\psi(r)|^2$ is related to the density of Cooper pairs. Furthermore, the extent of the wave function is parameterized by the coherence length ξ . In a compromise with BCS theory, ξ can be thought of as the size of a Cooper pair. The Josephson effect demands that the wave functions of source and lead overlap significantly. The length L of the junction thus must be much smaller than ξ . This is schematically shown in Fig. 2.9(a). The normal region in this case is called a weak link, which can also be just a thin tunnel barrier or a constriction of a normal metal system. Furthermore, two identical superconductors in Fig. 2.9(a) have the phase difference $\phi = \phi_1 - \phi_2$, which is zero in case of a perfect coupling, but can differ for a partial coupling.

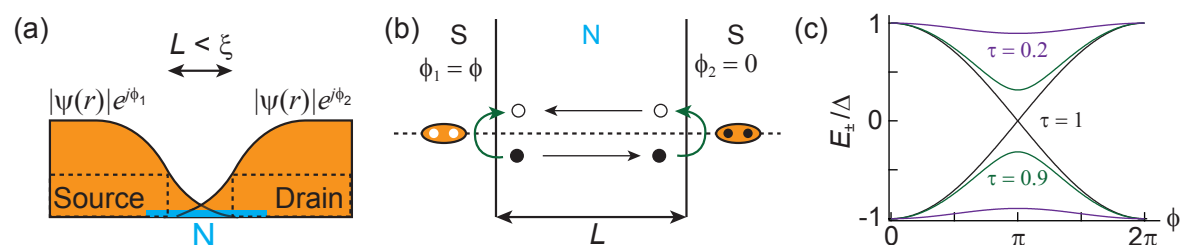


Figure 2.9. Josephson junctions (a) Overlap of Ginzburg-Landau order parameter near the weak link in effecting a finite Cooper pair density in the normal section. The magnitude of the supercurrent depends on the relative phase difference. (b) Formation of supercurrent carrying ABS from the interference of MAR cycles of an electron or hole excitation in the weak link. (c) Energy of two ABS for different transmission probabilities of the Josephson junction.

To calculate the magnitude of the supercurrent, we follow a microscopic theory of MAR [56] for a single channel. We consider a situation shown in Fig. 2.9(b), where an electronic excitation in the normal region moving from left to right reflects into a hole upon an Andreev reflection. The hole travels to the left and reflects again into an electron completing a transfer of a Cooper pair in one cycle. Due to the interference of infinite cycles, standing wave patterns are formed leading to so-called *Andreev bound states*. These are localized in the weak link. The phase acquired in a cycle of single Cooper pair transport, depicted in Fig. 2.9(b), is given by [56]

$$\Delta\phi_1 = 2 \cos^{-1}(E/\Delta) - \phi, \quad (2.20)$$

where E is the energy of the bound state. We have ignored the dynamical phase for short junctions $L \ll \xi$. There can also exist a process where the electrons travel from right to left such that Cooper pairs are transferred to the left superconductor. In this case the phase acquired in one cycle reads as

$$\Delta\phi_2 = 2 \cos^{-1}(E/\Delta) + \phi. \quad (2.21)$$

To satisfy the bound states, $\Delta\phi_{1,2}$ must be a multiple of 2π . Using the identities above for the case of perfect transmission, we get the ABS energies for left- and right-moving supercurrent as $E_{\pm} = \pm\Delta \cos(\phi/2)$. For a general transmission $\tau \leq 1$ accounting for scattering at the two S-N interfaces, the energies are modified to [57]

$$E_{\pm} = \pm\Delta[1 - \tau \sin^2(\phi/2)]^{1/2}. \quad (2.22)$$

These are plotted in Fig. 2.9(c) for different values of τ . It is apparent that at low τ , two states lie close to the superconducting gap. The supercurrent can be evaluated by treating charge and phase as conjugate variables [51] to yield

$$I_S = \frac{2e}{\hbar} \sum_{\pm} \frac{\partial E_{\pm}(\phi)}{\partial \phi} \tanh\left(\frac{E_{\pm}}{2k_B T}\right), \quad (2.23)$$

where the "tanh" factor describes the thermal population of the left and the right moving supercurrent. At small temperatures and in absence of quasiparticle exchange between the superconductor and two sub-gap ABS, only the lower-lying branch E_- carries the supercurrent. The current further simplifies in the tunnelling limit $\tau \ll 1$ into a simple sinusoidal form

$$I_S = I_C \sin(\phi), \quad (2.24)$$

where $I_C = e\Delta\tau/2\hbar$ is the maximum or the critical current of the junction. The phase difference can be simply tuned by an external magnetic field. The gauge invariance of the phase difference further requires that [51]

$$\frac{d\phi}{dt} = \frac{2e}{\hbar} V, \quad (2.25)$$

where V is the voltage across the junction. Equations 2.24 and 2.25 are known as the DC and AC Josephson effects.

In our case, a QD constitutes the weak link which leads to several transport regimes. If the lead couplings $\Gamma \gg E_C, \Delta$, there is negligible Coulomb blockade and the system effectively transforms to a S-N-S junction. In the other extreme limit $\Gamma \ll E_C, \Delta$, the system remains in strong Coulomb blockade, no supercurrent can therefore flow. However at the QD resonance, a coherent tunnelling of Cooper pairs can happen, leading to supercurrent [58, 59]. In the intermediate regime, $\Gamma \approx E_C \approx \Delta$, the system has enough charging energy to produce blockade, large couplings though can still lead to cotunnelling processes in the blockade, see section 2.5. Moreover, because two electrons are needed to sequentially transfer across the dot, the supercurrent is subject to the parity of the dot occupation [60].

2.6.3. Competing Kondo effect

Just like superconductivity, the Kondo effect is a manifestation of many-body physics. In a quantum dot, an unpaired electron hybridizes with the strongly coupled Fermi leads to create a global singlet. Consequently, an additional channel for electron transport is created via a spin-flip cotunnelling process depicted in Fig. 2.10(a). We stress that the collective process is coherent and resulting conductance can reach $g_n e^2/h$ for a dot level

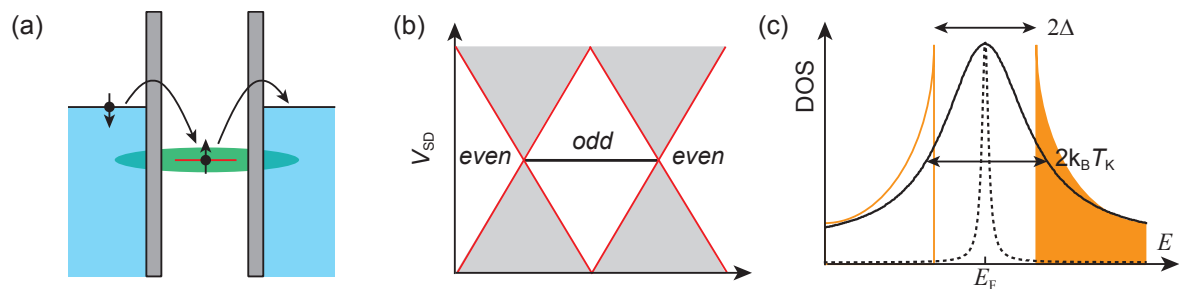


Figure 2.10. Kondo effect in QDs (a) Spin-exchange assisted cotunnelling event due to the Kondo effect in the case of normal leads. (b) Zero-bias conductance peaks for the odd occupancy of the dot. (c) Density of states of superconducting leads together with Kondo resonance in its normal state. Solid and dashed lines correspond to large and small Kondo temperatures respectively. Adapted from ref. [62].

with degeneracy of g_n . At finite bias, the chemical potentials of the leads are no longer aligned and the conductance drops. The effect is therefore manifested by a conductance ridge at zero bias shown in Fig. 2.10(b) for odd occupancy of the dot. The half width of the resonance at zero temperature is roughly given by the so-called Kondo temperature T_K . Its analogy to temperature is made to describe a minimum above which Kondo correlations can no longer occur. T_K can be furthermore related to the charging energy and total lead coupling as [61].

$$T_K = \sqrt{E_C \Gamma / 2} \exp \left[-\frac{\pi}{8 E_C \Gamma} |E_C^2 - 4\epsilon^2| \right] \quad (2.26)$$

where ϵ is the detuning of the resonant level measured from the centre of the Kondo ridge. Thus, T_K is minimum in the middle of the ridge at $\epsilon = 0$ and maximum at the crossing of the diamonds at $\epsilon = E_C/2$.

The situation becomes far more complex when the leads are superconducting. While the Kondo effect does provide a perfectly transmitting channel for odd occupation for normal leads, there are in principle no conduction electrons available for screening, due to the gap, in the superconducting leads. We can distinguish two regimes. In the limit $k_B T_K \ll \Delta$, Kondo correlations cannot develop suppressing any co-tunnelling, and thus supercurrent is negligible. For the other extreme $k_B T_K \gtrsim \Delta$, quasiparticle density of states of the superconductors overlaps with that of the Kondo resonance as shown in Fig. 2.10(c). The two phenomena now can not only exist simultaneously but also enhance the supercurrent [50].

2.7. Noise characterisation

So far we focused on the quantum transport in terms of an averaged quantity such as the mean current or conductance. It turns out that the same underlying physical process can also generate noise on top of the flowing current and may even provide more insights [26] that are otherwise not present in the averaged signal. In this section, we review basic electrical noise characteristics of two-terminal mesoscopic systems [19, 44] relevant for the experimental results obtained in this thesis.

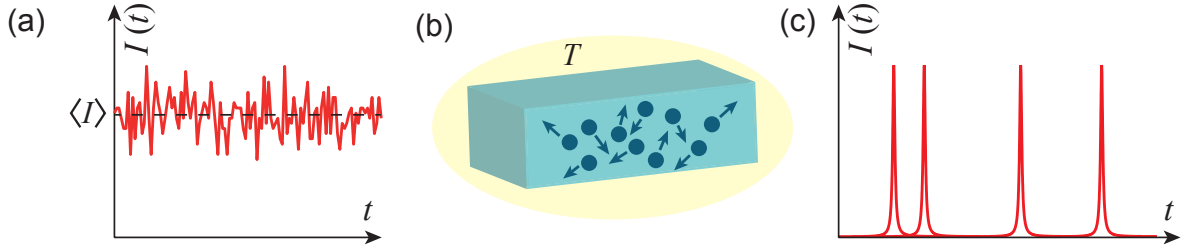


Figure 2.11. Current fluctuations (a) A typical variation of experimentally measured electrical current signal in time. The dashed line marks the mean value $\langle I \rangle$. (b) Equilibrium fluctuations of charge carriers in a two-terminal mesoscopic 1D conductor at a bath temperature T . A thermal noise is generated despite a zero net current. (c) Non-equilibrium charge pulses flowing through an opaque tunnel barrier producing shot noise. Each pulse represents transmission of a unit charge.

A typical electrical signal varying in time is shown in Fig. 2.11(a). The fluctuations around the average measured quantity $\langle I \rangle$ are then $\Delta I(t) = I(t) - \langle I \rangle$. The noise is characterized by the current-current correlator given by

$$C(\tau) = \langle \Delta I(t) \Delta I(t + \tau) \rangle \quad (2.27)$$

The formalism can be understood in two extreme limits. When the time difference τ is small, the auto-correlation reduces to

$$C(0) = \langle \Delta I^2(t) \rangle > 0, \quad (2.28)$$

which is simply the variance of the current fluctuations. On the other hand, when τ is very large, the function converges to zero. This is to say that current fluctuations at an instant are completely uncorrelated to the fluctuations far ahead or back in time. The decay of correlation function can be approximated with an exponential decay $C(\tau) = C(0) \exp(-\tau/\tau_c)$, where τ_c is the decay constant [44].

Given the limited bandwidth of any detector, it is desirable to express such fluctuations by a distribution of frequency components. To this end, the current spectral density can be defined as

$$\tilde{S}_I(\omega) = \int_{-\infty}^{\infty} C(\tau) e^{-j\omega\tau} d\tau. \quad (2.29)$$

The frequency in the Fourier transform can be both negative and positive and can be understood as the emission and absorption spectrum of the system. At relatively low frequencies $|\hbar\omega| \ll k_B T, eV_{SD}$, these two processes become indistinguishable, that is $\tilde{S}_I(\omega) = \tilde{S}_I(-\omega)$. The total current spectral density $S_I(\omega)$ is defined as

$$S_I(\omega) = \tilde{S}_I(\omega) + \tilde{S}_I(-\omega) = 2 \int_{-\infty}^{\infty} C(0) e^{-\tau/\tau_c} e^{-j\omega\tau} d\tau = \frac{4\tau_c \langle \Delta I^2(t) \rangle}{1 + (\omega\tau_c)^2}. \quad (2.30)$$

It is apparent from the expression that $S_I(\omega)$ in the limit of $\omega \ll 1/\tau_c$ has negligible dependence on the frequency. The so-called white noise is the regime explored in this thesis. In the other limit $\hbar\omega \gg k_B T, eV_{SD}$ it is referred to as the quantum noise. This is dominated by zero point fluctuations of the electromagnetic environment and thus low bias dynamics of the system cannot be learned [63].

2.7.1. Thermal noise

At zero bias, there is no drift of charge carriers through a mesoscopic conductor. There are still thermal fluctuations of the occupation numbers in the reservoir inducing movement of charges in random directions. Though these always cancel each other on average producing zero net current, on short time intervals, there could always be more charges moving in one direction than in the other. So-called thermal noise stems from the statistical fluctuations of such short interval current $\langle \Delta I^2(t) \rangle$.

The spectral density of equilibrium noise is also called Johnson-Nyquist noise whose general dependence is given by [64]

$$S_I(\omega) = 4\hbar\omega G \left[\frac{1}{\exp(\hbar\omega/k_B T) - 1} + \frac{1}{2} \right]. \quad (2.31)$$

For the low frequency limit $\hbar\omega \ll k_B T$, the noise is described by $S_I(\omega) \approx 4k_B T G$. In contrast for $\hbar\omega \gg k_B T$, the expression simplifies to $2\hbar\omega G$. The latter is a result of the zero-point fluctuations of the environment, which can be qualitatively understood by replacing $k_B T$ with $\hbar\omega/2$ in the expression for low frequency limit.

2.7.2. Shot noise

At an applied bias, the mesoscopic conductors are driven out of equilibrium. Because of the discrete nature of the charge carriers, charges either pass through or get reflected, producing bursts of random current pulses. What results in the system is so-called *shot noise*.

For a quantitative derivation of shot noise, we consider a single channel tunnel barrier through which a mean current $\langle I \rangle$ flows at a fixed bias V_{SD} . This is shown in Fig. 2.11(c) and can be described by

$$I(t) = \sum_i e\delta(t - t_i), \quad (2.32)$$

assuming random charge pulses at time t_i . The noise correlation can be calculated from Eq. 2.27 and reads in a low transmission limit or the case of infrequent charge pulses [44] as follows

$$C(\tau) = e\langle I \rangle \delta(\tau). \quad (2.33)$$

The expression can now be plugged into Eq. 2.29 resulting in a zero frequency current spectral density of

$$S_I(0) = 2e|\langle I \rangle|, \quad (2.34)$$

which is also called the Schottky formula. The factor of two again stems from the summation over negative and positive frequencies. The formula is valid for completely random tunnelling events described by Poissonian statistics. To address the deviations from these, the Fano factor is defined as

$$F = S_I/2e|I|. \quad (2.35)$$

In this formalism, the shot noise for $F > 1$ is referred to as super-Poissonian while it is sub-Poissonian for $F < 1$. A generalized response of current spectral density

for a coherent conductor can be obtained by the Landauer-Büttiker formalism [19]. It is assumed that the conductor can support N transverse modes each with energy-independent transmission probability T_i in a two-terminal conductor. For fermionic channels with the maximum conductance of $2e^2/h$, the resulting S_I reads

$$S_I(0) = \frac{2e^2}{h} \left[4k_B T \sum_n^N T_n^2 + 2eV_{SD} \coth\left(\frac{eV_{SD}}{2k_B T}\right) \sum_n^N T_n(1 - T_n) \right], \quad (2.36)$$

where V_{SD} is again the applied bias voltage across the two terminal conductor. It is apparent that in the limit $eV_{SD} \ll k_B T$, the \coth -term can be expanded as $\coth(x) \approx 1/x$ and the result simplifies to the thermal noise at zero frequency. We generally work at low temperatures such that $eV_{SD} \gg k_B T$. In this regime the \coth -term ≈ 1 and the noise is dominated by the shot-noise contribution given by

$$S_I(0) = 2eV_{SD} \frac{2e^2}{h} \sum_n^N T_n(1 - T_n). \quad (2.37)$$

This suggests that the system produces no shot noise if either all transmission coefficients are one, as in case of ballistic transport or zero, as in the case of no current. Both cases are intuitive since no randomness is involved in the current. The maximum shot noise is produced if $T_n = 1/2$. Such dependence of shot noise on transmission has been experimentally confirmed in quantum point contacts [65, 66]. Furthermore if we assume that $T_n \ll 1$, a case for a tunnel barrier, the shot noise recovers to the Schottky formula derived in Eq. 2.35 where we have implicitly replaced the average current by $\langle I \rangle \approx V_{SD}(2e^2/h) \sum T_n$.

Information in shot noise

Unlike thermal noise, shot noise provides complementary information to bare conductance measurements of a mesoscopic conductor as mentioned below. These are hence also called *excess noise*. Some of these are also discussed at length in the chapters 7 and 8 in the context of the measurements.

- The shot noise contains information about the charge of particles that contribute to the current. For example in a S-N junction with a bias voltage smaller than superconducting gap, the current is carried by Cooper pairs so $e^* = 2e$ [23] (chapter 8). Moreover, fractional charge of Laughlin quasiparticles has been confirmed experimentally [24, 25].
- The shot noise can reveal whether the statistics by the charge carriers are governed by Fermi-Dirac or Bose-Einstein. If one would measure the cross-correlation of a beam split current, it will be negative for fermionic electrons and positive for Cooper pairs which are bosons [67].
- The shot noise can distinguish whether charge transport is diffusive, ballistic or carried by hot electrons. A metallic 1D wire depending on its length can be in the hot-electron regime (chapter 7) which exhibits a Fano factor $F = \sqrt{3}/4$ [68] while it is $1/3$ for diffusive regime [69]. In addition, one can tell if the charge scattering

is deterministic as in the case of the particle-picture or stochastic as in the case of the wave-picture [70].

- The shot noise has information about electron-electron interactions. In presence of Coulomb blockade, for example, charges move in a sequential fashion. Depending on the number of available channels and transition rates between those, the noise can be larger or smaller than the Schottky value (chapter 7).

2.7.3. Flicker noise

Another type of current noise is flicker or $1/f$ noise, the name originating from the $1/f$ -dependent spectral density. It is also a non-equilibrium phenomenon and requires a mean current to flow through a conductor. Though the origin of such noise is debatable [71], it is believed to be stemming from charging and discharging of traps in the current path. The individual traps translate into several noise sources with their own characteristic correlation decay time τ_c defined earlier.

Flicker noise is generally present in carbon resistors or in commercially available silicon transistors and are only relevant below 10 kHz. Since we measure at 3 GHz, these are greatly overshadowed by white contributions from the thermal and the shot noise. $1/f$ noise, nonetheless, is one of the main limitations behind the small coherence times of charge qubits.

3 Impedance Matching

Impedance of a system describes an opposition to the propagation of energy. Every physical property, whether acoustic, thermal or electromagnetic has its own intrinsic impedance, limiting the power transferred to a desired target. For example, we consider a standard voltage source connected to a load, shown in Fig. 3.1. The power dissipated across the load given by $Z_L[V_S/(Z_S + Z_L)]^2$ is maximal only when $Z_L = Z_S^*$ and otherwise reduced. The asterisk denotes the complex conjugate. It is, however in practice, not common to have similar values of Z_L and Z_S . A detector in the microwave regime has a characteristic impedance of $Z_0 = 50 \Omega$ while the nanodevices in the context of mesoscopic transport have $\sim 100 \text{ k}\Omega$. The mismatch causes a reduction in the transferred power by $\approx (Z_0/Z_S)^2$, justifying a need for impedance matching.

The job of an impedance matching is to transform the output (input) impedance Z_{out} (Z_{in}) seen by (into) the source to Z_S (Z_0), see fig. 3.1. The condition, for example, can be met when the intermediate impedance is a geometric mean of the load and source impedances, $Z^{\text{int}} = \sqrt{Z_S Z_0}$ [72]. One possibility is to implement lumped element resonant LC circuits where $Z^{\text{int}} = \sqrt{L/C}$ can be arbitrarily tuned. Moreover, the easy assembly makes them very appealing. However, at the desired operating frequency of 3 GHz and impedance of 100 k Ω , matching requires a large inductance $L = 120 \text{ nH}$ and a rather small capacitance $C = 24 \text{ fF}$. The latter is extremely challenging to realize reproducibly due to significant parasitic capacitances from the experimental setup.

Our approach to matching circuits is based on a pair of terminated transmission lines, called stub tuners [72–74]. In a nutshell, the length of the lines determines the operating frequency while their difference the matched load. Integration of the devices on chip further allows the matched loads to be in M Ω range even at GHz frequencies. Here, a comprehensive theoretical aspects of stub tuners is presented. We first discuss transmission line, the building block of stub tuners, and its practical realization in a planar geometry. Few characterization measurements are also provided.

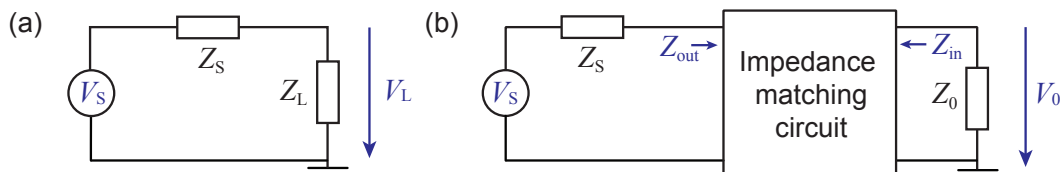


Figure 3.1. Power transfer (a) Schematic of a voltage source V_S with its intrinsic impedance Z_S attached to a load impedance Z_L . Voltage across load is reduced from V_S depending on the ratio of two impedances. (b) Use of an impedance matching circuit to transform the effective impedance of the load to the value of source.

3.1. Transmission line theory

A transmission line (TL) is an arrangement of inner and outer conductors to carry high frequency signals, schematically shown in Fig. 3.2(a). Its uniform cross sectional dimensions provide a constant impedance and facilitate a guided wave propagation with minimal reflections. Since their lengths are comparable to the wavelength, the voltages and currents vary over the distance and a global lumped element description cannot be applied. The line can however be divided into infinitesimal lengths dx over which signals can be assumed to be constant. To this end, a lumped element section shown in Fig. 3.2(b) can be modelled with four parameters \mathcal{R} , \mathcal{L} , \mathcal{G} and \mathcal{C} . All quantities are per unit length. Series resistor \mathcal{R} and inductor \mathcal{L} capture the resistivity and self-inductance of two conductors. The capacitance between two conductors is represented by a shunt capacitor \mathcal{C} while losses from the dielectric separating the conductors are accounted by the shunt conductance \mathcal{G} .

Using the model described above, a standard circuit theory can be applied to derive the voltage and current distributions along a TL [72]. In Fig. 3.2(b), we define a space and time varying voltage $V(x, t)$ and current $I(x, t)$ across the infinitesimal segment. Kirchhoff's voltage and current laws then lead to circuit relations

$$\begin{aligned} V(x, t) - V(x + dx, t) &= \mathcal{R}dxI(x, t) + \mathcal{L}dx\frac{dI(x, t)}{dt}, \\ I(x, t) - I(x + dx, t) &= \mathcal{G}dxV(x + dx, t) + \mathcal{C}dx\frac{dV(x + dx, t)}{dt}. \end{aligned} \quad (3.1)$$

In the limit of $dx \rightarrow 0$, one arrives at a set of linear differential equations, called Telegraph equations, that read as

$$\begin{aligned} \frac{dV(x, t)}{dx} &= -\mathcal{R}I(x, t) - \mathcal{L}\frac{dI(x, t)}{dt}, \\ \frac{dI(x, t)}{dx} &= -\mathcal{G}V(x, t) - \mathcal{C}\frac{dV(x, t)}{dt}. \end{aligned} \quad (3.2)$$

A particular solution can be formed in the lossless case $\mathcal{R} = \mathcal{G} = 0$, which is standard plane wave with time evolution given by $e^{j\omega t}$. Here, ω is the angular frequency. The solution can be extended to a general lossy case by separating time and space variations as $V(x, t) = V(x)e^{j\omega t}$ and $I(x, t) = I(x)e^{j\omega t}$. These transformations lead to a set of Helmholtz equations

$$\begin{aligned} \frac{\partial^2}{\partial x^2}V(x) - \gamma^2V(x) &= 0 \\ \frac{\partial^2}{\partial x^2}I(x) - \gamma^2I(x) &= 0, \end{aligned} \quad (3.3)$$

where the frequency dependence is absorbed in the complex propagation constant γ

$$\gamma = \sqrt{(\mathcal{R} + j\omega\mathcal{L})(\mathcal{G} + j\omega\mathcal{C})} = \alpha + j\beta. \quad (3.4)$$

The attenuation constant α accounts for an effective loss of the signal while the phase constant $\beta = 2\pi/\lambda$ captures the spatial periodicity with a wavelength λ . General solutions of Eq. 3.3 can be formed with a superposition of left (minus superscript) and

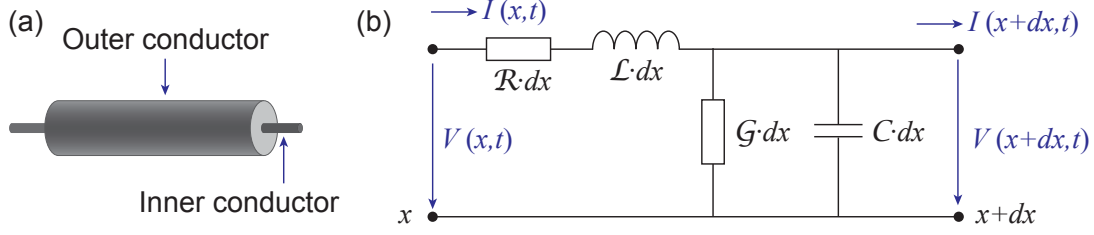


Figure 3.2. Transmission lines (a) A schematic of a transmission line consisting of an inner conductor separated from an outer conductor by a dielectric. (b) Lumped element equivalent circuit for an infinitesimal segment dx . Symbols are explained in the text.

right (plus superscript) moving waves with voltage and current amplitudes denoted by V_0^\pm and I_0^\pm , respectively, so that

$$\begin{aligned} V(x) &= V_0^+ e^{-\gamma x} + V_0^- e^{\gamma x}, \\ I(x) &= I_0^+ e^{-\gamma x} + I_0^- e^{\gamma x}. \end{aligned} \quad (3.5)$$

Finally a relation between current and voltage amplitudes can be derived with the help of Eq. 3.2

$$I(x) = \frac{\gamma}{\mathcal{R} + i\omega\mathcal{L}} [V_0^+ e^{-\gamma x} - V_0^- e^{\gamma x}]. \quad (3.6)$$

This equation allows us to deduce the characteristic impedance Z_0 of the transmission line. When comparing with Eq. 3.5, the ratio of voltage and current amplitudes results in a position independent Z_0 given as

$$Z_0 = \frac{V_0^+}{I_0^+} = -\frac{V_0^-}{I_0^-} = \sqrt{\frac{\mathcal{R} + i\omega\mathcal{L}}{\mathcal{G} + i\omega\mathcal{C}}}. \quad (3.7)$$

For a low loss circuit, which can be achieved with superconductors, the result simplifies to a frequency independent $Z_0 \approx \sqrt{\mathcal{L}/\mathcal{C}}$.

3.1.1. Terminated transmission lines

Effective total impedance of a transmission line terminated with a load with impedance Z_L can be derived from the boundary conditions of Eqs. 3.5 and 3.7. We construct a TL with length d such that the load is located at $x = 0$. An input impedance Z_{in} seeing into the load at $x = -d$ is then given as

$$Z_{\text{in}} = \frac{V(-d)}{I(-d)} = Z_0 \frac{V_0^+ e^{j\gamma d} + V_0^- e^{-j\gamma d}}{V_0^+ e^{j\gamma d} - V_0^- e^{-j\gamma d}}. \quad (3.8)$$

Additionally, the load sets a boundary condition ensuring

$$Z_L = \frac{V(0)}{I(0)} = Z_0 \frac{V_0^+ + V_0^-}{V_0^+ - V_0^-}. \quad (3.9)$$

Rearranging the two equations, one arrives at

$$Z_{\text{in}}(d) = Z_0 \frac{Z_L + Z_0 \tanh(\gamma d)}{Z_0 + Z_L \tanh(\gamma d)}. \quad (3.10)$$

The periodic nature of Z_{in} in d and ω can be understood by the fact that the unmatched load causes reflection of the propagating wave which then interferes with the incident part to create standing waves. Z_{in} for special cases of open and a shorted TL can be derived by setting $Z_L = \infty$ and $Z_L = 0$ respectively as

$$\begin{aligned} Z_{\text{open}} &= Z_0 \coth(\gamma d) \\ Z_{\text{short}} &= Z_0 \tanh(\gamma d). \end{aligned} \quad (3.11)$$

Above derivations show that the impedance of a load can be transformed using a segment of transmission lines. This property makes the basis for the engineering of our impedance matching circuits, stub tuners. These are discussed in section 3.3. Additionally, an unmatched load introduce reflections in the system. We can define a voltage reflection coefficient Γ_V as the ratio of reflected amplitude with the incident part

$$\Gamma_V = \frac{V_0^-}{V_0^+} = \frac{Z_L - Z_0}{Z_L + Z_0}. \quad (3.12)$$

The equation above is a general expression, and not just limited to transmission lines. In particular, Γ_V allows a quantitative determination of load mismatches from the standing wave ratios.

3.2. Coplanar transmission lines

A familiar example of transmission lines is the coaxial cable plugged in the receiver jack of our television sets. Coplanar transmission lines (CTL) or coplanar waveguides are a planar analogue of the same. Such circuits are made of a central conductor separated by semi-infinite ground planes as shown in Fig. 3.3. Because all planar conductors lie on the same substrate, only a single patterning step is needed in their fabrication. Due to the large ground planes in proximity, CTLs are well-isolated and the close packing avoids parasitic capacitances or inductances. In our case, the substrate consists of undoped silicon with a thin layer of thermally oxidized SiO_2 while the metal conductor is from a thin layer of superconductor. The superconducting film is essential to minimize conductor losses. Moreover, undoped silicon prevents free charge carriers to shunt microwaves and minimize the dielectric losses. The role of SiO_2 is to help the fabrication process and is explained in the chapter 4.

CTLs are thoroughly described in the reference [75, 76]. All CTL parameters are functions of the central conductor width S , gap width W and metallization thickness t . They support quasi-TEM (transverse electric and magnetic) modes i.e. both electric E and magnetic fields B are perpendicular to the direction of wave propagation. The currents flow at the edges of the central conductor and ground planes. When the returning currents in either ground planes are in phase, the mode is even. For odd modes, the potential of the central conductor does not change while it fluctuates for the

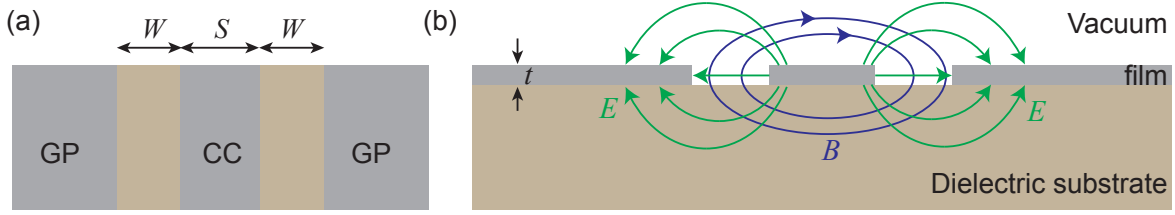


Figure 3.3. Coplanar transmission lines (a) A top view schematic of a CTL with a central conductor (CC) and ground planes (GP). The width of the central conductor and the gaps are W and S , respectively. (b) A cross section profile of electric and magnetic field of an even mode in the CTL. The thickness of the conductor is t .

ground planes [76]. We focus on the transmission line characteristics of even modes. Experimentally, the parasitic odd mode can be avoided by keeping the ground planes at the same potential via numerous wire bonds.

As shown in Fig. 3.3(b) roughly half of the field lines lie in vacuum while the other half in the dielectric substrate. The effective dielectric constant ϵ_{eff} hence can be approximated by $(1+\epsilon_r)/2$, where ϵ_r is the dielectric constant of the substrate. All parameters of CTL can be rigorously derived using conformal mapping [75]. The resulting geometrical inductance and capacitance per unit length are given by

$$\mathcal{L}_g = \frac{\mu_0 K(k')}{4 K(k)}, \quad (3.13)$$

$$\mathcal{C}_g = 4\epsilon_0\epsilon_{\text{eff}} \frac{K(k)}{K(k')}, \quad (3.14)$$

where ϵ_0 and μ_0 are the vacuum permittivity and permeability constants, respectively, and K the complete elliptical integrals of the first kind with $k = S/(S + 2W)$ and $k^2 + k'^2 = 1$. Moreover, the characteristic impedance can be calculated as

$$Z_0 = \sqrt{\frac{\mu_0}{\epsilon_0\epsilon_{\text{eff}}} \frac{K(k')}{4K(k)}} = \frac{30\pi}{\sqrt{\epsilon_{\text{eff}}}} \frac{K(k')}{K(k)}. \quad (3.15)$$

Since Z_0 depends on fixed parameters, a standard TL impedance of 50Ω can be easily planned. Moreover, CTLs can be widened into a larger launcher pads without changing the impedance, allowing easy connections with wire bonds.

3.2.1. Kinetic inductance

Geometric inductance of CTLs accounts for the energy stored in the magnetic field created by the propagating current. Besides, energy can also be stored in the kinetic energy of charge carriers in conductors. This leads to a kinetic inductance term, \mathcal{L}_k in series with the geometric value. A significant \mathcal{L}_k arises when inelastic scattering time is much longer than the inverse of signal frequency. For normal metals at microwave frequencies, charges collide frequently; therefore the effect is very small. For superconducting CTLs, magnitude of \mathcal{L}_k is derived in the reference [77]

$$\mathcal{L}_k = g_g \frac{\mu_0 \lambda_L^2}{Wt} \quad (3.16)$$

where λ_L is the London penetration depth and g_g is the geometric factor given by

$$g_g = \frac{1}{2k^2 K^2(k)} \left[-\ln \frac{t}{4S} - \frac{S}{S+2W} \ln \frac{t}{4(S+2W)} + \frac{2(S+W)}{S+2W} \ln \frac{W}{S+2W} \right]. \quad (3.17)$$

The derivation assumes a uniform current flow in the conductor. Since λ_L implicitly determines the skin depth over which supercurrent can flow, the formula above is valid only for $t < 2\lambda_L$. Because of the strong temperature dependence of the penetration depth, \mathcal{L}_K is also modified. It can be explicitly written as

$$\mathcal{L}_k(T) = \frac{g_g \mu_0 \lambda_0^2}{W t [1 - (T/T_c)^4]}, \quad (3.18)$$

where λ_0 is the penetration depth at 0 K and T_c the critical temperature of the superconductor. Surprisingly, the equation suggests the kinetic inductance to increase at increasing temperature where one would naively guess a smaller kinetic energy due to decreasing Cooper pair density. The reason lies in the velocity which needs to be higher to maintain the same current density in case of low number of Cooper pairs. The characteristics impedance is now modified to

$$Z_0 = \sqrt{\frac{\mathcal{L}_g + \mathcal{L}_k(T)}{C_g}}. \quad (3.19)$$

3.2.2. Superconducting resonators

An open or a short end in transmission lines acts like mirrors causing perfect reflection of an incident wave. Using two of such discontinuities, a transmission line analogue of a Fabry-Perot cavity can be constructed. The shortest version of TL resonator can be formed with the first mirror from open while the other one from short end. The arrangement forces two boundary conditions. Firstly, voltage (current) amplitudes must be zero at the short (open) ends. Secondly, the anti-nodes of voltage (current) must be

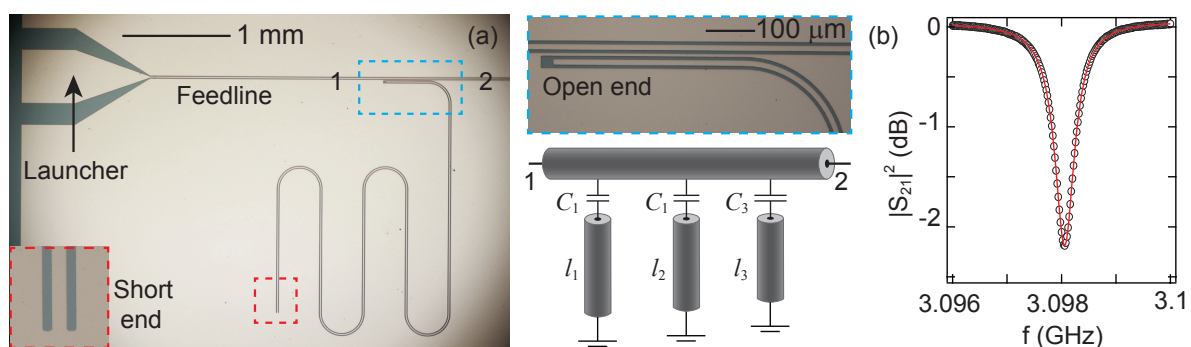


Figure 3.4. CTL hanger resonators (a) Optical pictures of one of many quarter-wave resonators, patterned on Nb, capacitively coupled to a common feedline. The schematic illustrates transmission line representation of the resonators with variable lengths l_i and coupling capacitances C_i with a two port feedline. (c) A transmission resonance measurement with a fit to Eq. 3.21 for a Nb hanger.

fixed at the open (short) end. These lead to resonance harmonics at $l = (2n + 1)\lambda/4$, where n is a positive integer and l is the length of the resonator. Our motivation for fabricating and measuring $\lambda/4$ resonators lies in extraction of attenuation constant α of CTLs. As explained in section. 3.3, loss plays a crucial role in the performance of the stub tuner. Other relevant parameters Z_0 and ϵ_{eff} can be merely calculated from the formulae provided in the section 3.2.

An optical picture of a quarter wave resonator patterned on Nb is shown in Fig. 3.4(a). The resonators are meandered to fit their long lengths. Moreover, the distance between the adjacent CTL is kept at least 7 times than its width ($S + 2W$) in order to reduce parasitic coupling [78]. Because of the characteristic shape, these resonators are also referred as hangers. The main advantage of this design is the common feedline which allows variable capacitive couplings (at open ends) of many hangers with variable lengths to allow statistics. The impedance of such transmission line resonators with length l can be written as

$$Z_{\text{in}} = \frac{1}{j\omega C} + Z_{\text{TLR}}, \quad (3.20)$$

where C is the coupling capacitance and $Z_{\text{TLR}} = Z_0 \tanh(\gamma l)$ for the shorted termination. The voltage transmission coefficient of the wave travelling from port 1 to 2 can be quantified with scattering parameter S_{21} and is given by $2/(2 + Z_0/Z_{\text{in}})$ [72]. Using $l = \lambda/4$ for the fundamental mode, Eq. 3.20 can be Taylor expanded around the resonance frequency f_0 . The latter contains the dependence on effective dielectric constant and kinetic inductance. Keeping the first order terms only, S_{21} simplifies to [78]

$$S_{21} = \frac{S_{21}^{\text{min}} + j2Q_1 \frac{\delta f}{f_0}}{1 + j2Q_1 \frac{\delta f}{f_0}}, \quad (3.21)$$

where $\delta f = f - f_0$ is the frequency detuning, $S_{21}^{\text{min}} = Q_c/(Q_i + Q_c)$ the depth of the resonance with internal quality factor $Q_i = \beta/2\alpha$, coupling quality factor $Q_c = 1/[8\pi(Z_0 f_r C)^2]$ and loaded quality factor $Q_1 = Q_i Q_c/(Q_i + Q_c)$. Depending on the magnitude of internal and coupling quality factors, two working regimes can be reached. For $Q_i \gg Q_c$, system is overcoupled and extraction of Q_i from fitting is unreliable. We therefore operate in an undercoupled regime where $Q_i \leq Q_c$. The coupling capacitance can be numerically simulated using Sonnet, a commercial finite element software, that solves Maxwell's equations for planar structures.

Measurements at 4.2 K

We now discuss measurements of such Nb hangers at a temperature of 4.2 K. The circuit after fabrication and wirebonding can be simply dunked in a helium dewar allowing fast characterizations, see section 4.5.3. Figure 3.4(b) presents the transmission spectrum of a fundamental resonance. Using the fit to the Eq. 3.21, we can extract $Q_i = 8000$ and $Q_c = 27000$ for the resonator length $l \sim 10$ mm. The characterization of low loss serves a confirmation of good superconducting film, on which one can continue to make the main circuit, stub tuner, and integrate quantum devices. We however find that the internal quality factors vary quite a lot from one superconducting film to another and sometimes even within the same film.

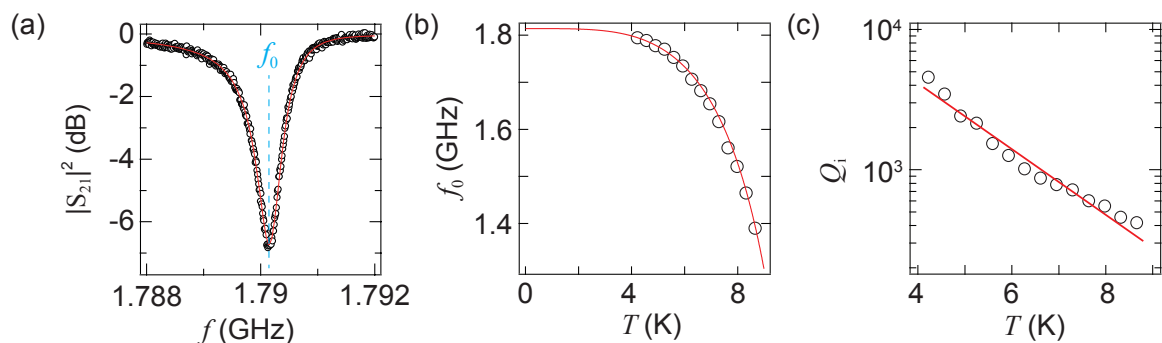


Figure 3.5. NbN resonators (a) A transmission measurement of a resonance with a fit to Eq. 3.21. (b) Temperature dependence of the resonance frequency. The solid line is a fit to Eq. 3.22 which implicitly contains temperature dependence of the London penetration depth. (c) Temperature dependence of the internal quality factor. The solid line is a guide to the eye.

To establish a good choice of superconductor for our stub tuner circuits, we also measure resonators from niobium nitride. Transmission spectrum for a NbN hanger is shown in Fig. 3.5(a). The fit in this case yields $Q_i = 4500$ and $Q_c = 4000$. From statistics, we do not find a clear improvement of Q_i of NbN over the ones of Nb. The measurements, however, give more insights into the properties of the NbN CTLs. The same length of 10 mm of the hanger resonator for NbN yields a $f_0 = 1.8$ GHz against 3 GHz for Nb. The down shift is because of a significant kinetic inductance present in NbN thin films. The temperature dependence of the fundamental resonance frequency is then given as

$$f_0(T) = \frac{1}{2\pi} \frac{1}{4l} \frac{1}{\sqrt{[\mathcal{L}_g + \mathcal{L}_k(T)]\mathcal{C}_g}}, \quad (3.22)$$

and can be seen in Fig. 3.5(b). From the fit to Eq. 3.22, we extract $\lambda_0 = 550$ nm and a kinetic inductance fraction $\alpha_L(0) = \mathcal{L}_k(0)/(\mathcal{L}_k(0) + \mathcal{L}_g) = 0.81$. Where we have used Eqs. 3.13 to obtain $\mathcal{L}_g = 411$ nH m⁻¹ and $\mathcal{C}_g = 175$ pF m⁻¹ for the CTL geometry $S = 12$ μ m, $W = 6.5$ μ m and $t = 100$ nm. For the same geometry and thickness, we find Nb films to have much smaller London penetration depth $\lambda_L = 60$ nm and $\alpha_L(0) = 0.1$. Kinetic inductance can have a twofold advantage for our circuits. Firstly, a relatively smaller length is needed to achieve the same desired operating frequency of 3 GHz. Secondly, higher characteristic impedance leads to a larger measurement bandwidth of the stub tuner, see section 3.3.4.

3.2.3. Microwave losses in superconducting resonators

Already discussed in the section 3.1, the microwave losses in transmission lines can be described by a series resistor \mathcal{R} and a shunt conductance \mathcal{G} . These parameters are dependent on the choice of superconducting materials and the dielectric substrates. Though the microscopic origin of these losses is, in general, very challenging to identify, we can still try to understand their behaviour in different regimes of our measurement control-parameters, such as temperature and RF input power.

For a NbN hanger, temperature dependence of Q_i is shown in the Fig. 3.5(c). We observe almost an exponential decrease of Q_i in this temperature regime for the most of our resonators. The thermally excited quasiparticles are, therefore, the main cause of losses since their population is proportional to $\exp(-1.76T_c/T)$ [51]. Coexistence of normal and superconducting electrons is well explained by a two-fluid model [51]. Below the critical temperature, a direct current flows with no resistance since the current always takes the lower ohmic channel out of the two. The situation differs for an AC excitation where normal electrons experience acceleration effecting ohmic losses.

Cooling down the superconducting circuits to 20 mK does not result in an indefinite increase of the quality factor. The bottleneck is caused by the dielectric losses from the substrate. These have been shown to result from two level states (TLSs) that sit in the defect sites of the substrate, and at the interfaces of the metal-air and the metal-substrate [79]. We see their manifestation in the power dependence of the quality factor. Because excitation of TLSs tend to get saturated at high input power, internal quality factor increases with power, against the general trend of power broadening.

Sapphire [80] and high resistive silicon [81] have been widely used as the favourite choices for the dielectric substrates. Sapphire, more so, because of its superior heat conductivity [82] allows good thermalisation of devices. Fabrication of quantum devices on sapphire is, however, problematic due to electrostatic discharges. Undoped silicon is better in this respect because it can still have a residual conductivity at room temperature. silicon dioxide on top introduces more losses, but a thin film can be useful for device fabrication.

Various superconductors have been employed in the community for the fabrication of high quality microwave resonators. The noted choices are aluminium [79], niobium [83], niobium titanium nitride [84, 85] and molybdenum rhenium [81]. While kinetic inductance in Al and Nb are negligible at 20 mK, it can be comparable to the geometric counterpart for NbTiN and MoRe. In terms of internal quality factor, none present a clear case of superiority. The choice thus has been mostly determined by their availability and fabrication needs. For example, MoRe films show better adhesion to graphene [86]. Nb and NbN films are sputtered with our in-house sputtering system. Though NbN can be useful for its large \mathcal{L}_K , we could not get controlled resonance frequencies and we observe a large spread of α_L between 0.5 and 0.9. The complication arises from a strong sensitivity of α_L to the film thickness and the sputtering conditions. All circuits in this thesis are therefore patterned on Nb where a thickness larger than λ_L ensures a low \mathcal{L}_k and reproducible resonance frequencies.

3.3. Stub tuner

Having discussed transmission lines and its realization in a coplanar geometry, we now turn to the main circuit, stub tuner, employed in this thesis. As shown in Fig. 3.6, it consists of two terminated transmission lines in parallel with lengths D_1 and D_2 . One line is shunted by a device of interest with load impedance Z_L while the other is kept open. The matching operation of the circuit can be explained with a simple analogy to optics. The T-junction acts as a beam splitter for the incident wave. The split waves undergo reflections at the line-ends such that for a specific $Z_L = Z_{\text{Match}}$, these interfere

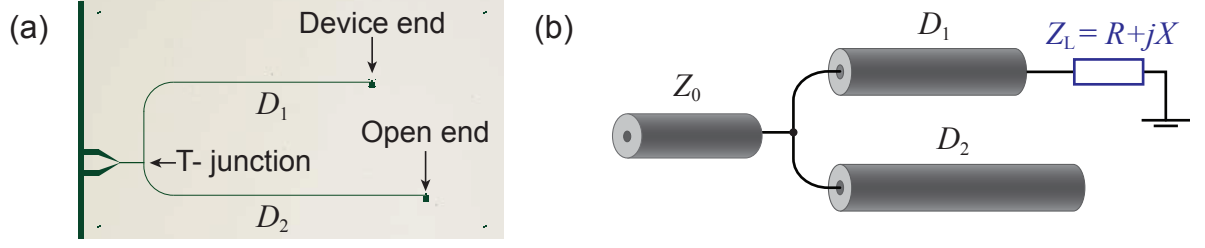


Figure 3.6. Stub tuner (a) Design of stub tuner from two terminated coplanar transmission lines, one ending with the device and the other with open. Two lengths merge at the T-junction. (b) The equivalent transmission line schematics of the same.

destructively, back at the junction. This results in a complete transfer of the signal power to the device even when $Z_L \gg Z_0$.

3.3.1. Impedance matching for lossless case

For a rigorous quantitative analysis of the circuit, a lossless case is described first. In this case, analytical solutions of lengths can be obtained for a desired frequency and matched load. The derivations capture essential properties of the circuit design which can be then generalized for the lossy case.

Input admittance of the circuit is calculated as the sum of two branches, $Y_{\text{in}} = 1/Z_{\text{in}} = 1/Z_{D1} + 1/Z_{D2}$, where Z_{Di} can be obtained from Eq. 3.10 for corresponding Z_L . For a load with explicit real and imaginary contributions $Z_L = R + jX$, the impedance of the load branch Z_{D1} reads as

$$Z_{D1} = Z_0 \frac{(R + jX) + jZ_0 \tan(\beta D1)}{Z_0 + j(R + jX) \tan(\beta D1)}, \quad (3.23)$$

where we have used the propagation constant $\gamma = j\beta$. The admittance of the load branch can be further separated as $1/Z_{D1} = G_1 + jB_1$ where

$$G_1 = \frac{R[1 + \tan^2(\beta D1)]}{R^2 + [X + Z_0 \tan(\beta D1)]^2}, \quad (3.24)$$

$$B_1 = \frac{1}{Z_0} \frac{R^2 \tan(\beta D1) - [Z_0 - X \tan(\beta D1)][X + Z_0 \tan(\beta D1)]}{R^2 + [X + Z_0 \tan^2(\beta D1)]}.$$

For the second branch terminated in open, R can be set to infinite, yielding purely imaginary impedance

$$Z_{D2} = Z_0 \cot(\beta D2) = 1/B_2. \quad (3.25)$$

Imposing the impedance matching means $Z_{\text{in}} = Z_0$. This results in the two conditions for the real and imaginary parts

$$G_1 = 1/Z_0 \quad \text{and} \quad B_1 = -B_2. \quad (3.26)$$

The first constraint results in a quadratic equation in $\tanh(\beta D1)$ whose analytic solutions are given as

$$\tan(\beta D1) = \frac{X \pm \sqrt{R[(Z_0 - R)^2 + X^2]}/Z_0}{R - Z_0} = \zeta(R, X). \quad (3.27)$$

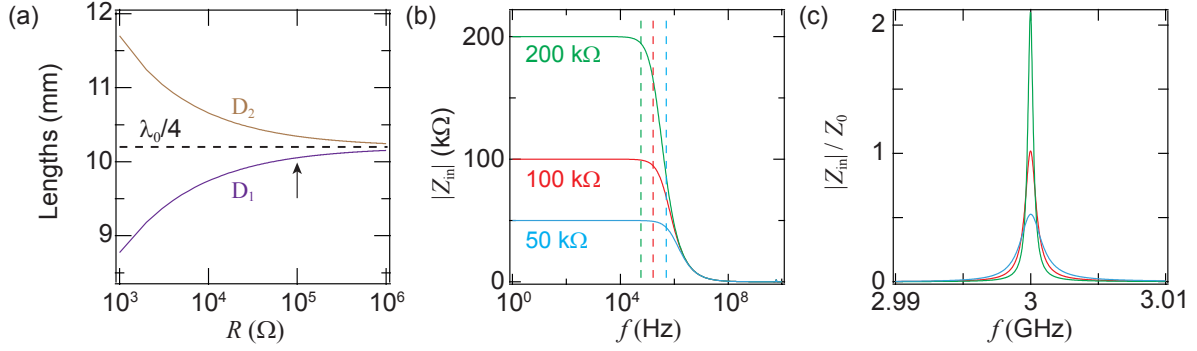


Figure 3.7. Input impedance of a lossless stub tuner (a) The lengths needed to match at a frequency of 3 GHz. An effective dielectric constant of 6 is assumed. The arrow denotes the lengths needed for matching 100 kΩ. (b) Input impedance for a large frequency range. Dashed lines represent the roll-off points. (c) Input impedance near the matching frequency.

The previous equation allows to calculate D_1 for matching at a desired load Z_L and frequency f_0 as

$$D_1 = \frac{c}{2\pi f_0 \sqrt{\epsilon_0 \epsilon_{\text{eff}}}} \tan^{-1}(\zeta), \quad \zeta \geq 0. \quad (3.28)$$

Similarly, using the second constraint D_2 can be calculated as

$$D_2 = -\frac{c}{2\pi f_0 \sqrt{\epsilon_0 \epsilon_{\text{eff}}}} \tan^{-1}(B_1 Z_0). \quad (3.29)$$

If one of the lengths turns out to be negative, for example when ζ is negative, $\lambda_0/2$ has to be added. The general results presented above get simplified if the matched load are real valued, $X = 0$. The two principal solutions for $R > Z_0$ are then given as

$$\begin{aligned} D_1 (D_2) &= \frac{\lambda_0}{2\pi} \tan^{-1} \sqrt{\frac{R}{Z_0}} \\ D_2 (D_1) &= \frac{\lambda_0}{2} - \frac{\lambda_0}{2\pi} \tan^{-1} \frac{R - Z_0}{\sqrt{R Z_0}}, \end{aligned} \quad (3.30)$$

where λ_0 is the wavelength at the matching frequency f_0 . The tangent terms cause periodicity in matching at length intervals of $\lambda_0/2$. For a load much larger than Z_0 , the two lengths approach $\lambda_0/4$ with one of them slightly longer and the other shorter, as seen in Fig. 3.7(a). At a desired matching load of 100 kΩ and matching frequency of 3 GHz, two lengths turn out to be $D_1 = 10.05$ mm, $D_2 = 10.35$ mm. The fabrication challenge clearly lies in matching large resistances where the length difference becomes really small. The lengths obtained experimentally can differ from the planned geometric value due to parasitic effects compensating asymmetrically for two branches. Such differences in lengths can, for example, arise if the metallic links, from circuit to the load, deviate from the characteristic impedance Z_0 . It is hence important that devices are integrated as close as possible to the circuit.

The input impedance of the circuit can be described by a general expression which

is also valid for the lossy case and arbitrary load conditions

$$Z_{\text{in}} = Z_0 \left[\tanh(\gamma D_2) + \frac{Z_0 + Z_L \tanh(\gamma D_1)}{Z_L + Z_0 \tanh(\gamma D_1)} \right]^{-1}. \quad (3.31)$$

The absolute value of Z_{in} is plotted in Fig. 3.7(b). In the zero-frequency limit, the input impedance is the same as the load impedance. The overall response can be qualitatively understood from a RC filter effect where the roll-off point increases in frequency with decreasing load. This behaviour is justified since the impedance due to the series inductance $j\omega L$ is much smaller than R . In contrast, at large frequencies, Z_{in} becomes a short causing perfect reflection of input signals. Around the matched frequency, a band pass filter effect is observed. At the resonance frequency and load of $100 \text{ k}\Omega$, Z_{in} is exactly Z_0 as expected for full matching. For R below matching it is always smaller than Z_0 while for R greater than the matched load, Z_{in} is larger than Z_0 around the resonance frequency.

3.3.2. Reflectance response

Input impedance is not an experimentally measured quantity. To characterize the stub tuner circuit, the response to the input signal is recorded in its reflected signal. The power reflectance is calculated as

$$\Gamma_{\text{stub}} = \left(\frac{Z_{\text{in}} - Z_0}{Z_{\text{in}} + Z_0} \right)^2, \quad (3.32)$$

where Z_{in} is explicitly given by Eq. 3.31. We first discuss the frequency response of $|\Gamma_{\text{stub}}|$ at different real-valued impedances as plotted in Fig. 3.8(a). The lengths are chosen to provide impedance matching at a conductance value of $G_{\text{Match}} = 10 \text{ }\mu\text{S}$ at 3 GHz , as explained in the previous section. There are two important observations. Firstly, the depth of resonance changes significantly for different loads. This is implicitly related to

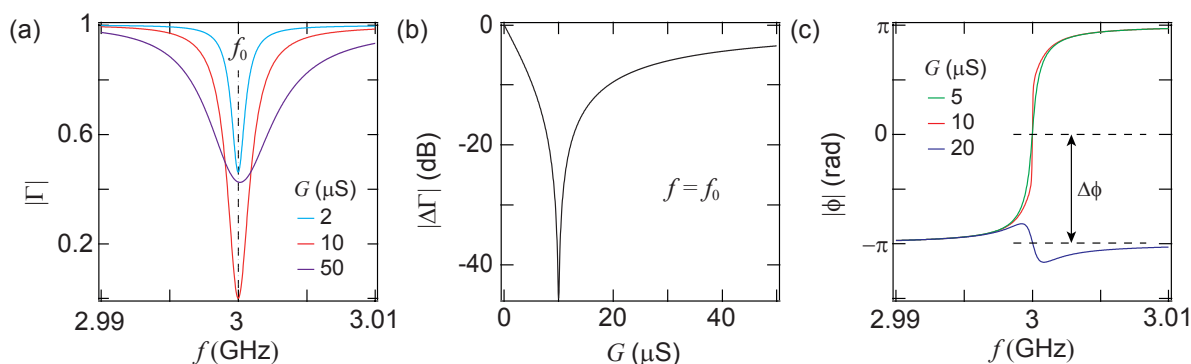


Figure 3.8. Reflectance response to real impedances (a) Resonance spectra of a lossless stub tuner for different values of load conductance. (b) Calculated variation of the depth at the resonance frequency against the load conductance. (c) The frequency response of the reflected phase for different loads. The phase at resonance is changed by π across the matched value.

variations in input impedance shown in Fig. 3.7(c). Secondly, the width of the resonance increases with increasing conductance. For a lossless circuit ($1/Q_i = 0$), total Q is given by the external quality factor. The load in our case hence acts like a mirror of a Fabry-Perot cavity with tunable transmission such that the signal loss is proportional to the conductance. We can moreover calculate the depth of the resonance $\Delta\Gamma$ against the load conductance at the resonance frequency. A non-monotonic behaviour can be seen in Fig. 3.8(b). The reflectance reaches unity for either case of very large impedance and low impedances.

The corresponding phase response for different load conductance is plotted in Fig. 3.8(c). At 3 GHz, phases are a multiple of π which is consistent with the fact that imaginary part of Z_{in} becomes zero at the resonance. Interestingly, the phase jumps by π when G crosses the matched value. This is because $(Z_{in} - Z_0)$ changes sign depending on whether the load is below or above matched value. The unique response of reflected phase together with the amplitude establishes a one to one correspondence between the magnitude of the load and the complex reflection coefficient.

We now consider the case where the load impedance has imaginary contributions too. This is relevant for our devices where quantum capacitance and inductance arise from a finite density of states. For a series RLC load, the total impedance is given by $R + j(\omega L - 1/\omega C)$. The effect of pure imaginary impedance ($R = 0$) is manifested in the shifts of the resonance frequency f_0 . The positive or negative shift furthermore can be related to the load being inductive or capacitive. The response however can also change in the resonance depths and widths if the magnitude of the real part is comparable to that of the imaginary part.

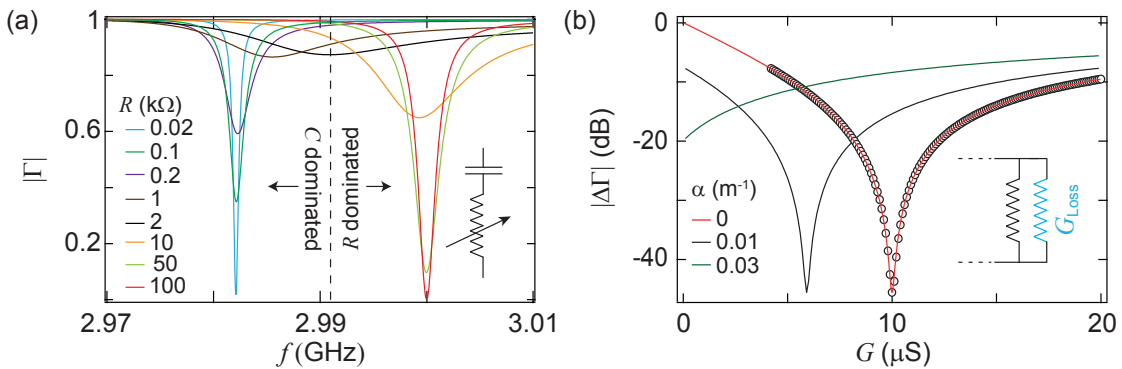


Figure 3.9. Response to complex impedances and losses (a) Resonance spectra of a lossless stub tuner for different values of load resistance and a fixed capacitance of 20 fF. Dashed line marks the middle of two extreme resonance frequencies. (b) Depth of resonance against real impedances at different internal losses of the circuit. Markers represent the same curve in black but offset in G . Inset shows a circuit equivalent of the load including losses.

We again consider the case with matching at 100 k Ω . Figure 3.9(a) shows frequency response to different complex impedances where load capacitance is fixed at 20 fF. For 3 GHz this translates into a negative imaginary impedance of $1/\omega C = 2652 \Omega$. We observe a complex behaviour of resonance frequency, width and depth. Two extreme cases can be easily visualized. If $R \gg 1/\omega C$, response is dominated by the real part

and produces very small frequency shifts. For increasing conductance, the width of the resonance gets larger while its depth decreases similar to Fig. 3.8(b). In contrast for $R \ll 1/\omega C$, the load becomes largely imaginary producing a new resonance frequency. The width of the resonance in this case becomes smaller at increasing conductance. At intermediate load conditions, matching is affected equally by real and imaginary contributions. Two regimes can be qualitatively separated as shown by a dashed line in Fig. 3.9(a) which also marks the middle of the two extreme resonance frequencies. The dashed line is also consistent with the resonance response for $R = 2 \text{ k}\Omega$ where real and imaginary contributions are almost equal.

3.3.3. Effect of losses

When taking losses into account, one cannot get analytical solutions of lengths to Eq. 3.31 any more. We hence rely on numerical calculations and minimization functions to obtain parameters needed for matching at a desired frequency and load.

We calculate the resonance depth from Eq. 3.31 while keeping the lengths D_i fixed. The response to losses for three values of $\alpha = (0, 0.01, 0.03) \text{ m}^{-1}$ is shown in Fig. 3.9(b). We find that responses including losses are merely shifted in G axis relative to the one with no loss. The shift is confirmed for the case of $\alpha = 0.01 \text{ m}^{-1}$ by black circles, representing the same black curve, but with a relative positive offset of $4.1 \text{ }\mu\text{S}$. This motivates us to define a new quantity $G_{\text{eff}} = G_{\text{Loss}} + G$ such that G_{Loss} is proportional to α . The proportionality constant depends on lengths and matching frequency and is hard to describe analytically. Moreover, for large losses $\alpha = 0.03 \text{ m}^{-1}$, full matching is precluded. This is referred to as the loss dominated regime.

The circuit for lossy case can hence be transformed to a lossless case by simply replacing the device conductance G with G_{eff} . In a schematic, this can be viewed as a loss conductance in parallel with the load. The Fig. 3.9(b) also confirms that full matching is always possible if the losses are compensated by the difference of lengths to push up the matching conductance. However, losses also reduce the measurement sensitivity of the load providing external coupling. This is because the internal quality factor starts to dominate the loaded quality factor.

3.3.4. Measurement bandwidth

In previous sections we see how the reflectance response can be used to deduce the complex-impedance of a device. The maximum measurement speed of such measurements is determined by the bandwidth BW of the circuit. To this end, an approximate expression for the stub tuner's BW is derived. For simple analytical analysis, we consider the case of a lossless circuit. G can be simply replaced with G_{eff} for lossy case. The stub tuner input impedance for $\alpha = 0$ is now expanded as

$$Z_{\text{in}} = Z_0 \frac{R \cot(\beta D_1) \cot(\beta D_2) + j Z_0(\beta D_2)}{Z_0(\beta D_1)(\beta D_2) + j R(\beta D_1) + j R(\beta D_2) - Z_0}. \quad (3.33)$$

The cotangent terms can be rewritten in terms of the relative frequency $\Delta f = f - f_0$ and $D_i = \lambda_0/4 \pm \Delta D$, with $+(-)$ sign for the larger (smaller) length. After expanding

for small arguments we get

$$\begin{aligned}\cot(\beta D_i) &\approx \cot \left[\frac{\pi}{2} + \frac{\pi}{2} \left(\frac{\pm \Delta D}{\lambda_0/4} + \frac{\Delta f}{f_0} \right) \right] \\ &\approx -\frac{\pi}{2} \left(\frac{\pm \Delta D}{\lambda_0/4} + \frac{\Delta f}{f_0} \right).\end{aligned}\quad (3.34)$$

Inserting Eq. 3.34 into 3.33 and imposing $\Delta f = 0$ and $Z_{\text{in}} = Z_0$ at the matching frequency, the length difference can be approximated in the limit $R \gg Z_0$ as

$$\frac{\pi}{2} \frac{\Delta D_i}{\lambda_0/4} \approx \pm \sqrt{\frac{Z_0}{R}}. \quad (3.35)$$

This is in agreement with the solutions derived for the general case in Eqs. 3.30. The cotangent terms can be now explicitly expanded in terms of load impedance and matching frequency as

$$\cot(\beta D_i) \approx \pm \sqrt{\frac{Z_0}{R}} - \frac{\pi}{2} \frac{\Delta f}{f_0}. \quad (3.36)$$

The approximation of cotangent can be now plugged into the input impedance of stub tuner. Ignoring higher order terms due to small R/Z_0 and $\Delta f/f_0$, we arrive at

$$Z_{\text{in}} \approx Z_0 \frac{\left(\frac{\Delta f}{f_0}\right)^2 - \frac{4Z_0}{\pi^2 R} - j\frac{2}{\pi} \frac{Z_0}{R} \frac{\Delta f}{f_0}}{-\frac{4Z_0}{\pi^2 R} - j\frac{4}{\pi} \frac{\Delta f}{f_0}}. \quad (3.37)$$

The resulting expression describes an amplitude Lorentzian whose full width half maximum (FWHM) is given by $\Delta f_0 = f_0 \frac{2}{\pi} \frac{Z_0}{R}$. The power bandwidth of the stub tuner can be obtained by simply multiplying Δf_0 with a factor two

$$\Delta f_{\text{Stub}} = f_0 \frac{4}{\pi} Z_0 G. \quad (3.38)$$

The FWHM simply describes an external quality factor of the circuit $(4Z_0 G/\pi)^{-1}$ which is inversely proportional to the conductance, as expected. Moreover, it scales with the characteristic impedance which can be increased for superconducting circuits with large kinetic inductance, see section 3.2.1.

3.3.5. Output impedance

So far we have discussed the circuit characteristics from looking into the device. Such properties are described in the reflectance signals. To understand the characteristics of signals emerging from the device itself, we look at the transmission properties of the circuit. To this end, we define Z_{out} as the impedance seen by the device towards the detector, as shown in Fig. 3.10. Using the impedance of a terminated transmission line from Eq. 3.10, the output impedance can be calculated as

$$Z_{\text{out}} = Z_0 \frac{Z_{\text{T}} + jZ_0 \tan(\gamma D_1)}{Z_0 + jZ_{\text{T}} \tan(\gamma D_1)}, \quad (3.39)$$

where Z_T is the output impedance at the T-junction given as

$$Z_T = Z_0 \frac{\cot(\gamma D_2)}{1 + \cot(\gamma D_2)}. \quad (3.40)$$

For the lossless case and real impedances, one can utilize the analytic solutions of lengths given in Eq. 3.30 to reach at $Z_{\text{out}} = R$ at matching. To put it all together, at matching the stub tuner transforms the input impedance to the characteristic Z_0 and output impedance to load Z_L .

The matching symmetry mentioned earlier is lost in the case of lossy circuits. Full matching is however always possible from both sides by compensating the losses in the stub tuner lengths. In the end, the relevant quantity is the power reaching the detector. Therefore even in the case, $Z_{\text{out}} = R$, a lot of signal can be lost due to losses in the transmission lines.

3.3.6. Transmission function

In this section, an expression for the transmission function of the stub tuner circuit is derived. To avoid the confusion, the load resistance is now referred as the source. We again consider the schematic shown in Fig. 3.10 where a voltage source V_S with a real source impedance R is attached at the end of a stub tuner length. What remains is to find the voltage drop $V_0(D_1)$ across the detector's resistor, Z_0 in this instance.

The wave propagation in transmission lines is derived in section 3.1 and described by $V(x) = V_0^+ e^{-\gamma x} + V_0^- e^{\gamma x}$ and $I(x) = I_0^+ e^{-\gamma x} + I_0^- e^{\gamma x}$, where voltage and current amplitudes are related by $Z_0 = V_0^\pm / I_0^\pm$. The coefficients are subject to the following boundary conditions

$$\begin{aligned} V(0) &= V_S - RI(0), \\ V(D_1 - \delta x) &= V(D_1 + \delta x) = V(D_1), \\ I(D_1 - \delta x) &= I(D_1 + \delta x) + \frac{V(D_1)}{Z_0}, \\ I(D_1 + D_2) &= 0, \end{aligned} \quad (3.41)$$

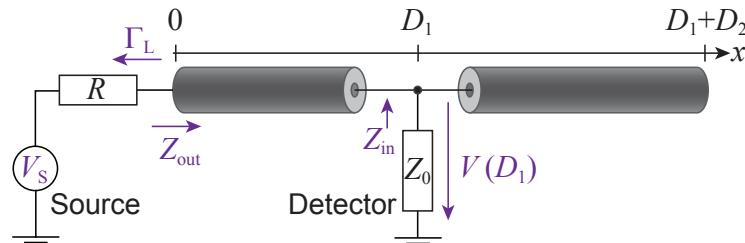


Figure 3.10. Stub tuner transmission A schematic of the stub tuner circuit to illustrate the voltage transmission from a voltage source with a real impedance R . The x axis defines the relative positions of the stub tuner lengths with respect to the source and the detector. Symbols are explained in the text.

where the positions $D_1 \pm \delta x$ denote the immediate left and right of the T-junction. After a lengthy calculation, one arrives at the voltage coefficients given as

$$\begin{aligned} V_0^- &= -V_S \frac{Z_0}{R + Z_0} \frac{1}{\Gamma_L + e^{2\gamma D_1} [1 + 2 \coth(\gamma D_2)]}, \\ V_0^+ &= -V_0^- e^{2\gamma D_1} [1 + 2 \coth(\gamma D_2)], \end{aligned} \quad (3.42)$$

where $\Gamma_L = (R - Z_0)/(R + Z_0)$ is the reflection coefficient at $x = 0$, when looking into the source. The voltage transmission function can now be defined as

$$\begin{aligned} t_V(f, R) &= \frac{V(D_1)}{V_S} = \frac{V_0^+ e^{-\gamma D_1} + V_0^- e^{\gamma D_1}}{V_S} \\ &= \frac{2Z_0}{R + Z_0} \frac{e^{\gamma D_1} \coth(\gamma D_2)}{\Gamma_L + e^{2\gamma D_1} [1 + 2 \coth(\gamma D_2)]}. \end{aligned} \quad (3.43)$$

The preceding result is a general expression and valid for lossy cases too. This can be simplified for a lossless case and a matched source impedance $R \gg Z_0$. Following a similar approach of cotangent expansion shown in section 3.3.4, the power transmission function is approximated as

$$|t_V(f)|^2 \approx \frac{Z_0}{4R} \frac{1}{1 + \left(\frac{\pi}{2} \frac{R}{Z_0} \frac{\Delta f}{f_0}\right)^2}. \quad (3.44)$$

The simplified expression describes a Lorentzian, and provides two useful information. Firstly, the transmission bandwidth at matching given by the FWHM = $4f_0 Z_0/\pi R$ is the same as the one derived in the case of reflectance, see section 3.3.4. Secondly, the maximum power density measured by the detector at the resonance frequency is $S_V/4R$, where S_V is the voltage spectral density of the source. The same value is achieved if one gets rid of the matching circuit and changes the impedance of the detector from Z_0 to R , a case of simple electrical impedance matching. The case of no impedance matching can be obtained by setting D_i to zero in the Eq. 3.43. The resulting power

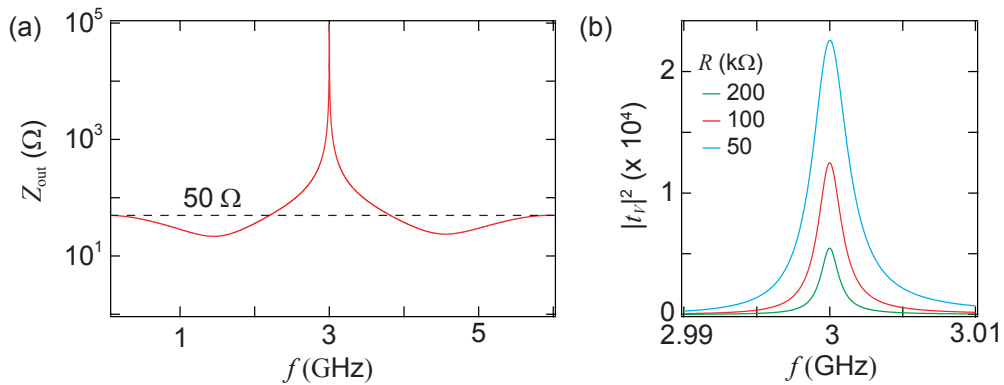


Figure 3.11. Transmission response to real impedances (a) Output impedance seen by the device towards the detector. (b) Frequency dependence of the voltage transmission function for different device resistance.

transmission is then given as $\approx (Z_0/R)^2$. The stub tuner hence provides a transmission enhancement up to a factor of $\sim R/Z_0$ within its bandwidth.

For numerical calculations, we again consider a lossless case where stub tuner is matched to 100 k Ω . The output impedance described by Eq. 3.39 is plotted in Fig. 3.11(a). As expected, Z_{out} transforms to 100 k Ω at the resonance frequency. On either side of the resonance, the impedance decreases non-monotonically and reaches a value of Z_0 . Higher harmonics of stub tuner show the same behaviour, though the maximum value of Z_{out} monotonically decreases when going away from the matched fundamental mode. The transmission response is plotted in Fig. 3.11(b). It is apparent that the heights and the linewidths are both proportional to $1/R$. The transmission peak for the matched case is an upper bound for any matching circuit and irrespective of the matching frequency. Experimentally, one measures power by integrating the spectral density around a bandwidth. Naturally, the amount of signal absorbed by any detector is critically dependent on its bandwidth.

3.3.7. Figure of merit

As seen in the previous section, the transmission bandwidth (BW) of the stub tuner is of the order of few MHz for device resistance of 100 k Ω . For the case of no impedance matching, the power spectral density is greatly reduced but a much larger bandwidth can be integrated over to enhance the signal. One can wonder if there is any benefit of the stub tuner or any matching circuit with limited BW over a wide band detection. We attempt to answer this question quantitatively.

The signal power detected over Z_0 after symmetrically integrating over a total bandwidth BW can be expressed as

$$P_{BW} = \int_{BW} \frac{V(D_1)^2}{Z_0} df = \frac{V_S^2}{Z_0} \int_{-BW/2}^{BW/2} |t_V|^2 df. \quad (3.45)$$

For a lossless stub tuner with a matched load $R \gg Z_0$, Eq. 3.44 can be analytically integrated to arrive at the total power

$$P_{\text{stub}}|_{BW} = \frac{V_S^2 f_0 Z_0}{\pi R^2} \tan^{-1} \left(BW \frac{\pi R}{4 f_0 Z_0} \right). \quad (3.46)$$

If one chooses the FWHM of the transmission response as the bandwidth, $4f_0 Z_0/\pi R$, the detected signal power at full matching reads as

$$P_{\text{stub}}|_{\text{FWHM}} = \frac{f_0 V_S^2 Z_0}{4 R^2}. \quad (3.47)$$

For no impedance matching, the transmission function is $t_V \approx Z_0/R$. The detected power over the bandwidth BW is then simply

$$P_{\text{wideband}} = BW \frac{V_S^2 Z_0}{R^2}. \quad (3.48)$$

It seems that the stub tuner provides an improvement in detected power only if $f_0/4 > BW$. However, a real strength of a successful measurement is captured in the signal

to background noise ratio (SNR). In our case the amplifiers, needed to overcome the detection limit of small emission signals, are the main source of the background noise S_A . SNR can be generally expressed as

$$\text{SNR} = \frac{P_{BW}}{S_A BW} = \frac{1}{S_A BW} \frac{V_S^2}{Z_0} \int_{-BW/2}^{BW/2} |t_V|^2 df. \quad (3.49)$$

The BW dependence of the SNR for stub tuner and no matching can now be calculated with help of Eq. 3.46 and 3.48. While SNR is independent of BW in case of a wideband detection, it peaks at zero BW for stub tuner. But the signal always increases with the BW . To capture the interplay of two quantities, we define a product which in case of stub tuner reads as

$$\text{SNR}_{\text{stub}} \cdot P_{\text{stub}} = \frac{1}{S_A BW} \left[\frac{V_S^2 f_0 Z_0}{\pi R^2} \tan^{-1} \left(BW \frac{\pi R}{4 f_0 Z_0} \right) \right]^2. \quad (3.50)$$

The product can be maximized by setting its derivative to zero resulting in an optimal integration bandwidth

$$BW^{\text{optimal}} = 1.39 f_0 \frac{4 Z_0}{\pi R}. \quad (3.51)$$

Since the bandwidth is always changing with R , fixing this to be the FWHM for the matched value is always a good rule of thumb.

The efficiency of the stub tuner for different matching conditions can now be compared with the wideband detection. To this end, we introduce a figure of merit $g_{\text{SNR}} = \text{SNR}_{\text{matching}}/\text{SNR}_{\text{wideband}}$. The resulting ratio at full matching for $BW = \text{FWHM}$ is

$$g_{\text{SNR}} = \frac{\pi R}{16 Z_0}. \quad (3.52)$$

Stub tuner clearly provides a great increase in the performance of emission measurements since the load resistance R in our devices is much larger than Z_0 . It can be shown that the same figure of merit is achieved with an LC circuit [87], however the bandwidth in this case scales as $\sqrt{Z_0/R}$. The latter can tremendously speed up data acquisition needed for time-resolved measurements.

3.3.8. Open stub tuner measurements

We now discuss measurements performed on an open stub tuner, $Z_L = \infty$. The CTL widths of the central conductor and the gap are 12 μm and 6.5 μm , respectively. For this geometry and substrate properties, Sonnet simulations estimate the line impedance of $Z_0 \sim 50 \Omega$. The Reflected power at two different temperatures for the circuit are shown in Fig. 3.12(a). From fitting the resonance curves using Eq. 3.32, we extract $D_1 \approx 10 \text{ mm}$, $D_2 \approx 10.2 \text{ mm}$ and $\epsilon_{\text{eff}} = 6.3$. The small deviations from the geometric lengths 10 mm, 10.3 mm can be due to a slightly different characteristic impedance Z_0 from 50 Ω . The corresponding losses are found to be $\alpha = 0.008 \text{ m}^{-1}$ and 0.016 m^{-1} for $T = 20 \text{ mK}$ and 1.2 K respectively. The observed frequency shift is because of the larger kinetic inductance at higher temperature, see section 3.2.1.

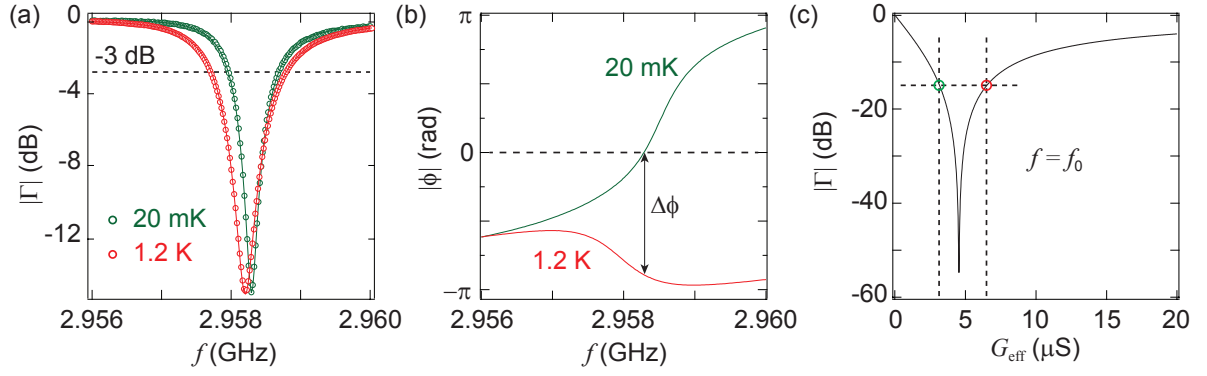


Figure 3.12. Stub tuner measurements (a) Reflectance power response at two different temperatures of the same circuit. Solid lines are the best fits to Eq. 3.32. (b) Corresponding measurements of phase response. (c) Calculated depth of the resonance using the parameters extracted from the fitting in panel (a). Circular markers denote the respective G_{eff} for two temperatures.

Coincidentally the depth of the resonance is the same for two temperature values, however the linewidth different with a bigger value at the higher T . Moreover, the phase response nearly changes by $\Delta\phi \sim \pi$ around the resonance frequencies. The fitting of the phase response is tedious because of the need to calibrate the phase evolution in the coax cables. We therefore rely on fitting the power spectra where background losses from cables can be easily subtracted by a frequency independent baseline.

The behaviour of phase change by π is expected if the load changes its impedance across the matching point, see Fig. 3.8(c). Since there is no load attached, an analogous picture can be formed with an effective conductance $G_{\text{eff}} = G + G_{\text{Loss}}$ which has been explained in the section 3.3.3. For $G = 0$, the G_{eff} is purely originating from the losses of the stub tuner. Using the parameters such as lengths D_1 , D_2 and the dielectric constant ϵ_{eff} , the depth of the resonance can be calculated using Eq. 3.32 against G_{eff} axis. This is plotted in Fig. 3.12(c) which can be used now to find $G_{\text{eff}} = 3.2 \mu\text{S}$ and $6.4 \mu\text{S}$ for 20 mK and 1.2 K respectively. The proportionality of G_{Loss} with internal losses α further justifies a model where losses can be treated as a shunt conductance parallel to the device load, see the inset of the Fig. 3.9(b).

3.3.9. Why 50 Ω ?

There are two criteria that determine the performance of the coax cables - loss and peak power handling. It turns out that both quantities are dependent on the line impedance. For air filled coaxes, minimum insertion loss happens at 77 Ω while the peak power handling, limited by the electric voltage breakdown, occurs at 30 Ω [72]. Thus, choice of 50 Ω acts as a good compromise between two criteria. Furthermore to avoid reflections, most of the instruments and microwave components are also planned to have the same input or output impedance.

4 Device fabrication, measurement and characterization techniques

Important benchmarks for any device are its exceptional performance, high yield production and reproducibility. With nanodevices, imperfect substrate and resist residues from processing can act as external perturbations and affect all the above. It is hence imperative that choice of resists for lithography, chemicals for etching and metals for contacting are carefully made. Moreover, one has to achieve compatibility of one step of the fabrication with the next such that none of the desired functionalities of the elements involved are compromised.

We aim to combine stub tuner circuits made of niobium with quantum devices from carbon nanotubes, InAs nanowires and graphene. For optimal performance of the microwave circuits, two requirements must be met. Firstly, the loss of the circuit should be as low as possible to enable load-dominated impedance matching at high resistance, and to facilitate efficient collection of emission signals. Secondly, the distance between the stub tuner and the device needs to be kept short to avoid RC low-pass filtering effect from stray capacitance of the link between stub tuner and the device, and high impedance of the device. In this chapter, we discuss the relevant fabrication methods to realize hybrid devices that meet the above requirements. We also briefly discuss the measurement setup. A thorough recipe of individual fabrication steps and details of the setup can be found in appendices A and B respectively.

4.1. Nb stub tuner

The fabrication of all hybrid devices discussed in this thesis starts with stub tuner. An undoped silicon substrate with 170 nm of thermally oxidized SiO_2 on top is first cleaned extensively with acetone, isopropanol, deionized water and piranha etch (mix of sulphuric acid and hydrogen peroxide) to get rid of any organic and inorganic dirt. *Undoped* substrate is important to minimize microwave losses. The role of SiO_2 is explained further below. We then sputter a film of Nb of thickness 100 – 150 nm at a rate of $\approx 1 \text{ \AA/s}$ in an ultra high vacuum (UHV) system with a background pressures below 10^{-9} mbar. We find that films sputtered at lower rates have relatively lower internal quality factors.

For patterning coplanar transmission lines, gaps need to be etched in the Nb film. UV mask lithography is employed (unless stated) because of the mm-long stubs involved and relatively small write-field of our ebeam writer. An important requisite that etching must meet, is to have smooth and chemically inert surface so that devices do not suffer from surface defects and roughness. We find that inductively coupled plasma (ICP)

from Ar/Cl₂ reproducibly produces good physical surfaces of SiO₂. After Nb etching, we briefly etch with Ar and then O₂ to get rid of top SiO₂ surface that could be chemically different from the pristine one. Ar/Cl₂ etching is however problematic for Si surfaces because of its three times higher etching rate compared to Nb. Any Nb residues hence act like a mask for Si, creating pillar like structures. Because of inclusion of Ar that tends to isotropically etch the resist, the wall profile of Nb is not strictly vertical. The slanted wall profile is, however, useful for contacting with smaller thickness in the subsequent evaporation step. Details of design and experimental characterizations of the stub tuner circuits are provided in the chapter 3.

4.2. CNT devices

CNT growth poses a significant challenge for integration of devices with niobium circuits. A growth-first approach followed by multiple lithography steps induce a lot of resist residues and imperfect interface contact. Moreover, the amorphous carbon deposited during the growth drastically reduces the quality factor of the stub tuner. A growth-last approach can lead to clean CNT spectra [88], however high temperatures $\sim 900^\circ\text{C}$ involved strongly prohibit the choice of contacting metals and even degrade the superconducting properties of Nb. We overcome both problems by transferring the CNTs from the growth substrate to the target substrate on which niobium circuit is already fabricated.

We describe two methods for the CNT transfer. In so-called deterministic stamping [89], CNTs are transferred in the last step on a prefabricated chip containing gates, contacts and circuits. The method allows us to check whether the CNTs are metallic or semiconducting before the completion of the device. Since such transfers are performed in the ambient conditions, we adopt a second method [87, 90] for contacting materials such as aluminium that oxidise in air. Here, CNTs are first transferred on the target substrate and subsequently contacted using standard lithography. We refer to this as a probabilistic stamping method.

4.2.1. Deterministic CNT device

We first create a pillar structure shown in Fig. 4.1(a,b) to host gates lines and source/drain contacts. The chip is then wirebonded on a PCB and CNTs are mechanically transferred using a micro manipulator setup. The process can be monitored with voltage measurements and repeated until a desired CNT is transferred. The transfer method thus precludes a fresh start of the lengthy device fabrication process if CNTs are destroyed, for example due to electrostatic discharges.

Bottom gates and contacts

In absence of a global backgate due to the requirement of an undoped substrate, local gates are needed for tuning the Fermi level. We aim to define narrow gates with small separation from each other and from the CNT to achieve strong lever arms and sharp confinement. A SEM image of bottom gates is shown in Fig. 4.1(c) with the cross

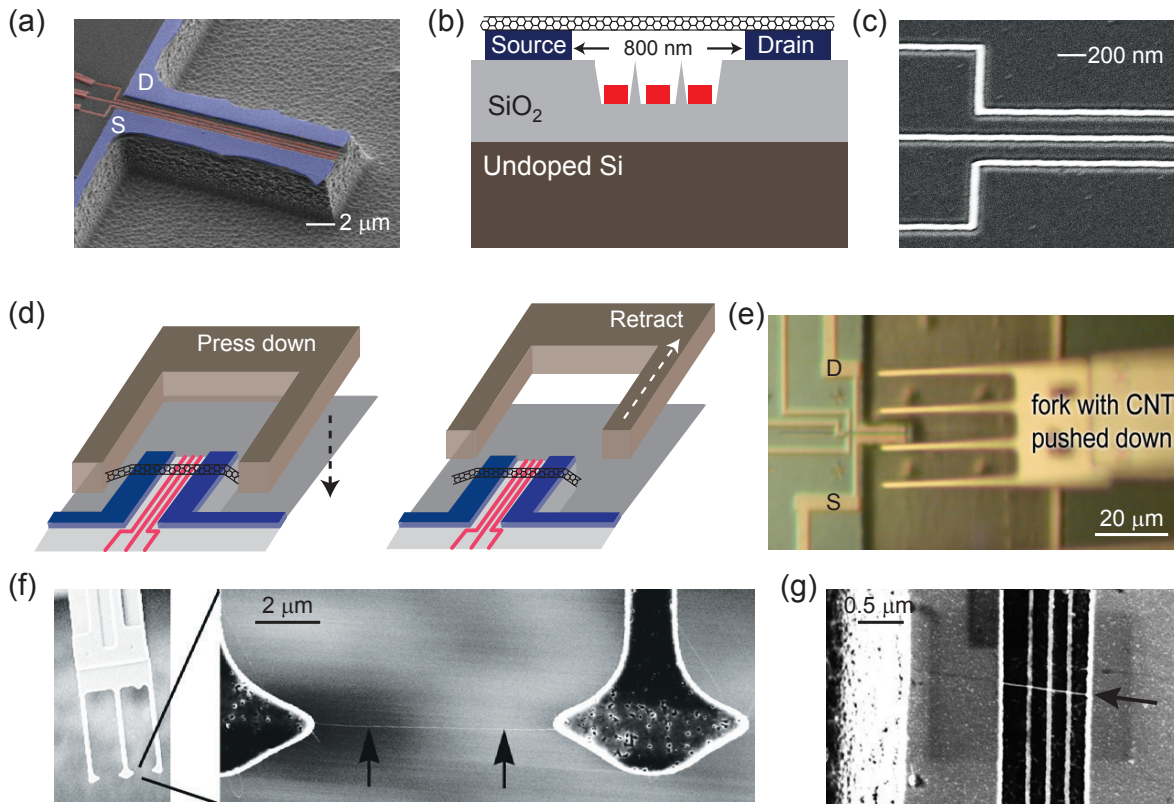


Figure 4.1. Deterministic transfer of CNTs (a) A SEM image of the final pillar structure with all relevant contacts. (b) A cross section schematic showing relative positions of the contacts and gates. (c) A SEM image of the bottom gates buried in SiO_2 . (d) Schematics of forks pressing down on and retracting from contacts. (e) Optical image of the forks aligned and pressed over source drain contacts during the transfer process. Pillar structure in the recess with source (S), drain (D) and three bottom gates can also be seen. (f) SEM images of the silicon forks with CNT grown on it. (g) SEM image of a transferred CNT on the source drain contacts. CNTs are marked by the solid arrows.

section in panel (b). The evaporated gates from Ti (5 nm)/Au (35 nm) are recessed (depth ~ 100 nm) to avoid direct electrical contacts with suspended CNTs.

Recess is produced by a combination of anisotropic reactive ion etching (RIE) from CF_4 and isotropic wet etching with hydrofluoric (HF) acid. The isotropic etching produces slanted profiles, and helps to avoid metal deposition on the walls from the evaporation. Wet etching is kept to an essential minimum because it limits the separation between the gates, especially if the adhesion of the resist is not good with the substrate. HF can then creep under, and cause a collapse of the resist-bridge between the recess. Bad adhesion can happen, for example, because of chemical and physical modification of the SiO_2 surface from RIE etching. An alternative to HF is to use CHF_3/O_2 for isotropic dry etching. We are able to achieve a linewidth of ~ 50 nm and separation of ~ 200 nm. We find that gates with width narrower than 30 nm tend to be destroyed due to electrostatic discharges and electro-migration. After gate fabrication, source/drain

contacts are evaporated close to the gate lines. We use Pd of thickness 90 nm as the choice of metal because of high success with CNT transfer compared to Ti/Au. The contacts are shown in false colored SEM (blue) in Fig. 4.1(a).

Pillar

Pillars are created by etching the substrate around the active area using RIE. For silicon etching, a mixture of SF₆ and O₂ is used. SiO₂ is however etched with CHF₃ because of much slower etching with SF₆. Etching can create different wall profiles depending on the oxygen amount [91]. Higher oxygen ratio increases the etching rate of both the resist mask and silicon, however reduces the anisotropy. We are able to achieve a pillar depth of 4 μm from a PMMA resist thickness of 1.2 μm.

Growth substrate

CNTs are grown on polycrystalline silicon fork-like structures using iron-loaded ferritin proteins as catalysts [92]. The poly-Si arms are 2 μm wide and the gap spanned by the CNTs ~ 8 μm. Growth is done in a chemical vapor deposition (CVD) chamber maintained at CH₄ + H₂ (155 mbar + 65 mbar) atmosphere and 850 °C for 15 minutes. Reference forks with CNTs are imaged under SEM to assess the density of the tubes and subsequently optimize the catalyst concentration. A low density is needed to ideally have one nanotube per fork. Growth characterizations on forks are done by Dr. Matthias Muoth at ETH Zurich.

Transfer process

The steps of the transfer are schematically presented in the Fig. 4.1(d). Just before transfer, a weak Ar plasma is used to clean the patterned structures to get rid of any residual organic dirt on contacts. The forks with pristine CNTs, not exposed to any electron beam or post-processing, are then mounted on a clamp and aligned with the source-drain contacts using the optical microscope of a micro-manipulator setup as shown in Fig. 4.1(e). This is followed by pressing the CNT onto the contacts using three-axis piezo control. The height of the pillar structure determines how much one can lower down the forks. We find 4 μm to be sufficient to perform the transfer.

CNT preselection

After completion of stub tuner and contacts fabrication, the chip can be already bonded on a printed circuit board (PCB). This allows successful CNT transfers to be real-time monitored through voltage biased (200 mV) resistance measurements. Voltages are then applied to the gates to determine the metallic or semiconducting nature of the tube. The forks are carefully retracted leaving the nanotube held on the source drain contact due to van der Waals force. We aim at good transparent contacts, meaning a low resistance. However, during the transfer the resistance is sometimes too low indicating that two or more CNTs have been transferred. One can simply apply a large bias voltage to remove all CNTs at once and try again. The assembly hence allows the

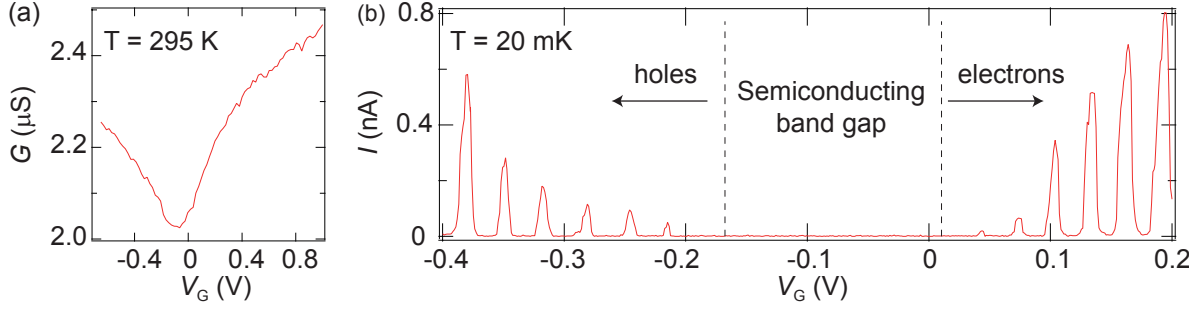


Figure 4.2. CNT preselection during mechanical transfer (a) Conductance as a function of gate voltage measured in ambient conditions showing features of a narrow bandgap semiconducting CNT. (b) Evolution of Coulomb resonances for electrons and holes at a bias voltage of 5 mV in the same device at 20 mK. Note that gate voltage range is different for two plots.

reuse of the same circuit with different tubes. We obtained 20% yield of transferring a single tube, with contact resistance generally more than $100 \text{ k}\Omega$ [93].

An example of room temperature characterization for CNT selection is shown in Fig. 4.2(a). It shows the measured conductance against a central gate voltage. The conductance dip around zero gate voltage is a feature of a semiconducting CNT [38]. The fact that the dip is rather shallow and does not go to zero, points to a narrow bandgap. A temperature of 295 K can thus thermally excite charge carriers above the bandgap. This is further confirmed when the device is cooled down to 20 mK. The device conductance now exhibits two series of Coulomb peaks separated by a zero current area due to the bandgap. Left peaks are due to holes, Fermi level in valence band while right ones are from electrons, Fermi level in conduction band. Asymmetry in current between two charge states are due to residual doping from the contacts, n -type in this case. The bandgap fixes a zero charge state on the quantum dot, therefore, exact occupation of dots can be assigned from counting Coulomb peaks on either side. Using the lever arm from the Coulomb diamond measurements, the bandgap is estimated to be around $\sim 30 \text{ meV}$ which is comparable to the room temperature thermal energy of $k_B T = 25 \text{ meV}$, where k_B is the Boltzmann constant.

4.2.2. Probabilistic CNT device

The target substrate is prepared by evaporating Ti/Au markers on a SiO_2 area with dimensions $200 \mu\text{m} \times 200 \mu\text{m}$ at the end of length D_1 of the stub tuner [the blue square at bottom in Fig. 4.3(a)]. The area is created already during Nb etching of the stub tuner. The markers are patterned with standard ebeam lithography using ZEP resist to minimize resist residues [94]. This is followed by preparing a stamp substrate on which CNTs are grown. The stamp substrate is now pressed on top of the target substrate with help of a mask aligner, resulting in CNT transfer. The device is completed by evaporating contacts and gates in subsequent lithography steps. Since we cannot check before the completion, whether devices are working, or if CNTs are metallic or semiconducting, this stamping method is probabilistic.

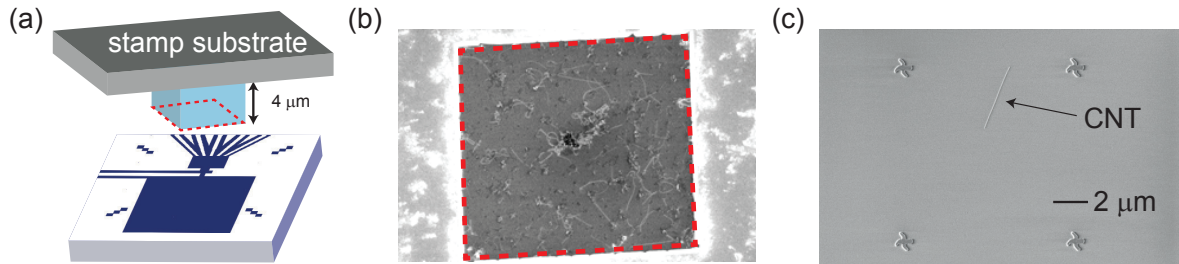


Figure 4.3. Probabilistic stamping of CNTs (a) A cartoon depicting the stamping process with the growth substrate on top and the target substrate at bottom. (b) A SEM image of top view of one of the stamp pillars, red square with edge length $50 \mu\text{m}$, showing a high density growth of CNTs. (c) An SEM image of a stamped CNT on the target substrate with markers.

Stamp substrate

The stamp substrate is obtained by creating pillars of $50 \mu\text{m} \times 50 \mu\text{m}$ in area and $4 \mu\text{m}$ height on the substrate. This is done by first wet etching SiO_2 from HF and then etching Si using RIE from SF_6 and O_2 . Pillars are separated from each other $50 \mu\text{m}$ in a grid of $2 \text{mm} \times 2 \text{mm}$ area. Highly concentrated Fe/Mo catalysts are spun on the substrate, and repeated at least five times to have a high coverage. CNTs are Grown in a CVD chamber with a flow maintained at $\text{CH}_4 + \text{H}_2$ ($1000 \text{ sccm} + 500 \text{ sccm}$) and temperature $950 \text{ }^\circ\text{C}$ for 10 minutes [95]. The recipe results in a high density growth of CNTs as shown in Fig. 4.3(b).

Stamping process

Stamp substrate is first fixed on a transparent glass plate using a soft glue (undiluted PMMA 950K) and mounted in the mask-slot of a UV mask aligner. It is then aligned with the stamping area and pressed together. It is important that the time between gluing and stamping is kept short so that the glue does not become hard, and horizontal surfaces could be maintained during the press down. Figure 4.3(c) shows an SEM image of a stamped CNT. On average, we find 5 straight CNTs of usable length within the stamping area. This is enough since we can connect only one to the stub tuner. Though the stamp substrate is opaque, its larger size compared to stamping area accounts for any misalignment. Few CNTs and catalyst particles can therefore be accidentally transferred directly to the transmission lines. These however do not create any shorts because of the oxidized surface of Nb. Alternatively, one can also use transparent quartz substrate for CNT stamps that could allow better alignment [90]. The pillar etching process in this case however is more tedious.

The yield of CNT transfer goes drastically down if the stamps are used a second time. We etch 25 nm of the top SiO_2 from the stamp substrate using HF and spin new catalyst for a fresh CNT growth. This way, stamp pillars with clean surfaces can be reused at least 5 more times till silicon oxide is completely gone. Careful cleaning of pillars before growth is needed in general to avoid particles that could act as spacers during stamping and prevent CNT transfer. For the same reason, the catalyst particles are sonicated for 2 hours to avoid large clusters before spinning.

CNT localization and metallization

Individual CNTs are imaged using SEM and located relative to the evaporated markers in the stamping area as shown in Fig. 4.3(c). To enhance the imaging sensitivity to the surface, we shoot electron beams with relatively low acceleration voltage ~ 1 keV. Furthermore, an in-lens detector is used. It is not possible to guess from the image contrast whether CNTs are single- or multi- wall, metallic or semiconducting, full of defects or pristine. The nanotubes are hence chosen randomly though we always go for straight ones which are shorter than $10 \mu\text{m}$ and appear relatively thinner under the same imaging conditions.

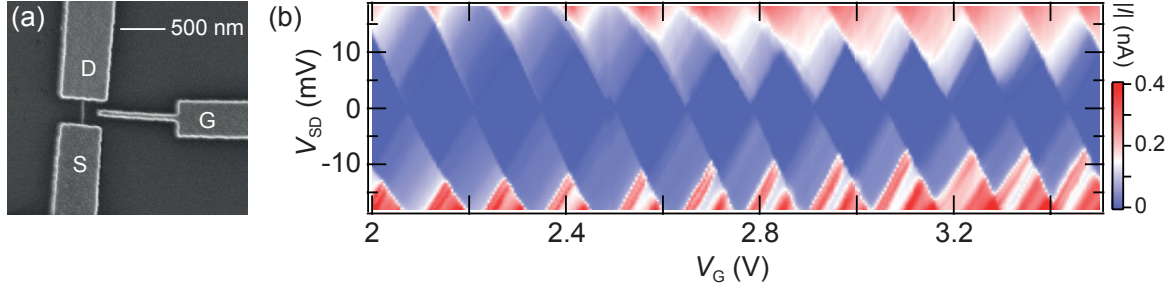


Figure 4.4. CNT metallization and quantum dot formation (a) A SEM image of a probabilistically stamped CNT with source (D), drain (D) contacts and a local gate (G) electrode. (b) Charge stability diagram of the device measured at 20 mK showing regular Coulomb diamonds.

After localization, we use standard ebeam lithography to pattern contacts on the CNT. An example of a CNT device is shown in Fig. 4.4(a) where source and drain contacts are separated by 300 nm. A side gate of width ~ 50 nm fabricated in the same lithography step is separated by ~ 150 nm from the CNT. In absence of a global gate, we rely on the single local gate to tune the dot occupation. Charge stability diagram for the same device is presented in Fig. 4.4(b). We can see sequential filling of dots and a regular pattern of Coulomb diamonds. For similar geometries, we find charging energies in the range of 10 – 20 meV.

The exact occupation of the dot in the absence of a semiconducting gap, however, cannot be determined. While for semiconducting CNTs, Schottky barriers and their bandgap [96] help in creating confinements of the quantum dots, it is usually not possible to know the location of the dots in a metallic CNT. In several devices, with a three terminal geometry and two CNT sections, we find only a single dot, tunable with both side gates. This suggests that the CNT is weakly coupled to the contacts and its orbitals are not limited to a CNT section but rather spread under the contacts.

4.2.3. Superconducting contacts

We choose aluminium as the choice of superconducting contacts because of its large coherence length required for Josephson and Andreev processes. In comparison with normal contacts, superconducting contacts are found to be extremely sensitive to processing resist type and steps of fabrication. Moreover, argon-mill cleaning before metal

evaporation cannot be done because of high risk of destroying the exposed CNT section. To have good wetting with CNTs, we evaporate a thin layer of Pd of ~ 5 nm before Al. The thickness acts as a good compromise between wetting the nanotube and keeping the Pd proximitized from the superconductor.

We first fabricate a batch of devices where both markers and contacts on stamped CNTs are processed using PMMA resist. We find that only two out of ten devices show contact resistance smaller than 500 k Ω at room temperature. We therefore switch to a cleaner ZEP resist [94] with which the contact yield boosts upto $\sim 70\%$. Moreover, we find that the resistance of contacts dramatically increase (50 k Ω to 1 M Ω) if an additional lithography step is carried out after Al evaporation. This is probably due to oxidation of Al during the baking of resist at elevated temperature ~ 180 degrees. The resistance however does not change for additional lithography steps hinting at a saturation of oxide formation. We hence perform the Al evaporation in the last step of the device fabrication and use ZEP to minimize the resist residues.

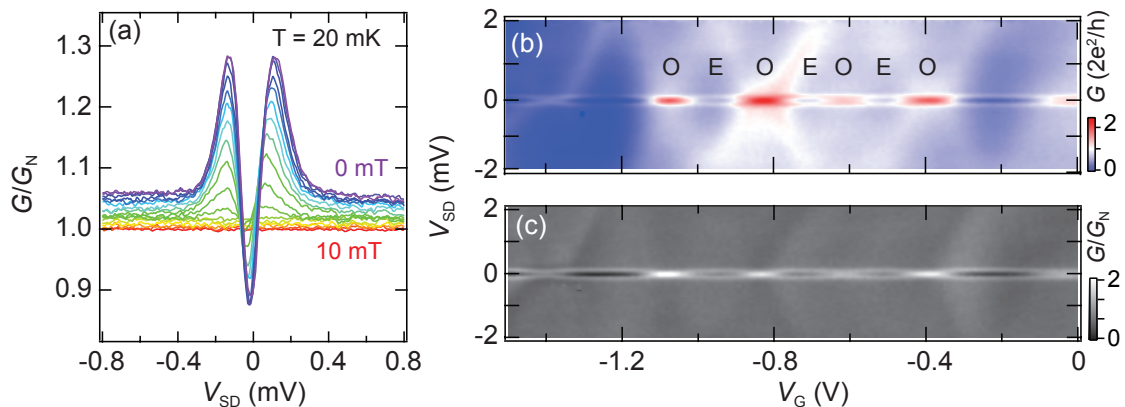


Figure 4.5. CNT coupled to superconducting leads (a) Shrinking of the superconducting gap in presence of a perpendicular magnetic field, increasing from top to bottom. Curves have offsets for clarity. (b) Presence of strongly coupled Kondo peaks in odd (O) and the bare superconducting gap in even (E) charge states. (c) Conductance in the superconducting state divided by the value in the normal state.

For a S-CNT-S device, normalized conductances G/G_N at different perpendicular magnetic fields are shown in Fig. 4.5(a). Here G_N is the conductance in the normal state of the Al leads. Quenching of the superconducting gap of 150 μeV at 10 mT is observed in all devices. The gap is smaller than the bulk value of Al ~ 180 μeV , probably due to the inclusion of the wetting layer [97]. A soft gap can result from a strong tunnel coupling. This is confirmed in the charge stability diagram presented in Fig. 4.5(b) where Kondo peaks with $G \approx 4e^2/h$ appear at the odd occupancy of the QD. To extract the role of superconductivity alone we divide G in the superconducting state by its value G_N in the normal state at 10 mT. As shown in Fig. 4.5(c), conductance is suppressed at zero bias in the even charge state while it is enhanced for the odd case [98]. The competing effect of Kondo and superconductivity is explained in section 2.6.3.

Out of four S-CNT-S devices fabricated with Pd/Al, we find three showing large lead coupling compared to the superconducting gap. This smears the subgap features.

However, large coupling is still interesting to study interplay of the Kondo effect and superconductivity through the shot noise measurements, see chapter 8.

4.3. InAs-Al nanowire devices

Our motivation to using InAs-Al nanowires is threefold. Firstly, these are strictly semi-conducting, unlike CNTs, which allows for gate controlled quantum-dot confinement, and provides transmission-control of Josephson junctions. More importantly, their in-situ epitaxial growth results in a domain-matched and impurity free semiconductor/superconductor interface [99] which is hard to achieve with CNTs and evaporated Al contacts. Moreover, in the absence of a wetting layer, larger proximity superconducting gaps can be achieved.

We receive nanowires from the group of Jesper Nygård. These are grown in the wurzite [001] direction on an InAs (111) substrate by employing molecular beam epitaxy (MBE). Gold nanoparticles of diameter 70 nm are used as catalysts [100] for its great alloying capability and inertness to oxidation. After the nanowires reach a usable length of 5 – 10 μm , growth is stopped by quenching the flux of the precursors and lowering the temperature to deactivate the catalysts. Without breaking the vacuum of the MBE chamber, Al is now grown at a low temperature by angled deposition till it reaches a thickness of 30 nm. A full-shell nanowires with epitaxial interfaces on all facets is achieved by rotating the growth substrate during Al growth.

4.3.1. Nanowire deposition and localization

The precise orientation and placement of nanowires requires a micro-manipulator setup with a far-field microscope. Since we aim at a gate tunable Josephson junction with a simple device geometry, the nanowires are transferred in a easier way as explained below. The substrate is prepared with markers in the same way as in the case of probabilistic CNT stamping. We then spin a resist on the substrate and open a window using ebeam

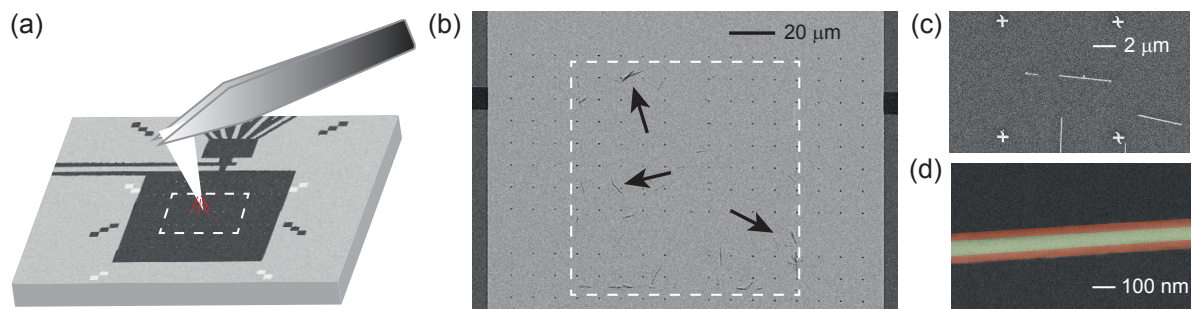


Figure 4.6. Nanowire deposition (a) A schematic showing nanowire dispersion using a cleanroom wipe (white) in a desired area marked by white dashed lines. (b) Contrast inverted SEM image of the transferred nanowires, pointed by the solid arrows, within the area. (c) Localization of the nanowires relative to the markers. (d) A false coloured SEM image at high acceleration voltage of 10 keV distinguishing the InAs core ~ 70 nm, in green, from the Al shell ~ 30 nm, in red.

lithography to receive nanowires. Nanowires are first picked up by bringing a piece of cleanroom wipe close to the growth substrate [101]. The attraction results from inherent differences in electrostatic charges and van der Waals forces. The wipe held with tweezers is then blindly rubbed over the resist window and the substrate inspected under an optical microscope to locate the nanowires. The process can be repeated till a desired number of nanowires is transferred to the active area. A schematic of the transfer is shown in Fig. 4.6(a).

After stripping the resist, the transferred nanowires are localized using SEM. An image in Fig. 4.6(b) shows all the nanowires placed within the white dashed square, where the resist window was created earlier. The transfer method thus avoids unnecessary nanowires on signal lines without needing any alignment. It is possible to distinguish the InAs core from the Al shell in the deposited nanowires under high acceleration voltage of ebeam ~ 10 keV, as shown in Fig. 4.6(d).

4.3.2. NW etching and metallization

To create S-NW-S devices, the Al section needs to be removed isotropically. We lithographically define a mask and wet etch using Transene type D. The rate of etching is temperature controlled to achieve reproducibility. After etching, samples are vigorously rinsed with deionized water to prevent capillary etching effect along the length of the nanowire. We find that palladium has a catalytic effect on Transene and entire nanowire including the core can be etched in a short time in its presence. It is hence important that contacts are evaporated after Al etching. A SEM image of a typical nanowire device is shown in Fig. 4.7(a). An etched linewidth ~ 100 nm is readily achieved. Nanowires are cleaned with in-situ argon milling to get rid of native Al oxide before contacts from Pd of thickness 130 nm are evaporated. The milling also helps to get rid of any resist residues and surface defects.

A transport measurement at a bias voltage larger than superconducting gap is shown in Fig. 4.7(b). The nanowire can be tuned to have electrons with Fermi level in the conduction band to an insulating state (Fermi level in the band gap). Due to a large

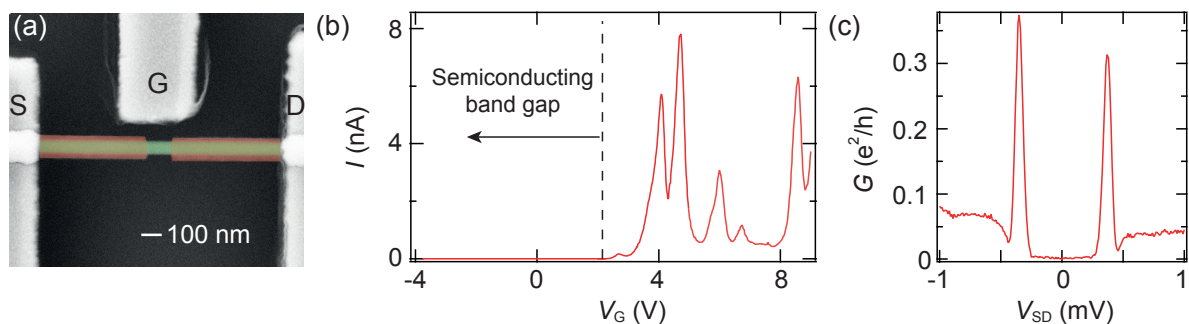


Figure 4.7. NW device fabrication and characterizations (a) A SEM image of a NW device fabricated by etching Al junction and evaporating Pd contacts and a local gate. (b) Gate dependence of current revealing transport only in the conduction band. (c) Bias dependence in a depleted NW regime showing a hard superconducting gap. Both measurements are done at the base temperature $T = 20$ mK.

band gap regime, a much higher negative gate voltage is needed to reach the hole regime and hence transport via valence band is not observed. Near the nanowire depletion, a bias dependence of conductance is shown in Fig. 4.7(c). The transport shows a BCS type of density of states with a superconducting gap $\sim 180 \mu\text{eV}$. The reason for the presence of the hard gap is a combination of defect free interface [102] and a good tunnel barrier between the superconductors, which provided by a pinched off density of states in the nanowire.

4.4. Graphene devices

We aim at capacitive coupling of graphene devices with the stub tuner circuit. After fabricating the stub tuner, a hexagonal boron nitride (hBN)/Graphene/hBN stack is simply placed at one of the open ends. The transfer method is adopted from the references [103, 104] with slight modifications. Since the device does not need any contacts, different stacks can be placed on the same stub tuner circuit. Firstly, a $4 \times 4 \times 1 \text{ mm}^3$ polydimethylsiloxane (PDMS) layer is placed on a glass slide. On this, we prepare a thin layer of polycarbonate (PC) using pipette drips pressed with another slide. After PC hardens in air, the sacrificial slide is carefully removed. hBN is mechanically exfoliated on a substrate, aligned with the PDMS of the glass slide and pressed together till hBN is transferred. The new slide shown in Fig. 4.8(a) can now be used to pickup other graphene and hBN crystals.

Graphene intended for pickup is now exfoliated on different SiO_2 substrate and localized using optical microscope. This is fixed on a chuck and aligned with respect to hBN of the newly made slide in a transfer microscope. After bringing them in contact, the chuck is heated to a temperature of 80°C . The heating further increases the contact between PC and the substrate. Heater is then switched off causing PC film to slowly retract from the substrate while graphene is picked up in the process. In a similar way, a second hBN layer is picked up forming a hBN-graphene-hBN stack hanging from the PC film, see Fig. 4.8. The success of the method lies in the fact that the van der

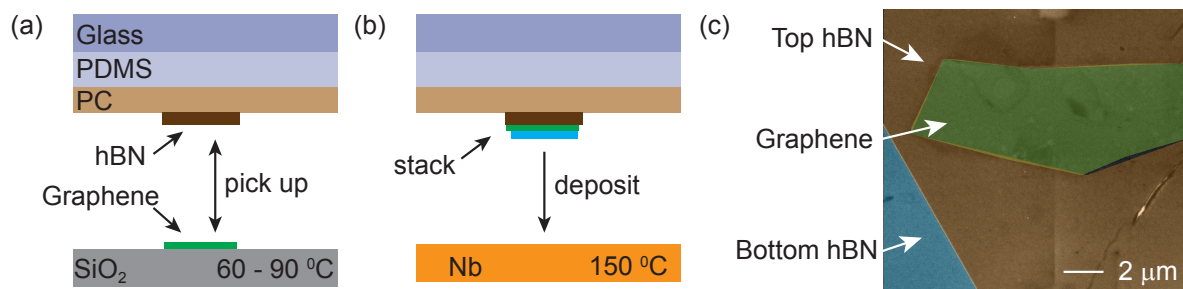


Figure 4.8. Graphene stack transfer (a) A schematic of graphene pickup from a substrate using glass slide with facing down hBN crystal, which is exfoliated on a PC layer in an earlier step. (b) Stack release on the target substrate heated to an elevated temperature. (c) False colored SEM image of a hBN-graphene-hBN stack near the high impedance end of a stub tuner after the transfer. Note that the sequence of the pickup is reversed on the transferred stack.

Waals force between the atomically flat hBN and graphene is stronger than between the graphene or the hBN and the rough SiO₂ substrate.

In the next step, the stub tuner substrate is fixed on the chuck and the deposition of the stack done. Here again, the stack is brought in contact with the substrate and the chuck is now heated to 150°C. High temperature melts the PC and PC-stack is released on the substrate. PC is removed by dissolving it in chloroform. We found 50 % success of stack transfer on Nb as opposed to almost 100 % on SiO₂ substrate. This is expected because of a larger roughness of Nb film. The final stack can be etched with SF₆/Ar/O₂ to create well defined shapes. All stack-transfers have been done by graduate student Simon Zihlmann from our group.

4.5. Measurement setup

A requisite of measurements with superconductors and quantum dots is to cool down the devices to milli-Kelvin temperatures. This ensures small thermal energies so that charges stay in their ground state at equilibrium. In our case, T_c of Nb and Al is ~ 9 K and ~ 1 K respectively, while addition energy of quantum dots ~ 15 meV. With help of a dilution refrigerator we can reach temperature of 20 mK which is two orders of magnitude lower than the smallest energy scale, the gap of Al. However, smaller phonon-electron coupling at lower temperatures prevents cooling of electronic devices to the base temperature. Special arrangements are therefore made in the filtering and thermalisation of electronic and microwave components.

4.5.1. Dilution refrigerator

We customize a cryogen-free dilution refrigerator from Oxford Instruments to facilitate measurements of microwave reflectometry, emission noise and direct current. The fridge offers plenty of space at cold plates to accommodate bulky RF components. Importantly, a closed ⁴He circuit precludes regular filling and provides precooling of the fridge in place of a conventional liquid bath. Its bottom loading option is furthermore useful in sample exchanges without the need for a full warm up and shields removal. The fridge is equipped with a vector magnet with fields reaching 1 T in all three directions. We find that a field strength of 150 mT is already enough to quench the superconducting state of Al even when applied parallel to the film while not causing too much the losses in the stub tuner.

A photograph of the cryostat without shields and magnets is shown in Fig. 4.9(a). There are five different stages namely PT1, PT2, still, cold plate (CP) and mixing chamber (MC). Each stage is thermodynamically controlled to have distinct temperatures which decreases from top to bottom. Moreover, metallic shields attached to each stage prevent heat radiations and vacuum suppresses heat exchange. The fridge operates in two closed cooling circuits. The precooling is done by a pulse tube and an exchange gas from helium brings all the stages to an intermediate temperature of ~ 10 K. In the second part, a mixture of ³He and ⁴He is condensed into a pot at MC and continuously circulated using a pump. Endothermic movement of ³He through a phase boundary created with ⁴He cools the fridge down to 20 mK.

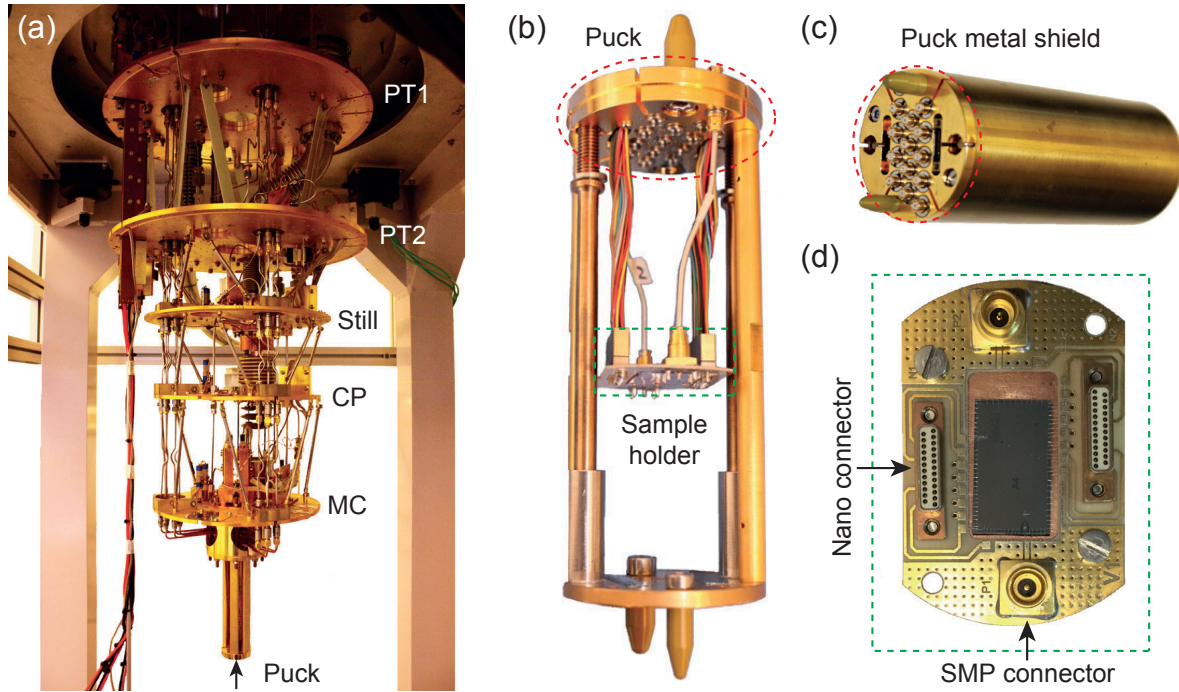


Figure 4.9. Oxford Triton dilution refrigerator (a) The bottom loading cryostat without any shields and magnets. There are five cooling stages. Arrow denotes the docking station where the sample puck is mounted. (b) The sample puck with DC and RF cables leading to the sample holder. (c) Side view of the puck with the metal shield. Part on the left with SMP and DC nano connectors connect to the docking station with counter connectors (not shown). (d) A sample holder PCB with a wire bonded device. Images are adapted from reference [87].

The devices are wire bonded on a PCB containing SMP and nanoconnectors as shown in Fig. 4.9(d). This is then mounted inside a puck and closed with a metal shield. The puck is plugged into the docking station of the cryostat which has counter connectors leading to the top of the fridge via DC loom and RF coaxes. The bottom loading of puck can be done after closing all the shields and even with a running precooling circuit of the fridge. Average cool down time of the fridge with (without) magnet is 24 (48) hours. The sample exchange takes roughly 12 hours mostly because of the need to collect the helium mixture before the transfer and condense it back afterwards.

4.5.2. Fridge wiring

A comprehensive fridge wiring is shown in Fig. 4.10. Input RF signal from a vector network analyzer (VNA) travels through a series of attenuators at each stage of the cryostat before reaching the sample. Attenuators serve three important purposes. Firstly, black body radiation leaking from high temperature to the low-temperature side is damped. Secondly, a galvanic connection between the inner and outer connector provides a thermalisation of the inner conductor. Thirdly, these provide impedance matching and prevent standing waves. Stainless steel coax cables are used to connect components from one stage to the next because of its small heat conductivity.

At MC stage, a directional coupler further attenuates the input signal by 20 dB and creates a separate path for the reflected signal. From the directional coupler to the sample, both lying on the MC stage, copper coax cables are used for its exceptional thermal conductivity. Together with losses from coax cables (~ 2 m long), the input signal is roughly attenuated by ~ 72 dB from the value at top of the fridge. The reflected RF signal then passes through a couple of circulators before reaching the cryogenic amplifier sitting at 4 K. Circulators prevent the noise of the amplifier from reaching the sample. Their third ports are terminated by cryogenic 50Ω resistors. Presence of the first circulator at MC stage is important to ensure that the thermal noise sent down to the sample by the 50Ω resistor is minimal.

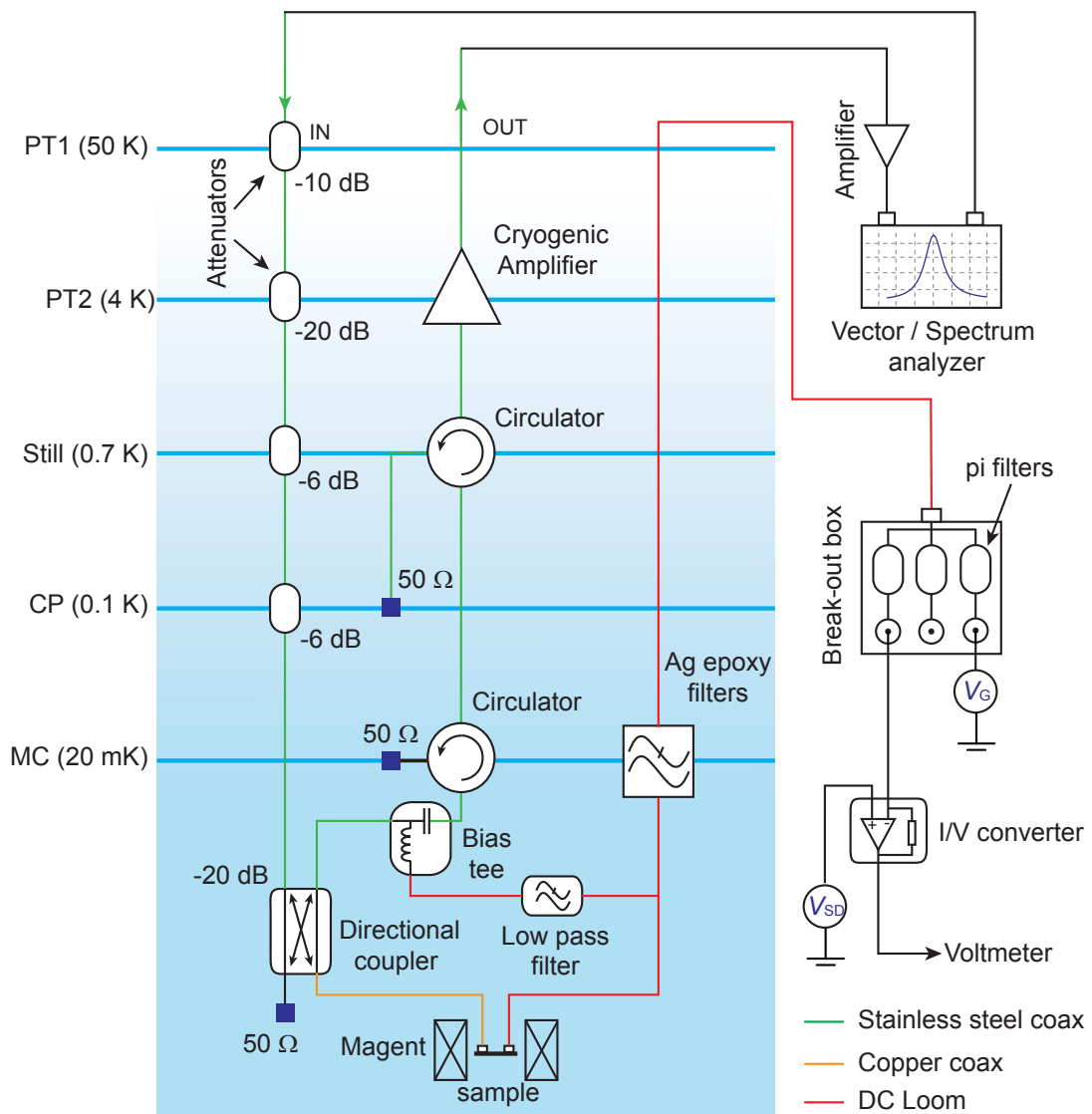


Figure 4.10. Fridge wiring A sketch of components utilized in device measurements of RF signals and direct current. For reflectometry measurements, a vector network analyser records the reflected power and phase. For noise measurements, input line is not connected and output power measured using a spectrum analyser.

The cryogenic amplifier has a gain of 35 dB and a noise temperature of 5 K at 3 GHz. The output signal is then multiplied with the input by VNA to perform a homodyne detection of the reflectance. Noise measurements on the other hand do not need any input RF signal. Output power is then measured as the power dissipated across a 50 Ω resistor by a spectrum analyser. Simultaneous DC measurement is facilitated by a bias tee placed at the MC stage of the cryostat. Source/drain biasing is provided via the offset voltage of an I/V converter and current measured with a digital multimeter. DC loom connects to the source of the devices while drain is connected to the ground plane of the transmission lines to effect immediate RF grounding of the device. However, the difference in the material of the lines through which electrical current flows and returns, results in a Seebeck voltage of 6.9 meV. All measurements presented in following chapters have been corrected for this offset. Moreover, we find that applying a low-frequency excitation to the I/V converter and recording the voltage with a lock-in produces extremely noisy results, probably due to ill defined DC ground. One way to circumvent aforementioned issue is to use a second bias tee on chip next to drain. This way, RF is still grounded via a large capacitance while DC part can be fed into the same loom cancelling any thermal voltage and creating a well defined current path.

Filtering of high temperature radiation for DC lines are done at two stages. Already at room temperature, commercially available pi-filters provide a low pass filtering above 10 MHz. More importantly, at the MC plate, each line is connected to a silver epoxy filter rod. This consists of a copper core of diameter 3 mm around which one meter of an isolated Cu wire is wound around and then covered with silver epoxy [105]. Inductance of the coil together with the stray capacitance ≈ 2 pF lead to an LC filtering effect with a 3 dB point at 6 MHz. Small skin depth at high frequencies reduces the current cross-section and further contributes to the filtering. High surface area of the filter and good thermal conductivity of silver also provides a thermalisation of the DC lines. This is confirmed using a Coulomb blockade thermometer, from Aivon, containing 33 tunnel junctions in series. Here the temperature can be deduced from the width of the conductance dip in Coulomb blockade [106]. We obtain an electronic temperature of 30 mK at the base temperature of the cryostat. The epoxy filters are made by Dr. Thomas Hasler. The author contributed to its installation and experimental characterizations.

4.5.3. RF dipstick

For faster characterizations such as critical temperature and quality factors of our circuits from niobium film, measurements can be performed using a dipstick. Moreover, cryogenic properties of microwave components can be checked before its installation in the dilution refrigerator. A photograph of the dipstick is shown in Fig. 4.11(a). It is a hollow stainless steel tube, housing two rigid steel coax cables and DC lines leading till its head. Each RF line provides an attenuation of ~ 12 dB at 3 GHz. At the bottom, the sample box is mounted to the steel lines with SMA connectors of hand formable coax cables. The sample box can be covered with a lid and also enclosed in a copper can to prevent its direct contact with liquid helium.

To cool down, the dipstick is simply lowered into a ^4He Dewar. The sliding seal around the steel tube prevents rapid fall of the dipstick into the Dewar and allows a slow cool-down, important for a low consumption of He. It takes approximately 30 minutes to

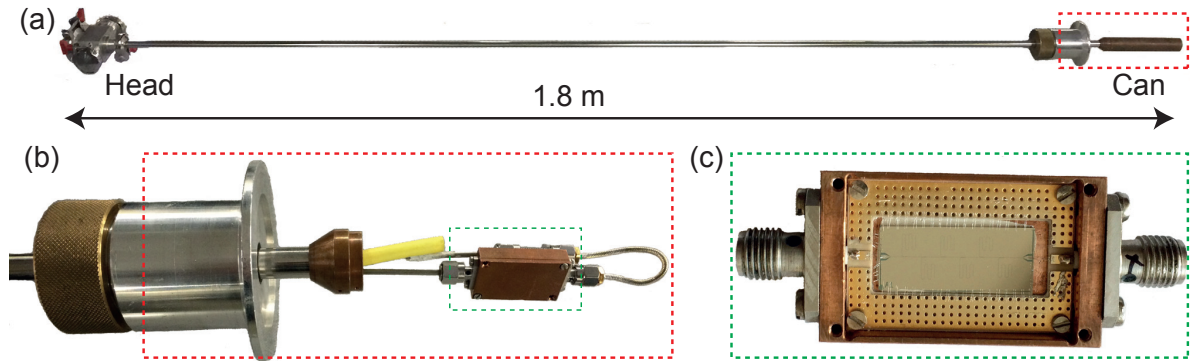


Figure 4.11. RF dipstick (a) A photograph of the dipstick. The dashed red box on right shows the sample housing with a copper can while the left part, head, contains two RF and several DC connectors in yellow case. (b) The sample housing showing a sample box connected to two SMA connectors. (c) The sample box after removing the lid showing wirebonded hanger resonators.

reach the base temperature of 4 K. The temperature can be further monitored using the thermometer installed next to the sample box. Though there is no heater, the temperature of the sample can be increased by lifting the dipstick upwards. In the end, a temperature of 4 K is well below the critical temperature of Nb to allow measurements of $\lambda/4$ hanger resonances (see chapter 3) or spurious modes in the spectrum. This is important for preselecting the Nb film or the circuit design before a complete device is fabricated using them and measured in the dilution refrigerator.

Reflectance and transmission measurements of RF circuits are performed using a VNA without any amplifier. In absence of circulators and attenuators, reflectance signals suffer from a background of standing waves. This can be calibrated by replacing the sample with 50Ω , short and open terminations at room temperature. Fortunately, the setup properties do not change a lot upon cooling down to 4 K and the calibration works well at low temperatures too.

5 Reflectometry of CNT Quantum Dots using GHz matching circuits

Coupling mesoscopic devices to microwave circuits offers a significant increase in bandwidth and signal-to-noise ratio. These facilitate fast non-invasive readouts important for quantum information processing, shot noise and correlation measurements. In particular, carbon nanotubes (CNT) have recently demonstrated their potential as low disorder one-dimensional electron systems [11, 93], which have been used to probe the physics of spin-orbit [107] and electron-phonon coupling [108] as well as to perform initialization and manipulation of spin qubits [12]. Carbon nanotubes suspended over local gates not only offer a decoupling from the surface but also mechanical resonances with high quality factors [109], creation of arbitrary local potentials and tight confinement with charging energies in excess of 50 meV [110].

In this chapter, we demonstrate the coupling of locally tunable CNT quantum devices to an impedance-matching circuits based on superconducting transmission lines. Different to previous works [111–114] where half wave resonators are employed for dispersive and a minimally invasive measurement, our circuit is aimed at providing an efficient channel to transfer (collect) microwave radiation into (from) a quantum device. Additionally, the circuit offers bandwidths (BW) in the MHz range even for device impedances on the order of $M\Omega$. These features, on one hand, allow us to perform high BW measurements for deducing both conductance and susceptance changes in the quantum device at GHz frequencies, and on another hand, provide near unity collection of emitted radiation power for fast shot noise measurements. We start with basic reflectometry characterizations of the stub tuner resonances. Two working regimes of the stub tuner, namely load-dominated and loss-dominated are elucidated. Reflec-

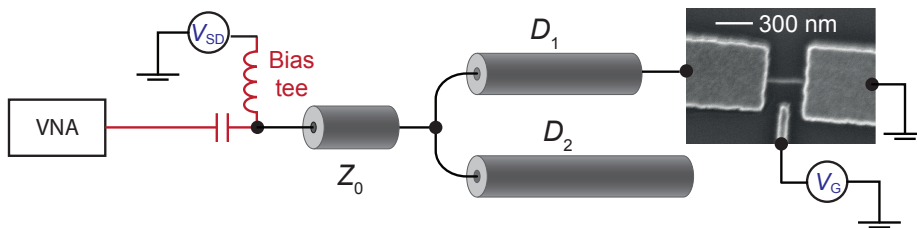


Figure 5.1. Measurement setup for reflectometry SEM image of a CNT device fabricated using probabilistic stamping and subsequent evaporation of contacts and a side gate. The device is coupled to a stub tuner with transmission line lengths D_1 and D_2 . Reflectance amplitude and phase are recorded by a vector network analyser. A bias tee facilitates simultaneous DC measurements.

ometry measurements are then presented on single, double and triple quantum dots. All devices presented here are fabricated using stamping techniques explained in the chapter 4. In particular, double and triple dots are realized on a device obtained from deterministic stamping. All circuits are patterned on a 150 nm thick Nb film, sputtered on an undoped Si substrate with 170 nm of SiO₂ on top, using photolithography and subsequent dry etching. The central conductor of the transmission line is 12 μm wide, while the gaps are 6.5 μm wide. For this geometry, Sonnet simulations yield the line impedance of $Z_0 \approx 50 \Omega$ and effective dielectric constant of $\epsilon_{\text{eff}} \approx 6$. Spurious microwave modes due to the T-junction are suppressed using on-chip wire bonds.

5.1. Matching at high impedance

The measurement setup for reflectometry is presented in Fig. 5.1. The source contact of the CNT is connected to the central conductor of length D_1 while the length D_2 ends in open. The drain contact is contacted to the ground plane of the circuit. Simultaneous RF and DC measurements are enabled by a bias tee. Reflectance spectra for different G_{CNT} are plotted in Fig. 5.2(a). For increasing G_{CNT} , the depth of the resonance increases and goes down to -30 dB for $G_{\text{CNT}} = 6 \mu\text{S}$ signifying a complete transmission of the applied input power. Alternatively, at this conductance the circuit effectively transforms the impedance of the CNT device close to 50 Ω. An interesting feature to note is the change in the reflectance spectrum when G_{CNT} is negative. Here the depth and bandwidth of the resonance decrease. This behaviour of negative differential conductance imitates an effective smaller microwave loss of the circuit.

We describe the reflectance $\Gamma = [(Z_{\text{in}}e^{j\phi} - Z_0)/(Z_{\text{in}}e^{j\phi} + Z_0)]^2$, where the phase ϕ accounts for standing waves from the measurement setup and the input impedance Z_{in} derived in chapter 3 reads as

$$Z_{\text{in}} = Z_0 \left(\tanh(\gamma D_2) + \frac{Z_0 + Z_{\text{CNT}} \tanh(\gamma D_1)}{Z_{\text{CNT}} + Z_0 \tanh(\gamma D_1)} \right)^{-1}, \quad (5.1)$$

with $\gamma = \alpha + i\beta$ the propagation constant, α the attenuation constant, $\beta = \sqrt{\epsilon_{\text{eff}}}2\pi f/c$ the phase constant and c the speed of light. We first fit the resonance in the Coulomb blockade by setting $G_{\text{CNT}} = 0$, yielding $D_1 = 10.16 \text{ mm}$, $D_2 = 10.52 \text{ mm}$, $\alpha = 0.019 \text{ m}^{-1}$ and $\epsilon_{\text{eff}} = 5.9$. These parameters are now fixed and resonance spectra outside the blockade fit to extract G_{CNT} . This is shown in Fig. 5.2(a) for $G_{\text{CNT}} = 6 \mu\text{S}$ validating the preciseness of the extracted quantities. Using the extracted parameters, the resonance depth can be calculated as a function of G_{eff} and G_{CNT} as shown in Fig. 5.2(b). The calculations yield a $G_{\text{Match}} \approx 15 \mu\text{S}$ with $G_{\text{CNT}} = 7 \mu\text{S}$ and the rest of G_{eff} contained in losses G_{Loss} . The theoretical resonance bandwidth given by $(4/\pi)f_r Z_0 G_{\text{Match}} \approx 2.8 \text{ MHz}$ is also in agreement with the measured full linewidth at half maxima of 2.6 MHz near matching. Frequency shifts of the order of 100 kHz corresponding to 100 aF can be attributed to the quantum capacitance of the CNT [115].

Figure 5.2(b) also captures the effect of microwave losses on the stub tuner response. Especially, if G_{Loss} is larger than G_{Match} , full matching cannot be achieved at any positive G_{CNT} . This is called the loss-dominated regime. We observed several samples to display such behavior. An example is shown in Fig. 5.2(c) where the resonance depth

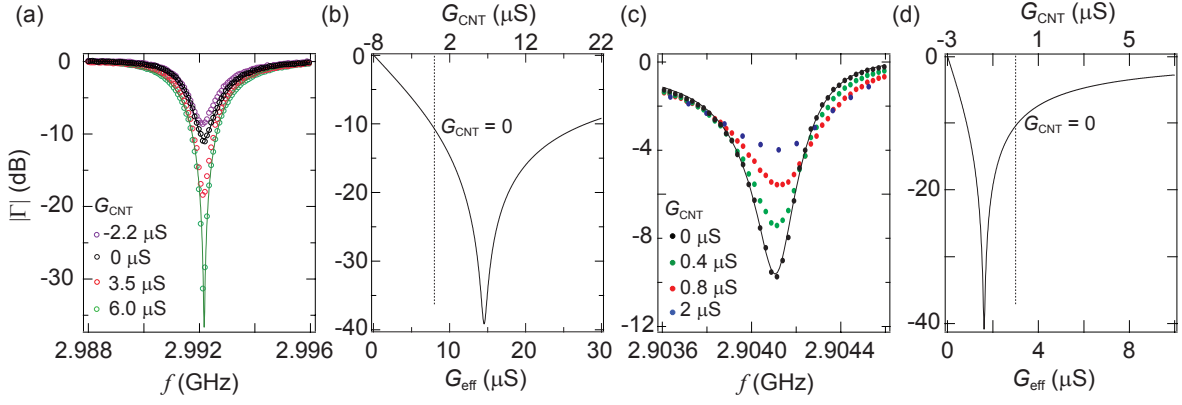


Figure 5.2. Impedance matching in CNT devices (a,c) Measured reflectance response versus frequency in quantum dots formed in CNT for two different hybrid devices. Solid curves are least square fits to Eq. 5.1. (b,d) Numerically calculated reflectance at corresponding resonance frequencies using the stub tuner parameters extracted in blockade. Plots in panels (b) and (d) correspond to load- and loss- dominated working regimes of the stub tuner.

strictly decreases upon increasing G_{CNT} . By performing a similar fitting in blockade, we extract $D_1 = 10.56$ mm, $D_2 = 10.44$ mm, $\alpha = 0.008$ m $^{-1}$. Despite a lower loss compared to Fig. 5.2(a), the sample is in the loss dominated regime due to a lower $G_{\text{Match}} = 1.6$ μS compared to $G_{\text{Loss}} = 3.2$ μS which is set by the length difference of D_1 and D_2 . We note that the designed length difference for this case is 300 μm . We attribute the differences between the designed and extracted quantities to the deviation of characteristic impedance from 50 Ω . The latter happens at the links of source/drain contacts to the RF lines changing the effective length of the transmission lines and can be compensated for in the design.

5.2. Single quantum dot regime

We now perform simultaneous measurement of direct current and reflectometry at a fixed frequency near the resonance. Such measurement namely dispersive readout is often employed in circuit quantum electrodynamics (cQED) [112] relying on frequency shift of the resonance. In our case there is an important difference for the phase measurements which cannot be directly related to frequency shifts. This is because a change in conductance alone can produce a different effective input impedance seen at the T-junction and produce phase changes, see the section 3.3.2 for more details.

Figure 5.3 shows simultaneous measurement of direct current I , change in reflectance amplitude Γ and phase ϕ . Series of Coulomb diamonds can be recognized in each map. The charging energy of 10 meV is typically found in several samples with similar geometry. The difference of the reflectance plots with respect to the current plot is due to the fact that reflectometry probes differential conductance. One can alternatively think of this as a lock-in measurement done at GHz frequency done with relatively small power, -110 dBm (corresponding to an AC bias of 0.7 μV), while still maintaining a good signal to noise ratio. We observed signs of photon assisted tunneling in current at

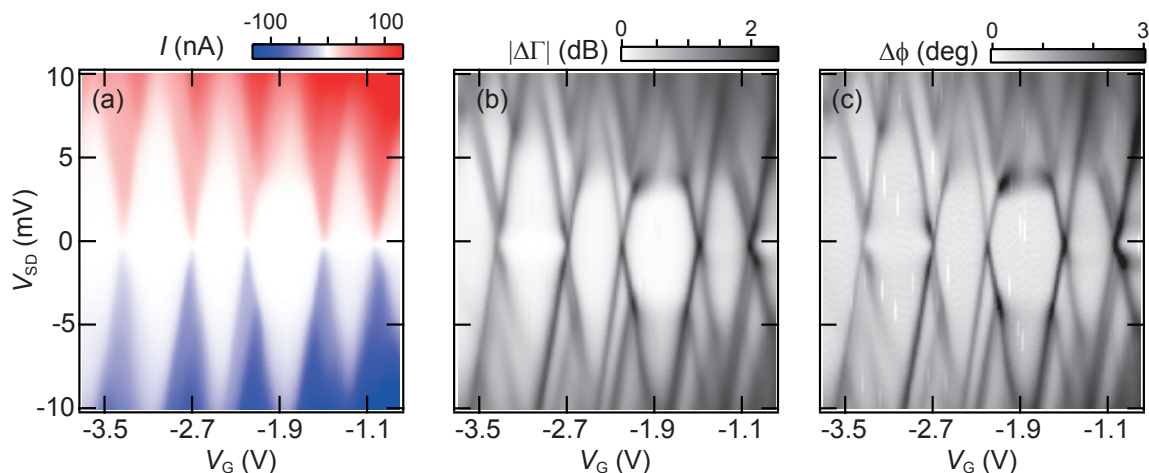


Figure 5.3. Charge stability and RF reflectometry of single quantum dots V_G and V_{SD} color maps of simultaneously measured (a) direct current (b) reflectance amplitude and (c) phase near the resonance frequency. RF input power of -110 dBm is applied. The qualitative differences in reflectance plots with the DC plot is due to the fact that RF probes differential conductance.

RF input power larger than -90 dBm [113]. Here, a large oscillating bias can facilitate a resonant tunneling of charges across tunnel barriers [116]. The possibility to measure at low power is an important requisite in the context of quantum electrodynamics.

While the stub tuner is designed to match at a single conductance value, the reflectance plot of the single dot shows good RF sensitivity to a range of G values. In particular, low current features such as excited states and inelastic cotunnelling are clearly visible in both amplitude and phase plots. This is despite the fact that the stub tuner operates in a loss dominated regime with maximum depth of the resonance in the Coulomb blockade. Since reflectance can be performed with a larger bandwidth, we gain a faster readout method to characterize our devices.

5.2.1. High frequency conductance

The maximum speed at which conductance can be measured is set by its RC time constant. For a typical R of 100 k Ω and stray cable capacitance of 1 nF, the cut off frequency $f_c = 1/(2\pi RC)$ comes to be few kHz. We saw in the section 5.1 that use of stub tuner can push the measurement bandwidth to MHz. In the following, we show how the reflectance amplitudes can be directly converted into conductance values using the relevant parameters of the stub tuner. One, however, needs to be careful that the frequency shifts are negligible to validate the assumption of changes in $|\Gamma|$ coming solely from conductance changes. Moreover, one can see from Fig. 5.2(b) that the same depth of resonance can correspond to two different conductance values, one before and one after the matching. In this case, the distinction between the two values is made using the unique phase response, see section 3.3.8.

We first fit a resonance spectrum in the Coulomb blockade [Inset of Fig. 5.4(a)] to get the relevant parameters $D_1, D_2, \epsilon_{\text{eff}}, \alpha$. We can then calculate changes in $|\Delta\Gamma|$ at the

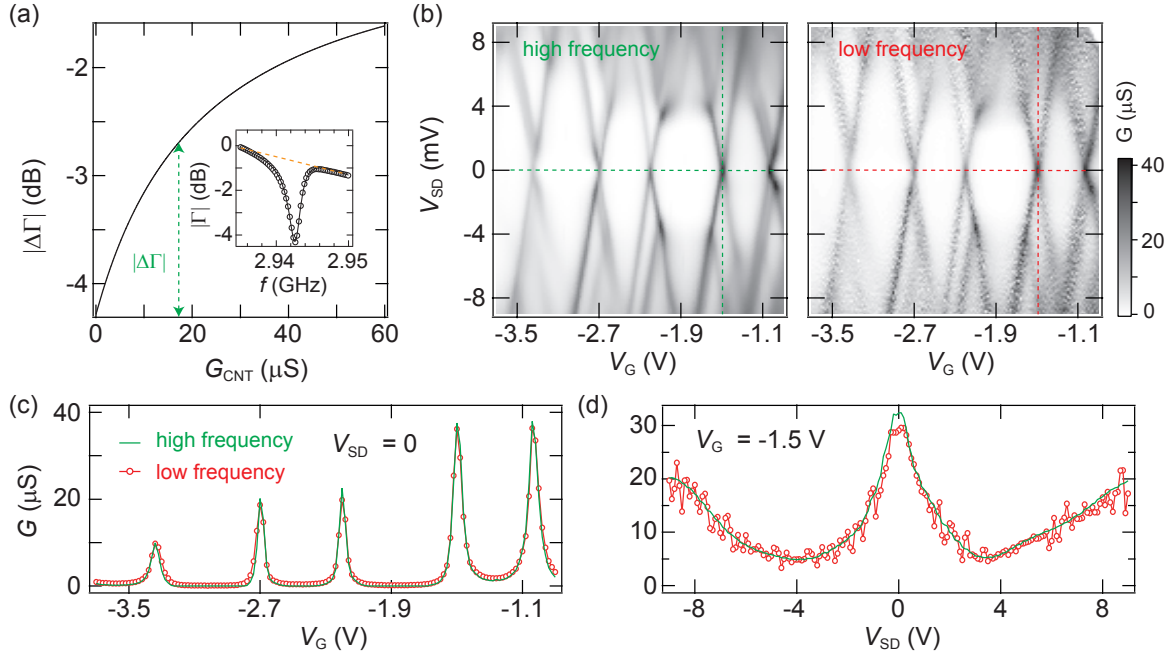


Figure 5.4. DC and RF conductance (a) Inset: Fit of a reflectance response in the Coulomb blockade. Dashed line shows a background slope. Main panel: Calculated reflectance amplitude versus G_{CNT} at the resonance frequency. (b) Grayscale plots of conductance extracted from panel (a) and directly deduced from the numerical derivative of direct current. (c) and (d) Cuts of G in panel (b) marked by dash lines show an excellent comparison between high frequency and low frequency extractions of the differential conductance.

resonance frequency as a function of G_{CNT} , as shown in Fig. 5.4(a). Note that a slope resulting from standing waves in the setup needs to be taken into account as well. We then back-convert $|\Delta\Gamma|$ in Fig. 5.3(b) to a conductance map shown in Fig. 5.4(b). The numerical derivative dI/dV is also plotted side by side to show a direct comparison of features. One can qualitatively observe similar contours of Coulomb diamonds, excited states and inelastic cotunnelling. We further take cuts from two conductance maps at fixed source drain and gate voltage. These are plotted in panel (c) and (d) showing an excellent overlap. Such reliable high-bandwidth extraction of G at GHz frequencies holds promises for probing quantum charge-relaxation resistance, which can deviate from its usual DC counterpart described by the Landauer formula [117, 118].

The high bandwidth of gigahertz resonant circuits has been exploited to perform fast readout of double-dot stability diagrams. Using a Josephson parametric amplifier, a team from Jason Petta group in Princeton could perform such measurements in just 20 ms [119]. In our group, we have not completely utilized the large bandwidth so far. This is because of lack of equipments such as a fast analog-to-digital converter and buffered readout with gigasamples per second. The high frequency extraction of G nonetheless provides a good check for the validity of the stub tuner parameters needed in the calibration of noise spectral densities, see Chapter 7. In addition, internal charge relaxation resistance can be deduced without needing to pass any DC currents or needing contact electrodes, see Chapter 6.

5.3. Double quantum dot regime

Room temperature characterization during deterministic CNT stamping allows us to perform several CNT mechanical transfer trials on the same device and choose nanotubes based on their gate dependence, see section 4.2.1. In particular for semiconducting nanotubes, we can use the gates to locally shift the Fermi level above or below the valence and conduction bands of the nanotube. The semiconducting nature and multiple bottom gates further allow for creating gate-defined confinement potentials along the nanotube and for tuning the location, size and number of quantum dots [93]. Below, we present measurements of a device with three bottom gates, shown in Fig. 4.1(a). In this case, polymer-free CNT is suspended on the source/drain contacts suppressing perturbations from the substrate.

With no RF power applied to the stub tuner and the middle gate $V_{MG} = 0$ V, we measure the charge stability diagram of the CNT device. A gate sweep using left (V_{LG}) and right gates (V_{RG}) at $V_{SD} = 10$ mV is shown in the Fig. 5.5(a). The current response clearly displays an ambipolar behavior of QDs around a semiconducting gap of ~ 30 meV with V_{LG} and V_{RG} tuning the CNT into n-n, n-p, p-n and p-p double dots. Here we have used a gate lever arm of ≈ 0.2 meV/mV extracted from the Coulomb diamond measurements. In addition, we observe the exact charge occupation of electrons and holes at corresponding gate voltages [11]. Starting from the bandgap edge, electrons or holes are added one by one to the dots if the gate voltages are increased or decreased. The high conductance in the n-n regime is possibly due to n-doping near the source/drain contacts. We also found p-doping for many samples for the same Pd contacts and do not exactly understand the nature of the observation.

The frequency response of the reflectance for this device is already presented in the Fig. 5.2(c), that shows the stub tuner to operate in a loss dominated regime. We now perform simultaneous DC and RF measurements in the p-p regime. Figure 5.5(b) shows a qualitatively similar honeycomb charge stability diagram in current, amplitude and phase responses taken at $V_{SD} = -10$ mV bias. We clearly observe cotunneling lines [48, 112], long edges of the honeycomb, in all plots. Here, the charge transport happens owing to a second order tunneling, when one dot is resonant with its respective lead. We also note an important distinction of the stub tuner. For half wave resonators, the RF signal of cotunneling lines strongly depend on the strength of capacitive coupling to the respective lead-dot transitions and their rates with respect to the resonance frequency [49]. A DC coupled stub tuner in contrast always responds through conductance changes that provide an external coupling by shunting microwaves via the drain contact into the ground plane. This is further seen in Fig. 5.5(b) where larger current results in larger reflectance difference $|\Delta\Gamma|$.

In addition, we also observe hybridized double dots at degeneracy, the boundary of two honeycombs at the two smaller edges, marked by dashed circles in Fig. 5.5(b), in the phase and amplitude plots. The signal results from the susceptance changes caused by dipole coupling of the hybridized charge states to the microwave resonator. Since this process does not involve transfer of charges between the leads, no direct current is produced. The reflectance responses at different charge degeneracy is different due to the distinct dot coupling energies t_c which are affected by all gate voltages in our multi-gated device.

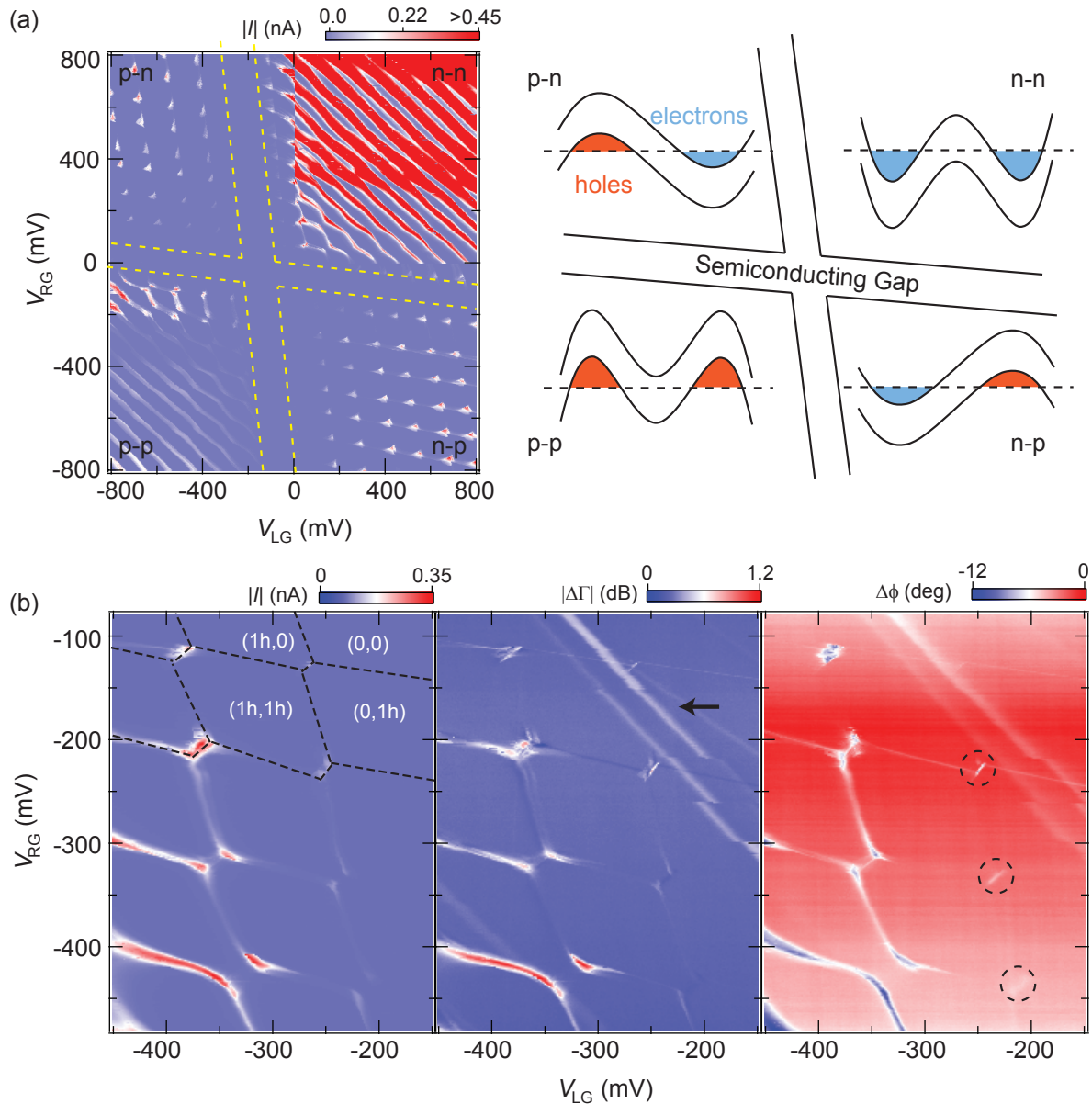


Figure 5.5. Charge stability and RF reflectometry of CNT double quantum dots (a) DC measurements at $V_{SD} = 10$ mV and $V_{MG} = 0$ show a semiconducting gap and the formation of bipolar double dots around it when V_{LG} and V_{RG} are swept. We observe the addition of electrons and holes in each regime starting from complete depletion in the bandgap. n-n double dots show relatively large conductance due to n-doping of the contacts. Schematics show different confinement configurations of the double dots. (b) Simultaneous measurements of current, reflected amplitude and phase at the resonance frequency in the p-p double dot region at -10 mV bias. Cotunnelling lines are clearly visible in all the plots. Inter-dot coupling lines not present in DC plot are visible in the amplitude and phase response due to frequency shifts at gate voltages marked by dashed circles. The arrow points at spurious gate-tunable lines most likely resulting from charge traps which do not necessarily contribute to the current but do change the susceptance.

5.3.1. Inter-dot coupling

The confinement potential of the double quantum dots can further be tuned through the middle gate voltage V_{MG} . In this case, we go to the p-p double dot regime and increase V_{MG} to positive values to raise the tunnel barrier between hole dots. In the DC measurements, the strength of the tunnel coupling can be visualized by the separation between the charge triple points with the larger value corresponding to a stronger coupling or weaker barrier. In terms of dot wave functions, charges are highly delocalized in a strongly coupled regime, effectively forming a single dot, and vice-versa. These are shown in Fig. 5.6 for different values of V_{MG} .

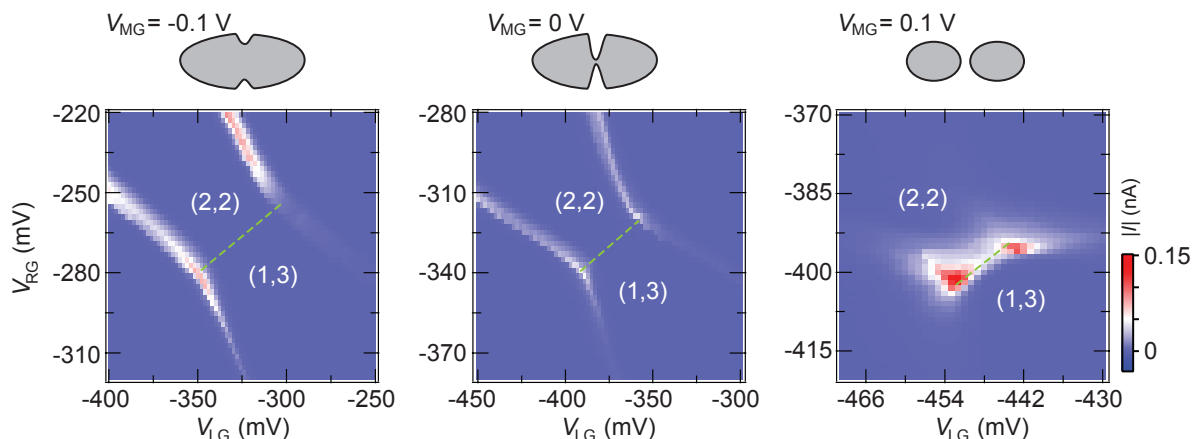


Figure 5.6. Tuning inter-dot coupling between the double quantum dots DC measurement of a p-p double dot regime for different values of V_{MG} at $V_{SD} = -5$ mV. Increasing the middle gate voltage V_{MG} to positive values increases the barrier strength between the dots thereby decreasing the tunnel coupling. Note that the corresponding gate voltages for charge triple points are different in each plot due to confinement potential being affected by all gates.

In our device, the confinement potential is affected by all the local gates. Consequently, a change in V_{MG} also shifts the charge triple points corresponding to a specific dot state. For example, in the measurements shown in Fig. 5.6, both V_{LG} and V_{RG} shift to more negative voltages on increasing the V_{MG} . Quantitatively, a change in V_{MG} by 100 mV causes both V_{LG} and V_{RG} to shift by approximately 60 mV each.

Despite the visible changes in the separation between the triple point, extraction of inter dot coupling energy is difficult from a DC plot. The main cause of this is the inter-dot capacitance C_t which alone can cause the separation of the triple points due to electrochemical shift of one dot due the charge state of the other. This is as if the left dot is gating the right dot and vice versa. Moreover, C_t is strongly dependent on the size and distance between the two dots which can change at different voltage configurations. The RF measurement however is able to probe signals across the energy detuning axis ϵ which is perpendicular to the line connecting two triple dots. This axis is not influenced by the inter-dot capacitance and hence enables extraction of inter-dot coupling energies as explained below.

5.3.2. Dipole coupling of hybridized double dots to a resonator

For a quantitative analysis of inter-dot coupling, the phase response of the stub tuner can be measured using a weak probe power (-130 dBm) near the hybridization of two charge states $(m, n+1)$ and $(m+1, n)$. We operate in the zero-bias regime, allowing the dots to stay in equilibrium and rule out any conductance changes ($G_{\text{CNT}} \approx 0$) which could affect the phase response. Such a phase shift is shown in Fig. 5.7(b) close to (2,2) to (1,3) hole transition. We infer the frequency shifts Δf from the phase variations which are almost linearly correlated near resonance frequency [see Fig. 5.7(c), error $< 10\%$ in our case].

We model the system similar to a standard microwave resonator capacitively coupled to a qubit formed by two charge states on a (nanotube) double quantum dot, see Fig. 5.7(a). The Hamiltonian of this system is a variant of the well-known Jaynes-Cummings model

$$H_0 = \omega_r \hat{a}^\dagger \hat{a} + \omega_d \hat{\sigma}^+ \hat{\sigma}^- + g(\hat{a}^\dagger \hat{\sigma}^- + \hat{a} \hat{\sigma}^+) \quad (5.2)$$

where the qubit energy is $\omega_d = \sqrt{\epsilon^2 + 4t_c^2}$, the resonator-qubit coupling is $g = g_0 \sin \vartheta$, and the mixing angle is $\sin \vartheta = 2t_c/\omega_d$. In these expressions, \hbar is set to unity, ϵ the detuning between the two relevant charge states and t_c the tunnelling amplitude.

Including the microwave drive and in the rotating frame of the drive the Hamiltonian reads

$$H = -\Delta_r \hat{a}^\dagger \hat{a} - \Delta_d \hat{\sigma}^+ \hat{\sigma}^- + g(\hat{a}^\dagger \hat{\sigma}^- + \hat{a} \hat{\sigma}^+) + \Omega(\hat{a} + \hat{a}^\dagger) \quad (5.3)$$

where we introduced the driving strength Ω and the detuning of the microwave drive from the resonator $\Delta_r = \omega_{\text{drive}} - \omega_r$ and the qubit $\Delta_d = \omega_{\text{drive}} - \omega_d$.

Additionally, we take into account resonator (κ) and qubit relaxation (γ) as well as qubit dephasing (Γ_ϕ) rates. These can be described with a Markovian master equation approach with

$$\dot{\rho} = -i[H, \rho] + \kappa \mathcal{D}[\hat{a}]\rho + \frac{\Gamma_\phi}{2} \mathcal{D}[\hat{\sigma}_z]\rho \quad (5.4)$$

$$+ \gamma(n_{\text{th}} + 1) \mathcal{D}[\hat{\sigma}^-]\rho + \gamma n_{\text{th}} \mathcal{D}[\hat{\sigma}^+]\rho \quad (5.5)$$

where $\mathcal{D}[\hat{A}] = \hat{A}\rho\hat{A}^\dagger - \{\hat{A}^\dagger\hat{A}, \rho\}/2$ is the Lindblad dissipator and average photon number at temperature T given by $n_{\text{th}} = [e^{\hbar\omega_d/(k_B T)} - 1]^{-1}$. This gives rise to the following equations of motion

$$\langle \dot{\hat{a}} \rangle = +i\Delta_r \langle \hat{a} \rangle - \frac{\kappa}{2} \langle \hat{a} \rangle - i\Omega - ig \langle \hat{\sigma}^- \rangle \quad (5.6)$$

$$\langle \dot{\hat{\sigma}}^- \rangle = +i\Delta_d \langle \hat{\sigma}^- \rangle - \left(\frac{\gamma}{2} + \Gamma_\phi \right) \langle \hat{\sigma}^- \rangle + ig \langle \hat{a} \hat{\sigma}_z \rangle. \quad (5.7)$$

In a semiclassical decoupling approximation, i.e. assuming $\langle \hat{a} \hat{\sigma}_z \rangle \approx \langle \hat{a} \rangle \langle \hat{\sigma}_z \rangle$, we can solve for the steady state

$$\langle \hat{\sigma}^- \rangle_{\text{ss}} = \frac{+ig \langle \hat{a} \rangle \langle \hat{\sigma}_z \rangle}{\left(\frac{\gamma}{2} + \Gamma_\phi \right) - i\Delta_d} \quad (5.8)$$

and we then obtain

$$\langle \hat{a} \rangle_{\text{ss}} = \frac{-i\Omega}{\frac{\kappa}{2} - i\Delta_r - \frac{g^2 \langle \hat{\sigma}_z \rangle}{\left(\frac{\gamma}{2} + \Gamma_\phi \right) - i\Delta_d}} \quad (5.9)$$

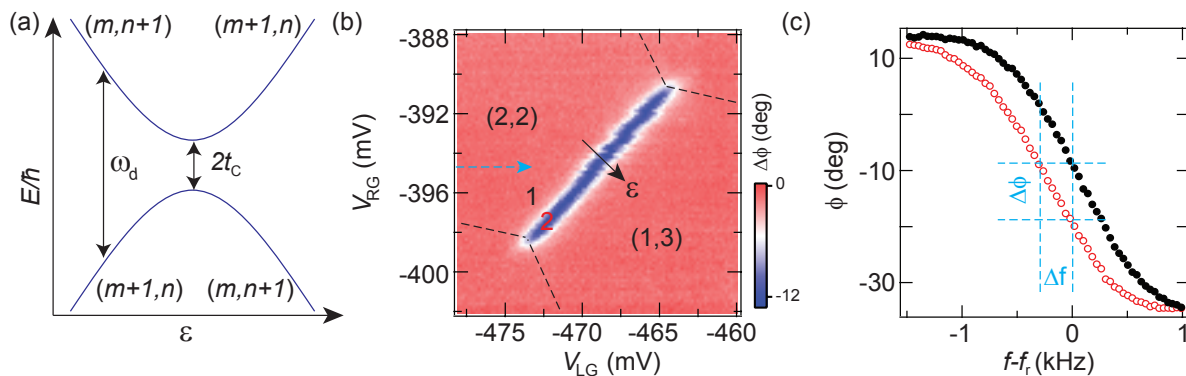


Figure 5.7. Reflectometry response of inter-dot coupling (a) Energy levels of a double quantum dot with an inter-dot hybridization energy of t_c , forming a two level system with energy ω_d . (b) The phase response measured at the resonance frequency as a function of V_{LG} and V_{MG} yields a pronounced inter-dot transition due to hybridization of the charge states (2,2) and (1,3). (c) The stub tuner phase response at $V_{MG} = 130$ mV around the dot degeneracy (open circles) and uncoupled dots (solid circles) marked by points 2 and 1 in panel (b) respectively.

where we implicitly assumed that the coupling to the driven resonator does not change the qubit polarization $\langle \hat{\sigma}_z \rangle$, i.e. the qubit remains in thermal equilibrium with the electronic bath and $\langle \hat{\sigma}_z \rangle = \frac{-1}{2n_{th}+1}$ so we have the thermal qubit polarization as $\langle \hat{\sigma}_z \rangle = -\tanh \frac{\hbar\omega_d}{2k_B T}$.

If the system remains in the weak coupling limit, $g \ll \gamma$, this expression is well approximated by

$$\langle \hat{a} \rangle_{ss} = \frac{-i\Omega}{\frac{\kappa}{2} - i\Delta_r + i\chi \langle \hat{\sigma}_z \rangle} \quad (5.10)$$

where we have introduced the susceptibility

$$\chi = +i \frac{g^2}{\left(\frac{\gamma}{2} + \Gamma_\phi\right) - i\Delta_d} \approx \frac{g^2}{-i\left(\frac{\gamma}{2} + \Gamma_\phi\right) + (\omega_d - \omega_r)}. \quad (5.11)$$

Its real and imaginary parts lead to qubit-dependent shifts of the resonator frequency ω_r and the resonator linewidth κ

$$\Delta\omega_R = \text{Re}[\chi] \langle \hat{\sigma}_z \rangle = \frac{g^2 \Delta \langle \hat{\sigma}_z \rangle}{\Gamma_{tot}^2 + \Delta^2} \quad (5.12)$$

$$\Delta\kappa = -2\text{Im}[\chi] \langle \hat{\sigma}_z \rangle = \frac{-2g^2 \Gamma_{tot} \langle \hat{\sigma}_z \rangle}{\Gamma_{tot}^2 + \Delta^2} \quad (5.13)$$

where we have introduced the full linewidth $\Gamma_{tot} = \frac{\gamma}{2} + \Gamma_\phi$ and the detuning between qubit and the resonator frequencies $\Delta = \omega_d - \omega_r$. We easily see that the frequency shifts and linewidth changes are very small when $\Delta \gg \Gamma_{tot}, g$. Moreover, the sign of the frequency shift is positive if $\omega_d < \omega_r$ and negative when $\omega_d > \omega_r$. The linewidth is, however, always larger than that of the the bare resonator.

5.3.3. Dephasing of hybridized double dots

Using the semi-classical approach described in the previous section, we can now extract the charge qubit energy in the CNT double-dot system and its dephasing. We use the Eq. 5.12 to first extract g_0 in a regime where t_c is large (V_{MG} is small) so that $\omega_d \geq 2t_c \gg \omega_r, \Gamma_{tot}$. This yields a dependence of the frequency shift Δf proportional to $4g_0^2 t_c^2 / (\epsilon^2 + 4t_c^2)^{3/2}$, now independent of Γ_{tot} . A fit with this equation to the data at $V_{MG} = 130$ mV is shown in Fig. 5.8(a), yielding $g_0/2\pi = 37$ MHz. We find the same g_0 for $V_{MG} = 110$ mV supporting the assumption that Γ_{tot} is relatively small in this regime. We could not determine the electronic temperature from Coulomb peaks and hence take $T = 0$ for all the fits.

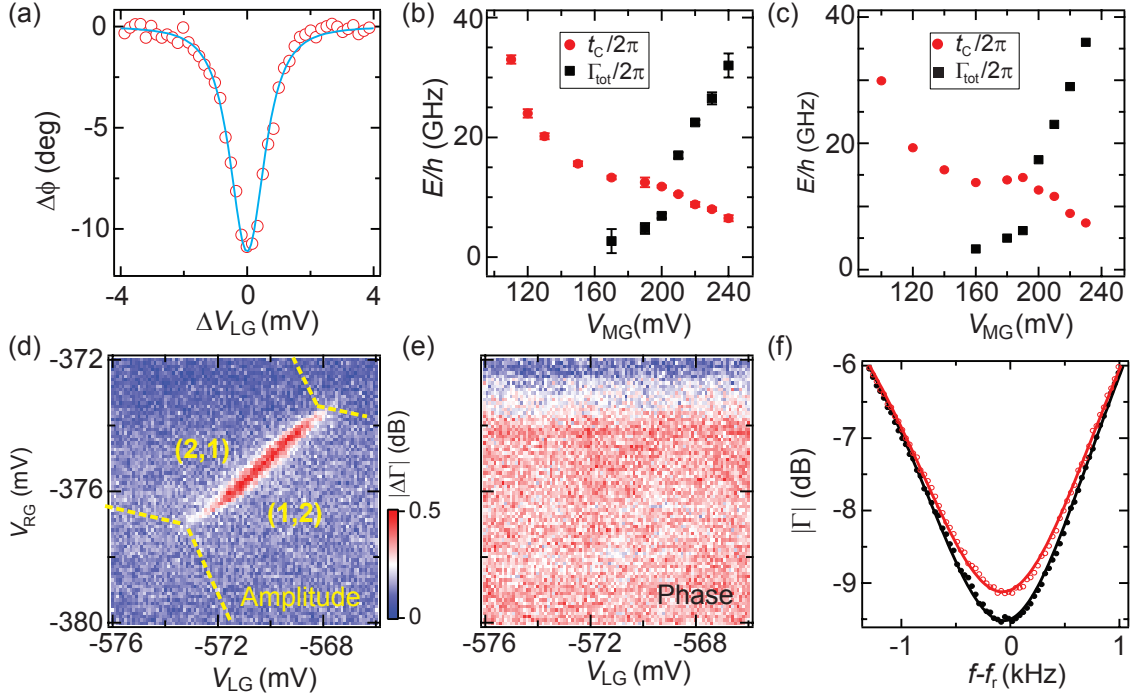


Figure 5.8. Dephasing of hybridized double dots (a) A cut indicated by the dashed arrow in Fig. 5.8(b) with a fit to eq. 5.12 to extract the inter-dot coupling energy t_c and g_0 . (b,c) Extracted t_c and Γ_{tot} as a function of V_{MG} for (2,2) to (1,3) and (2,1) to (1,2) hole transitions. Error bars represent uncertainties in the least square fitting. (d,e) Amplitude and phase response at $V_{MG} = 260$ mV. (f) The reflected power response at $V_{MG} = 260$ mV displays near-resonant absorption despite negligible dispersion. Solid lines are the fits to Eq. 5.1. Symbols have the same meaning as in Fig. 5.7(c).

We now fit the phase responses at other V_{MG} after fixing the extracted g_0 and plot the extracted t_c and Γ_{tot} in Fig. 5.8(b,c) across two dot degeneracy. For both cases, we observe a reduction of t_c on increasing V_{MG} , reflecting a reduction in the tunnel coupling strength between the dots. For simplicity, we have further assumed a constant Γ_{tot} at a fixed V_{MG} . In reality, this should also vary when qubit energy changes with ϵ or V_{LG} . The phase response starts to be suppressed for V_{MG} larger than 200 mV due to increasingly fast double dot dephasing, yielding $\Gamma_{tot} > t_c$.

The inverse dependence of Γ_ϕ on t_c has been seen in similar systems [114, 120] and could be due to the $1/f$ charge noise environment [121] of the nanotube. The sign of the frequency shift always remains negative, further signifying that the resonator energy is always smaller than $2t_c$. Increasing V_{MG} to more than 250 mV, we do not notice any dispersion because of the large Γ_{tot} . However, the hybridized dots still show a response in the reflectance amplitude, see Fig. 5.8(d,e). For $V_{MG} = 260$ mV across (2,1) to (1,2) hole transition, the stub tuner response for coupled and uncoupled dots regimes is presented in Fig. 5.8(f). The fit to the resonance at the double dot degeneracy (open circles) shows a smaller depth and $\alpha = 0.0086 \text{ m}^{-1}$ compared to the one in the uncoupled regime (solid circles) with $\alpha = 0.0082 \text{ m}^{-1}$. This behavior is a result of an added loss channel i.e. absorption from the two-level hybridized dots when $2t_c$ becomes comparable to ω_r , which is also consistent with the change in the resonance depth due to the conductance increase for our device operating in loss dominated regime. This can be also understood using Eq. 5.12 and Eq. 5.13, where in the regime of large Γ_{tot} , frequency shift becomes quite small while the change in the resonator linewidth can still be noticeable.

5.4. Triple quantum dot regime

We use the same device which is discussed in the previous section. The middle gate is now tuned to a larger positive voltage $V_{MG} = 1$ V while left and right gates are swept in the negative values. This gate configuration results in a p-n-p triple quantum dot in series, illustrated by a schematic in Fig. 5.9(a). It is not the aim of this section to analyse the measurements in detail. We simply highlight twofold advantages of our device, first in the RF measurements and second in the control over the local confinement potential along the length of the CNT.

We again perform simultaneous measurements of DC current and reflectance at $V_{SD} = -10$ mV. Charge stability diagram displays three clear slopes, expected for three QDs connected in series. These are shown by solid lines in Fig. 5.9(b). Blue and red lines are the same slopes observed in the double dot diagram of Fig. 5.5 dictating filling of left and right dots, while the green slope determines the occupation of the middle dot. The fact that the green slope is roughly in the middle of the blue and red slopes, means that occupation of the middle dot is equally affected by the left and right gates. A schematic of the dot filling is presented in Fig. 5.9(c). The occupation of left/middle/right QDs changes by one if crossing the blue/green/red lines. Note that at increasing negative gate voltages, electrons in the middle dot starts to empty while left and right dots increase in hole numbers.

The RF measurements in Fig. 5.9(b) unlock signals that are not present in the DC plot. Moreover, signal strengths, at places, are relatively larger compared to the DC plot. These RF signals again are due to the frequency shift in resonance caused by charge hopping. Nearest neighbour charge hopping can be recognized, as shown in Fig. 5.9(d). We can classify them into two categories. First one is inter-dot tunnelling where the total number of charges on QDs stays conserved e.g. (m, n, p) to $(m, n + 1, p + 1)$. Here m, p are hole occupation of the left and right dots, and n is the electron occupation of the middle dot. Second case is the charge hopping from leads onto

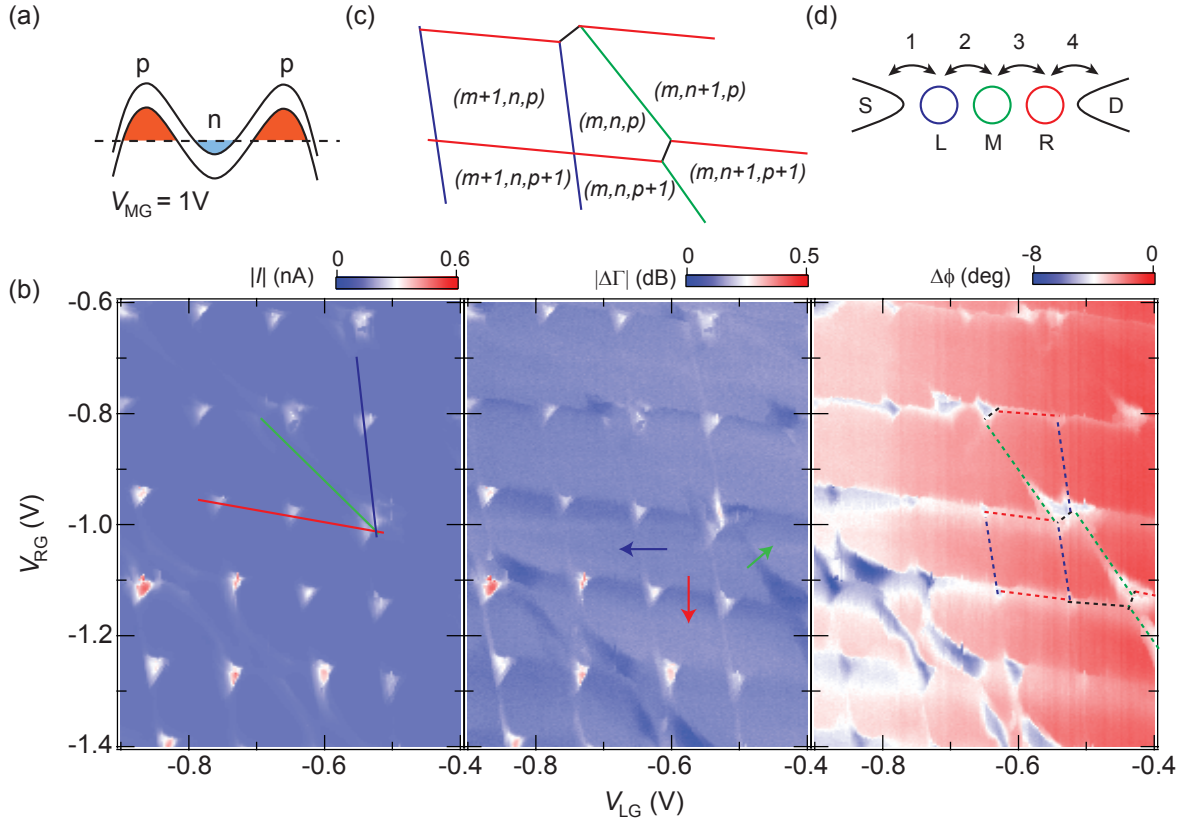


Figure 5.9. Charge stability and RF reflectometry of triple quantum dots (a) Middle gate is fixed at 1 V while left and right gates are tuned to negative voltages to create p-n-p dots. (b) Simultaneous DC and RF measurements of I , Γ and ϕ near the resonance frequency at $V_{SD} = -10$ mV. Lines and arrows represent the slopes and directions of respective dot filling. (c) Lines same as the dashed lines in panel (b) to illustrate the dot filling. (d) Different nearest-neighbour charge hopping.

dots. These fluctuate dot occupation by one, as shown by the leftmost and rightmost double arrows in Fig. 5.9(d). None of processes produces any net current, however, do change the effective susceptance seen by the microwave resonator. Naively, one would expect the relative strength of such signals to depend on the detuning of the resonance frequency with respect to the hopping frequency and its dipole coupling strength, similar to Eq. 5.12.

5.5. Summary and discussion

In summary, we have operated RF superconducting impedance-matching circuits to measure quantum dots fabricated using stamping of CNTs. The circuit is a simple planar fabrication of a pair of shunted transmission lines. The matched conductance, as expected, is found to be dependent on the length difference and microwave losses of the transmission lines. We have shown that one can quantitatively deduce admittance changes in μS resolution by measuring the complex reflectance Γ . This sensitivity can be used to deduce basic parameters of a CNT double-dot operating as a charge qubit,

such as the inter-dot tunnel coupling strength and the dephasing rate. More importantly, conductance can be deduced using a simple analytic formula with measurement bandwidth reaching few MHz even for device impedance of $1\text{ M}\Omega$.

The measurements leave an important open question about the source of dephasing of the hybridized double dot. Why is Γ_ϕ so large $\sim\text{GHz}$ despite the fact that the CNT is suspended? One reason could be the high electronic temperature of our device. The main limitation often discussed is the charge noise of the environment. A recent work on a CNT double dot system has attempted to suppress the effect of the noise by strongly decreasing the charging energy E_C . The latter is designed to be very small $\sim 2\text{ meV}$, and Γ_ϕ found to be as low as 4 MHz [122]. The behavior can be understood in analogy with superconducting Transmon qubits [123] where small E_C , due to large microscopic capacitor pads, has been instrumental in boosting the coherence times. On contrary, the E_C in our double dot device is quite large $\sim 20\text{ meV}$.

To conclude, we have demonstrated impedance matching with a tremendous microwave coupling in the measured quantum dot devices. For example, we see from Fig. 5.2(a,b) that we achieve $|\Gamma| \approx -40\text{ dB}$ at $G_{\text{CNT}} \approx 7\ \mu\text{S}$. This relates to a reflectance probability of $\sim 0\%$, hence 100% is transmitted into the matching circuit and CNT device. Taking into account the internal loss described by $G_{\text{Loss}} = 7\ \mu\text{S}$ yields a substantial power transmission of $\sim 50\%$ from a $150\text{ k}\Omega$ device to a $50\ \Omega$ transmission line. This is beneficial for high throughput detection of emitted noise from the quantum device defined in the CNT wire and shot noise measurements. The latter are discussed in chapters 7 and 8.

6 Quantum Capacitance and Dissipation in Graphene p-n junctions

In the past decade, extensive studies on graphene have unraveled interesting physics of Dirac particles on chip [37, 124]. Up to now, the main technique to investigate the electronic properties has been low frequency lock-in where contact metallization is needed to pass a current and measure the resulting voltage drop. The key drawbacks of contact electrodes are highly doped regions in the vicinity of the contacts resulting in unwanted p-n junctions [125] and scattering [126] of charge carriers. In addition, leftover resist residues from lithography can degrade the metal-graphene interfacial properties [127] or even the overall device quality. An important example is graphene spintronics [128], where device performance is often limited by contacts causing spin-relaxation and decrease in spin-lifetime [129]. Therefore contact-less characterization from, for example, microwave absorption [130] can open up new ways to probe inherent electrical properties of the studied system.

In this chapter, we present results of graphene devices capacitively coupled to gigahertz resonant circuits made from stub tuner. From the response of a microwave resonance, we are able to extract quantum capacitance in agreement with graphene density of states. Moreover, the intrinsic charge relaxation resistances are deduced in the absence of any contacts. The graphene encapsulation in a hexagonal boron nitride sandwich [131] further separates the bulk from the external perturbations, and allows studies of graphene p-n junctions, a potential building block of electronic lenses [132], beam splitters [133] and Fabry-Perot interferometers [134, 135].

6.1. Device layout

Figure 6.1(a) shows the layout of a typical device. The stub tuner circuit based on transmission lines with two lengths D_1 and D_2 is patterned using ebeam lithography. The ground plane near D_1 end is separated by a slit from the central conductor as shown in Fig. 6.1(b) where we have placed a graphene flake encapsulated in hexagonal boron nitride (hBN). The hBN/graphene/hBN stack is prepared using the dry transfer method described in ref. [104]. The stack is positioned in the middle of the slit such that parts of the flake lie on both the signal plane (area A_1) and on the ground plane (area A_2). We then etch the stack with SF_6 in a reactive ion etcher to create a well defined rectangular geometry. Some bubbles resulting from the transfer can also be seen in Fig. 6.1(c). Raman spectra have been taken to confirm the monolayer graphene

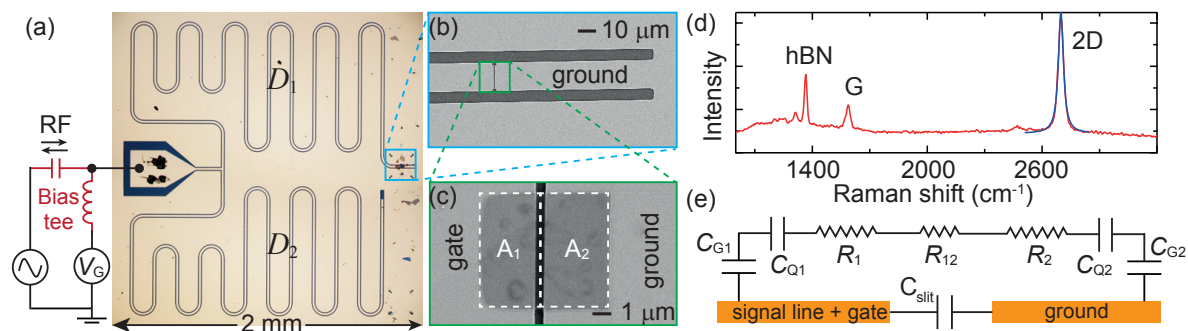


Figure 6.1. Device layout. (a) An optical picture of the stub tuner with two arm lengths D_1 and D_2 . Central conductor and gap widths of the transmission lines are $15 \mu\text{m}$ and $6 \mu\text{m}$ respectively. (b) An SEM image near the D_1 end showing a narrow slit between the signal line and the ground plane (c) An SEM image of a hBN-Graphene-hBN sandwich for device B placed over the slit. Areas A_1 and A_2 correspond to the parts of graphene lying on the signal line and the ground plane, respectively. (d) A Raman spectrum of the stack showing peaks related to hBN and graphene. Solid blue line is the least squared fit to single Lorentzian. (e) An equivalent circuit with lumped capacitance and resistance elements. Symbols are explained in the text.

flakes as shown in Fig. 6.1(d).

Since there are no contacts on the graphene, the same circuit can be employed for different stack geometries. We first fabricate the hybrid device with a stack dimensions $W \times L$ of $6.5 \mu\text{m} \times 13 \mu\text{m}$ (device A), where W and L respectively denote the width and length of rectangular graphene. After measurements on device A, the stack is etched into new dimension of $6.5 \mu\text{m} \times 7.2 \mu\text{m}$ (device B). For both devices, a graphene area of $6.5 \mu\text{m} \times 3.4 \mu\text{m}$ stays on the signal/gate line, see Fig. 6.1(c). On ground plane lies graphene areas of $6.5 \mu\text{m} \times 9.6 \mu\text{m}$ for device A, while this is $6.5 \mu\text{m} \times 3.8 \mu\text{m}$ for device B. Device A is hence asymmetric while B is quasi symmetric around the slit. More importantly, two devices on the same circuit with the same graphene flake but different geometry provide consistency checks. A third symmetric device C of dimensions $5 \mu\text{m} \times 12 \mu\text{m}$ with a separate resonator circuit and a separate graphene stack is also measured. Slit width for device C is 250 nm compared to 400 nm as in the case for devices A and B.

6.1.1. Measurement principle

We extract the graphene properties by measuring the complex reflection coefficient from the stub-tuner which is dependent on the radio frequency (RF) admittance of a load [136]. The reflected part of the RF probe signal (fed into the launcher port of the circuit) is measured using a vector network analyzer. To tune the Fermi level of the graphene, a DC voltage V_G is applied to the launcher port with the help of a bias tee, as shown in Fig. 6.1(a). The gate voltage changes the carrier density and hence the quantum capacitance. By analysing the response of the circuit, changes in differential capacitance, related to quantum capacitance C_Q and in dissipation, related to the charge relaxation resistance R can be inferred. All reflectance measurements are

performed at an input power of -110 dBm and the base temperature 20 mK of our dilution refrigerator. The power corresponds to an AC excitation amplitude of $0.7 \mu\text{V}$ which is much smaller than what is used in transport measurements.

To understand the effect of gating, we divide the graphene into two areas denoted by A_1 and A_2 in Fig. 6.1(c). A gate voltage on the signal line induces charges on the part of graphene flake lying above it. Since the total number of charge in graphene in absence of a contact cannot change, charge on one part must be taken from the other. For a pristine graphene (Fermi level at charge neutrality without gating), this results in the formation of a p-n junction near the slit at each gate voltage. However, when a finite offset doping is present, an offset voltage has to be applied to reach the charge neutrality (CNP). The CNP is reached twice, once for each part of graphene. At voltages higher than the offset voltages, a p-n junction is present in the graphene. The charge density changes rapidly close to the slit, but it is constant far away. The voltage drop across the part 1 (2) is furthermore given by the weighted average of the total as $V_{1(2)} = V_G \left(\frac{A_{2(1)}}{A_1 + A_2} \right)$. This translates to a different gating of two graphene parts resulting in different charge densities $n_1(V_G)$ and $n_2(V_G)$. The total charge on the two sides nonetheless are equal and opposite in sign.

In transmission line geometry, the RF electric field emerges from the signal plane and terminate on the ground plane (see section 3.2). While the field lines are quasi-perpendicular to the graphene surface on the planes, these near the slit are parallel and relatively stronger in magnitude. The field distribution hence probes both the properties of the bulk graphene (homogeneous charge distribution) and the junction graphene (inhomogeneous charge distribution). For simplicity, we model the graphene as lumped one dimensional elements of capacitance and resistance as shown in Fig. 6.1(e). The graphene impedance can thus be simply given as $Z_G \sim R + 1/(j\omega C)$ with the total series capacitance C and resistance R as

$$\frac{1}{C} = \frac{1}{C_{G1}} + \frac{1}{C_{Q1}} + \frac{1}{C_{G2}} + \frac{1}{C_{Q2}}, \quad (6.1)$$

$$R = R_1 + R_{12} + R_2, \quad (6.2)$$

where $\omega = 2\pi f$ is the angular frequency. Thus $C_Q = C_{Q1}C_{Q2}/(C_{Q1} + C_{Q2})$ and $C_G = C_{G1}C_{G2}/(C_{G1} + C_{G2})$ are the total quantum and geometric capacitances of the graphene device. We have assumed that the junction capacitance C_{12} is relatively small so that the junction resistance $R_{12} \ll 1/(\omega C_{12})$. Moreover, we ignore the parallel slit capacitance C_{slit} which is relatively small and gate independent. Together with the load Z_G , the reflectance response Γ of the stub tuner can now be described by $[(Z_{\text{in}} - Z_0)/(Z_{\text{in}} + Z_0)]^2$ where the input impedance Z_{in} is given as

$$Z_{\text{in}} = Z_0 \left(\tanh(\gamma D_2) + \frac{Z_0 + Z_G \tanh(\gamma D_1)}{Z_G + Z_0 \tanh(\gamma D_1)} \right)^{-1}, \quad (6.3)$$

with $Z_0 \sim 50 \Omega$ the characteristic impedance of the transmission line, $\gamma = \alpha + i\beta$ the propagation constant, α the attenuation constant, $\beta = \sqrt{\epsilon_{\text{eff}}}\omega/c$ the phase constant, ϵ_{eff} the effective dielectric constant and c the speed of light. The derivation of Z_{in} is provided in the chapter 3.

6.2. Reflectance results

Figure 6.2(a) shows a color map of frequency and gate voltage response of the reflected signal for device B. Large frequency shifts at two gate voltages can be observed near $V_G = 0$. These can be identified as points where either part of the graphene flake is driven into the charge neutrality. At higher gate voltages, *p-n* junctions are formed in between the unipolar regimes. The behaviour is observed in all our devices, suggesting the presence of an offset doping in the system. From the vertical cuts of the map shown in Fig. 6.2(b), changes in the resonance-depth, -width and -frequency are apparent. Naively, a pure capacitive load should shift the resonance frequency while a pure resistive load changes dissipation of the system. The frequency response to complex impedance has been numerically calculated and presented in section 3.3.2.

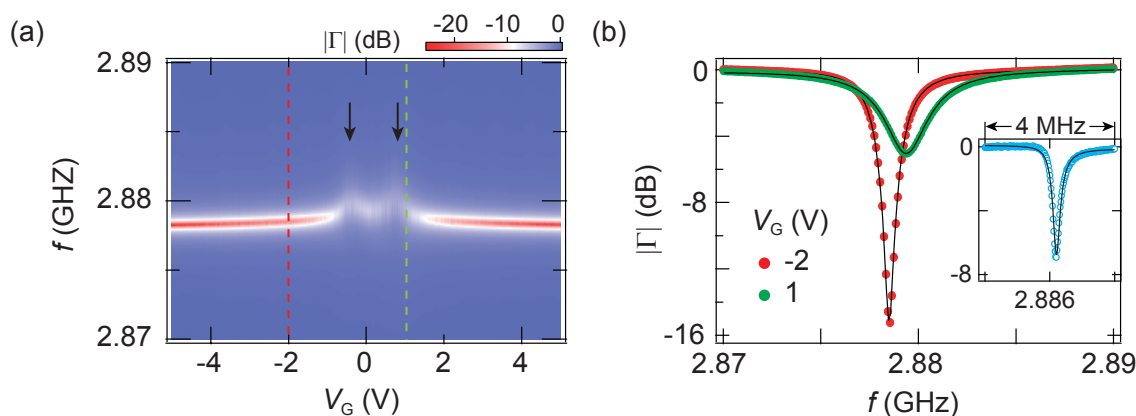


Figure 6.2. Reflectance response of the stub tuner (a) A color map of the measured reflectance power near the resonance frequency versus different gate voltages. Arrows denote the charge neutrality points. (b) Main panel: Cuts of the reflectance curves at two different gate voltages with fits to the Eq. 6.3. Inset: The reflectance response of the same circuit but without any graphene stack. The input RF power is -110 dBm which corresponds to an AC excitation amplitude of $0.7 \mu\text{V}$. Note that the range of frequency is different in the inset.

To quantitatively extract the complex impedance of graphene Z_G , we first need to extract the stub tuner parameters l , d , α and ϵ_{eff} from the reflectance measurements of the same circuit but without any graphene stack. The frequency response is shown in the inset of Fig. 6.2(b) which is fit to Eq. 6.3 with $Z_G = \infty$. We extract $D_1 \approx 10.57$ mm and $D_2 \approx 10.39$ mm, $\alpha \approx 0.0025 \text{ m}^{-1}$ and the effective dielectric constant $\epsilon_{\text{eff}} \approx 6.1$. The loss constant corresponds to an internal quality factor of 25,000. The extracted lengths are within 1% of the designed geometric lengths. Moreover, the resonance frequency of the open stub tuner (2.886 GHz) is larger than the values observed in Fig. 6.2(a), confirming the capacitive nature of the load. We now fix the extracted parameters from open circuit, and fit the resonance spectra to deduce R and C . As shown in the main panel of Fig. 6.2(b), the fitting to Eq. 6.3 yields $R = 118 \Omega$, $C = 18.2$ fF for $V_G = -2$ V and $R = 328 \Omega$ and $C = 17.2$ fF for $V_G = 1$ V. Similar fitting routine is performed at all gate voltages for different devices and deduced C , R plotted in Fig. 6.3 and 6.4 and discussed below.

6.2.1. Quantum capacitance

As shown in Fig. 6.3, we observe for all devices a double dip feature of extracted capacitance near $V_G = 0$ and its saturation at higher voltages. While the double dips have similar widths for device B and C, these are quite different for device A. This originates again from the asymmetric gating of two areas of graphene. To understand the general dependence, we look back at the individual capacitance contributions in Eq. 6.1. Geometric capacitance C_{Gi} with $i = 1, 2$ is simply given by $A_i \epsilon_0 \epsilon_{\text{BN}} / d$, where ϵ_0 is the vacuum permittivity, ϵ_{BN} the dielectric constant, and $d = 21.5$ nm the thickness of the bottom hBN estimated from AFM measurements. Additionally, the quantum capacitance can be derived from the density of states (DoS) as $C_Q = e^2 \cdot \text{DoS}$. The dependence of C_Q in graphene with gate voltage V is explicitly given as [137–140]

$$C_{Qi}(V) = A_i \frac{4\pi e^2}{h v_F \sqrt{\pi}} \sqrt{n_i(V)}, \quad (6.4)$$

with $i = 1, 2$ and v_F the Fermi velocity and h the Planck's constant. The gate induced carrier density is $n_i(V) = (V_i - V_i^0) C_{Gi} / (A_i e)$, where V_i^0 accounts for the offset in CNP from zero and $V_{1(2)} = V_G \left(\frac{A_{2(1)}}{A_1 + A_2} \right)$ accounts for different carrier densities on two graphene parts due to their different areas. Using Eq. 6.1 and 6.4, we see that the C is dominated by the C_G at large gate voltages causing the saturation. The saturation values are different for different devices because of different flake areas and/or hBN thickness yielding different C_G .

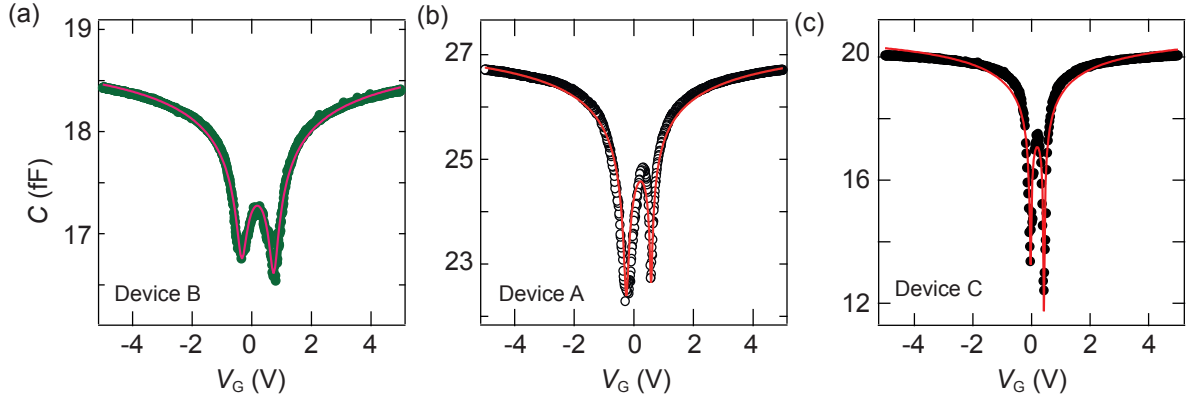


Figure 6.3. Quantum capacitance of graphene The extracted capacitance from the fitting to color maps of reflectance response for three devices. Error bars are smaller than the symbol size. Solid lines are the best fits to Eq. 6.1.

In contrast, near charge neutrality, $C_Q < C_G$, and the quantum capacitance starts to dominate. The fact that C does not approach zero can be attributed to the impurity induced doping $\langle n_{\text{imp},i}^2 \rangle$, with $i = 1, 2$, resulting from charge puddles [141]. To this end, we replace $n_i(V)$ with a total carrier density $\sqrt{n_i^2(V) + n_{\text{imp},i}^2}$. The knowledge of most of the relevant parameters allows us to fit the C curves with ϵ_{BN} , n_{imp} and v_F . This is shown by solid curves in Fig. 6.3. The excellent fits capture both the depth and width near the Dirac charge neutrality points and justify the series model of the graphene impedance with C arising from the total graphene area. For device A(B),

we extract $\epsilon_{\text{BN}} \approx 4(4)$, $v_{\text{F}} \approx 1.05(0.95) \times 10^6$ m/s and $n_{\text{imp},1} \approx 5(7) \times 10^{10}$ cm $^{-2}$ and $n_{\text{imp},2} \approx 1(6) \times 10^{10}$ cm $^{-2}$. The low impurity carrier concentration is consistent with transport measurements in graphene devices encapsulated with hBN [141].

6.2.2. Renormalization of Fermi velocity

For device C, which has a different stub tuner circuit and a different hBN-graphene-hBN stack, we fit the total capacitance again using Eq. 6.1 and extract $\epsilon_{\text{BN}} \approx 4.25$, $v_{\text{F}} \approx 1.54 \times 10^6$ m/s and $n_{\text{imp},1} = 4 \times 10^9$ and $n_{\text{imp},2} \approx 3.5 \times 10^9$ cm $^{-2}$, where we have used the thickness ~ 26.5 nm of the lower hBN. Variations of ϵ_{BN} from one flake to another is readily observed in the transport measurements done in our group. A striking feature of device C is the presence of much lower impurity density and a higher Fermi velocity. Low n_{imp} is also confirmed when looking the relative height of the dips in Fig. 6.3. From device C to A to B, depth becomes shallower and extracted n_{imp} increases. Low n_{imp} has an important consequence for the band structure of graphene which starts to deviate from its linear dispersion [142]. This is because the charge density near CNP starts to vanish and electronic-electronic Coulomb interaction starts to play a significant role. The phenomenon accounted by the renormalized Fermi velocity has been observed both in capacitance [140] and transport measurements [142–144] in graphene.

6.2.3. Charge relaxation resistance

We now discuss the real part of the graphene impedance which relates to the dissipation of the microwave resonance. The extracted R for two devices fabricated from the same hBN-graphene-hBN stack are plotted in Fig. 6.4(a). Two peaks are visible again, which are similar to the charge neutrality points in transport measurements. The position of

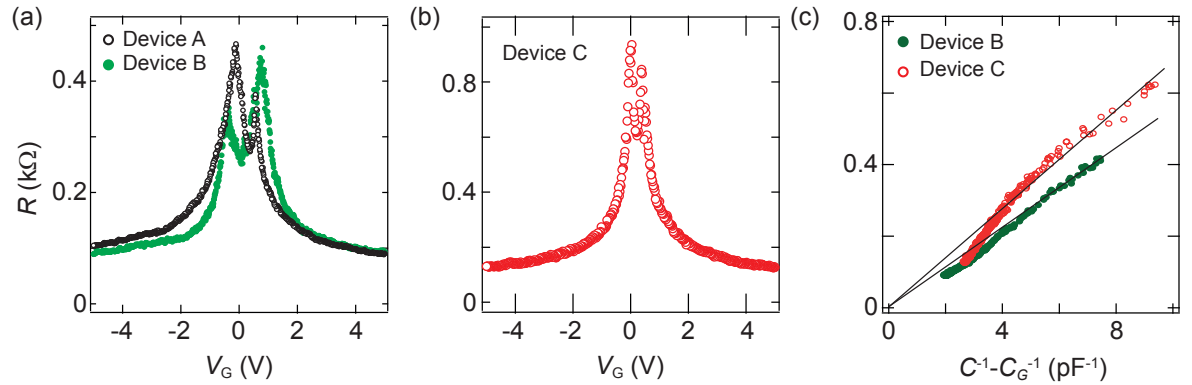


Figure 6.4. Dissipation in graphene (a) The extracted charge relaxation resistance for devices A and B fabricated on the same hBN-graphene-hBN stack. The same loss constant is used in fitting the reflectance map. (b) The extracted R for device C with a different stack and a different circuit. (c) The extracted charge relaxation resistance as a function of inverse quantum capacitance, obtained by subtracting geometric capacitance from the simultaneously measured total capacitance. Solid lines both passing through zero are guide to the eye.

the peaks coincide with the minima of the extracted capacitance. Especially at large gate voltages where residual impurities play negligible role, the resistances start to saturate around similar values despite the fact that the device A is twice longer than the device B. In absence of contacts, this points to the direction that the resistance dominated by the p-n junction at high doping. A similar behaviour is seen in the device C. Close to the charge neutrality, resistance arising from the bulk graphene becomes larger than that of the p-n junction.

The bulk carrier transport in graphene can be further characterized by the diffusion constant. Since the doping profile in our devices is not homogeneous, we can only give an estimate for the diffusion constant D . For this, we analyse the symmetric devices B and C where equal and opposite charge densities appear on two parts of graphene. To obtain D , we can use the Einstein relation ($\sigma = e^2 \cdot \text{DoS} \cdot D$), which can be rearranged with known quantities into

$$D = \frac{(L/2)^2}{RC_Q}, \quad (6.5)$$

where σ is the conductivity. In Fig. 6.4(c) we plot the inverse of the measured quantum capacitance, obtained by subtracting the geometric contribution C_G from the total C against the simultaneously measured resistance. We have removed the points between the two CNP where no p-n interace is present. In both devices, we observe almost linear dependence especially at large resistance values. Similar behavior has been reported in reference [145] suggesting an energy independent D or energy independent scattering time, as can be seen in Fig. 6.4(c). At lower resistances, occurring at large gate voltages, deviations from linear behaviour are apparent. Whereas at high doping the two sides of the graphene have similar doping concentration, at low gate voltages, the difference in the doping (hence R and C_Q) becomes more pronounced, and deviation from Eq. 6.5 can be expected. From the slopes we furthermore extract $D = 0.29$ (0.51) $\times 10^4$ cm^2/s for device B (C). The mean free path can be calculated as $l_e = 2D/v_F$ to yield 0.6 (1) μm for device B (C), which are reasonable values reported in transport measurements. The larger mean free path for device C is also consistent with lower impurity density compared to that of device B.

6.3. Summary and discussions

In summary, we have capacitively coupled encapsulated graphene devices to microwave resonators and observed clear changes in the resonance-linewidth and -frequency. We show a reliable extraction of capacitance in good agreement with the density of states of graphene. Moreover, the charge relaxation resistance is simultaneously inferred from the resonance response and a lower bound of diffusion constant estimated. The results highlight fast characterizations of the graphene devices without requiring any contacts which could compromise the device quality.

An uncertainty of given measurements lies in the extracted R due to the loss constant of the circuit which can vary from one cool-down of the device to the next. From fitting the reflectance response with a different α , we find that the extracted R at different circuit losses are merely offset to each other. The extracted C however is not affected. The behaviour can be understood by replacing the loss constant with a resistor R_{Loss}

in series with the graphene resistor R . This behaviour is explained through numerical calculations in the section 3.3.3. α can be, however, accurately separated in the quantum Hall regime which can be realized with copper resonators [146]. The presented ability to measure contact-free can be useful to study band modification of graphene due to proximity spin orbital effects [147] or Moire superlattices [148]. The method can furthermore be useful for other material systems on which ohmic contacts are difficult to obtain.

7 Quantum dot spectroscopy through shot noise

Typical impedance of a quantum dot of $R \sim 100 \text{ k}\Omega$ causes emission signal to reduce by a factor $\sim (Z_0/R)^2 \approx 10^{-7}$ at the detector, where $Z_0 = 50 \text{ }\Omega$ is the standard input impedance of the detector. A way to enhance the collection efficiency is to employ a wide bandwidth (BW) detector such as a rectifying diode [65]. The key drawback lies in the voltage amplifiers which are needed to measure the signal within the detection limit of an instrument, but also end up adding a background amplifier noise, proportional to the BW , to the desired emission signal. To this end, a quantum limited amplifier such as Josephson parametric amplifier (JPA) can dramatically suppress the background noise and improve the signal to noise ratio. However, the limited bandwidth of few MHz of presently existing JPA [36] hinders the wide-band detection.

In this chapter, we use a resonant superconducting stub tuner operating at GHz frequency to measure classical shot noise from a quantum dot confined in a CNT [149]. The stub tuner provides a high transmission window owing to impedance matching within a BW of a few MHz. Despite the smaller BW compared to the one of a diode, a large signal to noise ratio is achieved in the end due to the smaller background noise from the amplifiers. The chapter starts with the detection scheme and our method to calibrate the measured noise. We then present shot noise results and draw comparisons with the corresponding Schottky value. We see clear changes in the noise spectrum when transport channels are added or removed from the bias window. A theoretical model based on master equations is also provided that qualitatively captures the observed noise suppressions and enhancements both outside and inside the Coulomb diamonds of the charge stability diagram.

7.1. Noise detection scheme

The experimental setup for the noise measurements can be seen in Fig. 4.10. The stub tuner and other components such as circulators, directional couplers and microwave amplifiers are designed to operate around 3 GHz. This choice of resonant frequency ensures that $1/f$ flicker noise is negligible. Moreover, at a bias voltage V_{SD} of $15 \text{ }\mu\text{V}$, the system emits classically and an electronic temperature of 100 mK typically achievable is also close to 3 GHz. We thus measure only white noise. For $hf \gg k_B T, eV_{SD}$, the system emits in the quantum regime where vacuum fluctuations of the electromagnetic environment start to matter. SIS junctions from Al with probe frequency of $f \approx 80 \text{ GHz}$ have been, for example, used to observe quantum noise in mesoscopic systems [150]. We are interested in the classical shot-noise emerging from the quantization of charges.

In Fig. 7.1 we outline the essential components which affect the signal transmission and detection. A device such as a quantum dot with resistance R can be thought of as connected in parallel to a current noise source with a spectral density S_I . This produces a voltage spectral density of $S_V = R^2 S_I$ across the device. The signal then passes through the stub tuner. Due to the band pass filter effect, the white noise now looks like a Lorentzian set by the voltage transmission coefficient t_V of the stub tuner. This produces a signal $(R^2 S_I)|t_V|^2$ at the Z_0 end of the stub tuner. We note that t_V depends both on the probe frequency and the resistance of the device.

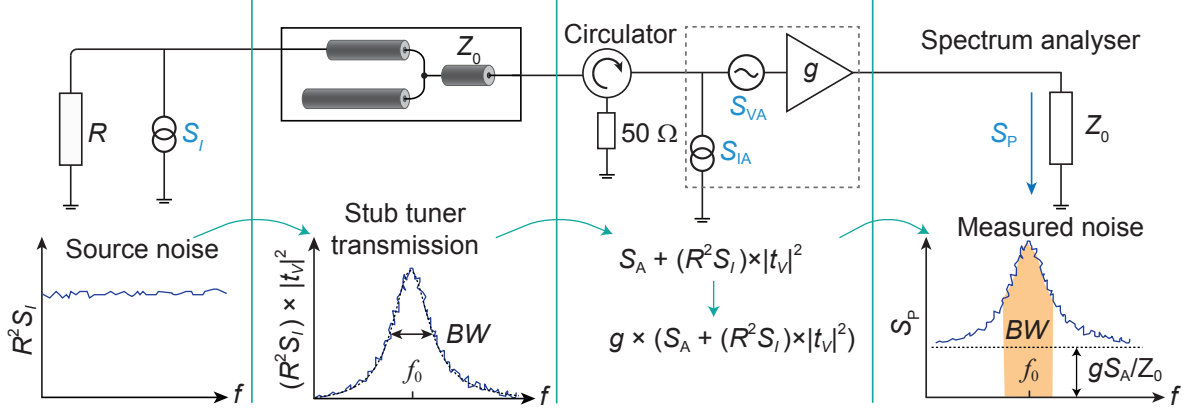


Figure 7.1. Noise detection scheme The noise generated at the device is filtered by the stub tuner with a high transmission around the resonance frequency. Amplifiers in addition to amplifying the signal also add background amplifier noise due to inherent voltage and current noise sources. The final signal is then measured as the power dissipated across a 50Ω resistor built in a power spectrum analyser. Symbols are explained in the text. Adapted from reference [87].

The signal is now amplified by a chain of cold and room temperature amplifiers. More importantly, amplifier adds a background voltage noise S_A to the desired signal due to inherent current (S_{IA}) and voltage noise sources (S_{VA}) at their inputs. The amplifier's current noise can be effectively converted into a voltage noise by the impedance it sees towards the sample. In our case, the low ohmic 50Ω termination of the circulator ensures a R -independent and low contribution of S_{IA} to S_A . Since the gain of all our amplifiers are comparable, only the first amplifier in the measurement chain contributes considerable to S_A . In our case, the cold amplifier sitting at the 4 K stage of the fridge is the first amplifier, with a noise temperature of $\sim 5 \text{ K}$. The signal is then fed into a power spectrum analyser where it is measured as the power dissipated across a standard Z_0 . The voltage fluctuations are hence converted into in a power spectral density S_P as follows

$$S_P(f, R) = g \frac{S_A + (R^2 S_I)|t_V(f, R)|^2}{Z_0}, \quad (7.1)$$

where g is the effective gain of the signal due to amplifiers and cable losses. The measured power $\langle P \rangle$ at the spectrum analyser can then be described by integrating S_P over the high transmission BW of the stub tuner. This results in

$$\langle P \rangle = \langle P \rangle_0 + \langle \delta P \rangle = \langle P \rangle_0 + g \left(\frac{R^2}{Z_0} \right) S_I \int_{BW} |t_V|^2 df. \quad (7.2)$$

Here, we utilize the frequency independent S_I for shot noise at GHz frequencies. $\langle P \rangle_0$ is the effective background noise power in the integration BW . After rearranging the terms, one arrives at the following equation to calibrate the current spectral density S_I produced by the device with corresponding conductance G .

$$S_I = G^2 Z_0 \frac{\langle P \rangle - \langle P \rangle_0}{g \int_{BW} |t_V|^2 df}. \quad (7.3)$$

7.1.1. Gain extraction

The importance of knowing the gain g precisely can be understood by the fact that an error of 3 dB leads to a 100% error in the Fano factor $F = S_I/2eI$. To this end, shot noise of a diffusive metallic wire is measured for which Fano factors are reliably known. One can also use a single tunnel barrier with $F = 1$, however its large resistance necessitates impedance matching. The latter additionally adds uncertainties to gain extraction due to the calibration of the transmission function of the matching circuit. With a metallic wire, the resistance can be planned close to 50Ω so that no impedance matching is needed for optimizing signal collection.

Figure 7.2(a) shows different length L regimes of theoretically predicted Fano factors of a metallic wire [151]. In case of L shorter than the mean free path l , charges move in a ballistic fashion with unity transmission. The absence of randomness produces no noise and $F = 0$. For lengths larger than l but shorter than the electron-electron scattering length l_{e-e} , the wire stays in the phase coherent regime and exhibits $F = 1/3$ [69, 152]. On further increasing the length, the system then enters the hot electron regime. Here electrons under a bias voltage accelerate through the wire and create a new equilibrium energy distribution due to electron-electron scattering. The latter results in an elevated wire temperature relative to the reservoir. These hot electrons then diffuse to the cold reservoirs creating a bellshaped temperature profile along the length of the wire. It turns out that S_I in this regime stays proportional to the current with $F = \sqrt{3}/4$ [68, 153]. For L larger than electron-phonon scattering length l_{e-ph} , the wire is in a macroscopic limit. Here individually fluctuating domains sum up in an uncorrelated way and average to zero. We choose to stay in the hot electron regime where wire lengths of tens of microns can be easily fabricated to produce residual resistances close to 50Ω .

A SEM image of the calibration device is presented in Fig. 7.2(b). A gold wire of length $50 \mu\text{m}$, width 680 nm and thickness 30 nm is evaporated on an undoped silicon substrate. We find the resistance of the wire R_{wire} to reduce with temperature starting from 90Ω at room temperature and saturating at 39Ω below 10 K . The wire is connected to large copper pads of area $300 \times 300 \mu\text{m}^2$ and thickness 500 nm which act like heat sinks. Using the literature [154, 155] for our wire parameters, we find $l_{e-e} = 20 \mu\text{m}$ and $l_{e-ph} = 600 \mu\text{m}$ at a reservoir temperature $T = 0.1 \text{ K}$. This places the wire length clearly in the hot electron regime. The wire device is fabricated by Dr. Thomas Hasler from our group. The author of this thesis performed the measurements and analysis.

We current-bias the wire and measure the noise spectral density S_P using a spectrum analyzer (SSA) at 3 GHz . These are plotted in Fig. 7.2(c) for different base temperatures T of the fridge. For bias currents I up to $5 \mu\text{A}$, noise densities exhibit linear behavior. At larger currents phonons start to compete and the curves start to flatten

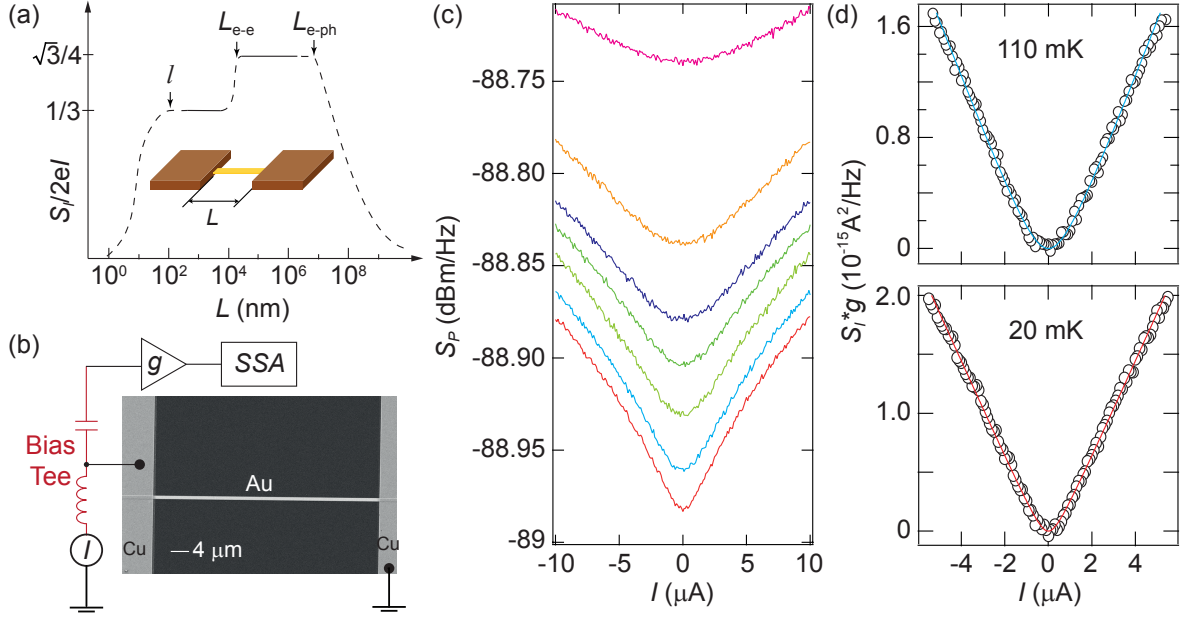


Figure 7.2. Gain calibration of the setup (a) Length dependence of the Fano factor for a metallic wire. Adapted from the reference [68]. (b) A SEM picture of the gold wire with copper pads. The wire is current biased and the noise is measured directly using a spectrum analyzer SSA. (c) Power spectral densities of the wire for different base temperatures of our fridge. From top to bottom in mK: 820, 450, 340, 250, 180, 110, 20. (d,e) Calibrated current noise densities for two temperatures. Solid lines are the least square fits to Eq. 7.4.

out. Additionally, with increasing temperature the zero-current baseline and the curvature around it increase. The former can be attributed to the thermal noise given by $4k_B T_e / R_{\text{wire}}$, where k_B is the Boltzmann constant and T_e the electronic temperature. S_P is converted to $S_I \times g$ using Eq. 7.1 with the voltage transmission $t_V = Z_0 / (Z_0 + R_{\text{wire}})$. We take $S_P(I = 0)$ as the background containing S_A and thermal noise. S_I for such wire in the hot electron regime is given by [68]

$$S_I = \frac{2k_B T_e}{R} \left[1 + \left(\nu + \frac{1}{\nu} \right) \tan^{-1} \nu \right], \quad (7.4)$$

where $\nu = \sqrt{3}eIR_{\text{wire}}/2\pi k_B T_e$. We first fit the calibrated noise at a higher temperature where T_e can be assumed to be the same as the fridge temperature T . At lower temperatures, a smaller phonon-electron coupling prevents cooling of the electronic devices to the fridge temperature. Figure 7.2(d) shows such a fit, after subtracting the thermal contribution, at 110 mK to extract the gain $g = 94.6 \pm 0.1$ dB. The gain g is reasonable considering roughly 35 dB gain of three amplifiers in series and roughly 10 dB losses from coaxes. We get the same g from fitting the data at 250 mK. Next the data at $T = 20$ mK is fitted by fixing the gain. This gives an upper bound on the T_e of 50 mK. We further use the gain to estimate the background amplifier noise. From the data sheet, noise temperature of the amplifier is ~ 5 K. This should produce a background of $10 \times \log(k_B T \times 1000) + g = -97$ dBm/Hz. Deviation of 8 dB from the observed value of -89 dBm/Hz is due to cable losses between the device and the amplifier.

7.2. Shot noise in single quantum dot regime

We now discuss shot noise measurements in a single quantum dot formed in a CNT. As explained in the chapter 2, electronic interactions play an important role in determining the statistics of electronic noise in mesoscopic systems. In particular for a QD system, the Coulomb charging energy (E_C) imposes a sequential tunnelling of electrons. Local electrodes further tune the electrochemical potential of the dot and allow one or more channels in the bias window thereby modifying the electronic transitions. The interactions can be further modified by the energy dependence of the tunnelling- in and out-rates of the dot. The QDs thus provide a rich playground for noise studies.

7.2.1. Sample layout

A SEM image of the device measured is shown in Fig. 7.3(a). A Nb stub tuner is fabricated in the first step. The CNT is then probabilistically stamped and the source, drain contacts evaporated from Pd (4.5 nm)/Al (75 nm) separated by 300 nm. A side gate ~ 100 nm in width and ~ 200 nm away from the CNT tunes the dot occupation. Since we work in high bias regime $V_{SD} \gg 200 \mu\text{eV}$, the effect of superconductivity from Al can be ignored. Reflectometry spectra for this sample are already provided in Fig. 5.2(a,b). The latter provides useful extraction of stub tuner parameters such as the lengths D_1 , D_2 and the loss constant α .

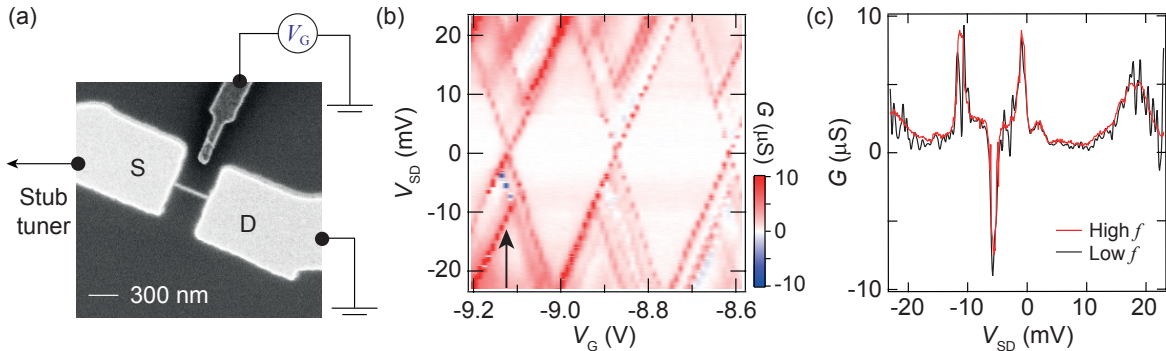


Figure 7.3. Device characterization (a) SEM picture of the measured CNT device with source, drain and a side gate contact. The source (S) is connected to the stub tuner (not shown) while drain (D) is grounded. Dot occupation is tuned by a side gate V_G . (b) Conductance map extracted from reflectance at 3 GHz. Red points display positive conductance while blue points negative. (c) Cuts of the conductance map at the gate voltage marked by the arrow in panel (b), extracted from the reflectance (high frequency) and the numerical derivative of the direct current (low frequency).

The circuit operates in the load dominated regime reaching impedance matching near $G = 7 \mu\text{S}$. To characterize the quantum dot transport, series of Coulomb diamonds are mapped. This is shown in Fig. 7.3(b) extracted from the reflectance amplitude, see section 5.2.1 for the extraction method. Clear excited states outside the Coulomb diamond and cotunnelling features inside the diamond can be observed. Moreover, negative conductance values are also seen. To validate the stub tuner parameters,

this G is compared with the one from the numerical derivative of the simultaneously measured direct current at low frequency [136, 149]. We find an excellent agreement between the two, as shown in Fig. 7.3(c).

7.2.2. Stub transmission function

After the reliable extraction of stub tuner parameters from the reflectance spectra, we now calculate its voltage transmission function $|t_V|$ seen by the device. This is needed to calibrate the noise densities as seen from the Eq. 7.3. To this end, we use the following equation derived in section 3.3.6 (symbols are explained in chapter 3)

$$t_V(f, R) = \frac{2Z_0}{R + Z_0} \cdot \frac{e^{\gamma D_1} \cdot \coth(\gamma D_2)}{\Gamma_L + e^{2\gamma D_1} \cdot [1 + 2 \coth(\gamma D_2)]}, \quad (7.5)$$

where $\Gamma_L = (R - Z_0)/(R + Z_0)$ is the reflection coefficient seen directly at the device end before the matching circuit. Figure 7.4(a) shows the calculated voltage transmission response for different conductance values using the stub tuner parameters. As expected, the bandpass filter effect of the circuit is also present in transmission, similar to reflection. For the circuit loss of the device $\alpha = 0.019 \text{ m}^{-1}$, the transmission maximum at $G = 4 \text{ } \mu\text{S}$ is $|t_V^{\text{max}}|^2 \approx 1.6 \cdot 10^{-5}$. For a lossless case $\alpha = 0$, this reaches twice as much $\approx 3.8 \cdot 10^{-5}$ for the same conductance. Within a bandwidth $BW = 5 \text{ MHz}$ (shaded in orange) the circuit hence provides more than two orders of magnitude larger transmission than the case with no matching $\approx (Z_0/R)^2 = 4 \cdot 10^{-8}$.

Experimentally measured power spectral densities S_P in and out of Coulomb blockade are shown in Fig. 7.4(c). For blockade, $G = 0$, the measured S_P does not change versus frequency. In absence of current and thermal noise, $S_I = 0$. The measured quantity hence effectively reflects the amplifier background noise of the setup, as evident from Eq. 7.1. In contrast, S_P for conducting regime, in this case $V_G = -9.2 \text{ V}$, $V_{SD} = 23 \text{ mV}$, and $G = 5 \text{ } \mu\text{S}$, shows a Lorentzian lineshape as predicted from Eq. 7.5. Both curves with 1001 points are measured in a time period of 6 ms implying a $6 \text{ } \mu\text{s}$ acquisition time

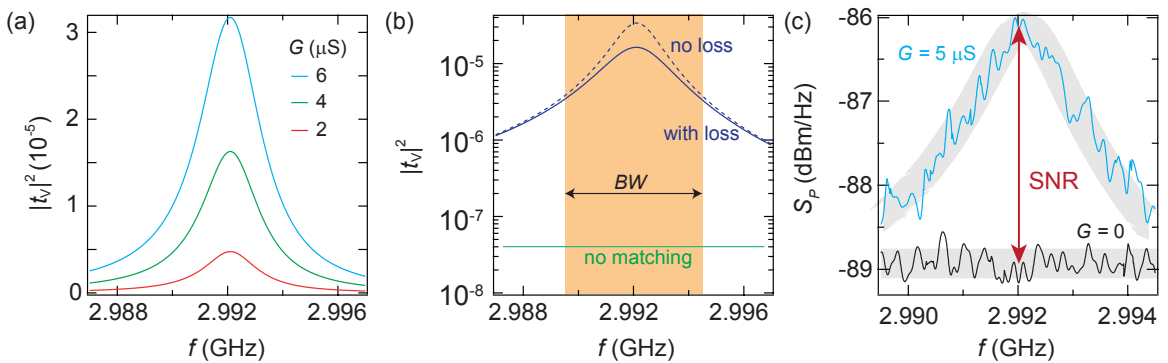


Figure 7.4. Stub tuner transmission (a) Calculated power transmission response for several $G (= 1/R)$ values. (b) Comparison of the transmission function for matching with and without losses and for case of no matching at $G = 4 \text{ } \mu\text{S}$. (c) Experimentally measured power spectral density in and out of Coulomb blockade near the resonance frequency of the stub tuner.

for single point. Additionally, the signal to noise ratio (SNR) acquired at the resonance frequency is ~ 3 dB. These features demonstrate the importance of a stub tuner for fast readout of small signals with significant SNR. We clarify again that by signal here we mean the desired emission to be measured, while the noise or the signal spread, of ± 0.12 dB here, accounts for the uncertainties in the amplifier gain and the amplifier background noise.

To get the noise power, we simply integrate the noise spectral density around a bandwidth BW . As shown in the section 3.3.7, the optimal integration bandwidth for maximal signal to noise ratio is achieved when $BW \approx 1.4 \cdot \text{FWHM}$, with FWHM the full width half maxima. However, we note that the FWHM is conductance dependent and thus a compromise has to be made while fixing the BW . The FWHM for the concerned stub tuner circuit near matching is ~ 3 MHz, see Fig. 5.2(a). We thus choose a BW of 5 MHz and average the noise power $\langle P \rangle$ 100 times. With a resolution bandwidth of 100 kHz of our spectrum analyser, it takes roughly 0.6 second of measurement time for each bias-gate voltage setting.

Grayscale maps of $\langle P \rangle$ and I are simultaneously measured for the same V_G and V_{SD} range as in Fig. 7.3(b). Raw noise power is shown in Fig. 7.5(a) with the Coulomb diamond contours taken from the G map. The finite noise power ~ -22 dBm inside the Coulomb diamonds is again the amplifier background noise. With the knowledge of gain g and transmission function $t_V(f, G)$, we now calibrate $\langle P \rangle$ using Eq. 7.3 to arrive at the noise current density S_I for each bias and gate voltages. Since there can be a drift in the amplifier noise, $\langle P \rangle$ at $V_{SD} = 0$ is taken as the $\langle P \rangle_0$ for individual vertical scans of Fig. 7.5(a). Moreover, the contribution of thermal noise at an electronic temperature of ≈ 50 mK is negligible for our bias voltage range.

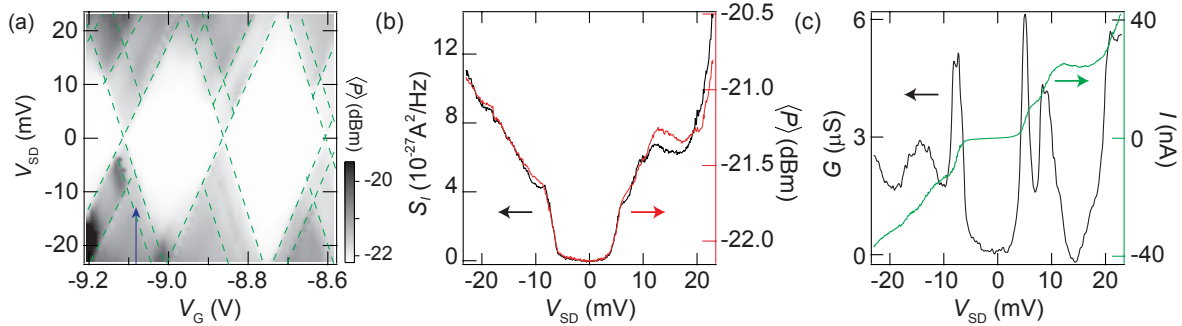


Figure 7.5. Noise calibration (a) Measured grayscale map of noise power integrated over a bandwidth of 5 MHz around the resonance frequency of the stub tuner. (b) Calibrated noise current density together with uncalibrated noise power at the gate voltage shown by the arrow in panel (a). (c) Corresponding conductance and current measurements.

A cut of calibrated S_I together with raw value $\langle P \rangle$ at $V_G = -9.08$ V is shown in Fig. 7.5(b). We see a qualitative similarity of the two curves despite dramatic changes in conductance [see Fig. 7.5(c)] for the same range. This can be understood when one looks at Eq. 7.5 for $R \gg Z_0$. In this case, $\Gamma_L \approx 1$, and $|t_V|^2$ becomes proportional to G^2 . Inserting this in Eq. 7.3, S_I calibration does not depend on G any more. The raw data therefore already provides a good visualization of noise properties.

7.2.3. Shot noise results

We now present a grayscale map of calibrated S_I for the entire gate voltage range. Since the bias voltage range $V_{SD} \gg k_B T$, the measured quantities are classical shot noise. This is shown in Fig. 7.6 together with the Schottky noise given by $2e|I|$. The latter is the current noise density for the case with constant Fano factor $F = S_I/2e|I| = 1$ everywhere. Grayscale range is kept the same for both maps to provide a direct comparison. To quantitatively deduce the differences, we plot $S_I - 2e|I|$, namely excess Poissonian noise S_I^{EP} . Enhanced noise compared to Schottky value called super-Poissonian is visible in blue while reduced noise in red. White regions have $F = 1$. Interestingly, the regions enclosed by contours taken from the conductance map display clear super or sub Poissonian noise bands. Enhanced and suppressed noise bands are also visible in the Fano factor map shown in Fig. 7.6(d). These observations suggest that the number of transport channels strongly affect the current fluctuations. In the following sections we discuss several transport regimes.

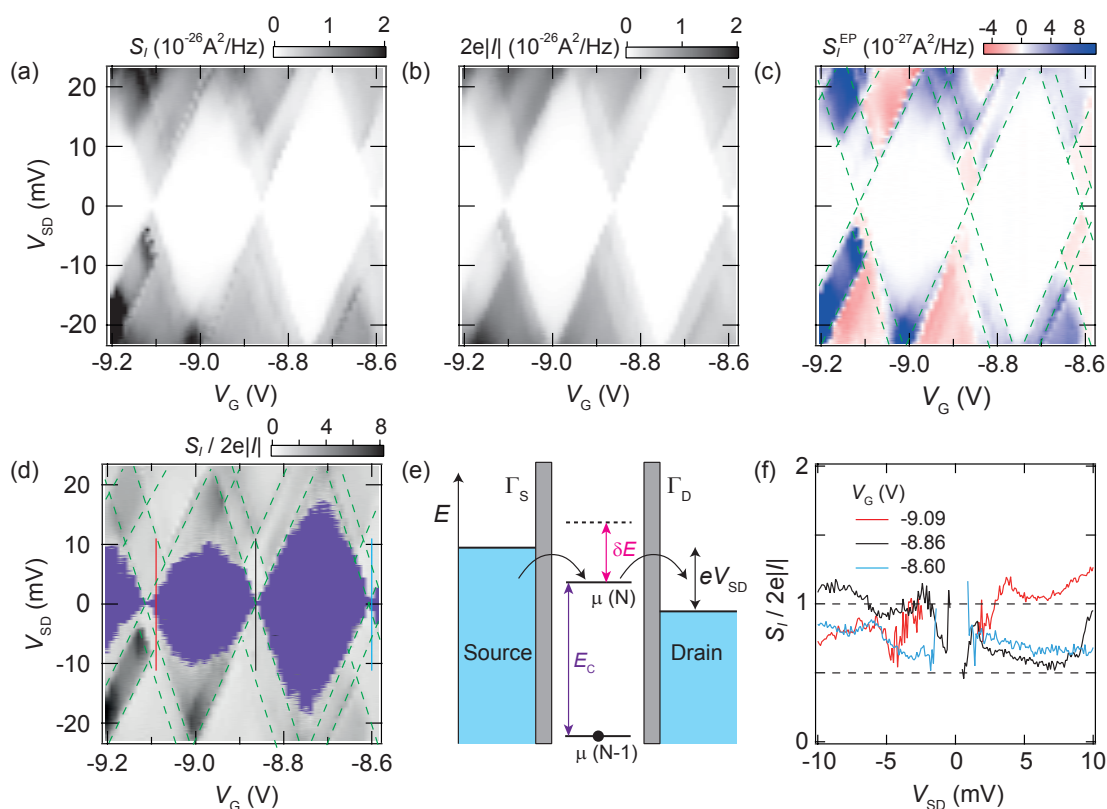


Figure 7.6. Shot noise of the quantum dot (a) Calibrated current noise density as a function of bias and gate voltages. (b) Corresponding Schottky noise obtained from the measured current. (c) Excess Poissonian noise obtained by subtracting panel (b) from (a). Super-Poissonian noise is presented in blue while sub-Poissonian in red. (d) Fano factor F grayscale map obtained by dividing panel (a) by (b). Coloured areas denote the points where the division is unreliable due to the small current in Coulomb blockade. (e) Sequential tunnelling in low bias regime strictly allows one-channel charge transport. (f) Cuts of F at constant gate voltages marked by dashed lines in panel (d).

7.2.4. Noise suppression in single channel regime

If the bias $|eV_{SD}|$ is smaller than the level spacing δE , the charge transport happens strictly via a single channel and through two tunnel barriers with rates Γ_S, Γ_D , see Fig. 7.6(e). For a non-interacting system, the Fano factor is simply given by the weights of two tunnelling rates $(\Gamma_S^2 + \Gamma_D^2)/(\Gamma_S + \Gamma_D)^2$ [19]. Two extreme cases can be formulated. When the tunnelling rates are asymmetric i.e. one is much larger than the other, we get $F \approx 1$. Physically, the transparent barrier quickly fills or empties the dot while the opaque barrier produces fluctuations of the transport. This situation thus boils down to having a single tunnel barrier where $F = 1$. For the other case of the tunnelling rates being symmetric $\Gamma_S = \Gamma_D$, the Fano factor is $1/2$. This can be naively understood as follows. When a charge from the inner-circuit $+e$ tunnels into the dot, equal screening charges $-e/2$ appear on source and drain contacts. Upon a second tunnelling event from the dot, the net transfer of charge felt by the outer circuit hence is only $+e/2$ while the other half seems to be reflected back to the inner circuit in form of a screening charge.

From the conductance map, a level spacing δE of the order of ~ 5 meV can be seen. For smaller bias voltages therefore single channel charge transport can be assumed. The G values of the order of $10 \mu S < e^2/h$ seen in Fig. 7.3(b) suggest highly asymmetric tunnel resistance of the barriers and should yield $F = 1$. In contrast, cuts of F near diamond crossings at low bias in Fig. 7.6(f) show non-constant values that roughly lie between 1 and $1/2$. This means that a non-interacting picture of two tunnel barriers in series does not hold in this case. Moreover, it has been shown by Hershfield *et al* [156] that tunnelling rates in presence of Coulomb blockade are not simply given by tunnelling resistances but rather depend on Gibb's free energy. The latter is the difference between the charging energy of the quantum dot and work done by the bias voltage source. Consequently, asymmetries in the tunnel resistance can be compensated by asymmetries in the energy gain and tunnelling rates could become similar. A special consequence of energy dependent tunnelling rates has been seen for Coulomb staircase to cause periodic suppression of F from 1 to $1/2$ between the plateaus [157].

7.2.5. Inelastic cotunnelling assisted sequential tunnelling

As explained in section 2.5.1, currents can flow even inside Coulomb blockade due to second order tunnelling process called cotunneling. Elastic cotunnelling (EC) happens irrespective of the bias voltage and does not change the ground state of the dot. However, if $|eV_{SD}| > \delta E$, an excited state can be available in the bias window. During cotunnelling there is hence a finite possibility that the system changes from ground state to the excited state, referred to as inelastic cotunnelling (IEC). If the dot relaxation rate is relatively small, tunnelling events via the excited state as shown in Fig. 7.7 can take place. This sequential charge transfer keeps happening until the system relaxes to its original ground state and current is blocked. Since cotunnelling rates are much lower than the sequential processes, the outer circuit of the dot experiences a bunched charge transfer during an IEC event. The resulting shot noise hence can be larger than its Schottky value even though the actual currents are small [158–162].

Figure 7.7(c) shows a dependence of $S_I/2e|I|$ in the IEC regimes. We see Fano factors larger than 1 and its enhancement up to 5 in the positive bias and 3 in the negative bias

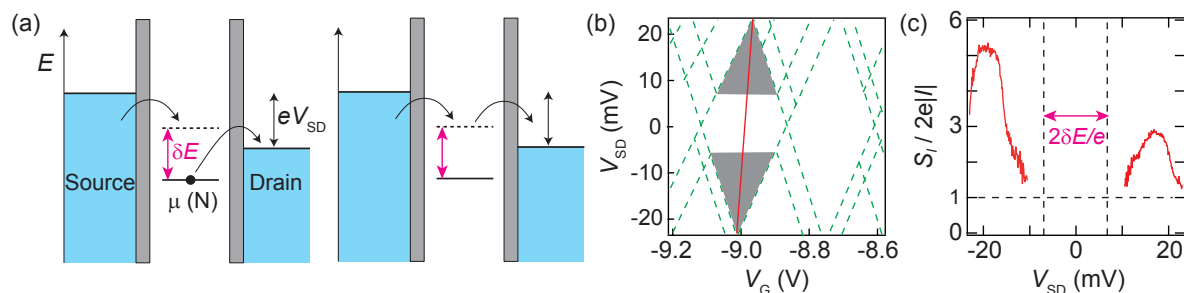


Figure 7.7. Shot noise for the inelastic co-tunnelling (a) Energy level diagrams to illustrate sequential tunnelling via first excited state following an event of inelastic cotunnelling. (a) Green dashed Coulomb diamonds contours with shaded regions where IEC is experimentally observed. (c) A cut of experimentally measured F in IEC regimes denoted by a solid line in the panel (b). At low bias, current from elastic cotunnelling is too small to perform a numerical division.

regime. At bias voltages closer to $\pm\delta E/e$, F values are close to 1. This suggests that the dot relaxes to its ground state faster than the charge can tunnel out from the excited state. The process becomes equivalent to an EC event which produces uncorrelated tunnelling events similar to Schottky noise and hence $F = 1$. At bias voltages reaching the top or bottom edge of the Coulomb diamond, F drops towards 1 as well. Strong variation of F observed here again suggests an energy dependence of tunnelling and relaxation rates in the quantum dots.

7.2.6. Excited blocking states

At large bias V_{SD} though smaller than E_C , more than one orbital state can become available in the bias window. Let us take a two channel situation without any dot relaxation as shown in Fig. 7.8(a). Parallel charge transport from both channels is not allowed because of the charging energy. Charges hence must tunnel either via the ground state or the excited state. If both channels are equally coupled to the leads, currents are statistically equally divided between the two. The situation is equivalent to having a single channel transport. Consequently, the Fano factor lies between 1/2 and 1 as described earlier. An interesting case arises when the coupling of the two channels are very different. The charge transport can thus be blocked at times through the opaque channel. This produces a bunching of charges similar to the inelastic cotunnelling assisted sequential tunnelling discussed in the previous section.

We observe super-Poissonian noise in several regions in the gate/bias voltage map for the many-channel case. Two examples are highlighted by the shaded bands in Fig. 7.8(b). For both cases, a transition from the sub-Poissonian regime of single channel transport to the super-Poissonian case can be seen from the green contour dashed lines in Fig. 7.6(c). In particular, the bottom-left shaded region presents an interesting case, where the excited state displays negative conductance of about $-10 \mu\text{S}$ visible as blue data points in Fig. 7.3(b). This already suggests that the new channel added to the transport is a blocking state [163] producing smaller currents at increasing bias. The corresponding shot noise per unit current is however not small. This is confirmed in the

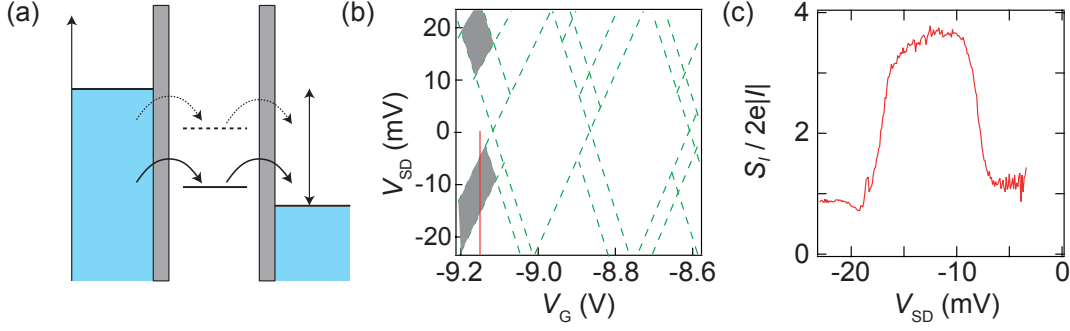


Figure 7.8. Shot noise for many channel transport (a) Energy level diagram showing two channels involved in the transport. Dashed arrows show weaker tunnel coupling while solid arrows stronger coupling. (b) Green dashed Coulomb diamonds contours with shaded regions where super-Poissonian noise is observed for multi-channel charge transport. (c) Experimentally measured F for a blocking state at a fixed gate voltage, denoted by the vertical solid line in the panel (b).

measured Fano factor plotted in Fig. 7.8(c) where we see F enhancement up to 3.5. In contrast, for the top-left shaded band, the conductance is always positive. This hints that the newly added channel, though a blocking state, is not long lived and therefore a fast relaxation makes sure that most of the transport happens via the ground state.

7.3. Theoretical Model

Having discussed the shot noise measurements in several regimes of charge transport we now turn to a theoretical model, in an aim to understand the noise enhancement at specific dot configurations. The latter is based on full counting statistics (FCS) master equation, originally developed in the reference [163] and only briefly explained below. The MATLAB code for numerical calculations is written by Dr. Gergő Fülöp.

The FCS is based on a Markovian master equation within a T-matrix model and valid as long as $k_B T, eV_{SD}, \delta E \gg \Gamma$, where $\Gamma = \Gamma_S + \Gamma_D$. In this approach, the master equation is limited to the occupation probabilities p_k for the quantum dot states labelled by a (collective) index k . In our case, we restrict the spinless model to four configurations, namely the dot being empty ($k = 1$) or in ground state ($k = 2$) or excited state ($k = 3$) or doubly occupied ($k = 4$). Their general time evolution

$$\frac{dp_k}{dt} = -p_k \sum_{k' \neq k} \Gamma_{kk'} + \sum_{k' \neq k} p_{k'} \Gamma_{k'k} \quad (7.6)$$

can be simply arranged in a matrix equation $d\mathbf{p}/dt = \mathcal{M}\mathbf{p}$, where \mathcal{M} is a 4×4 matrix for four dot configurations. The transition rates $\Gamma_{kk'}$ are obtained from the Fermi's golden rule and depend on the tunnel coupling strengths of the leads. The first summation of the equation generates the diagonal terms of the matrix \mathcal{M} while the second summation off-diagonal terms. For sequential tunnelling, the transitions simply connect the neighbouring charge states. Including the leads, $\alpha/\beta = S/D$, rates for adding an

electron on the dot are given by

$$\Gamma_{kk'} = \sum_{\alpha} \Gamma_{\alpha} |M_{kk'}^{\alpha}|^2 f_{\alpha}(\varepsilon), \quad (7.7)$$

where $k' = 2, 3$ if $k = 1$ and $k' = 4$ if $k = 2, 3$, and $f_{\alpha}(\varepsilon)$ is the Fermi Dirac distribution accounting for the bias dependence. $M_{kk'}^{\alpha} = (M_{k'k}^{\alpha})^*$ are the transition elements connecting the dot configurations, which are treated as tunable parameters in our calculations. Similarly, rates for removing an electron from the dot are

$$\Gamma_{k'k} = \sum_{\alpha} \Gamma_{\alpha} |M_{k'k}^{\alpha}|^2 [1 - f_{\alpha}(\varepsilon)]. \quad (7.8)$$

For example, if the dot is empty ($k = 1$), an electron can be added to either the ground state ($k = 2$) with a transition rate $\Gamma_{2,1}$ or to the excited state ($k = 3$) with a transition rate $\Gamma_{3,1}$. The transition rates for the second order cotunnelling processes however involve tunnelling in and out of two leads that may excite the dot but leaves the charge state intact. The rates $\Gamma_{kk'}^{\alpha\beta}$ thus contain a product of left and right lead couplings and product of matrix elements. Moreover the relaxation from the excited state to the ground state also changes the occupation probability and can be incorporated via an additional parameter γ_{rel} , which is independent of tunnel coupling strengths.

In FCS we generally describe the probability $P(n, \Delta t)$ of n electrons traversing across the dot in a measurement time Δt . For numerical calculations, it is more convenient to work with $S(\chi, \Delta t)$, the cumulant generating function (CGF), defined as

$$e^{S(\chi, \Delta t)} = \sum_n P(n, \Delta t) e^{jn\chi} \quad (7.9)$$

where χ is the counting field. In this formalism the average current can be obtained by the first derivative $\frac{e}{\Delta t} \frac{\partial S}{\partial (j\chi)} \Big|_{\chi \rightarrow 0}$ and noise from the second derivative $\frac{e^2}{\Delta t} \frac{\partial^2 S}{\partial (j\chi)^2} \Big|_{\chi \rightarrow 0}$. The counting probability $P(n, \Delta t)$ can be further resolved by summation over all dot configurations and then Fourier transformed, resulting in a counting-field master equation

$$\frac{d\mathbf{p}(\chi, \Delta t)}{dt} = \mathcal{M}(\chi) \mathbf{p}(\chi, \Delta t). \quad (7.10)$$

In the Markovian approximation, the stationary solution to this equation can be obtained from the eigenvalue Λ of $\mathcal{M}(\chi)$ with the smallest real part [164] as

$$S(\chi, \Delta t) = \Delta t \Lambda_{\text{min}}(\chi). \quad (7.11)$$

All that remains to calculate current and noise is to construct χ dependent matrix and solve for at least three small values of $\chi = (0.001, 0, -0.001)$ to get χ dependent eigenvalues, which are then used to approximate the derivatives of $S(\chi)$ with finite differences. It turns out that χ dependent transition rates for sequential tunnelling can be simply expressed as [164]

$$\Gamma_{kk'}^{\alpha/\beta}(\chi) = \Gamma_{kk'}^{\alpha/\beta} e^{\pm j\chi}, \quad (7.12)$$

where \pm signs account for processes into/out of the counting lead α . For the cotunnelling case [163] the rates are given in terms of Kronecker delta as

$$\Gamma_{kk'}^{\alpha\beta}(\chi) = \Gamma_k^{\alpha\beta} (\delta_{\alpha\beta} + \delta_{\alpha S} \delta_{\beta D} e^{j\chi} + \delta_{\alpha D} \delta_{\beta S} e^{-j\chi}). \quad (7.13)$$

The complex matrix elements of $\mathcal{M}(\chi)$ can now be created at each gate and bias voltage points. By default, parameters such as charging energy is set to 1 meV and dot-lead transition elements $M_{kk'}^\alpha = 1$. Moreover we choose quantum mechanical excitation energy $\delta E = 0.25$ meV and symmetric lead coupling energies of 10^{-3} meV which is much smaller than other energy scales to neglect broadening effects. Moreover, the transition rates for adding or removing electrons are symmetrical i.e. $M_{k,k'}^\alpha = M_{k',k}^\alpha$, which we choose to be real valued.

We first generate a stability diagram in Fig. 7.9(a,b) for the case where both source and drain contacts are strongly coupled to two transitions - we choose $M_{3,1}^\alpha = M_{4,3}^\alpha = 2$. Next, we choose the relaxation rate to be fast for panel (a), $\gamma_{\text{rel}} = 1$ and a much slower $\gamma_{\text{rel}} = 10^{-3}$ for panel (b). A transport via excited states are easily visible in both panels (a,b) of conductance plots where four excited state lines emerge outside the diamond edges. Faint line near the vertices is merely the continuation of the excited states from the opposite bias direction. A slow relaxation leads to cotunnelling assisted sequential tunnelling [165] causing F enhancement inside the diamond [163], shown in panel (b). For the case of fast relaxation, the second transport pathway is eliminated, and $F = 1$ is recovered, characteristic for elastic cotunnelling.

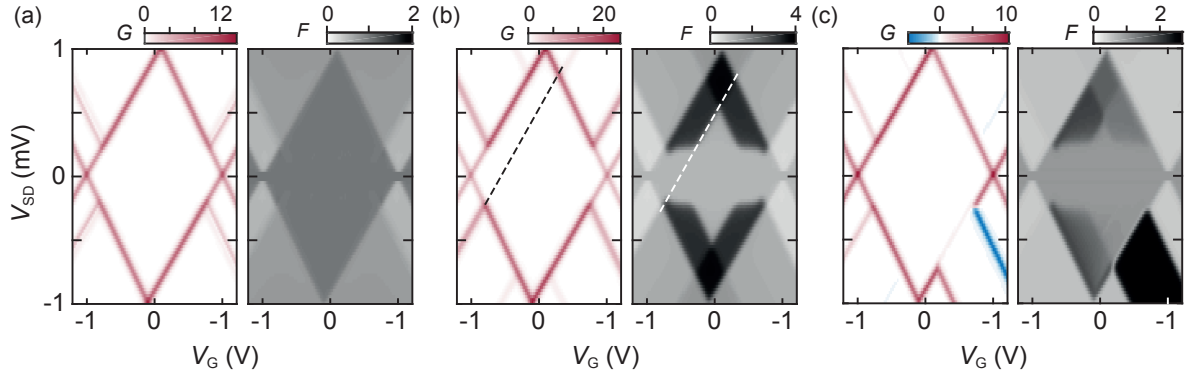


Figure 7.9. Calculated stability diagrams of G and F (a,b) The ground and excited state have the same transition elements $M_{kk'}^\alpha$ in calculations. Inside the diamonds, cotunnelling assisted sequential tunnelling leads to noise enhancements, when the relaxation is slow [panel (b)] or produces Poissonian noise for fast relaxation [panel (a)]. Dashed line highlights the continuation of an excited state towards the opposite diamond edge. (c) Excited blocking state has a smaller weight $M_{4,3}^S = 0.1$ in calculations. An enhanced noise band coincides with the contour of the negative differential conductance. Thermal noise is subtracted from both Fano factor calculations.

We start fresh again with default settings of $M_{kk'}^\alpha = 1$. The lead coupling is now reduced to a specific transition such that $M_{4,3}^S = 0.1$ while keeping the relaxation rate quite low $\gamma_{\text{rel}} = 10^{-5}$. What results is a blocking state with negative differential conductance shown by blue in Fig. 7.9(c). This again leads to F enhancement in a band where two dot transitions coexist in the bias window. In all grayscale plots of Fig. 7.9, F is 1/2 for strictly single channel transport and 1 for elastic cotunnelling.

Despite the tunnel coupling energies and relaxation rates being energy independent, the simple rate equations help us to reproduce most of the experimental features. Especially near the vertices inside the diamonds in Fig. 7.9(b), the Fano factor is relatively

larger, which is also observed in our measurements, see Fig. 7.6(d). Moreover, the consequence of long lived excited state is more pronounced in the Fano factor plot and the conductance plots do not yield such information in Fig. 7.9(a,b). Besides, a blocking state could be explicitly introduced in the calculations and is shown to produce enhanced noise, also consistent with the measurements.

7.4. Summary and discussion

We have employed a GHz stub tuner to measure shot noise from a QD confined in a CNT which has an average resistance of the order of 150 k Ω . The simple planar structure of the circuit from coplanar transmission lines is easy to design and fabricate with standard lithography. We demonstrate quantitative parameter extraction of the stub tuner circuit to enable simple calibration of the noise signals. More importantly, the large transmission achieved in bandwidths on the order of a few MHz is utilized to perform fast measurements of small signals with significant signal to noise ratio. We see selective enhancement and reduction of the current noise densities from their Schottky value depending on the type and number of transport channels involved. The noise features match well with the existing experimental and theoretical studies on QDs.

To quantify the advantage of a stub tuner over wide bandwidth detection, we define a figure of merit $g_{\text{SNR}} = \text{SNR}_{\text{matching}}/\text{SNR}_{\text{nomatching}}$. Here SNR is the ratio of desired noise signal with the background amplifier noise, given as $\langle \delta P \rangle / \langle P \rangle_0$ from the Eq. 7.2. The case of nomatching is obtained by setting D_1 and D_2 to zero in the equation. A derivation of g_{SNR} is provided in the section 3.3.7. It turns out that the upper bound for the lossless case with FWHM taken as the bandwidth is

$$g_{\text{SNR}}^{\text{max}} = \frac{\pi}{16} \frac{R_{\text{Match}}}{Z_0}. \quad (7.14)$$

This is ≈ 500 for our case of matching at $G = 7 \mu\text{S}$. Even after including losses of the stub tuner, this value can be calculated by integration of transmission function in Eq. 3.49 and is ≈ 200 at the same conductance. The figure of merit is exactly the same for an LC circuit [149] even when it has a larger FWHM for the same G_{Match} . This can be qualitatively understood as following. At full matching, irrespective of the circuit, $|t_V|^2$ is given by $1/4 \cdot Z_0/R$ to allow maximum power collection, which is 1/4 of the generated value. Only the integration bandwidth is different for two cases. But again, increase in BW also leads to an enhanced background noise so the ratio remains the same. Larger BW of the LC circuit is however desirable for a faster time-resolved read-out.

An alternative way to improve SNR is to minimize the background amplifier noise. This can be achieved with Josephson parametric amplifiers where g of 30 dB is readily achievable. The noise added in this case is just the vacuum fluctuations of the electromagnetic environment with energy $\sim \hbar\omega$ for each mode with frequency ω . A JPA for example has been employed to measure emission noise from double dots in InAs nanowires [166] and GaAs two-dimensional gas [167]. In our group, we are working on combining a lumped LC circuit with Josephson junctions to simultaneously achieve impedance matching and parametric amplification.

8 Shot noise of quantum dots coupled to superconducting leads

Compared to normal leads, superconductors contain Cooper pairs which are protected by an energy gap Δ from the quasiparticle states. The charging energy of the quantum dots, to the first order, however restricts electrons to pass one by one. Coupling quantum dots to superconductors hence creates a direct conflict of two phenomena. Interest in such competing effects have thus gained attention not only for fundamental studies of Andreev bound states [13], Majorana bound states [16, 168], Josephson effect [50] but also for its potential applications in supercurrent transistors [169], nano-SQUIDs [170, 171] and entangled Cooper-pair based quantum computing [14, 15]. Most of these phenomena have been studied through averaged current or conductance.

In this Chapter, we study the competing effects of quantum dots (QD) and superconductors (S) through shot noise measurements. Two devices are presented, one fabricated on an InAs nanowire and another on a carbon nanotube. Both devices are contacted with Al leads and integrated on chip with stub tuner circuits. The devices operate in the large lead coupling regime to allow second order cotunnelling processes. The latter enables us to study behaviours in the off-resonant and resonant cases using the same device. In the first device, we address multiple charge transfers resulting from Andreev reflection and associated shot noise. More importantly, measurements of supercurrent emissions at zero bias are presented. In the second device, effects of Kondo correlations are also included. Circuit and gain calibration techniques of the devices have been already provided in Chapter 7 and not repeated here.

8.1. Andreev transport in few transport channels

What happens to the electrical transport when a superconductor is connected to a normal metal (N) is best described by Andreev reflections, i.e. when an electron or a hole in the normal region hits the superconductor, a hole or an electron is reflected with the same energy and constitutes a transfer of a Cooper pair into the superconductor. In the case of coherent S-N-S junctions, even higher order multiple Andreev (MAR) reflections can contribute to the current (see Chapter 2). In the following, we address the case where the normal region is made from a quantum dot.

An SEM image of the device discussed in this section is presented in Fig. 4.7. A InAs junction of width 150 nm is proximitized with an epitaxial Al shell which also serves as the contact electrode. The lateral local gate placed 100 nm away tunes the electrochemical potential of the bare nanowire. The source electrode is connected to one of the ends of a stub tuner and the drain to the ground plane. At negative gate

voltages, the nanowire is completely depleted. We characterize the resonance response of the stub tuner circuit in this regime and extract the two lengths $D_1 = 10.42$ mm and $D_2 = 10.24$ mm, effective dielectric constant $\epsilon_{\text{eff}} = 6.2$ and loss factor $\alpha = 0.065$ m $^{-1}$. Unfortunately, large α forces the circuit in the loss-dominated regime and more importantly reduces the collection efficiency of the noise signals. The electronic temperature of 50 mK is estimated from shot noise from a diffusive metallic wire, see section 7.1.1.

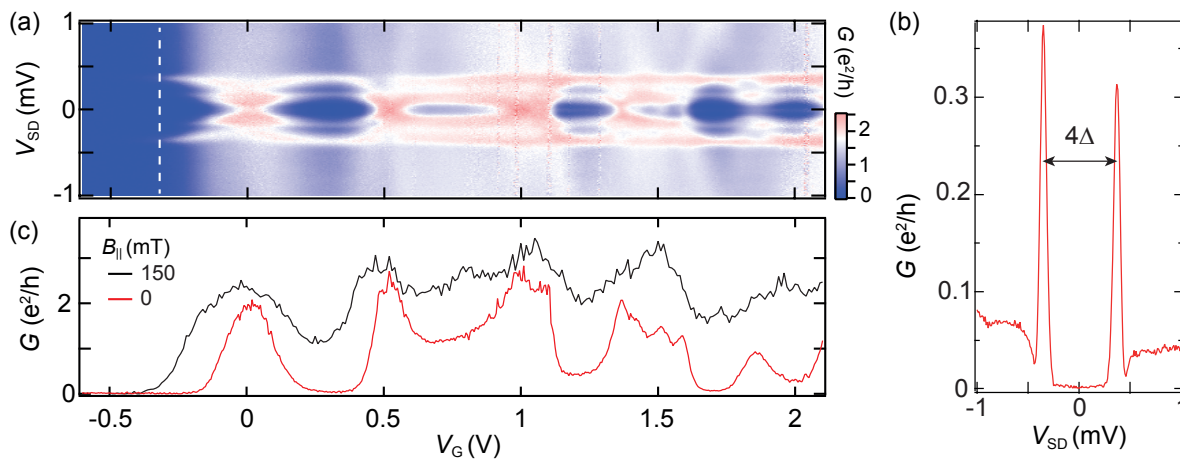


Figure 8.1. Andreev transport in a superconducting junction (a) Differential conductance of an Al-InAs-Al junction as a function of gate and bias voltages. The junction is depleted at negative gate voltages. At positive voltages, sub gap features resulting from high order quasiparticle transport can be seen. (b) A vertical cut of the conductance denoted by dashed line in the panel (a) shows a hard superconducting gap of $4\Delta \approx 0.72$ meV. (c) The zero bias conductance traces in the superconducting and the normal state of the leads.

To characterize the transport through the junction, the differential conductance G is inferred from the reflectance measurements (see section 5.2.1 for the extraction method). The corresponding color map is plotted in Fig. 8.1(a). At negative voltages, the nanowire is completely depleted. In this regime, the nanowire acts as a good tunnel barrier and the resulting conductance shown in Fig. 8.1(b) displays sharp quasiparticle peaks with a hard gap [102]. The superconducting gap Δ is found to be around 180 μeV , consistent with the bulk gap of aluminium. At first sight, the general behaviour of the color map at positive voltages is rather complex. There are fixed conductance ridges at $V_{\text{SD}} = \pm 2\Delta$ due to the singular quasiparticle density of states at the edge of the superconducting gap. In addition, there are ridges at $V_{\text{SD}} = \pm \Delta$ that bend, for example near gate voltages $V_{\text{G}} = [0, 0.5, 1, 1.3]$ V, but are otherwise constant in energy against gate voltages. The sub-gap conductance of a voltage biased junction arises from multiple Andreev reflection (MAR), as explained in Chapter 2. The zero bias conductance is shown in Fig. 8.1(c) for the superconducting and the normal state achieved by applying 100 mT of parallel magnetic field B_{\parallel} . Conductance values larger than $2e^2/h$ suggest that there is more than one sub-band occupied in the InAs nanowire. Moreover, there is a weak gate dependence for $|V_{\text{SD}}| > 2\Delta$.

The poor visibility of the Coulomb blockade in Fig. 8.1(a) and the large G values are due to the lead couplings Γ being comparable to the charging energy. Large Γ and

smaller charging energy however enhances the probability to observe MAR processes that are suppressed in the opposite limit [172]. This brings us to the near-resonant behaviour in Fig. 8.1(a), the bending of subharmonic G peaks at $\pm\Delta$ towards zero bias. A similar behaviour was observed in the references [55, 97] in an Al-CNT-Al system. It turns out that those MAR trajectories which connect the resonant dot-level to the superconducting leads' BCS spectral density can dramatically enhance the current. The enhanced conductance peaks thus arise when either the dot level stays aligned with the Fermi level of the leads or follows the gap edge as an initial or final state of the Andreev process [52, 53, 55]. In simple words, the dot level serves as a gate tunable transparency of the superconducting junction. Tuning of transparency has also been realized with atomic arrangements of Al break junctions where the subgap current becomes significant due to higher order MAR processes at increasing transmission and a conductance peak emerges at zero bias [54].

8.1.1. Shot noise results

Now we turn to the shot noise measurements and analyse the off-resonant case. In this low-transmission regime, the probability of n th-order MAR process is diminished by a factor τ^n . Especially, when $\tau \ll 1$, effective charge defined as $S_I/2eI$ becomes quantized [173, 174] due to coherent transfer of charges across the junction. At low transmission, however, the current and resulting noise become too small challenging the measurement sensitivity of the setup.

We focus on the $I - V$ characteristics near $V_G = 0.3$ V as shown in Fig. 8.2(a). To estimate the transmission and number of channels, we fit the non-linear curve using the complete MAR theory developed in reference [173]. Black curve is for single channel while the red curve assumes two channels. We find that two channel case fits the data better than the single channel case. However, the current is mostly carried by one channel ~ 41 % than the other ~ 5 %. Corresponding calibrated current spec-

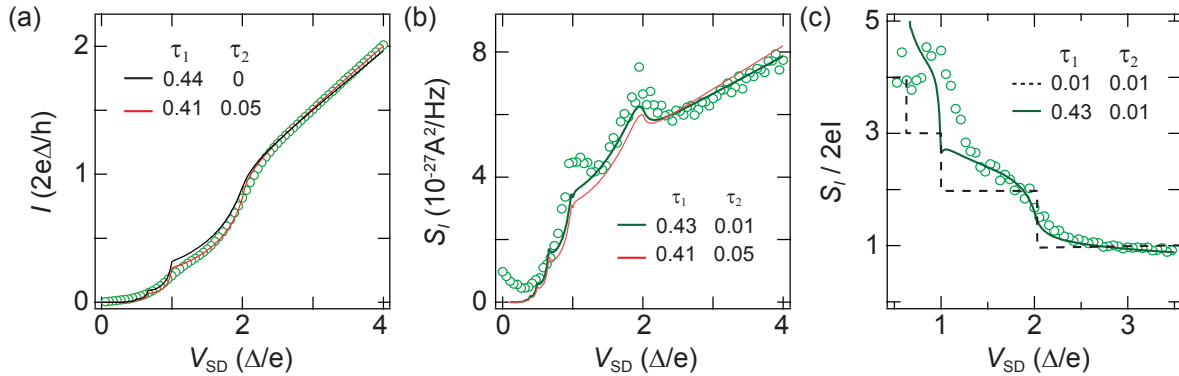


Figure 8.2. Multiple charge transfer (a) Non linear $I - V$ characteristics at $V_G = 0.3$ V obtained from the numerical integration of conductance. Solid lines are fits from the MAR theory [173] for single and double channel cases. (b) Corresponding calibrated noise and fits to MAR theory. (c) Increasing effective charge with reducing bias voltage. Note that the bias voltage axis is normalized by the superconducting gap $\Delta = 190$ μ eV which is deduced from the $I - V$ fit.

tral density is plotted in Fig. 8.2(b). The non-linearity in current is also evident in the noise curve. Solid lines are calculated theoretical curves and match the data well within 10% accuracy of the transmission values extracted from the $I - V$ plot. Finally, the effective charge plotted in Fig. 8.2(c) increases with decreasing bias voltage - a hallmark of *multiple Andreev reflections*. Dashed line corresponds to the expected staircase behaviour when $\tau \ll 1$. For rather large transmissions, as in our case, higher order MAR processes can interfere, thus washing out the staircase. The noise data at arbitrary transmission can nonetheless be compared to the theory [173] and is plotted as a solid line. The deviations from theory at low bias are probably due to the channel transmissions being energy dependent and uncertainties in the extracted amplifier gain and the superconducting gap.

8.1.2. Supercurrent: noisy or silent?

In addition to the non-equilibrium noise stemming from MAR, a finite equilibrium noise peak can be observed in Fig. 8.2(b) at zero bias voltage. While inelastic Andreev scattering may lead to partial reflection of electrons at small bias voltages $V_{SD} \ll \Delta$, the resulting classical shot noise is very small [175]. Moreover at exactly zero bias, barring the inherent fluctuations of the voltage sources, one would intuitively expect a coherent dissipation-less transfer of Cooper pairs across a weak-link, that is the supercurrent from the Josephson effect.

The presence of large equilibrium noise due to the supercurrent was addressed through Green's function calculations of a QPC junction in reference [176]. The microscopic theory treats supercurrent to be carried by subgap states, called Andreev bound states (ABS), which are localized in the point contact. For a single transverse channel, the energy of ABS branches for an arbitrary transmission τ is given by [57]

$$\pm E_A = \pm \Delta [1 - \tau \sin^2(\phi/2)]^{1/2}. \quad (8.1)$$

where ϕ is the superconducting phase difference of two electrodes. It was shown that the supercurrent noise arises from an interplay between quasiparticles and supercurrent coherence. In their formalism, the flow of DC supercurrent can be considered stochastic, that is, quasiparticle exchange between the leads and ABS cause the supercurrent to switch between two values. The resulting spectral density at low frequencies and small relaxation rates from the excited quasiparticle states to the ground state, is approximated by an intuitive Lorentzian [176]

$$S_I(\omega) = \frac{1}{2\pi} \left(\frac{I_S(\phi)}{\cosh(E_A/2k_B T)} \right)^2 \frac{\gamma}{\omega^2 + \gamma^2}, \quad (8.2)$$

where k_B is the Boltzmann constant, T the temperature, $I_S(\phi)$ the phase and transmission dependent supercurrent given as $I_S(\phi) = (e\Delta\tau/2\hbar) \sin(\phi)/[1 - \tau \sin^2(\phi/2)]^{1/2}$ and γ the rate of quasiparticle exchange. The latter is roughly proportional to the sub-gap density of states in the superconducting leads and should vanish for the ideal BCS case [177]. The equation shows that the noise can be quite large at zero frequency even at very low temperatures because of the decrease of γ . The theory was furthermore extended for finite bias voltages $V_{SD} \ll \Delta$ where the phase difference continuously evolves

$d\phi/dt = 2eV_{SD}/\hbar$ due to the AC Josephson effect. It was shown that S_I monotonically decreases with bias voltage and has $1/V$ dependence in the limit $eV_{SD} \gg \hbar\gamma$. The same has been experimentally confirmed in reference [178], though in a case of diffusive metallic weak link.

Unlike metallic weak links, we can study the supercurrent noise for different gate voltage settings near the quantum dot resonance. Three conductance traces are shown in Fig. 8.3(b) which are vertical cuts from the color map presented in the panel (a). Black and cyan curves are off-resonance cases showing a gap-like feature at zero bias. In contrast, the red curve is for the on-resonance case showing a conductance peak due to the large transmission. The corresponding noise is plotted in the panel (c). For a faithful calibration of zero-bias signals, we measure the amplifier background noise at a frequency different from the stub tuner resonance. When the QD is off-resonant, we see large noise peaks at zero bias reaching $2.5 \times 10^{-26} \text{ A}^2/\text{Hz}$ corresponding to a thermal noise temperature of 10 K for $G \sim e^2/h$. Moreover the full width at half maxima of the peaks is roughly 0.08 meV, corresponding to 19 GHz. The latter is much larger than both the linewidth of the stub tuner circuit ($\sim 3 \text{ MHz}$) and the resonance frequency itself (3 GHz). Thus, it is safe to say that we are not measuring any coherent AC Josephson emission [179, 180] from oscillating currents.

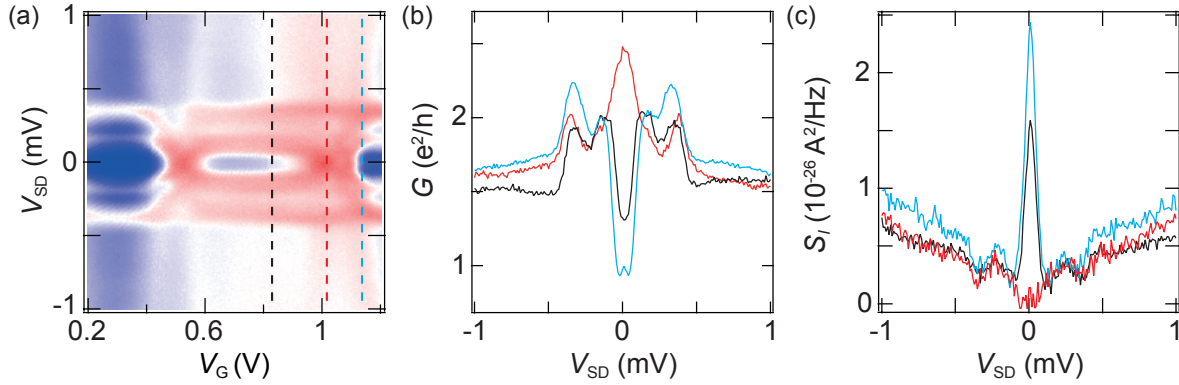


Figure 8.3. Noise near QD resonance (a) A zoom-in of the measured differential conductance presented in Fig. 8.1. (b) Vertical cuts of the conductance at three gate voltages denoted by dashed lines in panel (a). The red curve corresponds to the QD resonant case while the rest are for off-resonance scenarios. (c) The corresponding current spectral density plotted against the bias voltage. Large noise peaks are present at zero bias for the off-resonance cases, but absent for on-resonance case.

Surprisingly, the noise peak for the cyan curve is larger than that of the black curve in Fig. 8.3 despite the former having smaller G at $V_{SD} = 0$. But the most striking feature is for the on-resonance or the largest transmission case. The noise at zero bias completely disappears. We now investigate the noise response at other QD resonances. A color map of the noise power together with the corresponding G is plotted in Fig. 8.4(a). The QD resonances are marked with vertical dashed lines. We see again that the corresponding noise power near the QD resonances is suppressed at zero bias. This behaviour is more understandable in a shot noise regime at large transmission of a QPC. Since the observed equilibrium noise peaks are much larger in magnitude than the expected classical shot

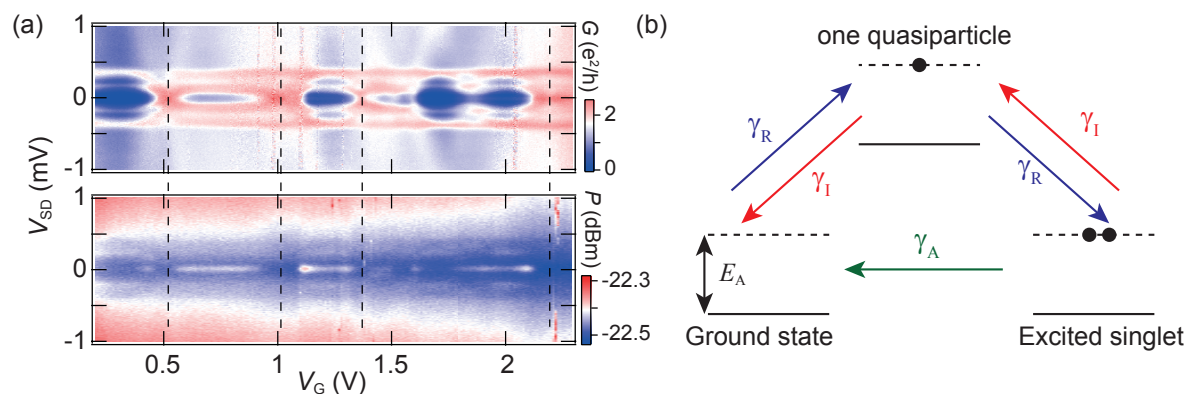


Figure 8.4. Periodic suppression and revival of equilibrium noise (a) Color maps of conductance and the corresponding noise power. Zero bias noise is suppressed at the voltages highlighted by the dashed lines while QD resonances are observed in the conductance plots. (b) Transitions between different ABS excitations due to quasiparticle exchange causing changes in their population and stochastic supercurrent. Symbols are explained in the text.

noise [175], a different phenomenon must play a part in its suppression. In the following section, we attempt to understand the observation in terms of quasiparticle relaxation.

8.1.3. Quasiparticle relaxation

Equation 8.2 is simple yet powerful enough to capture the noise stemming from thermalization of supercurrent between the quasiparticle excitations of the ABS. This two-level noise model however makes an important assumption that the quasiparticle relaxation rates are energy independent which in principle should be strongly dependent on the phononic and photonic environment [181]. To understand the dynamics of the quasiparticles, we review the processes affecting their population in the weak link, depicted in Fig. 8.4(b). The ABS is spin-degenerate and can host $n = 0, 1, 2$ quasiparticles. The resulting supercurrent is given by $I_S(1 - n)$, where $I_S = (2e/\hbar)(\partial E_A/\partial\phi)$. Thus, the supercurrent is zero when a single quasiparticle is trapped in the weak link and negative or exactly opposite to the one in ground state when doubly occupied.

Three principal processes can change their relative populations. An ionization process with a rate γ_I , excites the quasiparticles into the delocalized energy continuum $E > \Delta$ of the leads. The opposite process is the refill (γ_R), where a quasiparticle is re-trapped in the ABS. At sufficiently low temperature, the number of quasiparticles occupying the continuum is extremely small, suppressing γ_R . Another process involves breaking a Cooper pair into a quasiparticle and exciting the other one into the continuum. This is also slow. Lastly, a doubly excited singlet can be annihilated to reach the ground state with a relaxation rate γ_A .

All of the aforementioned rates are generally slow \sim kHz [181] and depend on the bound state energy E_A rather than the phase difference or the transmission across the junction. Several cases can be formulated depending of the relative rates. Generally γ_A is quite strong [182, 183] thus the excited singlet is rarely occupied. This means, that the ground state supercurrent stochastically drops to zero when one quasiparticle

is trapped. Again, if $\gamma_I \gg \gamma_R$, ABS is always emptied by the ionization. This situation was observed in the reference [184] where the relaxation of quasiparticles was shown to have two orders of larger magnitude for $E_A > 0.5\Delta$ due to a stronger ionization induced by an environmental photonic mode $hf_p \sim 0.5\Delta$ [181]. The photonic environment in our case is a stub tuner which is not driven for noise measurements and its operating frequency 3 GHz is much smaller than Δ/h . Even from higher harmonics of the stub resonance, a photon mode cannot explain the noise observed in Fig. 8.4(a). In contrast to reference [184], quasiparticles in our case seem to live longer in regimes that have low transmission or large bound state energy E_A .

We note that the previous works have been centred around phase biased junctions and at present none, to the best of our knowledge, addresses the relaxation mechanisms in voltage biased junctions. The latter is a challenging problem because of strongly correlated electrons in MAR. Moreover, the ABS can evolve adiabatically or undergo Landau-Zener transition at $\phi = \pi$ for a continuously evolving phase difference. Owing to such complications together with the environment, we have not been able to understand the noise suppression at QD resonance.

8.2. Kondo effect in QD with superconducting leads

We now turn to a second device where the quantum dot, in addition to coupling to superconducting leads, also exhibits the Kondo effect [185]. A competition in such a system arises because of the fact that the magnetic exchange of an unpaired electron on the QD needs to be screened by the leads to sustain Kondo correlations. Superconductors on the other hand have a spin-singlet ground state. In the following, we address such interplay through differential conductance and shot noise measurements.

The QD is formed in a carbon nanotube (CNT), and tuned by a side gate, as shown in Fig. 5.1. Source and drain contacts are made from Pd/Al (4.5 nm/70 nm) and separated by 300 nm. A side gate tunes the dot occupation. Integration of the niobium stub tuner circuit and CNT device is achieved using probabilistic CNT stamping. We first characterize the circuit by measuring a reflectance resonance in Coulomb blockade (Chapter 5). The fit extracts lengths $D_1 = 10.46$ mm and $D_2 = 10.26$ mm, effective dielectric constant $\epsilon_{\text{eff}} = 6$ and loss factor $\alpha = 0.054 \text{ m}^{-1}$. The latter corresponds to a quality factor Q of 1200. While it does not change up to a temperature of 1 K, this drops to 1000 at a parallel magnetic field $B_{\parallel} = 150$ mT. The stub tuner circuit with resonance frequency at 3 GHz also operates in the loss dominated regime.

The conductance response to sweeping source-drain voltage and a side gate voltage is shown in Fig. 8.5. Kondo ridges at zero bias for odd charge occupation are apparent. In addition, for the even dot occupation, a narrow strip of suppressed G due to the superconducting gap can also be seen. This goes away at $B_{\parallel} = 150$ mT confirming the destruction of the superconducting state. A vertical cut at $V_G = 3.3$ V is shown in the panel (b) estimating the gap Δ to be $125 \mu\text{eV}$, significantly smaller than the bulk gap of $180 \mu\text{eV}$. The latter is probably due to the wetting layer of Pd. Moreover, the superconducting gap is rather soft and no subgap MAR features are observed. Both observations are consistent with large lead couplings $\Gamma \sim 0.8 \text{ meV} \gg \Delta$ extracted from fits to Breit-Wigner function [45] of a Coulomb resonance at large negative voltages,

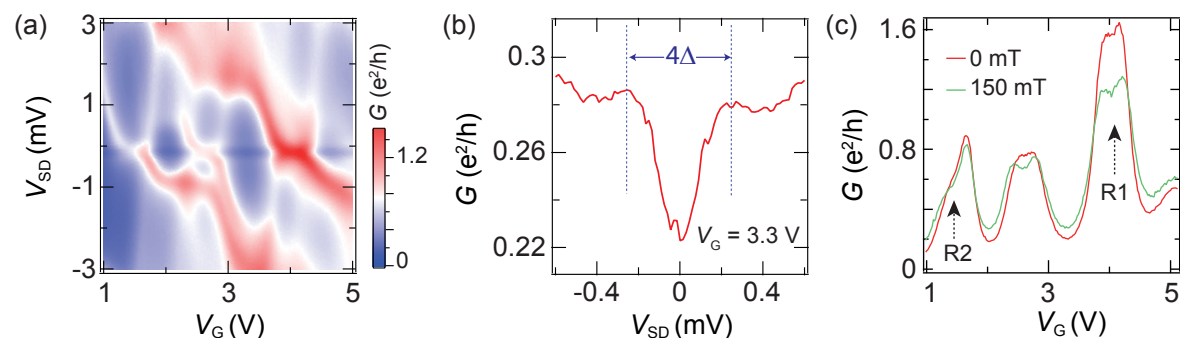


Figure 8.5. Kondo effect in QD with superconducting leads (a) Appearance of Kondo ridges for odd occupancy in absence of any magnetic field and at the base temperature. (b) A vertical cut in panel (a) at $V_G = 3.3$ V showing suppressed conductance due to the superconducting gap. (c) Zero bias conductance traces for two magnetic fields. Dashed arrows labelled R1 and R2 represent two Kondo ridges.

where the Kondo effect is absent and blockade is strong.

The fact that superconducting gap ridges do not appear for all dot occupations hints at strong Kondo correlations $k_B T_K \geq \Delta$ in the system, where T_K is the Kondo temperature. To isolate the influence of the superconducting leads on the Kondo resonances we compare the zero bias G with that from the normal state shown in Fig. 8.5(c). In particular, we find the Kondo ridge R1 to show enhancement in G from $1.2e^2/h$ up to $1.6e^2/h$. This suggests $k_B T_K$ being larger than Δ [98]. To confirm this we did two checks. A temperature dependence of the Kondo resonance (not shown) in the normal lead state shows the peak height to merely change from $1.2e^2/h$ at 20 mK to $1.1e^2/h$ at 1 K. We further fit a Lorentzian to the normal state Kondo resonance at 20 mK and extract the half-width at half-maxima of ~ 0.4 meV. In contrast for Kondo ridge R2, G does not increase or decrease in the superconducting state suggesting $\Delta \sim k_B T_K$.

8.2.1. Shot noise results

We focus on the ridge R1 for the noise measurements. Colour maps of conductance and noise power are shown in Fig 8.6(a,b). Unlike the device shown in the previous section, we do not see any hints of zero-bias noise neither in the resonant or the off-resonant cases. A likely cause could be the bad coherence of Cooper pairs in the longer junction ~ 300 nm. This is supported by the absence of any MAR peaks in both conductance and noise measurements. Unfortunately, the electronic temperature $T \sim 150$ mK is also found to be higher in this case¹. Nonetheless, the differences of the shot noise in comparison to the case when contact leads are normal can be interesting.

V_G is now fixed in the middle of the Kondo ridge R1 and traces of current I and noise power are simultaneously measured. Figure 8.6(c) shows I and respective G at two parallel magnetic fields of 0 mT and 150 mT. To separate the shot noise from the

¹We also observed DC currents near QD resonances at zero bias suggesting a hotter source than the drain contact. A new directional coupler and cryogenic terminators were installed in the setup later. The nanowire device was measured in the improved setup.

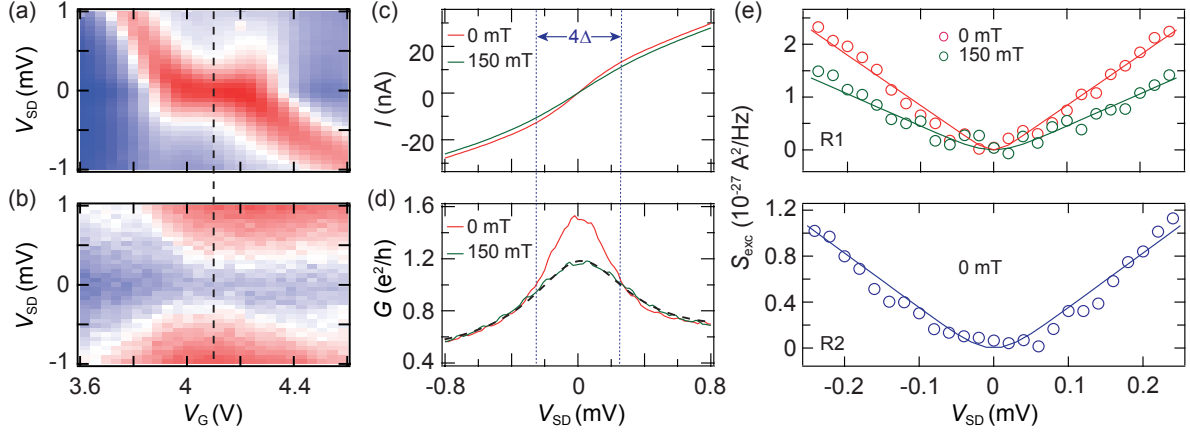


Figure 8.6. Shot noise in Kondo regime. (a) Differential conductance of Kondo ridge R1 and (b) corresponding raw noise power. Red and blue represent higher and lower magnitudes respectively. (c) Direct current and corresponding (d) differential conductance of a Kondo resonance at the gate voltage denoted by the dashed line in panel (a). G is enhanced only within the superconducting gap. (e) Calibrated excess noise S_{exc} for $-2\Delta < V_{SD} < 2\Delta$ for Kondo ridges R1 (top) and R2 (bottom). Solid lines are predictions using Eq. 8.4 assuming an electronic temperature of 150 mK.

thermal contributions, excess noise S_{exc} is further defined as

$$S_{exc} = S_I - 4k_B T_e G, \quad (8.3)$$

where S_I is the calibrated current noise density after subtracting the amplifier background noise. The calibrated S_{exc} for R1 at two field values are now plotted in Fig. 8.6(e) for $-2\Delta < eV_{SD} < 2\Delta$. A relatively large noise power is observed in the superconducting state compared to that of the normal case. Unfortunately, very few theoretical and experimental works have addressed shot noise in such regimes. A lone work in reference [186] suggests that for large T_K , the Kondo resonance effectively makes the junction behave like a highly transparent non-interacting weak link. Since G does not exceed G_Q in our measurements, we choose to perform an effective charge analysis where the shot noise for a single channel with transmission τ is given by

$$S_{exc} = 2e^* V_{SD} G_Q \tau (1 - \tau) [\coth(\nu) - 1/\nu], \quad (8.4)$$

where e^* is the effective charge and $\nu = e^* V_{SD} / 2k_B T_e$. In a small bias window, τ is assumed to be a constant given by $G(V_{SD} = 0) / G_Q$. We have also included the electronic temperature T_e and described the current as $I = V_{SD} G_Q \tau$. We note that the formalism is to only account for differences in the enhanced noise and does not claim coherent multiple charge transfer like in section 8.1.1. We plot such predictions as solid lines in Fig. 8.6(e). For the ridge R1 with leads in the superconducting state, $e^*/e = 2.2$ fits the data well while the effective charge drops to $e^*/e = 1$ in its normal state. For R2 excess noise can be well explained by $e^*/e = 1$. To summarize, Kondo resonances with $k_B T_K > \Delta$ are enhanced in both the conductance and in the shot noise [186].

Whether shot noise in the Kondo regime can be treated by a non-interacting picture has been a subject of debate [19]. Recently, in both theoretical [187, 188] and

experimental [189, 190] efforts, it has been argued that two-particle scattering can enhance the shot noise above the non-interacting case and has striking differences between different SU(N) symmetries. In particular, the Fano factor increases with decreasing temperature despite the fact that Kondo resonance becomes more transmissive. This motivates us to analyze the data also for the case where leads are normal i.e. bias voltages $e|V_{SD}| > 2\Delta$. We extract the lead couplings Γ_S and Γ_D using the Breit-Wigner formula for the SU(2) Kondo case in the normal state²

$$G = \frac{2e^2}{h} \frac{\Gamma_S \Gamma_D}{(eV_{SD})^2 + (\Gamma_S + \Gamma_D)^2/4}. \quad (8.5)$$

A fit for ridge R1 is shown by the dashed curve in Fig. 8.6(d) yielding $\Gamma_{S/D} = 0.8$ meV, $\Gamma_{D/S} = 0.08$ meV in the normal state. For a non-interacting case of a resonant state coupled to two tunnel barriers [19], the Fano factor is simply given as $F = (\Gamma_S^2 + \Gamma_D^2)/(\Gamma_S + \Gamma_D)^2 = 0.84$. For comparison, we extract $F = S_{\text{exc}}/2eI$ at $V_{SD} = \pm 1$ V to be 0.8, the same for both magnetic fields. The excellent comparison suggests that the non-interacting picture holds in the tails of the Kondo resonance. The small deviation can be attributed to uncertainty in amplifier gain.

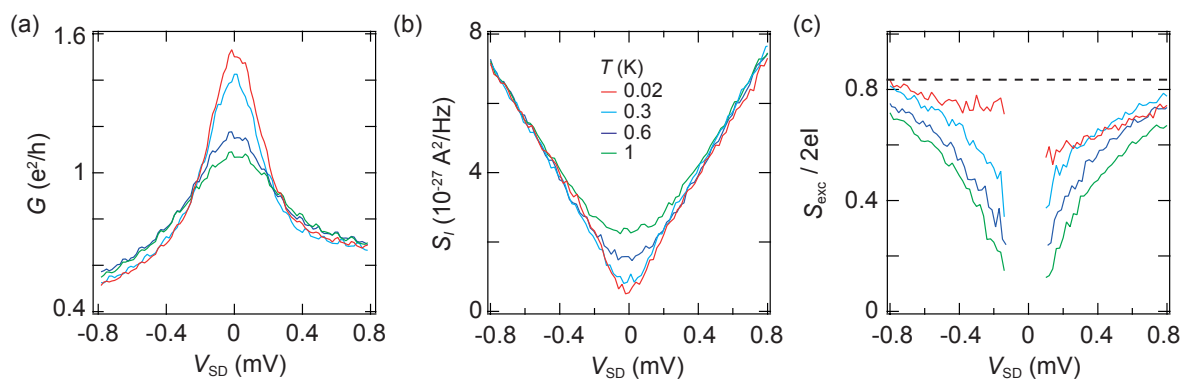


Figure 8.7. Temperature dependence of shot noise. (a) Differential conductance for different fridge temperatures for Kondo ridge R1. Wiggles are artefacts from the measurement setup. (b) Corresponding calibrated current noise. For small bias, crossover from shot noise to thermal noise can be seen. (c) Corresponding Fano factor $F = S_{\text{exc}}/2eI$. Dashed line is the value predicted from the non-interacting case.

To address the low bias regimes, we also study the temperature dependence of the Kondo ridge R1. Increasing the temperature not only causes the suppression of the superconducting properties but also of the Kondo correlations. G at different fridge temperatures is plotted in Fig. 8.7(a). A monotonic decline in G at zero bias for increasing T is observed. We further take current noise measurements as shown in Fig. 8.7(b). Especially at small bias, a clear crossover of shot-noise to thermal noise can be seen. We now plot the Fano factors in Fig. 8.7(c). While at high bias, F tends to the zero temperature non-interacting value of 0.84, it increases with decreasing temperature at lower bias, even for energies $e|V_{SD}| > 2\Delta$. It is safe to say that Kondo correlations are noisy even though a perfect transmission can be achieved in the electronic transport in quantum dots.

²Four-fold shell filling is not observed.

8.3. Summary and discussions

In summary, we have measured differential conductance and shot noise in quantum dots coupled to superconducting leads. In the first part, we observe crossovers of multiple charge transfers associated with multiple Andreev reflections. Specifically, thermal noise associated with supercurrent is found to be sensitive to the position of the QD level with respect to the leads i.e. the noise is much larger in off-resonant cases but gets suppressed on resonance. In the second part, we observe enhancement of the Kondo effect when the Kondo temperature is larger than the superconducting gap. The associated shot noise is also found to be larger due to larger effective charge transfer despite the increasing transmission.

The shot-noise response in S-QD-S systems is clearly interesting, though a complete understanding of underlying physics requires more work. A good follow-up device would be one where junctions are phase biased and inductively coupled to the microwave resonator near its low impedance end. A frequency dependence of the noise is also desirable, though it is a subject to wideband detection. Especially for Kondo interactions, quantitative dependence of enhanced noise against T_K and lead symmetry can be useful, which could not be done in our device due to device limitations. The presented results are of great importance in establishing the quasiparticle dynamics in superconducting junctions at different environmental conditions.

9 Summary and outlook

This thesis aimed at developing a gigahertz impedance matching circuit to perform sensitive measurements of admittance and shot noise in high impedance devices. For this purpose, a stub tuner based on transmission lines was designed, fabricated and integrated with mesoscopic devices. Owing to the simple design, we could predict the frequency response of a stub tuner in terms of the standard circuit model. We initiated certain necessary fabrication adaptations to achieve integration of niobium circuits with devices. In particular, a reliable stamping of carbon nanotubes from the growth substrate to the target substrate was accomplished, improving both the device quality and yield. All along, a dedicated setup for simultaneous DC and RF measurements was built and constantly improved. Below we review the main results of the thesis.

Impedance matching in quantum dots Reflectance measurements of quantum dots formed in carbon nanotubes were presented. We showed that the matched value is simply dependent on the length difference and microwave losses of the transmission lines. All stub tuner parameters could be reliably extracted and utilized to deduce differential conductance from the reflected signals. In particular, the circuit allows the measurement bandwidth to extend to a few MHz even at the impedance value of $\sim M\Omega$. Typically for low frequency DC measurements it is of the order of $\sim \text{kHz}$. In another experiment, double quantum dots were tunnel coupled to create charge qubits. The reflectance in such systems unlocked signals which could not be observed in DC measurements. Using the phase response of the circuit, qubit energy and dephasing rates were extracted. We found an increase in the dephasing rate at decreasing qubit frequencies, probably due to the residual $1/f$ charge noise in the environment.

Quantum capacitance of graphene We extended the measurement principle of the stub tuner to graphene devices where we eliminated any contact electrodes. We showed that the microwave response could provide quantitative information about the equilibrium density of states as well as internal scattering mechanisms of p-n junctions. In particular, residual doping was shown to affect not only the mean free path but also the Fermi velocity. We saw that at small doping $\sim 10^9 \text{ cm}^{-2}$ electron-electron interactions could modify the Fermi velocity and that the dispersion relation could deviate from linearity.

Shot noise of quantum dots The main advantage of the stub tuner was tested in the noise measurements of highly resistive quantum dots. We showed a simple quantitative calibration of raw noise power through a circuit model. The large bandwidth and signal to noise ratio (SNR) enabled us to measure extremely clean noise power densities at

high speed and draw comparisons with the corresponding average current. We introduced a figure of merit g_{SNR} , a ratio between the SNR for matching and no matching, and found it to be as high as 200 at a resistance of 150 k Ω . Besides, clear changes in the noise spectrum were seen when a transport channel was added or removed from the bias window. In particular, we observed noise enhancement outside the Coulomb diamonds due to blocking states. The explanations of noise enhancement were backed up by the theoretical framework of full counting statistics where slow relaxation of excited dot states was shown to play the key role.

Shot noise of Andreev processes We investigated noise properties of quantum dots when leads are superconducting. In the limit of large tunnel coupling, noise measurements were performed in both the blockade and at the dot resonance. Distinct charge transfers due to multiple Andreev reflections were visible in the shot noise. The main finding, however, was the thermal noise at zero bias. We observed its periodic suppression and emergence across the quantum dot resonance. The microscopic mechanism is not yet understood. In another device, shot noise due to the Kondo effect was found to be enhanced in the superconducting state when the Kondo temperature exceeds the value of the superconducting gap.

9.1. Future directions

Further improvements are sought after in the performance of the stub tuner circuit. An in-situ tuning of frequency could be useful in achieving matching at a range of impedances rather than at a fixed value. This can be achieved, for example, with SQUIDs. The latter also provide an opportunity to integrate a quantum limited parametric amplifier [191] on a chip. Moreover, high magnetic field operation of the circuit is not possible because of niobium substrates. To this end, fabrication and characterization of copper resonators [146], at the expense of relatively large microwave losses, are currently being pursued in our group. This will enable microwave detection of spin related phenomena and quantum Hall effect.

To achieve larger measurement bandwidths to enable faster detection than that by the stub tuner, the development of LC circuits is also in progress. The main challenge is to understand and mitigate the sources of parasitic capacitances. Even so, performance of the stub tuner detection can already be improved by installing a cryogenic HEMT amplifier with a much lower noise temperature. At the moment, it is ~ 5 K at 3 GHz. If one could reduce it to 1 K the averaging time could be easily reduced by a factor of 5. Moreover, replacing the HEMT with a quantum limited parametric amplifier on chip can lead to a tremendous improvement of the background noise.

9.1.1. Admittance measurements

The thesis presents proof of principle experiments to demonstrate high sensitivity of RF admittance measurements in quantum dots. A quantity not addressed in this thesis is the kinetic inductance of the CNT or nanowires, important in the context of a collective plasmonic excitation. One-dimensional carriers, in contrast to those in metallic wires,

have a much lower density, yielding a large kinetic energy stored in the current flow. Though this effect will co-exist with quantum capacitance, it can be easily separated since the resulting frequency shifts of the microwave resonance will be positive for inductive, and negative for capacitive, loads.

Especially with graphene devices, we showed that there is no need for source/drain electrodes and that all relevant quantities such as conductance and density of states can be inferred from the resonance response. This ability can be used to probe the spin physics in graphene where the spin-life times have been predicted to be quite long [192], but are generally reduced by several orders of magnitude due to the contacts [129]. Moreover, band structure modifications due to ad-atoms, induced spin orbit couplings and super-lattice effects can be investigated without any invasion from the contacts.

Measurements without source/drain contacts can be further useful for probing an Andreev molecule [193] in a Cooper pair splitting geometry [14], where coupling to normal leads needs to be very small. In this case, the split Cooper pairs on two quantum dots can hybridize due to its exchange with the superconductor, leading to a novel two-level transition. A good material candidate is a strongly proximitized InAs nanowire with epitaxial Al shell [99], which was also employed in Chapter 8. In absence of DC currents, RF measurements can still probe the charge fluctuations on the dots.

9.1.2. Noise measurements

We demonstrated the potential of a GHz impedance matching circuit in the shot noise detection of highly resistive quantum dots. The sensitivity of the circuit can be utilized in studies of other high impedance systems which have remained unexplored so far. One example is the resonant two particle tunnelling and inelastic Andreev tunnelling in S-QD-N systems [194]. Shot noise measurements in these regimes can provide more information on scattering and relaxation mechanisms and highlight the differences between sub-gap resonant and inelastic transport. Moreover, large bandwidths can be exploited to perform full counting statistics of the charge transport.

Another possible direction could be to continue the efforts of Chapter 8 to study the role of strongly coupled quantum dot resonance in the supercurrent noise. For this purpose, a new device geometry is needed where Josephson junctions from InAs nanowires are phase biased and inductively coupled to a microwave resonator. The fixed phase bias could shed more light into the quasiparticle relaxation. Especially with a fast-flux line, a control over adiabatic phase evolution and Landau-Zener transitions between the Andreev bound states can be implemented.

Phase biased Josephson junctions from InAs nanowires can be, furthermore, employed to realize topological Majorana bound states (MBS) on which noise studies are still lacking. Such studies could benefit from the fact that current phase relationship in the trivial regime is 2π periodic while it is 4π periodic in the topological regime [195]. If the SQUID is, therefore, biased at a phase difference $\Delta\phi = \pi$, noise will be zero for the trivial junction for any transmission $\tau < 1$, while it should remain large for the topological case. So far only zero-bias conductance peaks [16] have been attributed to the emergence of the MBS and therefore independent noise studies could constitute the next validation. Needless to mention, such studies involving superconductors will be subject to the dynamics of quasiparticles.

Bibliography

- [1] Y. V. Nazarov and Y. Blanter, *Quantum Transport* (Cambridge university press, New York, 2009).
- [2] P. W. Anderson, E. Abrahams, and T. V. Ramakrishnan, *Phys. Rev. Lett.* **43**, 718 (1979).
- [3] R. A. Webb, S. Washburn, C. P. Umbach, and R. B. Laibowitz, *Phys. Rev. Lett.* **54**, 2696 (1985).
- [4] P. A. Lee and A. D. Stone, *Phys. Rev. Lett.* **55**, 1622 (1985).
- [5] B. J. van Wees, H. van Houten, C. W. J. Beenakker, J. G. Williamson, L. P. Kouwenhoven, D. van der Marel, and C. T. Foxon, *Phys. Rev. Lett.* **60**, 848 (1988).
- [6] L. P. Kouwenhoven, D. G. Austing, and S. Tarucha, *Reports on Progress in Physics* **64**, 701 (2001).
- [7] L. P. Kouwenhoven, T. H. Oosterkamp, M. W. S. Danoesastro, M. Eto, D. G. Austing, T. Honda, and S. Tarucha, *Science* **278**, 1788 (1997).
- [8] R. C. Ashoori, H. L. Stormer, J. S. Weiner, L. N. Pfeiffer, K. W. Baldwin, and K. W. West, *Phys. Rev. Lett.* **71**, 613 (1993).
- [9] K. Ono, D. G. Austing, Y. Tokura, and S. Tarucha, *Science* **297**, 1313 (2002).
- [10] D. Goldhaber-Gordon, H. Shtrikman, D. Mahalu, D. Abusch-Magder, U. Meirav, and M. A. Kastner, *Nature* **391**, 156 (1998).
- [11] F. Pei, E. A. Laird, G. A. Steele, and L. P. Kouwenhoven, *Nat Nano* **7**, 630 (2012).
- [12] E. A. Laird, F. Pei, and L. P. Kouwenhoven, *Nat Nano* **8**, 565 (2013).
- [13] J.-D. Pillet, C. H. L. Quay, P. Morfin, C. Bena, A. L. Yeyati, and P. Joyez, *Nat Phys* **6**, 965 (2010).
- [14] L. Hofstetter, S. Csonka, J. Nygård, and C. Schönenberger, *Nature* **461**, 960 (2009).
- [15] L. G. Herrmann, F. Portier, P. Roche, A. L. Yeyati, T. Kontos, and C. Strunk, *Phys. Rev. Lett.* **104**, 026801 (2010).
- [16] V. Mourik, K. Zuo, S. M. Frolov, S. R. Plissard, E. P. A. M. Bakkers, and L. P. Kouwenhoven, *Science* **336**, 1003 (2012).
- [17] M. T. Deng, S. Vaitiekėnas, E. B. Hansen, J. Danon, M. Leijnse, K. Flensberg, J. Nygård, P. Krogstrup, and C. M. Marcus, *Science* **354**, 1557 (2016).

- [18] D. Loss and D. P. DiVincenzo, *Phys. Rev. A* **57**, 120 (1998).
- [19] Y. Blanter and M. Büttiker, *Physics Reports* **336**, 1 (2000).
- [20] J. B. Johnson, *Phys. Rev.* **32**, 97 (1928).
- [21] H. Nyquist, *Phys. Rev.* **32**, 110 (1928).
- [22] W. Schottky, *Annalen der Physik* **362**, 541 (1918).
- [23] F. Lefloch, C. Hoffmann, M. Sanquer, and D. Quirion, *Phys. Rev. Lett.* **90**, 067002 (2003).
- [24] L. Saminadayar, D. C. Glatthli, Y. Jin, and B. Etienne, *Phys. Rev. Lett.* **79**, 2526 (1997).
- [25] R. de Picciotto, M. Reznikov, M. Heiblum, V. Umansky, G. Bunin, and D. Mahalu, *Nature* **389**, 162 (1997).
- [26] C. Beenakker and C. Schönberger, *Physics Today* **56**, 37 (2003).
- [27] Y. Xu, C. Chen, V. V. Deshpande, F. A. DiRenno, A. Gondarenko, D. B. Heinz, S. Liu, P. Kim, and J. Hone, *Applied Physics Letters* **97**, 243111 (2010).
- [28] T. S. Abhilash, J. P. Mathew, S. Sengupta, M. R. Gokhale, A. Bhattacharya, and M. M. Deshmukh, *Nano Letters*, *Nano Lett.* **12**, 6432 (2012).
- [29] R. J. Schoelkopf, P. Wahlgren, A. A. Kozhevnikov, P. Delsing, and D. E. Prober, *Science* **280**, 1238 (1998).
- [30] H. Qin and D. A. Williams, *Applied Physics Letters* **88**, 203506 (2006).
- [31] M. C. Cassidy, A. S. Dzurak, R. G. Clark, K. D. Petersson, I. Farrer, D. A. Ritchie, and C. G. Smith, *Applied Physics Letters* **91**, 222104 (2007).
- [32] D. J. Reilly, C. M. Marcus, M. P. Hanson, and A. C. Gossard, *Applied Physics Letters* **91**, 162101 (2007).
- [33] C. Barthel, M. Kjaergaard, J. Medford, M. Stopa, C. M. Marcus, M. P. Hanson, and A. C. Gossard, *Phys. Rev. B* **81**, 161308 (2010).
- [34] N. E. Flowers-Jacobs, D. R. Schmidt, and K. W. Lehnert, *Phys. Rev. Lett.* **98**, 096804 (2007).
- [35] D. Bozyigit, C. Lang, L. Steffen, J. M. Fink, C. Eichler, M. Baur, R. Bianchetti, P. J. Leek, S. Filipp, M. P. da Silva, A. Blais, and A. Wallraff, *Nat Phys* **7**, 154 (2011).
- [36] M. A. Castellanos-Beltran and K. W. Lehnert, *Applied Physics Letters* **91**, 083509 (2007).
- [37] A. H. Castro Neto, F. Guinea, N. M. R. Peres, K. S. Novoselov, and A. K. Geim, *Rev. Mod. Phys.* **81**, 109 (2009).
- [38] E. A. Laird, F. Kuemmeth, G. A. Steele, K. Grove-Rasmussen, J. Nygård, K. Flensberg, and L. P. Kouwenhoven, *Rev. Mod. Phys.* **87**, 703 (2014).

-
- [39] C. Zhou, J. Kong, and H. Dai, *Phys. Rev. Lett.* **84**, 5604 (2000).
- [40] V. V. Deshpande, B. Chandra, R. Caldwell, D. S. Novikov, J. Hone, and M. Bockrath, *Science* **323**, 106 (2009).
- [41] R. Wagner and W. Ellis, *Appl. Phys. Lett.* (1964).
- [42] S. Dayeh, D. P. Aplin, X. Zhou, P. K. Yu, E. Yu, and D. Wang, *Small* **3**, 326 (2007).
- [43] C. Blömers, *Electronic Transport in Narrow-Gap Semiconductor Nanowires*, Ph.D. thesis, RWTH Aachen University (2012).
- [44] T. Ihn, *Semiconductor Nanostructures: Quantum states and electronic transport* (Oxford University Press Inc., New York, 2010).
- [45] C. W. J. Beenakker, *Phys. Rev. B* **44**, 1646 (1991).
- [46] J. O. Schindele, *Observation of Cooper Pair Splitting and Andreev Bound States in Carbon Nanotubes*, Ph.D. thesis, University of Basel (2014).
- [47] W. G. van der Wiel, S. De Franceschi, J. M. Elzerman, T. Fujisawa, S. Tarucha, and L. P. Kouwenhoven, *Rev. Mod. Phys.* **75**, 1 (2002).
- [48] S. J. Chorley, J. Wabnig, Z. V. Penfold-Fitch, K. D. Petersson, J. Frake, C. G. Smith, and M. R. Buitelaar, *Phys. Rev. Lett.* **108**, 036802 (2012).
- [49] T. Frey, P. J. Leek, M. Beck, J. Faist, A. Wallraff, K. Ensslin, T. Ihn, and M. Büttiker, *Phys. Rev. B* **86**, 115303 (2012).
- [50] A. Martin-Rodero and A. Levy Yeyati, *Advances in Physics* **60**, 899 (2011).
- [51] M. Tinkham, *Introduction to Superconductivity*, 2nd ed., Dover Books on Physics (Dover Publications, 2004).
- [52] A. L. Yeyati, J. C. Cuevas, A. López-Dávalos, and A. Martín-Rodero, *Phys. Rev. B* **55**, R6137 (1997).
- [53] G. Johansson, E. N. Bratus, V. S. Shumeiko, and G. Wendin, *Phys. Rev. B* **60**, 1382 (1999).
- [54] E. Scheer, P. Joyez, D. Esteve, C. Urbina, and M. H. Devoret, *Phys. Rev. Lett.* **78**, 3535 (1997).
- [55] M. R. Buitelaar, W. Belzig, T. Nussbaumer, B. Babić, C. Bruder, and C. Schönberger, *Phys. Rev. Lett.* **91**, 057005 (2003).
- [56] T. Heikkilä, *The physics of nanoelectronic*, Oxford master series in condensed matter physics (Oxford University Press Inc., 2013).
- [57] M. F. Goffman, R. Cron, A. Levy Yeyati, P. Joyez, M. H. Devoret, D. Esteve, and C. Urbina, *Phys. Rev. Lett.* **85**, 170 (2000).
- [58] C. W. J. Beenakker and H. van Houten, “Resonant josephson current through a quantum dot,” in *Single-Electron Tunneling and Mesoscopic Devices* (Springer Berlin Heidelberg, Berlin, Heidelberg, 1992) pp. 175–179.

- [59] J. Gramich, A. Baumgartner, and C. Schönenberger, *Phys. Rev. Lett.* **115**, 216801 (2015).
- [60] J. A. van Dam, Y. V. Nazarov, E. P. A. M. Bakkers, S. De Franceschi, and L. P. Kouwenhoven, *Nature* **442**, 667 (2006).
- [61] N. E. Bickers, *Rev. Mod. Phys.* **59**, 845 (1987).
- [62] R. Delagarange, *Josephson effect and high frequency emission in a carbon nanotube in the Kondo regime*, Ph.D. thesis, University Paris, Saclay (2016).
- [63] R. J. Schoelkopf, P. J. Burke, A. A. Kozhevnikov, D. E. Prober, and M. J. Rooks, *Phys. Rev. Lett.* **78**, 3370 (1997).
- [64] H. B. Callen and T. A. Welton, *Phys. Rev.* **83**, 34 (1951).
- [65] M. Reznikov, M. Heiblum, H. Shtrikman, and D. Mahalu, *Phys. Rev. Lett.* **75**, 3340 (1995).
- [66] A. Kumar, L. Saminadayar, D. C. Glattli, Y. Jin, and B. Etienne, *Phys. Rev. Lett.* **76**, 2778 (1996).
- [67] G. Burkard, D. Loss, and E. V. Sukhorukov, *Phys. Rev. B* **61**, R16303 (2000).
- [68] A. H. Steinbach, J. M. Martinis, and M. H. Devoret, *Phys. Rev. Lett.* **76**, 3806 (1996).
- [69] M. Henny, S. Oberholzer, C. Strunk, and C. Schönenberger, *Phys. Rev. B* **59**, 2871 (1999).
- [70] S. Oberholzer, E. V. Sukhorukov, and C. Schönenberger, *Nature* **415**, 765 (2002).
- [71] F. N. Hooge, *IEEE Transactions on Electron Devices* **41**, 1926 (1994).
- [72] D. M. Pozar, *Microwave Engineering*, 3rd ed. (John Wiley & Sons Inc., New York, 2005).
- [73] G. Puebla-Hellmann and A. Wallraff, *Applied Physics Letters* **101**, 053108 (2012).
- [74] S. Hellmüller, M. Pikulski, T. Müller, B. Küng, G. Puebla-Hellmann, A. Wallraff, M. Beck, K. Ensslin, and T. Ihn, *Applied Physics Letters* **101**, 042112 (2012).
- [75] R. Simons, *Coplanar Waveguide Circuits, Components, and Systems* (John Wiley & Sons Inc., New York, 2001).
- [76] I. Wolff, *Coplanar microwave integrated circuits* (John Wiley & Sons Inc., New Jersey, 2006).
- [77] K. Watanabe, K. Yoshida, T. Aoki, and S. Kohjiro, *Japanese Journal of Applied Physics* **33**, 5708 (1994).
- [78] R. Barends, *Photon-detecting superconducting resonators*, Ph.D. thesis, Technische Universiteit Delft (2009).

-
- [79] A. D. O’Connell, M. Ansmann, R. C. Bialczak, M. Hofheinz, N. Katz, E. Lucero, C. McKenney, M. Neeley, H. Wang, E. M. Weig, A. N. Cleland, and J. M. Martinis, *Applied Physics Letters* **92**, 112903 (2008).
- [80] M. Göppl, A. Fragner, M. Baur, R. Bianchetti, S. Filipp, J. M. Fink, P. J. Leek, G. Puebla, L. Steffen, and A. Wallraff, *Journal of Applied Physics* **104**, 113904 (2008).
- [81] V. Singh, B. H. Schneider, S. J. Bosman, E. P. J. Merks, and G. A. Steele, *Applied Physics Letters* **105**, 222601 (2014).
- [82] M. Wolfmeyer and J. Dillinger, *Phys. Lett. A* **34**, 247 (1971).
- [83] J. Goetz, F. Deppe, M. Haerberlein, F. Wulschner, C. W. Zollitsch, S. Meier, M. Fischer, P. Eder, E. Xie, K. G. Fedorov, E. P. Menzel, A. Marx, and R. Gross, *Journal of Applied Physics* **119**, 015304 (2016).
- [84] V. Ranjan, G. de Lange, R. Schutjens, T. Debelhoir, J. P. Groen, D. Szombati, D. J. Thoen, T. M. Klapwijk, R. Hanson, and L. DiCarlo, *Phys. Rev. Lett.* **110**, 067004 (2013).
- [85] A. Bruno, G. de Lange, S. Asaad, K. L. van der Enden, N. K. Langford, and L. DiCarlo, *Applied Physics Letters* **106**, 182601 (2015).
- [86] V. Singh, S. J. Bosman, B. H. Schneider, Y. M. Blanter, A. Castellanos-Gomez, and G. A. Steele, *Nat Nano* **9**, 820 (2014).
- [87] T. Hasler, *Microwave noise detection of a quantum dot with a stub impedance matching*, Ph.D. thesis, University of Basel (2016).
- [88] J. Cao, Q. Wang, and H. Dai, *Nat Mater* **4**, 745 (2005).
- [89] M. Muoth and C. Hierold, 2012 IEEE 26th International Conference on Micro Electro Mechanical Systems (MEMS) , 1352 (2012).
- [90] J. J. Viñnot, J. Palomo, and T. Kontos, *Applied Physics Letters* **104**, 113108 (2014).
- [91] H. Zou, *Microsystem Technologies* **10**, 603 (2004).
- [92] M. Muoth, T. Helbling, L. Durrer, S.-W. Lee, C. Roman, and C. Hierold, *Nat Nano* **5**, 589 (2010).
- [93] J. Waissman, M. Honig, S. Pecker, A. Benyamini, A. Hamo, and S. Ilani, *Nat. Nanotechnol.* **8**, 569 (2013).
- [94] J. Gramich, *Andreev and spin transport in carbon nanotube quantum dot hybrid devices*, Ph.D. thesis, University of Basel (2016).
- [95] B. Babić, J. Furer, M. Iqbal, and C. Schönenberger, *AIP Conference Proceedings* **723**, 574 (2004).
- [96] W. Mönch, *Reports on Progress in Physics* **53**, 221 (1990).
- [97] A. Eichler, M. Weiss, S. Oberholzer, C. Schönenberger, A. Levy Yeyati, J. C. Cuevas, and A. Martín-Rodero, *Phys. Rev. Lett.* **99**, 126602 (2007).

- [98] M. R. Buitelaar, T. Nussbaumer, and C. Schönenberger, *Phys. Rev. Lett.* **89**, 256801 (2002).
- [99] P. Krogstrup, N. L. B. Ziino, W. Chang, S. M. Albrecht, M. H. Madsen, E. Johnson, J. Nygård, C. Marcus, and T. S. Jespersen, *Nat Mater* **14**, 400 (2015).
- [100] P. Krogstrup, J. Yamasaki, C. B. Sørensen, E. Johnson, J. B. Wagner, R. Pennington, M. Aagesen, N. Tanaka, and J. Nygård, *Nano Letters*, *Nano Lett.* **9**, 3689 (2009).
- [101] T. W. Larsen, K. D. Petersson, F. Kuemmeth, T. S. Jespersen, P. Krogstrup, J. Nygård, and C. M. Marcus, *Phys. Rev. Lett.* **115**, 127001 (2015).
- [102] W. Chang, S. M. Albrecht, T. S. Jespersen, F. Kuemmeth, P. Krogstrup, J. Nygård, and C. Marcus, *Nat Nano* **10**, 232 (2015).
- [103] L. Wang, I. Meric, P. Y. Huang, Q. Gao, Y. Gao, H. Tran, T. Taniguchi, K. Watanabe, L. M. Campos, D. A. Muller, J. Guo, P. Kim, J. Hone, K. L. Shepard, and C. R. Dean, *Science* **342**, 614 (2013).
- [104] P. J. Zomer, M. H. D. Guimares, J. C. Brant, N. Tombros, and B. J. van Wees, *Applied Physics Letters* **105**, 013101 (2014).
- [105] C. P. Scheller, S. Heizmann, K. Bedner, D. Giss, M. Meschke, D. M. Zumbühl, J. D. Zimmerman, and A. C. Gossard, *Applied Physics Letters* **104**, 211106 (2014).
- [106] J. P. Pekola, K. P. Hirvi, J. P. Kauppinen, and M. A. Paalanen, *Phys. Rev. Lett.* **73**, 2903 (1994).
- [107] F. Kuemmeth, S. Ilani, D. C. Ralph, and P. L. McEuen, *Nature* **452**, 448 (2008).
- [108] A. Benyamini, A. Hamo, S. V. Kusminskiy, F. von Oppen, and S. Ilani, *Nat Phys* **10**, 151 (2014).
- [109] A. K. Huttel, G. A. Steele, B. Witkamp, M. Poot, L. P. Kouwenhoven, and H. S. J. van der Zant, *Nano Letters* **9**, 2547 (2009).
- [110] M. Jung, J. Schindele, S. Nau, M. Weiss, A. Baumgartner, and C. Schönenberger, *Nano Letters* **13**, 4522 (2013).
- [111] M. R. Delbecq, V. Schmitt, F. D. Parmentier, N. Roch, J. J. Viennot, G. Fève, B. Huard, C. Mora, A. Cottet, and T. Kontos, *Phys. Rev. Lett.* **107**, 256804 (2011).
- [112] T. Frey, P. J. Leek, M. Beck, A. Blais, T. Ihn, K. Ensslin, and A. Wallraff, *Phys. Rev. Lett.* **108**, 046807 (2012).
- [113] M. Delbecq, L. Bruhat, J. Viennot, S. Datta, A. Cottet, and T. Kontos, *Nat Commun* **4**, 1400 (2013).
- [114] J. J. Viennot, M. R. Delbecq, M. C. Dartiailh, A. Cottet, and T. Kontos, *Phys. Rev. B* **89**, 165404 (2014).
- [115] S. Ilani, L. A. K. Donev, M. Kindermann, and P. L. McEuen, *Nat. Phys.* **2**, 687 (2006).

-
- [116] L. P. Kouwenhoven, A. T. Johnson, N. C. van der Vaart, C. J. P. M. Harmans, and C. T. Foxon, *Phys. Rev. Lett.* **67**, 1626 (1991).
- [117] M. Büttiker, H. Thomas, and A. Prêtre, *Phys. Lett. A* **180**, 364 (1993).
- [118] J. Gabelli, G. Fève, J.-M. Berroir, B. Plaçais, A. Cavanna, B. Etienne, Y. Jin, and D. C. Glattli, *Science* **313**, 499 (2006).
- [119] J. Stehlik, Y.-Y. Liu, C. M. Quintana, C. Eichler, T. R. Hartke, and J. R. Petta, *Phys. Rev. Applied* **4**, 014018 (2015).
- [120] J. Basset, D.-D. Jarausch, A. Stockklauser, T. Frey, C. Reichl, W. Wegscheider, T. M. Ihn, K. Ensslin, and A. Wallraff, *Phys. Rev. B* **88**, 125312 (2013).
- [121] K. D. Petersson, J. R. Petta, H. Lu, and A. Gossard, *Phys. Rev. Lett.* **105**, 246804 (2010).
- [122] L. E. Bruhat, T. Cubaynes, J. Viennot, M. C. Dartiailh, M. Desjardins, A. Cottet, and T. Kontos, *arXiv:1612.05214* (2016).
- [123] J. Koch, T. M. Yu, J. Gambetta, A. A. Houck, D. I. Schuster, J. Majer, A. Blais, M. H. Devoret, S. M. Girvin, and R. J. Schoelkopf, *Phys. Rev. A* **76**, 042319 (2007).
- [124] S. Das Sarma, S. Adam, E. H. Hwang, and E. Rossi, *Rev. Mod. Phys.* **83**, 407 (2011).
- [125] G. Giovannetti, P. A. Khomyakov, G. Brocks, V. M. Karpan, J. van den Brink, and P. J. Kelly, *Phys. Rev. Lett.* **101**, 026803 (2008).
- [126] A. La Magna and I. Deretzis, *Nanoscale Research Letters* **6**, 234 (2011).
- [127] J. A. Robinson, M. LaBella, M. Zhu, M. Hollander, R. Kasarda, Z. Hughes, K. Trumbull, R. Cavalero, and D. Snyder, *Applied Physics Letters* **98**, 053103 (2011).
- [128] N. Tombros, C. Jozsa, M. Popinciuc, H. T. Jonkman, and B. J. van Wees, *Nature* **448**, 571 (2007).
- [129] M. Drögeler, C. Franzen, F. Volmer, T. Pohlmann, L. Banszerus, M. Wolter, K. Watanabe, T. Taniguchi, C. Stampfer, and B. Beschoten, *Nano Lett.* **16**, 3533 (2016).
- [130] J. Obrzut, C. Emiroglu, O. Kirillov, Y. Yang, and R. E. Elmquist, *Measurement* **87**, 146 (2016).
- [131] A. V. Kretinin, Y. Cao, J. S. Tu, G. L. Yu, R. Jalil, K. S. Novoselov, S. J. Haigh, A. Gholinia, A. Mishchenko, M. Lozada, T. Georgiou, C. R. Woods, F. Withers, P. Blake, G. Eda, A. Wirsig, C. Hucho, K. Watanabe, T. Taniguchi, A. K. Geim, and R. V. Gorbachev, *Nano Lett.* **14**, 3270 (2014).
- [132] V. V. Cheianov, V. Fal'ko, and B. L. Altshuler, *Science* **315**, 1252 (2007).
- [133] P. Rickhaus, P. Makk, M.-H. Liu, K. Richter, and C. Schönenberger, *Applied Physics Letters* **107**, 251901 (2015).
- [134] P. Rickhaus, R. Maurand, M.-H. Liu, M. Weiss, K. Richter, and C. Schönenberger, *Nature Communications* **4**, 2342 (2013).

- [135] A. L. Grushina, D.-K. Ki, and A. F. Morpurgo, *Applied Physics Letters* **102**, 223102 (2013).
- [136] V. Ranjan, G. Puebla-Hellmann, M. Jung, T. Hasler, A. Nunnenkamp, M. Muoth, C. Hierold, A. Wallraff, and C. Schönenberger, *Nature Communications* **6**, 7165 (2015).
- [137] Z. Chen and J. Appenzeller, *IEEE International Electron Devices Meeting 2008, Technical Digest, International Electron Devices Meeting*, 509–512. (2008).
- [138] J. Xia, F. Chen, J. Li, and N. Tao, *Nat Nano* **4**, 505 (2009).
- [139] S. Dröscher, P. Roulleau, F. Molitor, P. Studerus, C. Stampfer, K. Ensslin, and T. Ihn, *Applied Physics Letters* **96**, 152104 (2010).
- [140] G. L. Yu, R. Jalil, B. Belle, A. S. Mayorov, P. Blake, F. Schedin, S. V. Morozov, L. A. Ponomarenko, F. Chiappini, S. Wiedmann, U. Zeitler, M. I. Katsnelson, A. K. Geim, K. S. Novoselov, and D. C. Elias, *Proceedings of the National Academy of Sciences* **110**, 3282 (2013).
- [141] J. Xue, J. Sanchez-Yamagishi, D. Bulmash, P. Jacquod, A. Deshpande, K. Watanabe, T. Taniguchi, P. Jarillo-Herrero, and B. J. LeRoy, *Nat Mater* **10**, 282 (2011).
- [142] D. C. Elias, R. V. Gorbachev, A. S. Mayorov, S. V. Morozov, A. A. Zhukov, P. Blake, L. A. Ponomarenko, I. V. Grigorieva, K. S. Novoselov, F. Guinea, and A. K. Geim, *Nat Phys* **7**, 701 (2011).
- [143] L. A. Ponomarenko, R. Yang, R. V. Gorbachev, P. Blake, A. S. Mayorov, K. S. Novoselov, M. I. Katsnelson, and A. K. Geim, *Phys. Rev. Lett.* **105**, 136801 (2010).
- [144] J. Chae, S. Jung, A. F. Young, C. R. Dean, L. Wang, Y. Gao, K. Watanabe, T. Taniguchi, J. Hone, K. L. Shepard, P. Kim, N. B. Zhitenev, and J. A. Stroscio, *Phys. Rev. Lett.* **109**, 116802 (2012).
- [145] E. Pallecchi, A. C. Betz, J. Chaste, G. Fève, B. Huard, T. Kontos, J.-M. Berroir, and B. Plaçaais, *Phys. Rev. B* **83**, 125408 (2011).
- [146] M. J. Rahim, T. Lehleiter, D. Bothner, C. Krellner, D. Koelle, R. Kleiner, M. Dressel, and M. Scheffler, *Journal of Physics D: Applied Physics* **49**, 395501 (2016).
- [147] M. Gmitra, D. Kochan, P. Högl, and J. Fabian, *Phys. Rev. B* **93**, 155104 (2016).
- [148] G. L. Yu, R. V. Gorbachev, J. S. Tu, A. V. Kretinin, Y. Cao, R. Jalil, F. Withers, L. A. Ponomarenko, B. A. Piot, M. Potemski, D. C. Elias, X. Chen, K. Watanabe, T. Taniguchi, I. V. Grigorieva, K. S. Novoselov, V. I. Falko, A. K. Geim, and A. Mishchenko, *Nat Phys* **10**, 525 (2014).
- [149] T. Hasler, M. Jung, V. Ranjan, G. Puebla-Hellmann, A. Wallraff, and C. Schönenberger, *Phys. Rev. Applied* **4**, 054002 (2015).
- [150] R. Deblock, E. Onac, L. Gurevich, and L. P. Kouwenhoven, *Science* **301**, 203 (2003).
- [151] A. A. Clerk, M. H. Devoret, S. M. Girvin, F. Marquardt, and R. J. Schoelkopf, *Rev. Mod. Phys.* **82**, 1155 (2010).

-
- [152] C. W. J. Beenakker and M. Büttiker, *Phys. Rev. B* **46**, 1889 (1992).
- [153] K. E. Nagaev, *Phys. Rev. B* **52**, 4740 (1995).
- [154] B. L. Altshuler, A. G. Aronov, and D. E. Khmelnitsky, *Journal of Physics C: Solid State Physics* **15**, 7367 (1982).
- [155] M. Henny, *Shot Noise in Nanoconductors*, Ph.D. thesis, University of Basel (1998).
- [156] S. Hershfield, J. H. Davies, P. Hyldgaard, C. J. Stanton, and J. W. Wilkins, *Phys. Rev. B* **47**, 1967 (1993).
- [157] H. Birk, M. J. M. de Jong, and C. Schönenberger, *Phys. Rev. Lett.* **75**, 1610 (1995).
- [158] E. V. Sukhorukov, G. Burkard, and D. Loss, *Phys. Rev. B* **63**, 125315 (2001).
- [159] A. Cottet, W. Belzig, and C. Bruder, *Phys. Rev. B* **70**, 115315 (2004).
- [160] E. Onac, F. Balestro, L. H. W. van Beveren, U. Hartmann, Y. V. Nazarov, and L. P. Kouwenhoven, *Phys. Rev. Lett.* **96**, 176601 (2006).
- [161] Y. Zhang, L. DiCarlo, D. T. McClure, M. Yamamoto, S. Tarucha, C. M. Marcus, M. P. Hanson, and A. C. Gossard, *Phys. Rev. Lett.* **99**, 036603 (2007).
- [162] S. Gustavsson, M. Studer, R. Leturcq, T. Ihn, K. Ensslin, D. C. Driscoll, and A. C. Gossard, *Phys. Rev. B* **78**, 155309 (2008).
- [163] K. Kaasbjerg and W. Belzig, *Phys. Rev. B* **91**, 235413 (2015).
- [164] D. A. Bagrets and Y. V. Nazarov, *Phys. Rev. B* **67**, 085316 (2003).
- [165] B. Küng, C. Rössler, M. Beck, J. Faist, T. Ihn, and K. Ensslin, *New Journal of Physics* **14**, 083003 (2012).
- [166] Y.-Y. Liu, J. Stehlik, C. Eichler, M. J. Gullans, J. M. Taylor, and J. R. Petta, *Science* **347**, 285 (2015).
- [167] A. Stockklauser, V. F. Maisi, J. Basset, K. Cujia, C. Reichl, W. Wegscheider, T. Ihn, A. Wallraff, and K. Ensslin, *Phys. Rev. Lett.* **115**, 046802 (2015).
- [168] A. Das, Y. Ronen, Y. Most, Y. Oreg, M. Heiblum, and H. Shtrikman, *Nat Phys* **8**, 887 (2012).
- [169] P. Jarillo-Herrero, J. A. van Dam, and L. P. Kouwenhoven, *Nature* **439**, 953 (2006).
- [170] J.-P. Cleuziou, W. Wernsdorfer, V. Bouchiat, T. Ondarcuhu, and M. Monthieux, *Nat Nano* **1**, 53 (2006).
- [171] R. Maurand, T. Meng, E. Bonet, S. Florens, L. Marty, and W. Wernsdorfer, *Phys. Rev. X* **2**, 011009 (2012).
- [172] D. C. Ralph, C. T. Black, and M. Tinkham, *Phys. Rev. Lett.* **74**, 3241 (1995).
- [173] J. C. Cuevas, A. Martín-Rodero, and A. L. Yeyati, *Phys. Rev. Lett.* **82**, 4086 (1999).

- [174] R. Cron, M. F. Goffman, D. Esteve, and C. Urbina, *Phys. Rev. Lett.* **86**, 4104 (2001).
- [175] J. P. Hessling, V. S. Shumeiko, Y. M. Galperin, and G. Wendin, *Europhysics Letters* **34**, 49 (1996).
- [176] D. Averin and H. T. Imam, *Phys. Rev. Lett.* **76**, 3814 (1996).
- [177] D. Averin and A. Bardas, *Phys. Rev. B* **53**, R1705 (1996).
- [178] T. Hoss, C. Strunk, T. Nussbaumer, R. Huber, U. Staufer, and C. Schönenberger, *Phys. Rev. B* **62**, 4079 (2000).
- [179] D. Averin and A. Bardas, *Phys. Rev. Lett.* **75**, 1831 (1995).
- [180] P.-M. Billangeon, F. Pierre, H. Bouchiat, and R. Deblock, *Phys. Rev. Lett.* **98**, 216802 (2007).
- [181] D. G. Olivares, A. L. Yeyati, L. Bretheau, Ç. Ö. Girit, H. Pothier, and C. Urbina, *Phys. Rev. B* **89**, 104504 (2014).
- [182] M. A. Despósito and A. Levy Yeyati, *Phys. Rev. B* **64**, 140511 (2001).
- [183] C. Janvier, L. Tosi, L. Bretheau, Ç. Ö. Girit, M. Stern, P. Bertet, P. Joyez, D. Vion, D. Esteve, M. F. Goffman, H. Pothier, and C. Urbina, *Science* **349**, 1199 (2015).
- [184] M. Zgirski, L. Bretheau, Q. Le Masne, H. Pothier, D. Esteve, and C. Urbina, *Phys. Rev. Lett.* **106**, 257003 (2011).
- [185] J. Nygård, D. H. Cobden, and P. E. Lindelof, *Nature* **408**, 342 (2000).
- [186] Y. Avishai, A. Golub, and A. D. Zaikin, *Phys. Rev. B* **67**, 041301 (2003).
- [187] Y. Meir and A. Golub, *Phys. Rev. Lett.* **88**, 116802 (2002).
- [188] E. Sela, Y. Oreg, F. von Oppen, and J. Koch, *Phys. Rev. Lett.* **97**, 086601 (2006).
- [189] T. Delattre, C. Feuillet-Palma, L. G. Herrmann, P. Morfin, J.-M. Berroir, G. Fève, B. Placais, D. C. Glattli, M.-S. Choi, C. Mora, and T. Kontos, *Nat Phys* **5**, 208 (2009).
- [190] Y. Yamauchi, K. Sekiguchi, K. Chida, T. Arakawa, S. Nakamura, K. Kobayashi, T. Ono, T. Fujii, and R. Sakano, *Phys. Rev. Lett.* **106**, 176601 (2011).
- [191] X. Zhou, V. Schmitt, P. Bertet, D. Vion, W. Wustmann, V. Shumeiko, and D. Esteve, *Phys. Rev. B* **89**, 214517 (2014).
- [192] C. Ertler, S. Kunschuh, M. Gmitra, and J. Fabian, *Phys. Rev. B* **80**, 041405 (2009).
- [193] Z. Su, A. B. Tacla, M. Hocevar, D. Car, S. R. Plissard, E. P. A. M. Bakkers, A. J. Daley, D. Pekker, and S. M. Frolov, [arXiv:1611.00727](https://arxiv.org/abs/1611.00727) (2016).
- [194] J. Gramich, A. Baumgartner, and C. Schönenberger, [arXiv:601.00672](https://arxiv.org/abs/601.00672) (2016).
- [195] M. Snelder, M. Veldhorst, A. A. Golubov, and A. Brinkman, *Phys. Rev. B* **87**, 104507 (2013).
- [196] J. Furer, *Growth of Single-Wall Carbon Nanotubes by Chemical Vapor Deposition for Electrical Devices*, *Ph.D. thesis*, University of Basel (2006).

A Fabrication Recipes

Already in the chapter 4, fabrication techniques for devices on carbon nanotubes, InAs nanowires and graphene are discussed. The aim of this appendix is to provide details of the fabrication recipes. For all devices, stub tuner is fabricated in the first step.

Device substrate

- Dice an undoped Si wafer ($\rho > 5000 \text{ } \Omega\text{cm}$) with 170 nm of thermal oxide on top into a usable size 10 cm \times 10 cm.
- Sonicate for 10 minutes each in acetone, IPA and DI water and blow dry.
- Bake at 110°C for 2 minutes.
- Clean in the Piranha-etch 1:3 mix of H₂O₂ and H₂SO₄ for 15 minutes.
- Rinse in DI water for 2 minutes and blow dry.

Stub tuner

- Sputter a 100 – 150 nm thick Nb film at a rate 1 Å/s using Ar gas at a flow of 40 sccm, background pressure of 4 mTorr and RF power 160 W in AJA magnetron sputtering system.
- Spin coat a sacrificial photo resist AZ1512 and dice into small chip sizes.
- Clean with NMP, acetone and IPA in an ultrasonic bath and blow dry.
- Spin coat 1 μm thick resist AZ1512 HS and bake at 100° for 1 minute.
- UV exposure in Süss MicroTec mask aligner at a wavelength 365 nm, power 280 W and intensity 32 mW/cm² for 1.2 s.
- Develop for 17 s in MIF 726, stop in DI water for 30 s and blow dry.
- Nb etching in Sentech ICP machine with Ar/Cl₂ at flow of 25/40 sccm, background pressure 1 Pa, DC power 100 W and RF power 125 W producing an etch rate of $\sim 4 \text{ nm/s}$.
- Follow with etching few nanometers of SiO₂ surface with Ar and then O₂ without breaking the vacuum of ICP.
- Strip the resist in hot NMP at 70°C and hot acetone at 50°C for 30 minutes each. Clean in ultrasonic bath and blow dry.

Bottom gates

- Spin coat 300 nm of PMMA, bake at 180°C for 10 minutes.
- Ebeam lithography at acceleration voltage of 20 kV and a line dose of 2500 pC/cm. Cold develop at 5°C for one minute in a 1:3 mix of MIBK and IPA and stop in IPA for 10 s.
- 40 nm of anisotropic etching of SiO₂ with CF₄ in ICP at RF power 45 W, DC power 50 W, flow 40 sccm and pressure 0.8 Pa. Follow with 30 nm of isotropic etching in HF. Rinse vigorously in DI Water for 1 minute.
- Evaporate Ti(5 nm)/Au(35 nm) in Sharon evaporator.
- Lift-off in hot acetone and IPA and clean in ultrasonic bath.

Pillar

- After fabrication of bottom gates and source drain contacts, expose rectangular areas around these using eBeam lithography at acceleration voltage of 20 kV and area dose of 220 $\mu\text{C}/\text{cm}^2$ on a 1.2 μm thick PMMA.
- Etch SiO₂ with CHF₃ at 50 mTorr, 200 W, 8 sccm in Oxford reactive ion etcher producing a rate of 50 nm/min.
- Without breaking the vacuum, etch Si with SF₆/O₂ at 12.5/5 sccm, 75 mTorr, 100 W producing a rate of 1 $\mu\text{m}/\text{min}$.
- Leave in hot acetone for one hour and clean in ultrasonic bath. Blow dry.
- Argon/Oxygen plasma, if needed, to get rid of resist residues.

Deterministic CNT stamping

- Wire bond the stub tuner circuit with the pillar structure housing source drain contacts and bottom gates.
- Clean the device and PCB with Ar plasma in Oxford RIE machine for 20 s at flow of 50 sccm, background pressure 50 mTorr and DC power 200 W.
- Mount the PCB in the micro-manipulator setup and place the probe needles on the bond pads.
- Mount the CNT forks on a separate arm and align with the pillar using the optical microscope.
- Apply voltages to the source drain contacts and monitor the current while lowering the forks on the pillar. If no current recorded, proceed to the next fork.
- To remove the unwanted tubes, simply apply a large bias voltage till no current is recorded.

Markers

- Spin coat 300 nm of ZEP resist, bake at 180°C for 3 mins.
- Ebeam lithography: 20 kV, 68 $\mu\text{C}/\text{cm}^2$.
- Develop in Pentyl acetate for one minute and stop in 9:1 mix of MIBK and IPA and rinse in IPA for 10 s.
- Evaporate Ti(5 nm)/Au(45 nm) and lift-off in hot acetone.

Stamp substrate

- Spin coat a double layer of PMMA(300 nm, bake 180°C) and negative resist HSQ(1 μm , bake at 90°C)
- Ebeam lithography with area dose 200 $\mu\text{C}/\text{cm}^2$.
- Develop in TMAH (25% solution) for 25 s and stop in DI water and IPA.
- PMMA removal with O₂ etching in RIE: 16 sccm, 250 mTorr, 100 W.
- SiO₂ removal with HF etching
- Si etching in the same way as for the pillars.
- Wafer cleaving to have one stamp area 2 mm \times 2 mm per piece.
- CNT growth using the recipe from ref. [196].

Probabilistic CNT stamping

- Place the device substrate on the mask aligner stage.
- Mount a transparent glass plate in the mask slot and glue the stamp substrate in the middle using undiluted PMMA.
- Align two substrates using the optical microscope. This needs to be done sooner to avoid the glue getting harder.
- Perform the WEC alignment. Once it beeps "OK", make 6 complete turns on the knob to increase contact force.

Al contacts on CNT

- eBeam lithography with 300 nm thick ZEP: 10 kV, Area dose 34 $\mu\text{C}/\text{cm}^2$, line dose 240 pC/cm.
- Thermal evaporation in Bestec machine: chamber cooled to -180°C and head cooled to -30°C.
- First Ti (4.5 nm) and then Al (75 nm).
- Standard lift-off in hot acetone.

Nanowire transfer

- Expose a rectangular area using standard ebeam lithography over the stub tuner region to receive nanowires and subsequently develop.
- Hold a cleanroom wipe cut in shape of a flag, and bring it close the nanowire substrate.
- Rub the wipe on the exposed area and inspect under optical microscope to check the transferred nanowires. Repeat if necessary.
- Strip the resist in hot acetone. Avoid ultrasonic cleaning.

Nanowire etching

- Spin coat 200 nm thick PMMA. Ebeam exposure: $300 \mu\text{C}/\text{cm}^2$, $3000 \text{ pC}/\text{cm}$ at 20 kV. Standard development in MIBK:IPA.
- Etch 30 nm of Al in transene type D at 50°C for 12 s followed by rigorous rinsing in DI water for 30 s.
- Transfer to IPA and blow dry.
- Strip the resist in hot acetone and IPA. Blow dry.

Contacts to Nb

- Standard eBeam lithography with 400 nm thick PMMA and resist development in MIBK:IPA.
- Ar milling of Nb surfaces for 30 s, recipe number 2 at acceleration voltage of 500 V in Balzers evaporation system.
- Evaporate 70(100) nm of Pd for contacting Nb with thickness of 100(150) nm.
- Standard lift off in hot acetone.

Graphene transfer

- Place a $4 \times 4 \times 1 \text{ mm}^3$ PDMS layer on a glass slide. Cover the entire slide with polycarbonate layer.
- Mechanically exfoliate hBN and graphene on two separate substrates.
- Place the glass slide on a chuck and align the substrate with respect to the PDMS. Pickup hBN by bringing then in contact and heating the chuck to 80°C .
- Repeat for the graphene flake while aligning then in the microscope.
- To release the stack, heat the target substrate to 150°C .
- Etch the stack in RIE with $\text{SF}_6/\text{Ar}/\text{O}_2$: Flow 20/5/5 sccm, pressure 60 mTorr, Power 50 W.

B List of Setup Components

A detailed wiring of the Triton cryostat is presented in Fig. 4.10. Below, we provide technical specifications of the respective components, taken from [87].

Type	Brand and part number	Specifications
<i>Cryostat</i>	Oxford Triton 200 cryo-free dilution refrigerator	Base temperature 20 mK
<i>Magnet</i>	Oxford 3D vector magnet IPS power supply	Maximum field strength in - x -direction: 1 T - y -direction: 1 T - z -direction: 6 T
<i>Directional coupler</i>	Fairview microwave MC 2104-20	Frequency range 1 – 4 GHz
<i>Bias tee</i>	Mini-Circuits ZFBT-6GW+	Original frequency range 0.1 – 6 GHz, capacitance lowered to 22 pF
<i>Circulator</i>	QuinStar CTD0304KC	Frequency range 2.75 – 3.25 GHz
<i>Low-pass filter on the DC side of the bias tee</i>	Mini-Circuits VLFX-80	Pass-band DC - 80 MHz
<i>Low-temperature amplifier</i>	Low Noise Factory LNF-LNC1_12A	Frequency range 1 – 12 GHz, gain \sim 35 dB
<i>First room-temperature amplifier</i>	Miteq AMF-3F-01000400-08-10P	Frequency range 1 – 4 GHz, gain \sim 35 dB
<i>Second room-temperature amplifier</i>	Miteq NSP1000-NVG	Frequency range 0.1 – 10 GHz, gain \sim 35 dB
<i>Pi-filters in break-out box</i>	Tusonix 4201-001LF	Pass-band DC - 10 MHz
<i>DC wires</i>	Constantan loom	24 \times 2 wires (twisted pairs)
<i>Coaxial cable down to MC plate</i>	UT85	Centre and outer conductors stainless steel, operating frequency $<$ 18 GHz

B. List of Setup Components

Type	Brand and part number	Specifications
<i>Coaxial cable from MC plate to puck</i>	UT85	Centre and outer conductors copper, operating frequency < 18 GHz
<i>Coaxial cable inside puck</i>	Huber+Suhner EZ_47_TP_M17	Operating frequency < 100 GHz
<i>Sample holder PCB</i>	Designed with Design-Spark PCB, ordered from Probst Hightech	Substrate: Rogers RO4003C metals: Cu 40 – 43 μm , Ni 3 – 6 μm , Au 50-100 nm
<i>PCB mount SMP connectors</i>	Rosenberger 19K101-270L5	Material brass (gold plated), male
<i>PCB mount DC connectors (Nano-connector)</i>	Omnetics A42046-001 (MNPO-25-DD-C-ETH-M)	25 pins, male

Measurement instruments

<i>Vector network analyser</i>	R&S ZNB8	Frequency range 0.1 – 8.5 GHz
<i>Signal and spectrum analyser</i>	R&S FSW8	Frequency range 2 Hz – 8 GHz
<i>Digital multimeter</i>	Agilent 34410A	For DC measurements
<i>I/V-converter</i>	SP 938	Feedback resistance 10^7 or $10^8 \Omega$, home-made by the electronics workshop
<i>Voltage DAC</i>	SP 927	8 channel voltage source, home-made by the electronics workshop

Curriculum Vitae

Vishal Ranjan

Born on 21st January 1988 in Patna (India)

Education

- 3/2013–2/2017 **PhD in experimental physics at the University of Basel**
- Dissertation in the group of Prof. C. Schönenberger
“Admittance and noise detection in mesoscopic systems via GHz impedance matching”
- 9/2009–8/2011 **Masters of science at the University of Groningen**
- Master thesis in the group of Prof. B. van Wees
“Non-linear interactions between spin, heat and charge currents in graphene nanostructures”
 - Project thesis in the group of Prof. A. Herrmann
“Slippery DNA: study of repulsive forces between DNA strands through atomic force microscopy”
- 8/2005–5/2009 **Bachelors of technology in engineering physics at Indian institute of technology Bombay**
- Project thesis in the group of Prof. A. Mahajan
“Preparation and characterization of geometrically frustrated spin ladder systems”

Positions

- 9/2013–12/2016 *Teaching assistant for physics at the University of Basel*
- 9/2011–11/2012 *Research assistant at the Technical University of Delft*
- Group of Prof. Leo DiCarlo
“Probing dynamics of an electron-spin ensemble via a superconducting resonator”
- 5/2008–8/2008 *Summer intern at the University of Groningen*
- Group of Prof. Paul van Loosdrecht
“Infrared spectroscopy of geometrically frustrated rare earth titanates”

Publications

- **Nonlinear interaction of spin and charge currents in graphene** I. J. Vera-Marun, V. Ranjan, B. J. van Wees, *Physical Review B* **84**, 241408(R) (2011).
- **Nonlinear detection of spin currents in graphene with non-magnetic electrodes** I. J. Vera-Marun, V. Ranjan, B. J. van Wees, *Nature Physics* **8**, 313-316 (2012)
- **Probing dynamics of an electron-spin ensemble via a superconducting resonator** V. Ranjan*, G. De Lange*, R. Schutjens, T. Debelhoir, J. P. Groen, D. Szombati, D. J. Thoen, T. M. Klapwijk, R. Hanson, L. DiCarlo, *Physical Review Letters* **6**, 110 (2013).
- **Clean carbon nanotubes coupled to superconducting impedance-matching circuits** V. Ranjan*, G. Puebla-Hellmann*, M. Jung, T. Hasler, A. Nunnenkamp, M. Muoth, C. Hierold, A. Wallraff, and C. Schönenberger, *Nature Communications* **6**, 7165 (2015).
- **Shot noise of a quantum dot measured with gigahertz impedance matching** T. Hasler, M. Jung, V. Ranjan, G. Puebla-Hellmann, A. Wallraff, and C. Schönenberger, *Physical Review Applied* **4**, 054002 (2015).
- **Contactless characterizations of graphene p - n junctions** V. Ranjan, S. Zihlmann, P. Makk, K. Watanabe, T. Taniguchi and C. Schönenberger, [arXiv:1702.02071](https://arxiv.org/abs/1702.02071) (2017).
- **Quantum dot spectroscopy through shot noise** M. C. Harabula, V. Ranjan, R. Haller, G. Fülöp, M. Jung and C. Schönenberger, *in preparation*.

* Equal contribution

Talks

- *Impedance and noise measurements of CNT quantum dots using GHz superconducting matching circuits* QSIT Lunch Seminar, Zürich, July 2015
- *Probing quantum transport and shot-noise using impedance matching circuits* NCCR QSIT General Meeting, Arosa, February 2016
- *Quantum capacitance and dissipation in graphene pn junctions* Graphene workshop, Basel, October 2016

Poster Contributions

- *A hybrid superconductor-spin system for quantum information processing*
V. Ranjan, G. de Lange, R. Schutjens, T. Debelhoir, J. P. Groen, D. Szombati, D. J. Thoen, T. M. Klapwijk, R. Hanson, and L. DiCarlo, *Frontiers in Quantum Engineered Devices*, Obergurgl, August 2013
- *Single Carbon Nanotubes Integrated into GHz Impedance Matching Circuits*
V. Ranjan, G. Puebla-Hellmann, M. Jung, T. Hasler, M. Muoth, C. Hierold, A. Wallraff and C. Schönenberger, *Arosa General Meeting*, January 2014
- *Ultraclean carbon nanotubes coupled to superconducting matching circuits*
V. Ranjan, G. Puebla-Hellmann, M. Jung, T. Hasler, A. Nunnenkamp, M. Muoth, C. Hierold, A. Wallraff and C. Schönenberger, *Frontiers in Condensed Matter Physics*, San Sebastian, September 2014
- *Impedance and noise measurements of clean CNT quantum dots using GHz superconducting matching circuits*
V. Ranjan, T. Hasler, M. Jung, G. Puebla-Hellmann, A. Nunnenkamp, M. Muoth, C. Hierold, A. Wallraff and C. Schönenberger, *International Conference on Quantum Systems and Technology*, Monte Verita, June 2015
- *Impedance and noise measurements of clean CNT quantum dots using GHz superconducting matching circuits*
V. Ranjan, T. Hasler, M. Jung, G. Puebla-Hellmann, A. Nunnenkamp, M. Muoth, C. Hierold, A. Wallraff and C. Schönenberger, *Spin Tech VIII*, August 2015

Acknowledgments

It has been almost four years since I started my PhD in the nanoelectronics group. Especially, when starting a new project, things require a lot of collaboration to get moving. I feel lucky to have met so many people, who not only made sure that my research goes smooth, but also created an atmosphere to enjoy my stay in Basel. I would like to acknowledge everyone who helped me finish this thesis.

Firstly, I would like to express my gratitude towards my thesis advisor Prof. Christian Schönenberger for providing me an opportunity to work on a fascinating scientific and engineering topic. His determination in problem solving and confidence in trying something new has been truly motivating and essential for whatever I managed to produce. I am always amazed with the kind of enthusiasm he brings to the lab and group meetings. And to the skiing slopes. And who can forget our singing session, *Twelve years of PhD*,¹ at 2014 Arosa general meeting. I feel privileged to have learned, and shared knowledge and experiences alike, with an exceptional person who leads by example. I would also like to thank Prof. Hugues Pothier and Dr. Mark Buitelaar for taking part in my defence and reading the thesis.

Next, I would like to acknowledge Gergö and Floris for their enormous help in proof-reading my thesis. Their constant and critical suggestions have significantly improved my text. I also thank Miglé and Deva for their valuable comments.

Here in Basel, I really enjoyed working closely with Minkyung and Thomas for most part of my thesis. Their professional dedication was essential in setting up the project in a short time. I am thankful to Thomas for his massive efforts in stamping technique and calibration of the noise signals. We were later joined by Cezar, Roy and Gergö who have been pushing this project even further.

The thesis owes a lot to the collaborators for their invaluable help. In the beginning, Gabriel and Prof. Andreas Wallraff from ETH zürich introduced us to the stub tuner circuit. Also, Matthias Muoth and Christoph Hierold were kind enough to let us use their home-made micro-manipulator at FIRST cleanroom. Their support was crucial in initiating the first scientific results of the RF team. Andreas Nunnenkamp and Gergö happily contributed to the theory part. In the later half of my thesis work, we could even expand the RF project with nanowire team - Christian Jünger and Andreas Baumgartner and graphene team - Peter Makk and Simon Zihlmann.

I am also thankful to all former and current group members of the nanoelectronics group for their invariable support in device fabrications and scientific discussions. I mention them here: Andreas Baumgartner, Anton Vladkya, Arunav Bordoloi, Axel Fanget, Christian Jünger, Clewin Handschin, Cornelia Nef, David Indolese, Frederick Thomas, Gábor Fábíán, Gergö Fülöp, Gulibusitan Abulizi, Jan Overbeck, Jens Schindele, Jörg

¹Not related to the Hollywood movie "12 years a slave", released around the same time.

Gramich, Julia Samm, Kishan Thodkar, Lujun Wang, Maria El Abbassi, Masoud Baghernejad, Mathias Wipf, Matthias Bräuninger, Michel Calame, Mihai-Cezar Harabula, Minkyung Jung, Oliver Braun, Péter Makk, Peter Rickhaus, Quentin Berrahal, Ralph Stoop, Raphaëlle Delagrangé, Romain Maurand, Roy Haller, Samuel d'Hollosy, Simon Zihlmann, Stefan Nau, Thomas Hasler, Toni Fröhlich and Wangyang Fu. Moreover, I am really glad to have been part of so many group excursions, conferences, lunches and coffee breaks with them.

Special thanks goes to the department staff for their outstanding professional services. These include Michael Steinacher from the electronics workshop, Sascha Martin, Patrick Stöcklin, Daniel Sacker and Domink Sifrig from the mechanical workshop, and Barbara Kammermann and Astrid Kalt from the secretarial office. I could always count on them for any help I needed.

Lastly, I am indebted to my family and friends for their unconditional support and encouragement, especially in frustrating times. I cannot imagine, let alone this thesis, my life without them. Thank you for your understanding and sharing precious moments with me. On a personal note, I dedicate this thesis to my parents.